# Genesis and Shapes of Salt and Gypsum Solution Cavities Created by Density-driven Groundwater Flow: A Laboratory Experimental Approach

Inauguraldissertation

zur
Erlangung der Würde eines Doktors der Philosophie
vorgelegt der
Philosophisch-Naturwissenschaftlichen Fakultät
der Universität Basel

von
Daniel Gechter
aus Wohlen (BE)

Basel, 2008

Genehmigt von der Philosophisch-Naturwissenschaftlichen Fakultät

auf Antrag von Prof. Dr. Peter Huggenberger
Universität Basel

Dr. Philippe Ackerer
Centre national de la recherche scientifique (CNRS) et
Université Louis Pasteur Strasbourg

Basel, den 24. Juni 2008

Prof. Dr. Hans-Peter Hauri
Dekan

# Abstract

Density-driven groundwater flow in evaporite bearing sedimentary rocks and resulting karstification frequently cause geomechanical problems, such as land subsidence and collapses. These processes are also of major concern in the Muttenz-Pratteln region, located in the Tabular Jura, southeast of Basel, where a tabular interstratal karst was detected at the top of the Triassic rock salt layer. In this area, a section of the European North-South railway connection is also affected by land subsidence. To overcome the complexity of a field experiment, this thesis scaled down the analysis of salt and gypsum karstification to two different types of newly developed laboratory experiments. In rock salt dissolution experiments, freshwater was pumped from the side or from above into rock salt cores through an axial borehole. In the other setup, solute transport experiments were conducted in a 2D flow tank containing a water-saturated porous medium. The main objectives of these experimental investigations were to understand (1) the genesis of a solution cavity created by concentration-driven buoyant flow coupled with mineral dissolution within salt and gypsum rocks (by a horizontally-oriented borehole), (2) the genesis of an interstratal salt karst at the top of a salt layer (by an almost vertically or inclined-oriented borehole) and (3) to develop a suitable tank (benchmark) to test density-dependent flow computer codes.

In the rock salt dissolution experiments, halite dissolution took place only in the inflow of the rock salt cylinders. In the case of a horizontally-oriented borehole, the created solution cavities are approximately shaped like a half cone with a horizontal base facing upward. The halite dissolution took place at the horizontal ceiling and upper end of the facet so that the cavities enlarged under confined conditions by upward growth of the horizontal ceiling and also simultaneously by lateral growth at the upper end of the facet. A conceptual model was developed inspired by these results and based on theoretical, hydraulic-geochemical considerations, as well as on field observations in natural caves and/or man-made caverns. It proposes that triangular prism or conical shaped solution cavities develop in salt and gypsum rock under confined conditions with an artesian flow traveling from an underlying, practically insoluble aquifer into the soluble stratum. In the case of an almost vertical or inclined borehole, a tabular solution cavity developed at the upper end of the core cylinders. At first, these cavities generally enlarged radially outward from the borehole at the inlet side, subsequently they enlarged mainly in up dip direction. If NaCl-undersaturated water came into contact with a laterally lying insoluble material or upward lying salt, the cavity enlarged along the insoluble boundary laterally and downward or upward, respectively. The findings were scaled up and integrated into a conceptual model for interstratal salt karst development in the context of horst and graben structures as observed in the Muttenz-Pratteln region. For the latter region, this subsurface conceptual model may explain the detected land subsidence pattern, clearly influenced by the normal faults trend.

A resistance measuring cell was successfully developed for the solute transport experiments. It can measure in situ and indirectly solute concentrations over a wide range (up to halite saturation) and is suitable for 1D and 2D flow tank experiments. First solute transport experiments reveled that the build up benchmark has to be developed further.

Overall, the investigations reveal the necessity of small-scale dissolution experiments (in combination with hydrogeological, hydraulic and geochemical knowledge) when trying to understand the complex processes underlying natural karstification created by density-driven groundwater flow. Regarding the realized flow tank setup, this forms a good basis to finally obtain an excellent benchmark. This thesis will provide the base for new and additional discussions on subsurface salt dissolution and solute transport.

# Acknowledgments

I am grateful to all those who have contributed to this work in some way or other. However, there are too many to list individually.

Firstly, I wish to thank my advisors Peter Huggenberger and Philippe Ackerer for their guidance and support during my thesis. Both stimulated my work by academic freedom and many valuable suggestions and interesting discussions. I am also indebted to Peter Huggenberger to have given me the opportunity of "returning to the University" to complete a dissertation. Further, I should like to thank Peter Huggenberger for his patience at the end of my thesis.

I would like to express my gratitude to Niklaus Waber (University of Bern) and Alfred Wüest (Eawag) for their fruitful discussions and for encouraging remarks and advices, which greatly contributed to the submitted papers. I am also very grateful to Edi Meier (Edi Meier + Partner AG) for developing the resistance measuring cells and computerized data acquisition system. I am very much indebted to Hans-Ruedi Rüegg, Claude Schneider and Willy Tschudin of the University of Basel, and to Claude Veit, Johary Rasamimanana and Abdel Azizi of the University Louis Pasteur Strasbourg for their technical and laboratory assistance.

I am also grateful to all the people working during my thesis in the Section of Applied and Environmental Geology. In particular, Ralph Kirchhofer for his excellent support during computer problems and Ina Spottke for her assistance in presenting the geological setting of the study area. I also thank my colleagues of the Section of Hydrodynamique et Transferts en Milieux Poreux of the University Louis Pasteur Strasbourg, mainly Jérôme Carrayrou, François Lehmann and Anis Younes.

Furthermore, at the University of Basel I want to thank Willem Stern and Heinz Hürlimann (Institute of Mineralogy and Petrography), Markus Dürrenberger and Daniel Mathys (Center of Microscopy), Thomas Lehmann (New Media Center), Rudolf Gschwind (Imaging & Media Lab), and Lukas Hauber (Institute of Geology and Paleontology) for their individual contributions to this work. I thank Peter Mahler-Wenger (Fachhochschule Nordwestschweiz) for providing land subsidence data, and Emanuel Segal for some mathematical assistance. Special thanks go to Sylvie Peter for her linguistic revision.

Thanks also go to Taef Aswed und Mohammed Hayek for providing a family atmosphere during my stay in Strasbourg. I want to extend my gratitude to my family for their unlimited support and encouragement. Finally, I would also like to thank Eveline for her patience, love and to assure a balance in my life between research and free time.

*This study presented herein was sponsored by the Swiss National Science Foundation, Grants 21.65092.01 and 200020-105492, and by the Swiss Academy of Engineering Sciences, Grant SANW-02-01.*

# Contents

Appendices

Curriculum Vitae

# 1 Introduction

## 1.1 Motivation

Interstratal karstification of salt frequently causes geomechanical problems, such as land subsidence and collapse (e.g., Quinlan et al., 1986; Waltham, 1989). This is of major concern for a densely populated area southeast of the city of Basel that comprises a section of the new European North-South railway connection (Figure 1.1A). Leveling measurements revealed land subsidence in the west of the study area and a southwest-northeast-oriented, elongated subsidence bowl in Lachmatt, located near the northern entrance of the Adler tunnel completed a few years ago (Figure 1.1B). In the latter area, a section of the railway line is also affected by land subsidence. Furthermore, the regional subsurface is excessively used for solution mining of halite (NaCl) and groundwater extraction for industrial purposes (Figure 1.1B). The pumped groundwater in the Schweizerhalle area has relatively high $Na^+$ and $Cl^-$ concentrations (up to several hundreds $Cl^-$ per l) with frequent Na/Cl molar ratios around 1 (BMG Engineering AG, 1997). This suggests that the underground occurring salt is a possible source for groundwater salinization. It is not clear if none, one or both of these anthropogenic activities are the trigger and/or contributor of the existing salt karstification.

This thesis attempts to provide an increased understanding of the complex processes underlying natural and anthropogenically induced interstratal salt karstification – a key factor for effective planning control and engineering practice.

## 1.2 Study area

The (hydro)geologically studied area, located southeast of Basel, Switzerland (Figure 1.1A), comprises the small town of Muttenz, part of the small town of Pratteln and the industrial zone of Schweizerhalle near the river Rhine. In this area, the Rhine forms a natural border to Germany. The (hydro)geology in this area is well documented, however, subsidence data is scarce. This section first provides geological (Section 1.2.1) and surface leveling data (Section 1.2.1.1) and subsequently describes the hydrogeological conditions (Section 1.2.2) and potential subsidence-promoting anthropogenic activities (Section 1.2.3).

### 1.2.1 Geological setting

The study area is located in the Tabular Jura on the southeastern border of the Upper Rhine Graben (Figure 1.1A). The Triassic and Jurassic strata in this area form part of the sedimentary cover of the Variscan basement of the Black Forest. The sediments dip gently southward, generally 5–10° and are overlain by Quaternary sediments (Hauber, 1980). The most striking tectonic feature of the region is the presence of a large number of normal faults, mainly found in NNE–SSW direction, but also in WWN–EES direction resulting in faulted blocks, horsts and grabens (cf. Figure 1.1A, Figure 1.2A, and Figure 1.2B). These faults date back to the subsidence of the Rhine Graben in Eocene-Oligocene times (Pearson et al., 1991). The Rhine Graben is a rift valley separating the Black Forest from the Vosges (Hauber, 1980).

Figure 1.3 provides a schematic, stratigraphic section of the Middle Muschelkalk upwards, emphasizing units of hydrogeological significance in this region. In the following, the description of the sedimentary sequences is based on Pearson et al. (1991), its thicknesses on Bitterli-Brunner and Fischer (1988), if not specified otherwise.

The Middle Muschelkalk is dominated by evaporitic facies. The Lower Sulfatzone (a few m thick) is characterized by an alternation of shales and bedded massive anhydrite. The following rock salt layer (up to 50 m thick and more) consists of continuous salt beds with horizontal interbedded marls and anhydrite (Herzog, 1956; Hauber, 1971). The overlain Upper

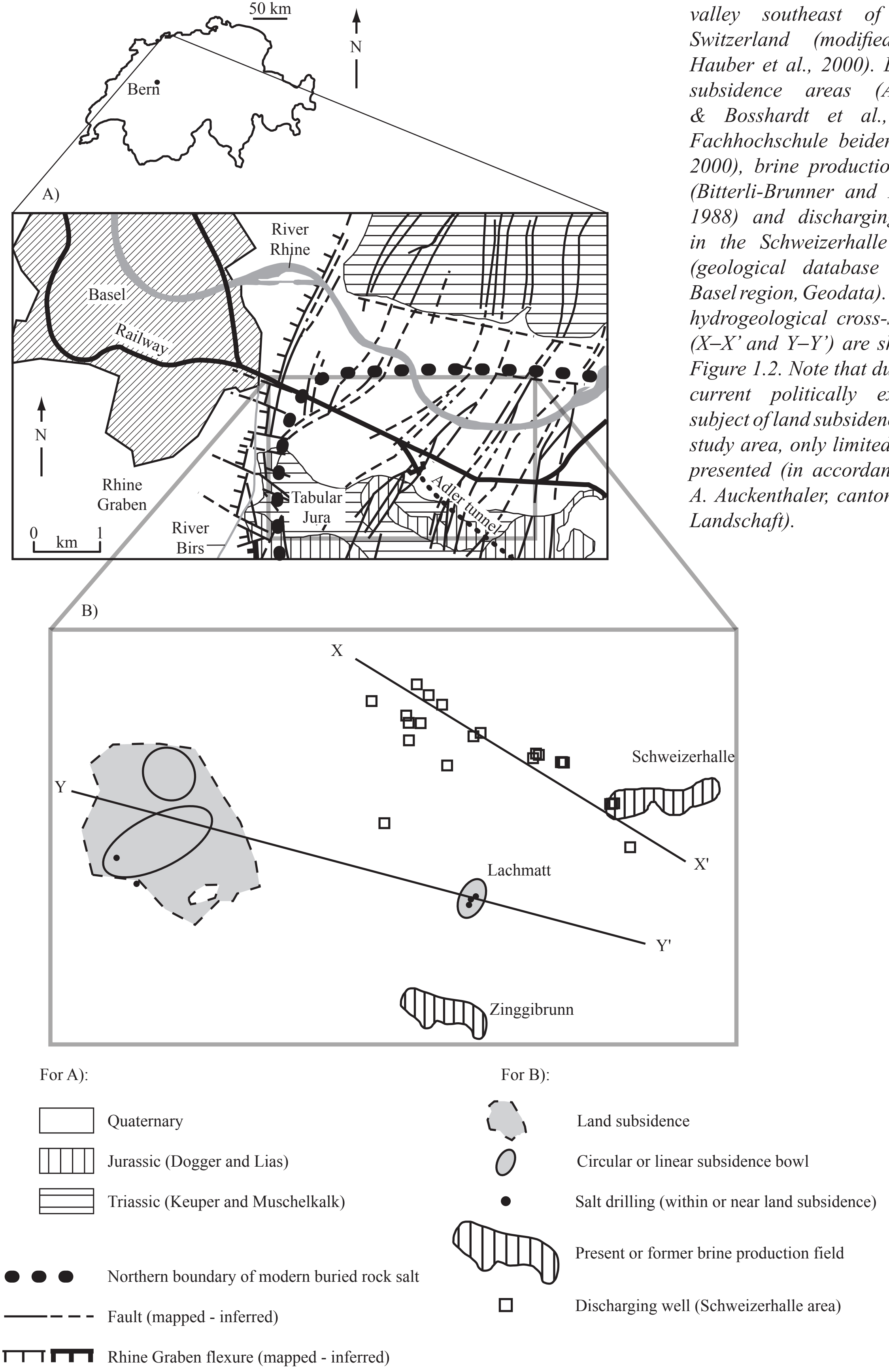

***Figure 1.1*** *A) Location map showing the position of the new railway line (Adler tunnel), the lithologies and the main tectonic structures of the Rhine valley southeast of Basel, Switzerland (modified from Hauber et al., 2000). B) Land subsidence areas (Aegerter & Bosshardt et al., 1999; Fachhochschule beider Basel, 2000), brine production fields (Bitterli-Brunner and Fischer, 1988) and discharging wells in the Schweizerhalle region (geological database of the Basel region, Geodata). The two hydrogeological cross-sections (X–X' and Y–Y') are shown in Figure 1.2. Note that due to the current politically explosive subject of land subsidence in the study area, only limited data is presented (in accordance with A. Auckenthaler, canton Basel-Landschaft).*

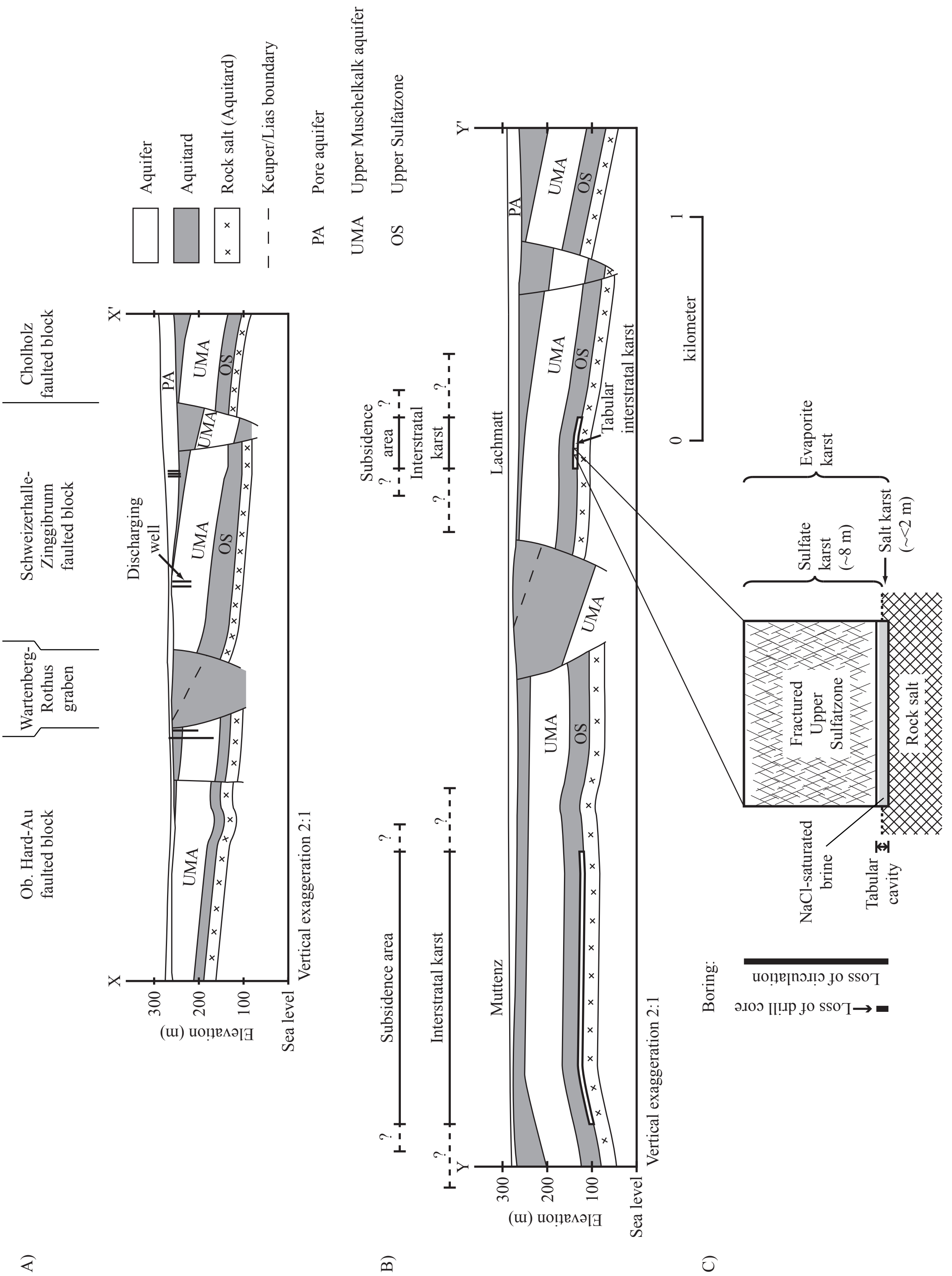

***Figure 1.2*** *Hydrogeological cross-sections (A) X–X' and (B) Y–Y' (lines of sections shown in Figure 1.1). The blocks and graben are named after Herzog (1956). Some discharging wells are presented in X–X'. C) Schematic close-up of interstratal evaporite karst in Lachmatt.*

Sulfatzone exhibits the same but a far thicker (up to 50 m and more) succession than the Lower Sulfatzone. The evaporitic sequence is capped by a ~10 m thick sequence of porous dolomite. The Upper Muschelkalk (50–60 m) consists of marine limestones overlain by a 15–25 m thick bituminous dolomite (Trigonodus-Dolomit).

The overlying Keuper unit is approximately 100 m thick (up to 150 m and more). The Lettenkohle of the Lower Keuper (~5 m) consists of porous dolomite beds separated by the thinner beds of shales. The Middle Keuper is mostly characterized by the thick Gipskeuper (60–100 m), a heterogeneous formation comprising gypsum or anhydrite, shale and dolomitic marls. The Gipskeuper is overlain by Schilfsandstein, which represents fluvial channel facies, and by the associated overbank deposits of the Untere Bunte Mergel, mainly consisting of variegated dolomitic marls. The total thickness varies from 20–25 m. A further sequence of up to 30 m thick variegated marls (Obere Bunte Mergel) is separated from the lower marls by an up to 10 m thick dolomite (Gansinger Dolomit). The Upper Keuper is characterized by rapid lateral facies changes varying in thickness from 1–5 m. Dark grey shales, fine-grained quartz sandstones and bonebeds are the dominant lithologies.

The Liassic (20–50 m) consists of thick argillaceous intervals including the Posidonia Shales, with intercalated nodular and well-bedded limestones, as well as a few ferruginous oolites. The Lower Liassic Arietenkalk (up to 5 m thick) is porous in some areas due to the occurrence of fractures and the presence of secondary porosity. The uppermost ~100 m of the Jurassic sediments comprise of a monotonous sequence of dark grey, silty, micaceous clays (Aalenian Opaliunus-clay).

An unconformity separates the Triassic and Jurassic strata from the unconsolidated Quaternary cover. This cover consists of fluvio-glacial gravel of up to 50 m thickness.

#### 1.2.1.1 Surface subsidence

Two larger subsidence areas were detected in this region, however, their real extension is unknown due to scarce data (Figure 1.1B). Furthermore, these subsidence areas are difficult to observe in the field.

The Fachhochschule beider Basel (2000; subsidence data, 2002) provided the database for the western subsidence area. Aegerter & Bosshardt et al. (1999) and Schmidt + Partner AG (subsidence data, 2002) supplied the data for Lachmatt's subsidence area. Based on the available data for the two subsidence areas, the following conclusions can be drawn (cf. also Geologisch-Paläontologisches Institut der Universität Basel, 2003):

- Land subsidence occurs over large areas. The size of the western subsidence area is at least ~1 km$^2$; the size of Lachmatt's subsidence area is at least ~0.4 km$^2$ (Figure 1.1B).
- Two centers of subsidence can be recognized within the western subsidence area: the southern center has an oval shape of ~300 × ~800 m elongated along the regional tectonic trend (parallel to the faults). The northern circular depression is up to ~300 m wide. Lachmatt's subsidence area reveals, as the southern center in the other subsidence area, an elongate subsidence bowl of at least ~150 × ~300 m with approx. the same longitudinal alignment.
- The examined areas subside gradually. The average maximum subsidence velocity detected

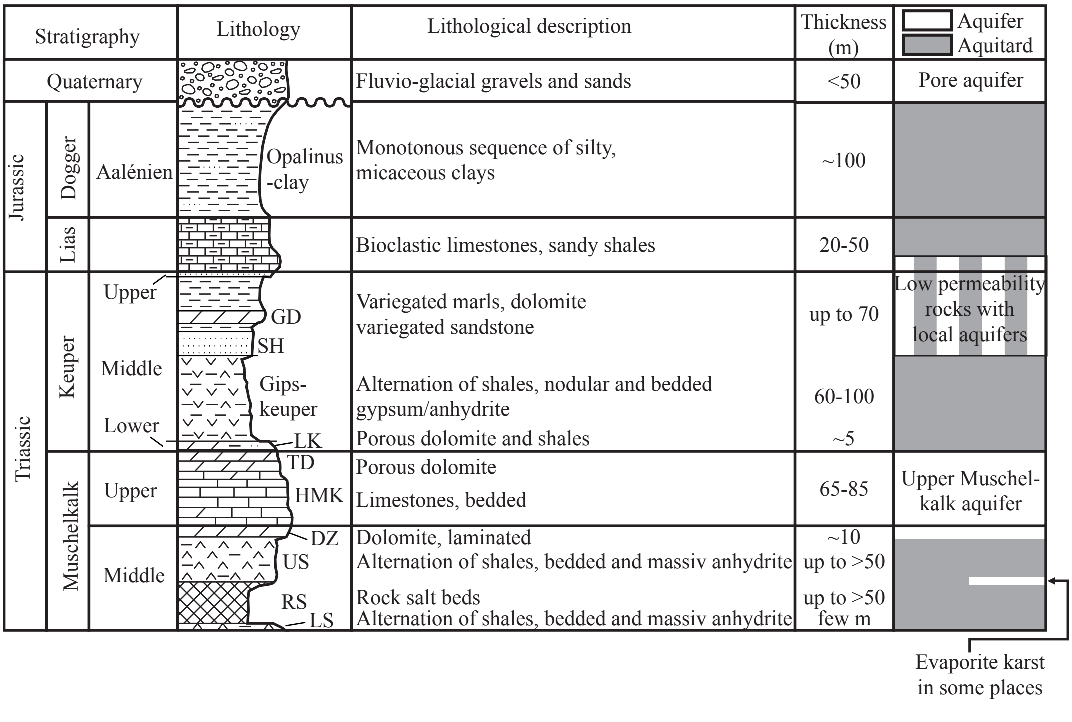

*Figure 1.3 Schematic, stratigraphic section showing hydrogeological characteristics of the study area (modified from Bitterli-Brunner and Fischer, 1988; modified from Pearson et al., 1991). GD = Gansinger Dolomit, SH = Schilfsandstein, LK = Lettenkohle, TD = Trigonodus-Dolomit, DZ = Dolomitzone, US = Upper Sulfatzone, RS = rock salt layer, LS = Lower Sulfatzone.*

for the western subsidence area and for the subsidence are in Lachmatt amounted to ~1.3 cm $y^{-1}$ and ~1 cm $month^{-1}$, respectively, which are considered extremely fast subsidence velocities in geological terms.

- Both vertical and horizontal displacements were detected in the Lachmatt's subsidence area.

## 1.2.2 Hydrogeological setting

### 1.2.2.1 General situation

Figure 1.3 presents a schematic, stratigraphic and hydrogeological profile of the study area. To focus on the existing interstratal evaporite karst in the study area, two hydrogeological cross-sections (oriented NW–SE and WNW–ESE, respectively) were constructed using the existing geological (borehole descriptions, geological maps, geological cross-sections)[1] and hydrogeological information (geological database of the Basel region; Geodata), including subsidence data (cf. Section 1.2.1.1). The line of section X–X' (Figure 1.2A) is located in the Schweizerhalle area close to the river Rhine. The line of section Y–Y' (Figure 1.2B) cuts through both subsidence areas (Figure 1.1B).

The Quaternary contains unconfined groundwater (pore aquifer). The underlying carbonate rocks (limestone, dolomite) and evaporites (gypsum, anhydrite, rock salt) are karstifiable. This results in the occurrence of different karst types or aquifers, respectively, situated one above the other.

The regional aquifer in the bedrock is the mainly confined Upper Muschelkalk aquifer (carbonate karst aquifer), which consists in this region of the formations of the Upper Muschelkalk (Trigonodus-Dolomit and Hauptmuschelkalk) and the Dolomitzone of the Middle Muschelkalk (Gürler et al., 1987; Pearson et al., 1991). The facies of the Lettenkohle may provide part of the Upper Muschelkalk aquifer (Pearson et al., 1991). The aquifer is up to roughly 100 m thick (Figure 1.3). Hydraulic barriers overlie (Gipskeuper) and underlie (Upper Sulfatzone) this Upper Muschelkalk aquifer. Between the Quaternary and Upper Muschelkalk aquifer, some spatially limited aquifers are present in the lower part of the Lias and upper part of the Keuper, e.g. some limestones, dolomites and sandstones (e.g., Pearson et al., 1991). According to Gürler et al. (1987), sulfate dissolution in the Gipskeuper is of minor relevance due to the limited or lack of open fractures. Due to the dip of the Mesozoic strata, the overlying pore aquifer of the Quaternary and the underlying Triassic karstified Upper Muschelkalk aquifer represent in some places a continuous aquifer in vertical direction (Figure 1.2A). The continuity of the bedrock aquifers is affected by faulting, however, these faults may possibly represent major groundwater flow paths favoring the vertical exchange of groundwater also across aquitards (Gürler et al., 1987; Pearson et al., 1991).

Until three salt drillings were conducted in the Lachmatt area in 1998, the less soluble Upper Sulfatzone was believed to protect the underlying highly soluble rock salt (halite) from dissolution (L. Hauber, 2003, personal communication). However, since the end of the 1990s we know that despite this protection, circulating Na-Cl-undersaturated groundwater is dissolving the halite at least below Lachmatt's subsidence area (cf. more in Section 1.2.2.2).

The groundwater flow in the study area is strongly influenced by the geometry and thickness of the Quaternary alluvial deposits, by the geological structure of the NNE-SSW-trending blocks, horsts and grabens and by the hydraulic boundary conditions, such as the Rhine river level, groundwater pumping and artificial recharge (Spottke et al., 2005). At Schweizerhalle, the Quaternary pore aquifer and/or Upper Muschelkalk aquifer are exploited for large-scale industrial water supply. Groundwater modeling results reveal that pumping affects the groundwater flow field in the Upper Muschelkalk aquifer at distances of up to 2 km to the south (Spottke et al., 2005). The well screen of the discharging wells may reach down to the base of the Upper Muschelkalk aquifer (Figure 1.2A). This is of importance, as deeper wells can enhance the discharge of lower lying saltwater and thus may accelerate salt karstification. The pumped Muschelkalk groundwater in the Schweizerhalle area contains relatively high concentrations of $Na^+$ and $Cl^-$ (up to several hundreds mg $Cl^-$ per l), and some discharging wells reveal Na/Cl molar ratios between 0.77 and 1.16. This suggests that the underground rock salt layer is a possible source of groundwater salinization (BMG Engineering AG, 1997). Thereby it has to be considered that the composition of the aquifer water in those wells can also be influenced by infiltration of Rhine water and by small artificial ponds/rivers (discharged water from the river Rhine) located northwest of Schweizerhalle used for artificial groundwater recharge (BMG Engineering AG, 1997; Spottke et al., 2005).

---

[1] A 3D geological model was constructed for the study area using the software package GOCAD (Geological Objects Computer Aided Design) (Spottke et al., 2005).

#### 1.2.2.2 Key findings of the three salt drillings in Lachmatt

Proof of the evidence of an interstratal evaporite karst below Lachmatt's subsidence area was obtained by three deep salt drillings in this subsidence area (Figure 1.1B). Borehole fluid logging was conducted in all the drillings (Geotest, 1998; Aegerter & Bosshardt et al., 1999; Hauber et al., 2000).

Aside from the unexpected existence of evaporite karst, the other results obtained from all three drill cores concurred with the anticipated data and are well-known from the numerous drillings conducted in this area. However, in a ~10 m thick zone directly over the top of the rock salt layer at ~150 m below ground level, an interstratal evaporite karst was drilled through. The most important observations and measurements can be summarized as follows:

- Loss of circulation was observed over this entire zone (Figure 1.2C).
- Loss of drill core directly over the top of the rock salt layer over a ~<2 m section was noticed (Figure 1.2C).
- A mixture of relatively insoluble components (solution residues) plus fragments from the lowest section of the Upper Sulfatzone was observed over the entire zone.
- Fluid electrical conductivity logs confirmed the occurrence of several Na-Cl-undersaturated water inflows (15–38 mS $cm^{-1}$ at 20°C) in a zone between ~1.5 and ~8 m over the top of the rock salt layer. However, even values <15 mS $cm^{-1}$ are considered for Na-Cl-undersaturated water due to mixing with the initially filled Na-Cl-saturated brine (~230 mS $cm^{-1}$ at 20°C) in the borehole.

Further down in the rock salt layer, no signs of leaching were detected except in one salt drilling between ~1.7 and ~2.4 m below the top of the rock salt layer where a cavity, filled with solution residues and gypsum crystals, was drilled through.

Based on these facts, it was concluded that a ~<2 m high open solution cavity (salt karst) filled with brine exists in Lachmatt at the top of the rock salt. Directly over it, the lowest section of the Upper Sulfatzone is fractured over a thickness of ~8 m (sulfate karst; Figure 1.2C). The water inflows must be attributed to hydraulically important open fractures and dissolution zones. The presence of flowing Na-Cl-undersaturated groundwater close to the top of the rock salt layer attests to the existence of on-going dissolution of halite and gypsum/anhydrite. Weathering residuum and gypsum crystals also clearly point to recent admission of undersaturated water. This interstratal karstification is part of a regional groundwater flow system. The supply of relatively fresh groundwater to the top of the rock salt layer is probably recharged from the Upper Muschelkalk aquifer down through permeable faults. Thus, this ~10 m thick zone is hydraulically connected over fractures with the upper multiaquifer formation.

This evaporite karst is responsible for the subsidence of the earth's surface (see Section 1.2.1.1), since the data from a borehole extensometer in this subsidence zone revealed that the overlying strata subside altogether. The rock salt layer itself proves to be stable, as it is not affected by subsidence (Aegerter & Bosshardt et al., 1999; Hauber et al., 2000). It can be assumed that only the deeper parts of the Upper Sulfatzone, close to the actual leaching area, are in fact broken up and have led with time to the development of a gypsum karst above the already existing salt karst (Hauber et al., 2000). Furthermore, the fact that saltwater enhances gypsum karstification by ionic-strength effect should also be accounted for (e.g., Harvie et al., 1982).

#### 1.2.2.3 Hypothesis extension of the tabular interstratal evaporite karst

Based on Geotest (1998), Aegerter & Bosshardt et al. (1999), Hauber et al. (2000) and on knowledge about such karst systems (e.g., Spackeler, 1957; Johnson, 1981, 1992; Reuter and Tolmačëv, 1990; Reuter et al., 1992; Reuter and Stoyan, 1993), it can be concluded that a tabular interstratal evaporite karst lies parallel to the stratigraphic sequence at the top of the rock salt layer at least below Lachmatt's subsidence area. The same kind of subsidence source can be reasonably assumed for the western subsidence area (Figure 1.1B, Figure 1.2B and Figure 1.2C). This assumption is also substantiated by the surface leveling data and borehole description of two salt drillings (Figure 1.1B) in or near this subsidence area (Geologisch-Paläontologisches Institut der Universität Basel, 2003).

### 1.2.3 Extraction of salt

Anthropogenic activities in this area, which could increase the amount of salt dissolution at the top of the rock salt layer, are (1) groundwater tappings from the Quaternary pore aquifer and/or Upper Muschelkalk aquifer resulting in saltwater (Na-Cl) upconing below pumping wells (see Section 1.2.2.1) and (2) extraction of salt by solution mining of halite.

The United Swiss Salt Works extract dissolved salt from inside the rock salt layer by solution mining of halite (e.g., Hauber et al., 1997). Na-Cl brine is still extracted in the south of the study area. A closed brine production field exists near the river Rhine (Figure 1.1). Unfortunately, information on the stability of the salt caverns etc. in this region is scarce, as data are not publicized for competitive reasons. Consequently, uncontrolled salt dissolution cannot be excluded from a scientific point of view.

## 1.3 Experimental laboratory approaches

An overall understanding of the complexity of the regional groundwater flow system can only be achieved by understanding each single aquifer/aquifer group and their interaction with each other. Furthermore, reliable data on the genesis of the interstratal evaporite karst is difficult to obtain for this region as:

(1) Piezometers reaching the salt layer are missing.

(2) Neither hydraulic data nor any reliable groundwater chemical analyses exist on this deep karst system.

(3) The regional groundwater flow system, hydraulically connected with the interstratal evaporite karst, is widely unknown. Particularly where NaCl-depleted water migrates downward (e.g., along faults) and/or maybe even laterally (e.g., from an aquifer opposite this karst system at a fault) to the salt beds, and where the resulting NaCl-enriched water escapes laterally and/or upward.

To overcome the complex problems and costs of field measurements, the study of salt karstification was scaled down to the laboratory.

Two general experimental setups were introduced: in the first setup, dissolution of rock salt (halite) was studied by pumping freshwater into undisturbed cores of rock salt through a horizontally, vertically or inclined-oriented borehole (rock salt dissolution experiments). These experiments were conducted to study the effect induced by freshwater contacting rock salt from below (horizontally-oriented borehole) or from above (vertically-oriented or inclined borehole). In the second setup, saltwater upconing in a freshwater aquifer was studied and numerically modeled in a 2D flow tank containing a porous medium (solute transport experiments). This setup was designed as a test problem (benchmarking) for density-dependent computer codes. Here fore an adequate non-commercial measuring technique had to be developed first to allow indirect measurement of solute concentrations of Na-Cl over a wide range in the flow tank.

The rock salt dissolution experiments were conducted at the University of Basel, the solute transport experiments at the University Louis Pasteur Strasbourg. Both these general experimental setups had to be developed and constructed for the required purposes. Seventeen experiments were conducted totally, fourteen in Basel and three in Strasbourg (Table 1.1).

## 1.4 Aims and structure of the present thesis

For this thesis, mainly laboratory-analog solute transport experiments in 2D and 3D flow tanks were originally planned to study and numerically model the saltwater upconing process above a high-density brine. Initially, the aforementioned rock salt dissolution experiments were only considered to be conducted as a single preliminary experiment to study the relationship between flow velocity and salt concentration (see application proposal; grant 21.65092.01). However, due to the unexpected discovery of a unusual dissolution cavity after the first rock salt dissolution experiment, this general experimental setup was further developed and additional dissolution runs were conducted. The latter general experimental setup allowed to understand through serendipity the genesis and morphologies of cavities with tip-down cavity cross-section in salt and gypsum deposits as well as interstratal salt cavities at the top of salt deposits and related overlying subsidence forms.

Although anthropogenic activities are well-known to possibly induce far more rapid and serious subsidences,

| | Number of experiments |
|---|---|
| Rock salt dissolution experiments: | |
| - Horizontally oriented borehole | 8 |
| - Vertically oriented or inclined borehole | 6 |
| | |
| Solute transport experiments | 3 |

***Table 1.1*** *Conducted experiments in this thesis.*

notably through mining and fluid withdrawal, causing accelerated salt dissolution (e.g., Waltham, 1989), the answer to the question whether the evaporite karst geohazard in the Muttenz-Pratteln region is natural and/or man-made is not the aim of this thesis nor can it be answered by the conducted experiments.

The present thesis comprises seven chapters; two were prepared for submission to scientific journals (Chapters 2 and 3). Note that the use of parameter abbreviations may change from one chapter to another. The topics and objectives of the individual chapters are outlined below:

Chapters 2 and 3 present the rock salt dissolution experiments with a horizontally oriented borehole. In Chapter 2, the experimental results are used to understand the genesis and shape of natural cavities within a salt body. These experimental results are also upscaled and compared to natural and man-made salt cavities on a field scale. The same experimental results are also used to understand the genesis and shape of gypsum cave passages with tip-down triangular cross-section, taking into account the existing models presented at the beginning as literature review (Chapter 3).

Chapter 4 contains the rock salt dissolution experiments with a vertical or inclined oriented borehole. The small-scale solution cavities obtained are integrated in a model for interstratal karst development in the context of horst and graben structures as observed in the Muttenz-Pratteln region. The reason for elongate subsidence troughs parallel to the fault system can thus be explained.

Chapter 5 describes the development of a new resistance measuring cell for in situ determination of solute concentration in laboratory tanks. In Chapter 6, this technique is then used in the newly developed and therein presented 2D flow tank designed as a test problem (benchmarking). The results and discussion on the conducted solute transport experiments indicate the need for further development of the experimental setup.

Chapter 7 summarizes the main conclusions, limitations and future perspectives.

## 1.5 References

Aegerter & Bosshardt, Geotechnisches Institut, and Prof. Dr. L. Hauber (1999), Setzungsproblematik/Massnahmen gegen Setzungen, Technischer Bericht, Bericht im Auftrag der SBB, unpublished.

Bitterli-Brunner, P., and H. Fischer (1988), *Blatt 1067 Arlesheim - Erläuterungen*, Geologischer Atlas der Schweiz 1:25’000, Landeshydrologie und -geologie, Switzerland.

BMG Engineering AG (1997), Chlorid-Belastung im Grundwasser Schweizerhalle West (Novartis Services AG, Werk Schweizerhalle) - Statusbericht, Bericht im Auftrag vom Amt für Umweltschutz und Energie, Kanton Basel-Landschaft, unpublished.

Fachhochschule beider Basel (2000), 6. Setzungsmessung im Gebiet Margelacker / Hinterzweien der Gemeinde Muttenz, Interner Technischer Bericht, unpublished.

Geologisch-Paläontologisches Institut der Universität Basel (2003), Senkungen an der 400 m Rundbahn in der Südhälfte des Sportplatzes Margelacker (Gemeinde Muttenz) - Ursachenanalyse, Bericht im Auftrag des Lenkungsgremium Untersuchung Deponien Muttenz, unpublished.

Geotest (1998), Adlertunnel, Setzungen Tagbaustrecke Nord, Lachmatt, Bohrlochgeophysik, Bericht im Auftrag der SBB, unpublished.

Gürler, B., L. Hauber, and M. Schwander (1987), *Die Geologie der Umgebung von Basel mit Hinweisen über die Nutzungsmöglichkeiten der Erdwärme*, Beiträge zur Geologischen Karte der Schweiz, Landeshydrologie und -geologie und Schweizerische Geotechnische Kommission, Switzerland.

Harvie, C. E., H. P. Eugster, and J. H. Weare (1982), Mineral equilibria in the six-component seawater system, Na-K-Mg-Ca-$SO_4$-Cl-$H_2O$ at 25°C. II: Compositions of the saturated solutions, *Geochim. Cosmochim. Acta*, *46*, 1603−1618.

Hauber, L. (1971), Zur Geologie des Salzfeldes Schweizerhalle-Zinggibrunn (Kt. Baselland), *Eclogae geol. Helv.*, *64/1*, 163−183.

Hauber, L. (1980), Geology of the salt field Rheinfelden-Riburg, Switzerland, in *Fifth Symposium on Salt*, vol. 1, edited by A. H. Coogan and L. Hauber, pp. 83−90, N. Ohio Geol. Soc., Cleveland, Ohio.

Hauber, L., L. Fournier, and M. Weidmann (1997), Salzlagerstätten, in *Die Mineralischen Rohstoffe der Schweiz*, edited by R. Kündig, T. Mumenthaler, P. Eckard, H.-R. Keusen, C. Schindler, F. Hofmann, R. Vogler and P. Guntli, pp. 356–370, Schweizerische Geotechnische Kommission, Switzerland.

Hauber, L., H. P. Noher, M. Meyer, and G. Horal (2000), Geologie im Bereich Adlertunnel, *tec21*, *49/50*, 9–12.

Herzog, P. (1956), Die Tektonik des Tafeljura und der Rheintalflexur südöstlich von Basel, *Eclogae geol. Helv.*, *49/2*, 317–362.

Johnson, K. S. (1981), Dissolution of salt on the east flank of the Permian Basin in the southwestern U.S.A., *J. Hydrol.*, *54*, 75–93.

Johnson, K. S. (1992), Evaporite karst in the Permian Blaine Formation and associated strata in Western Oklahoma, USA, *Int. Contributions to Hydrogeology*, *13*, 405–420.

Pearson Jr., F. J., W. Balderer, H. H. Loosli, B. E. Lehmann, A. Matter, Tj. Peters, H. Schmassmann, and A. Gautschi (Eds.) (1991), *Applied isotope hydrogeology - A case study in northern Switzerland*, Studies in Environmental Sciences 43, Elsevier, Amsterdam.

Quinlan, J. F., R. A. Smith, and K. S. Johnson (1986), Gypsum karst and salt karst of the United States of America, *Le Grotte d'Italia*, *4*(XIII), 73–92.

Reuter, F., K. J. Klengel, and J. Pašek (1992), *Ingenieurgeologie*, Deutscher Verlag für Grundstoffindustrie GmbH, Leipzig, Stuttgart.

Reuter, F., and D. Stoyan (1993), Sinkholes in carbonate, sulphate, and chloride karst regions: Principles and problems of engineering geological investigations and predictions, with comments for the destruction and mining industries, in *Applied karst geology*, *Proceedings of the fourth multidisciplinary conference on sinkholes and the engineering and environmental impacts of karst*, edited by B. F. Beck, pp. 3–25, A.A.Balkema, Rotterdam.

Reuter, F., and V. V. Tolmačëv (1990), *Bauen und Bergbau in Senkungs- und Erdfallgebieten. Eine Ingenieurgeologie des Karstes*, Schriftreihe für Geologische Wissenschaften, 28, Akademie-Verlag Berlin.

Spackeler G. (1957), *Berg- und Aufbereitungstechnik - Lehrbuch des Kali- und Steinsalzbergbaus*, W. Knapp Verlag, Halle.

Spottke, I., E. Zechner, and P. Huggenberger (2005), The southeastern border of the Upper Rhine Graben: a 3D geological model and its importance for tectonics and groundwater flow, *Int J Earth Sci*, *94*, 580–593.

Waltham, A. C. (1989), *Ground subsidence*, Blackie & Son, Glasgow and London.

# 2 Genesis and shape of natural solution cavities within salt deposits

Daniel Gechter[1], Peter Huggenberger[1], Philippe Ackerer[2], and H. Niklaus Waber[3]

[1]Department of Environmental Sciences, University of Basel, Basel, Switzerland

[2]Institut de Mécanique des Fluides et des Solides, Université Louis Pasteur, Strasbourg, France

[3]Institute of Geological Sciences, University of Bern, Bern, Switzerland

Submitted to Water Resources Research (accepted; except references to appendices)

## Abstract

Since the genesis and shape of natural deep-seated cavities within a salt body are insufficiently understood, the current study tries to shed some light on this topic. To this end, freshwater was pumped slowly through a horizontal borehole in rock salt cores. Due to fast halite dissolution kinetics, high solubility and slow inflow rate, halite dissolution took place only in the inflow of the rock salt cylinder. The shape of the created cavities is approximately a symmetrical half of a cone with a horizontal base facing upward. A conceptual model is presented inspired by the experimental results and based on theoretical, hydraulic-geochemical considerations, as well as on field observations. It proposes that triangular prism or conically shaped cavities develop within salt under confined conditions, where aggressive water flows upward along a fracture/conduit from an insoluble aquifer into the soluble stratum. Such cavity enlargements may cause land subsidence and structure collapse.

*KEYWORDS:* salt karst, buoyancy, halite dissolution, horizontal ceiling, facet, subsidence

## 2.1 Introduction

Salt deposits, such as rock salt, are widespread in continental regions (Kozary et al., 1968). However, due to their high solubility more than 99% of these deposits do not outcrop except for a few deposits in arid or cold regions (Ford and Williams, 2007). Circulating groundwater dissolves and selectively removes the buried salt layers leading to salt karstification. Salt karst, spread worldwide over extensive areas (e.g., Quinlan et al., 1986; Frumkin, 2000), causes land subsidences or catastrophic collapses that originate from dissolution cavities above or within the largely impermeable salt deposits (e.g., Anderson and Kirkland, 1980; Reuter and Stoyan, 1993; Martinez et al., 1998; Frumkin and Raz, 2001). Such solution cavities can occur at depths of more than 1000 meters below the surface (Ford and Williams, 2007). In addition, other common undesirable effects of salt karstification are associated with water quality, e.g., high mineralization and salinization (e.g., Johnson, 1981), geohazards induced by human activities, e.g., construction of dams and reservoirs (e.g., James and Kirkpatrick, 1980; James, 1992), mining (e.g., Waltham, 1989; Martinez et al., 1998; Cooper, 2002) or groundwater pumping (e.g., Waltham, 1989; Cooper, 2002). Moreover, salt cavities may have a serious impact on highly sensitive sites, such as radioactive waste repositories situated in salt rock units (Anderson and Kirkland, 1980; Dijk and Berkowitz, 2000).

Dissolution of deep-seated salt occurs when groundwater undersaturated with respect to the highly soluble salt minerals enters into contact with the salt body. Groundwater can interact with a salt body from above (e.g., Johnson, 1981; Reuter and Stoyan, 1993), from the side (e.g., McManus and Hanor, 1993), or from below (e.g., Anderson and Kirkland, 1980) resulting in different dissolution phenomena. In this study, we investigate the salt dissolution process induced by interaction of freshwater from below a salt body via a communicating fracture system as it might occur between a confined carbonate or clastic freshwater aquifer and an overlying practically impermeable, but highly soluble, salt body (Anderson and Kirkland, 1980). In such a setting, solution cavities are created by concentration-driven buoyant flow coupled with salt dissolution, thereby generating continuous gravitational brine movement (Anderson and Kirkland, 1980). Preferential dissolution thus occurs at higher elevation of a developing cavity leading to a cavity expanding selectively into the overlying salt rock and a broadening of the cavity upwards (Dijk and Berkowitz, 2000). When combined, the solution cavity morphology is a function of the interplay between water flow (i.e., forced convection), salt dissolution (i.e., equilibrium chemistry and dissolution kinetics), and buoyancy (i.e., free convection of stratified fluids with density gradients due to solute concentration gradients). Regarding buoyancy, fluids with higher solute concentrations fall, whereas fluids with lower concentrations rise elsewhere (e.g., Gebhart et al., 1988). Nevertheless, the natural genesis and shape of deep-seated brine-filled cavities within a salt body are poorly understood. To improve the conceptual understanding of the interplay between the relevant processes and the solution cavity morphology, particular focus was placed on visualizing the flowlines within such cavities during their growth and the cavity enlargement.

The study of fluid density effects in nature was scaled down to a laboratory dissolution experiment where freshwater was slowly pumped into rock salt cores through a horizontally oriented borehole (Figure 2.1A). Small scale experiments offer the possibility of managing boundary and initial conditions and repeating the experiments under very similar conditions. It is therefore very useful to improve our qualitative understanding of the processes even if some elementary processes like diffusion or gravity cannot be scaled down. To visualize the dynamics of concentration-driven buoyant flow coupled with halite dissolution in the newly forming cavities, the fluorescence property of uranine-containing water was used. The fast dissolution kinetics and high solubility of halite (e.g., Alkattan et al., 1997) make rock salt dissolution experiments suitable for studying such phenomena because the experiments are completed within a relatively short time. In addition, leakage within a block of rock salt material can be excluded because the primary porosity of rock salt is negligible. Kegel (1951) conducted an experiment based on a similar procedure. He showed that a conical cavity with a horizontal base facing upward develops when freshwater is injected into a salt block from below. The experimental results (demonstrated in this study) are upscaled and compared to both natural and man-made solution cavities.

This paper aims at elucidating the genesis and shape of natural cavities in salt formations. A good understanding of the hydrodynamics in salt karst coupled with salt dissolution mechanisms is crucial for assessing subsidence hazards, and for devising engineering precautions as well as management and protection measures of water resources in areas overlying salt formations. Furthermore, it facilitates determination of long-term waste storage strategies and optimization of industrial processes (e.g., salt mining) in natural salt formations.

## 2.2 Experimental procedure

### 2.2.1 Experimental setup

The experiments were set up to study the effect induced by freshwater contacting rock salt from below. Dissolution of rock salt (halite) was studied by pumping freshwater (tap water) into undisturbed cores of rock salt through a horizontally oriented borehole. It is of course an over-simplified representation of a natural system.

A constant inflow flow rate was ensured by a peristaltic pump (Ismatec model ISM 795) operated at low flow velocities (see below). The experimental setup is illustrated schematically in Figure 2.1A (cf. also Appendix A.1.1). The rock salt cylinders of ~10 cm in diameter and length were cut from drill cores of a Triassic rock salt layer southeast of Basel, Switzerland. A small borehole (Ø 4 mm) was then drilled into the center of each rock salt core. The polished ends of the core cylinders were molded in clear Plexiglas flanges with clear silicone rubber. The silicone-sealed ends of the cylinders prevented water circulation at the surfaces of the core ends. The flanges were connected via a Plexiglas tube (4 mm inner diameter) with the Tygon tubing and silicone tube (see Figure 2.1A). The Plexiglas tubes and borehole were sometimes slightly displaced from one another. Furthermore, it was not possible in the experiment to have a straight vertical cylinder end at the inflow (accuracy about ±1°). The tap water used originated from the municipal drinking water supply of Basel city ($Na^+$: 8.0–18.2 mg $l^{-1}$; $Cl^-$: 9.3–13.6 mg $l^{-1}$; initial pH: 7.2–8.2). The water temperature corresponded to the controlled room temperature (20.8 ± 1.7°C). Eight dissolution runs were conducted in total. The experimental conditions are given in Table 2.1. The dissolution runs in Table

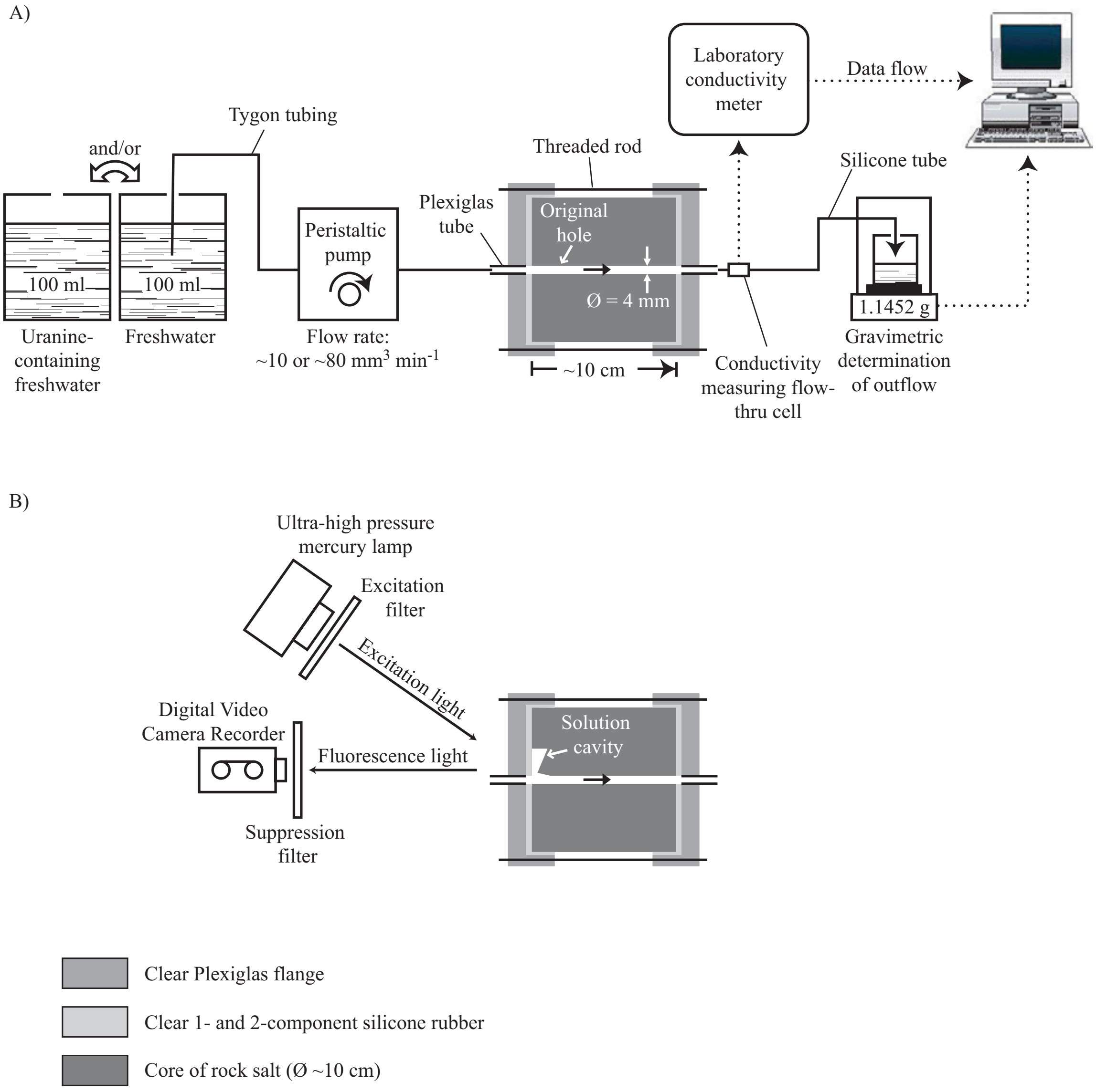

***Figure 2.1*** *A) Schematic view of the experimental setup for the laboratory dissolution runs. Note that the drilled borehole in the core sample as well as the inflow and outflow tubes were filled with a filtered, halite-saturated brine before starting a dissolution run. B) Diagram of experimental setup for visualizing flow circulation and cavity growth by incident light excitation of water with fluorescent dye (uranine).*

| | Drill core of rock salt | Drilling powder | Peristaltic pump | | Tracer input | | Interval recording | |
|---|---|---|---|---|---|---|---|---|
| Run number | Borehole length cm | Halite Weight-% | Average inflow rate $mm^3\ min^{-1}$ | Running time h | After start pumping h | Duration min | Interval time s | Recording time s |
| RS2 | 8.8 | 97 | 9.196 | 96.00 | | | | |
| RS10 | 10.9 | 99 | 8.628 | 46.90 | 38.60 | 45 | 30 | 0.5 |
| RS11 | 11.3 | 98 | 9.745 | 56.72 | | | | |
| RS15 | 10.2 | 98 | 85.15 | 4.80 | 4.50 | 5 | | Continuous |
| RS17 | 8.8 | 92 | 73.83 | 6.30 | | | | |
| RS19 | 10.5 | 95 | 23.34[a] | 31.04 | | | | |
| RS21 | 10.3 | 85 | 14.61[b] | 28.21 | | | | |
| RS23 | 9.9 | 94 | 77.06 | 6.80 | 0 | Continuous | 600 | 0.5 |

[a] 9.679 $mm^3\ min^{-1}$ for 24.44 h, afterwards 76.05 $mm^3\ min^{-1}$ for 6.60 h

[b] 83.27 $mm^3\ min^{-1}$ for 2.00 h, afterwards 9.162 $mm^3\ min^{-1}$ for 26.21 h

***Table 2.1*** *Experimental conditions for the eight dissolution runs (cf. also Appendix A.3).*

2.1 are termed as follows: RS2 refers to Rock Salt and dissolution run no. 2.

Prior to starting the experiments, the borehole and tubes were filled in vertical position from the bottom up with a filtered (Schleicher-Schuell membrane filter 0.45 µm) halite-saturated brine, which had been in contact with rock salt for several months, to avoid borehole wall dissolution before the actual start of the experiments. The brine's salts concentrations were similar to those of the NaCl-saturated brine from solution-mined caverns in the same rock material: NaCl = 300–310 g $l^{-1}$, $CaSO_4$ = 5.0–5.5 g $l^{-1}$, $MgSO_4$ = 0.3–0.4 g $l^{-1}$, and $MgCl_2$ = 0.1–0.2 g $l^{-1}$ (specification of NaCl-saturated brine; code-No. 9400; United Swiss Saltworks). The average volumetric inflow rate was measured as volume change of inlet freshwater between the start and the end of an experiment divided by running time. For the flow experiments, the average inflow rate was ~10 or ~80 $mm^3$ $min^{-1}$ over time scales of 4.8–96.0 hours (see Table 2.1). In an initially 4-mm diameter borehole, this corresponds to a mean horizontal initial water velocity of ~1.1 m $d^{-1}$ or ~8.8 m $d^{-1}$, which is realistic as within the velocity range of groundwater flow in a hypogenic underground karst system (e.g., Ford and Williams, 2007). In two dissolution runs (RS19 and RS21), the inflow rate was changed once during the experiment to determine its influence on cavity morphology (see Table 2.1). All dissolution runs were terminated before a solution cavity could reach the lateral surface area of the cylinder. The initial Reynolds number is defined here as

$$\mathrm{Re} = \frac{\rho \cdot v \cdot d}{\mu}$$

(e.g., Ford and Williams, 2007), where $\rho$ is the density, $v$ the mean horizontal velocity and $\mu$ the dynamic viscosity of the solution flowing through a borehole of diameter $d$. For a NaCl-saturated brine, $\rho$ is ~1.2 × $10^3$ kg $m^{-3}$ and $\mu$ is ~1.99 × $10^{-3}$ kg $m^{-1}$ $s^{-1}$ (Zaytsev and Aseyev, 1992). Thus, the initial flow was clearly laminar with Reynolds numbers <0.3. Preparation of halite-saturated brine, filling of the borehole/tubes and start of a dissolution run were always conducted successively and rapidly to avoid halite precipitation in the flow system.

Electrical conductivity (at 25°C) of the outflow brine was measured periodically in a flow-thru cell (WTW model TetraCon DU/T) connected to a laboratory conductivity meter (WTW model inolab Cond Level 2) with an error of ±1 mS $cm^{-1}$. Due to slow inflow rates, the injected water arrived with a time lag of up to an estimated several hours in the conductivity measuring flow-thru cell (see Figure 2.1A). The electrical conductivity of the initial freshwater was measured with an error of ±2 µS $cm^{-1}$. The solution emerging from the outflow tube was collected in a flask standing on a balance (Mettler Toledo model AG204) and its cumulative weight was measured periodically with an error of ±0.1 mg (see Figure 2.1A). Data were collected automatically at regular intervals using a data acquisition system. Data on electrical conductivity were recorded at hourly intervals, and on the discharging solution at 5-min intervals. The cumulative weight of the discharging solution was monitored to detect possible leaking or clogging (halite precipitation) during a dissolution run, which would be indicated by a decrease or constant value, respectively, in the cumulative weight of the discharging solution over time.

For visualization of the processes taking place at the entry area of the small borehole the freshwater was dyed with a small amount of water-soluble fluorescent tracer uranine (0.001 g uranine for 100 ml of freshwater). The added uranine (Na-fluorescein) concentration is negligible for mass balance calculation of the solution. Fluorescence intensity of uranine is strongest at the chosen dilution (Käss, 1998). Different instruments were used to record the fluorescence pattern: a suitable light source, strong in the near UV and visible short wavelength regions (Leitz ultra-high pressure mercury lamp, 200 W short arc mercury lamp), excitation and suppression filters (Schott model FITCA-40 and FITCE-45, respectively) and a digital video camera recorder (Sony model DCR-TRV27E) (Figure 2.1B). The dissolution runs RS10, RS15 and RS23 were captured in the darkroom on time-lapse video for subsequent qualitative analysis (cf. also Appendix A.1.1). To visualize and record flowlines (dissolution runs RS10 and RS15), the traced water was injected for 45 and 5 minutes, respectively, during the experiment (pulse input). For cavity enlargement (dissolution run RS23), traced water was injected throughout the experiment. The experimental data on tracer input and snapshot recording are presented in Table 2.1. The recordings were digitized and then extracted as single bitmap image frames and corrected for distortion. The correction error is about ±1 mm.

After the drill core was removed of the holder system, the undisturbed final solution cavities were inspected macroscopically and by means of scanning electron microscope (SEM) techniques.

### 2.2.2 Mineralogical analysis of the source rock

The drilling powder of all cores was examined using X-ray diffraction (Siemens model D5000) and -fluorescence (Siemens model SRS 3000). Since the drilling powder alone did not reveal minor minerals, the results from the mineralogical analyses of the filters coated with water-insoluble phases (see Section 2.2.3) were also considered. The studied rock mainly consists of 85–99 weight-% coarse halite (see Table 2.1) with minor amounts (impurities) of anhydrite, dolomite, quartz, and clay minerals illite-muscovite and chlorite (cf. also Appendix A.2). The minor minerals may occur as discrete thin layers or are disseminated within the halite.

### 2.2.3 Determination of dissolved halite volume

The volume difference between the initially drilled borehole and the final enlarged borehole was determined by the difference in weight of the NaCl-saturated brine used to fill the openings before and after the experiment. Undissolved particles that accumulated in the cavities were collected and weighted according to the method described by Clesceri et al. (1998). For the calculation of the solution residue volume, the undissolved particles were investigated by X-ray diffraction to estimate an average mineral density. The dissolved halite volume equals the measured volume difference minus the volume of rinsed-out impurities. The analytical error of the volume difference obtained is about ±0.1 cm$^3$.

## 2.3 Results

### 2.3.1 Electrical conductivity and fluid density

The data measured for the different dissolution runs are given in Table 2.2. The electrical conductivity of the initial NaCl-saturated brine ranged between 242 and 245 mS cm$^{-1}$ and that of the accessing freshwater between 0.398 and 0.413 mS cm$^{-1}$. The mean density was ~1.1971 g cm$^{-3}$ for the initial brine and ~0.9973 g cm$^{-3}$ for the freshwater. The electrical conductivity of the outlet brine varied between 242 and 247 mS cm$^{-1}$. In each run, an initial small increase in electrical conductivity was observed until stable values were attained (Figure 2.2A). The initial increase is close to the measurement accuracy and thus reveals only a minimal difference. This is supported by the linear increase in the cumulative weight of the outlet brine at a constant inflow rate in all dissolution runs (Figure 2.2B and Figure 2.2B*). The inflection point observed for dissolution runs RS19 and RS21 corresponds to the change in the inflow rate during the experiment (cf. Table 2.1).

### 2.3.2 Dissolved halite volume

The measured cavity volume difference per dissolution run ranged between 2.7 and 8.0 cm$^3$ and the measured weight of solution residues totaled 4.8–110.9 mg (Table 2.3). The mineral densities of the detected impurities (based on Deer et al., 1992) amount to 2.9–3.0 g cm$^{-3}$ (anhydrite), 2.86–2.93 g cm$^{-3}$ (dolomite), 2.65 g cm$^{-3}$ (quartz), and for the clay minerals 2.6–2.9 g cm$^{-3}$ (illite-muscovite) and 2.6–3.3 g cm$^{-3}$ (chlorite). Thus we assumed an average density of solution residue of 2.8 g cm$^{-3}$. Given this average

| | Initially filled NaCl-saturated brine | | Freshwater | | Outlet brine |
|---|---|---|---|---|---|
| Run number | Fluid density g cm$^{-3}$ | Electrical conductivity mS cm$^{-1}$ | Fluid density g cm$^{-3}$ | Electrical conductivity mS cm$^{-1}$ | Electrical conductivity mS cm$^{-1}$ |
| RS2 | 1.193 | 244 | 0.9962 | 0.402 | 244-247 |
| RS10 | 1.194 | 245 | 0.9972 | 0.407 | 244-247 |
| RS11 | 1.200 | 242 | 0.9973 | 0.398 | 242-247 |
| RS15 | 1.200 | 245 | 0.9975 | 0.413 | 245-247 |
| RS17 | 1.200 | 245 | 0.9969 | 0.408 | 245-247 |
| RS19 | 1.199 | 244 | 0.9979 | 0.403 | 244-247 |
| RS21 | 1.197 | 244 | 0.9980 | 0.406 | 244-246 |
| RS23 | 1.199 | 243 | 0.9982 | 0.400 | 243-246 |

***Table 2.2*** *Fluid density and/or electrical conductivity data of initially filled NaCl-saturated brine, injected freshwater and outlet brine of all dissolution runs (cf. also Appendix A.3).*

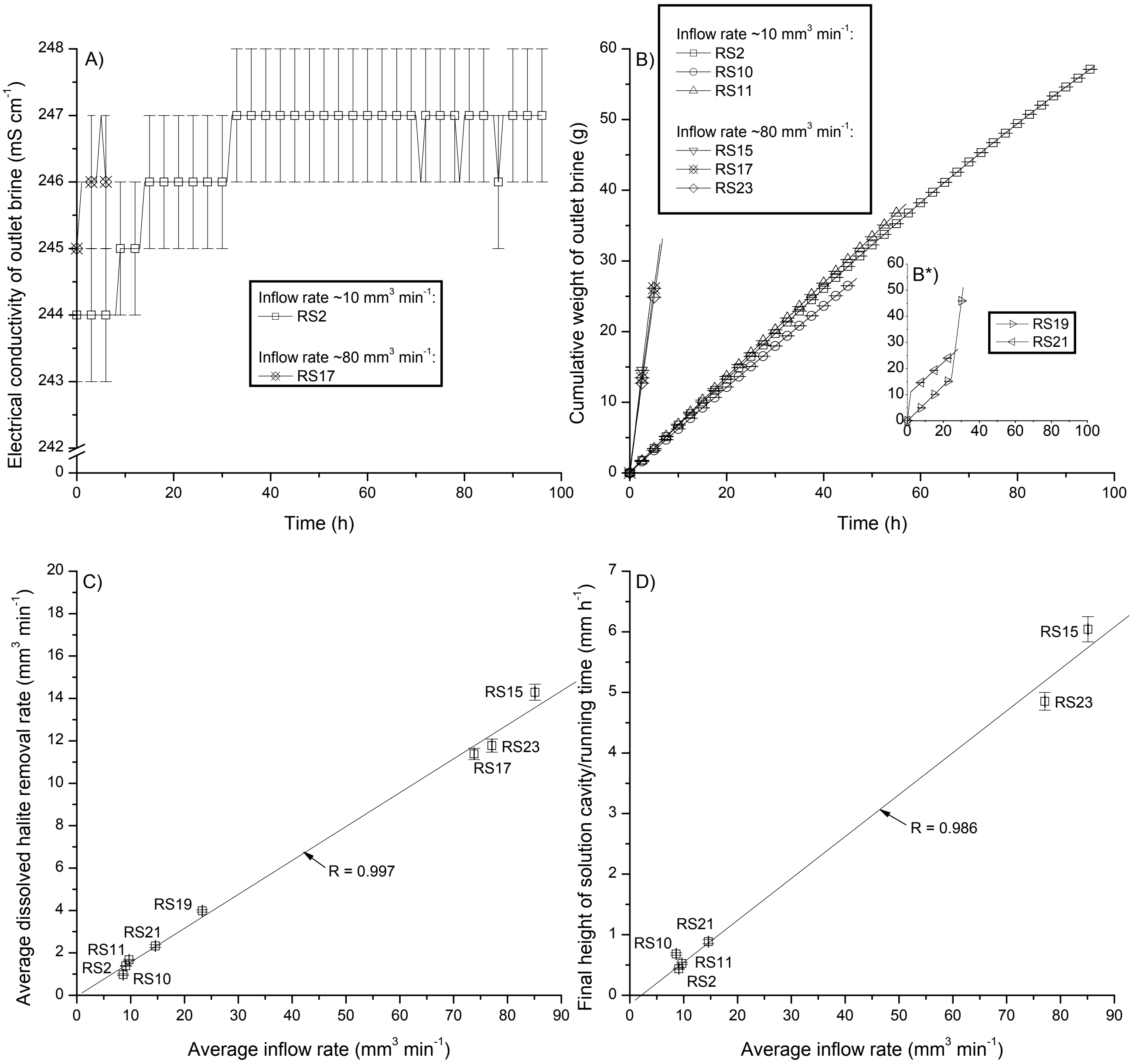

***Figure 2.2*** *A) Electrical conductivity of outlet brine as a function of time, represented by the dissolution runs RS2 and RS17. Every fourth data point is displayed as a symbol. B) Cumulative weight of discharging solution as a function of time of dissolution runs with constant inflow rate throughout the experiment. Every 30th data point is displayed as a symbol. B*) Cumulative weight of discharging solution as a function of time of dissolution runs with changing inflow rate once (dissolution runs RS19 and RS21). Every 90th data point is displayed as a symbol. C) Average dissolved halite removal rate versus average inflow rate of all dissolution runs. The solid line represents a linear fit. R = correlation coefficient. D) Final height of solution cavity/running time versus average inflow rate of dissolution runs with triangular outlines (without dissolution runs RS17 and RS19). The solid line represents a linear fit.*

density, the solution residue volume per dissolution run ranged between ~0.002 and ~0.040 cm$^3$ (Table 2.3), which is quite clearly below the overall error (see Section 2.2.3). Therefore, for the calculation of the dissolved halite volume, the solution residue volume can be neglected, so that the measured cavity volume difference corresponds approximately to the dissolved halite volume (Table 2.3). The average dissolved halite removal rate was ~1–~14 mm$^3$ min$^{-1}$. The results reveal a linear correlation between the average dissolved halite removal rate and average inflow rate (Figure 2.2C; cf. also Appendix A.3). Higher average inflow rates led to linear proportional higher mass transfer rates.

## 2.3.3 Final cavity morphology

### 2.3.3.1 Macroscopic features

The dissolution cavities viewed three-dimensionally

| Run number | Solution cavity | | | Cavity morphology | | |
|---|---|---|---|---|---|---|
| | Solution residue weight[a] | Solution residue volume | Dissolved halite volume | Inclination of facet[b] | | Final height of solution cavity |
| | | | | $\gamma_1$ | $\gamma_2$ | |
| | mg | cm$^3$ | cm$^3$ | ° | ° | cm |
| RS2 | 16.9 | 0.006 | 8.0 | 70 | 86 | 4.2 |
| RS10 | 14.0 | 0.005 | 2.7 | 75 | 83 | 3.2 |
| RS11 | 11.5 | 0.004 | 5.7 | | | 3.0 |
| RS15 | 17.9 | 0.006 | 4.1 | 78 | 84 | 2.9 |
| RS17 | 110.9 | 0.040 | 4.3 | | | |
| RS19 | 4.8 | 0.002 | 7.4 | - | - | - |
| RS21 | 45.3 | 0.016 | 3.9 | | | 2.5 |
| RS23 | 5.9 | 0.002 | 4.8 | 73 | 83 | 3.3 |

[a] Solution residue weight = Weight of filter with dried residue minus weight of filter

[b] Specification where the two equal sides (facet) of the triangular outlines are more or less straight

\- Not measured

***Table 2.3*** *Measured weight of solution residue, calculated volume of solution residue and dissolved halite as well as resulting cavity geometry (inclination of facet and final cavity height) of all dissolution runs (cf. also Appendix A.3).*

at the inlet are shaped roughly like a symmetrical half of a cone with a horizontal base facing upward, or expressed differently: when the top is sliced off of the cone (with the cut made parallel to the base), thus resemble a symmetrical half of a conical frustum. The base itself has the shape of a half-ellipsoidal surface (Figure 2.3A and Figure 2.4A). The ends of the cylinders at the inflow (xy plane; cf. Figure 2.4A) correspond largely to a vertical cross section through this introduced conical frustum. The major axis of the base lies within this cross section. The length of the semi-minor axis is about half of the semi-major axis. An extension ("tail cavity") was observed further down the borehole (Figure 2.4A). The outlines of the cavity walls at the inflow surface of the salt cores (xy plane) are presented in Figure 2.4B for the different dissolution runs (cf. also Appendix A.1.2). The morphological elements of the horizontal ceiling and facet are clearly visible and similar to those observed in some gypsum caves, from where the terminology is adapted (Biese, 1931; Kempe, 1972, 1996). The outlines correspond for the most part to isosceles triangles standing on the apex with a horizontal side facing upward (dissolution runs RS2, RS10, RS15, and RS23). Instead of legs, the lateral outline can also be shaped somewhat like a parabola/hyperbola opened upward (dissolution runs RS11 and RS21). Only dissolution run RS17 reveals a bizarre outline attributed to a lot of discrete thin layers of less soluble anhydrite. However, the macroscopic dissolution features were similar, independent of inflow rate and disseminated impurity content. Furthermore, changes in inflow rate during a dissolution run did not reveal any observable modifications in morphology (dissolution runs RS19 and RS21). The (final) height of the solution cavity is defined in Figure 2.4B. They were measured by ruler with an accuracy ±0.1 cm (Table 2.3). There is a simple positive correlation between the final height of the solution cavity divided by running time and the average inflow rate of dissolution runs with triangular outlines (Figure 2.2D; cf. also Appendix A.3). Higher average inflow rates led to linear proportional higher

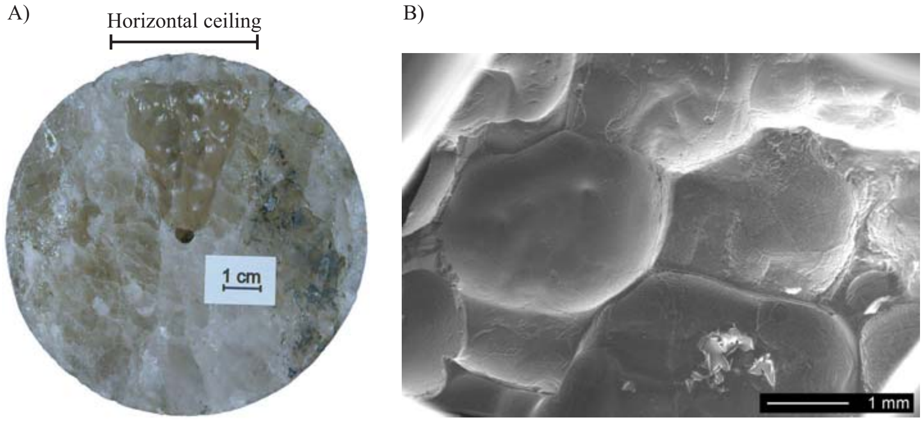

***Figure 2.3*** *A) Photograph of inlet view with final cavity shape (dissolution run RS2). B) SEM photograph of cup-shaped (concave) solution pits at the horizontal ceiling (dissolution run RS19).*

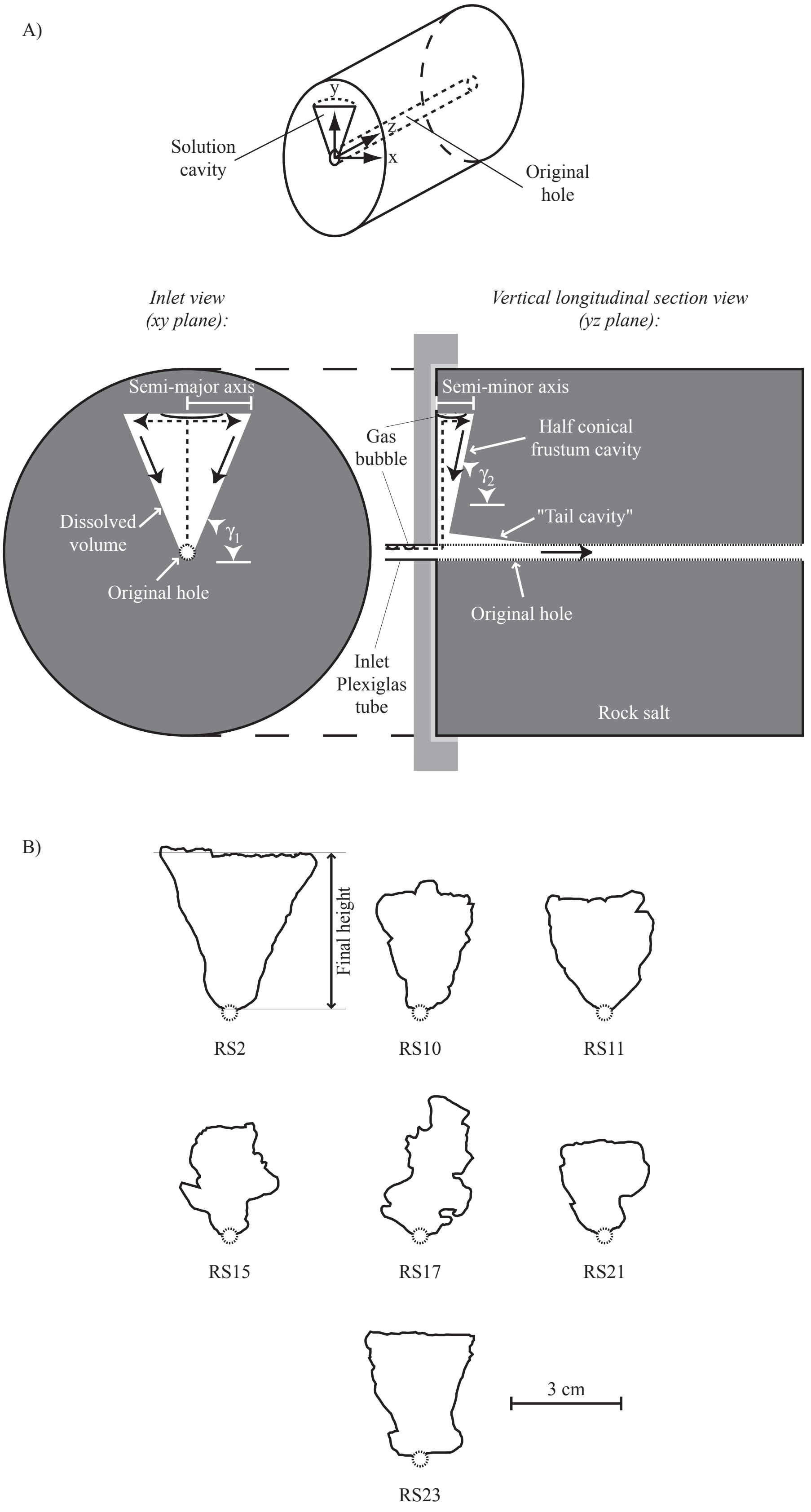

***Figure 2.4*** *A) Schematic diagram of the core sample with solution cavity and indication of the flowlines B) Outlines at the inlet at the end of the dissolution runs (dissolution run RS19 is not illustrated because it was sectioned).*

upward growth rates of the horizontal ceiling. Salt dissolution in the original borehole occurred only around the upper third section (height ~1.5 mm) and only within the first ~3 cm along the original borehole (Figure 2.3A and Figure 2.4A).

In the dissolution runs RS2, RS10, RS15, and RS23 the

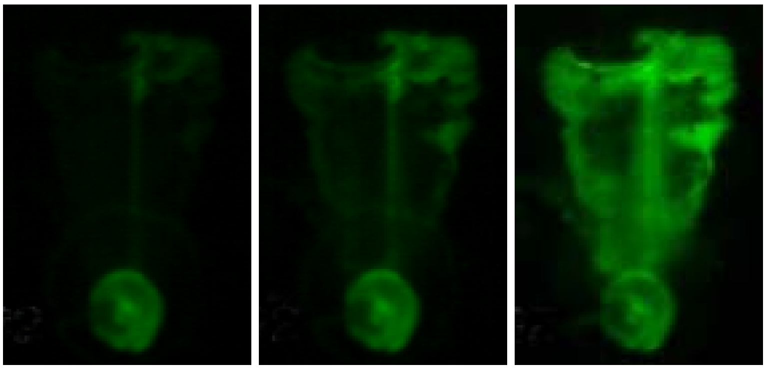

t ~2 min　　t ~8 min　　t ~22 min

*Figure 2.5* *Time-lapse, videotape recording of the flowlines at elapsed times (t) ~2, ~8 and ~22 minutes after injection of uranine-containing water into the cavity (dissolution run RS10; cf. Table 2.1). Notice the gas bubble at the horizontal ceiling (images, left-hand side). Important factors: (1) uranine dye is not a salinity indicator, (2) the visible circle below is caused by a silicone blob molding the Tygon tubing into the Plexiglas tube. It therefore does not correspond to the original opening, (3) the outline of the dye cloud is not equal to the outline of the dissolution run RS10 (cf. Figure 2.4B). Width of image corresponds to 3.3 cm.*

inclination of the facet at the inflow surface ($\gamma_1$) varied in a narrow range between 70 and 78°, with an error of ±1° (Figure 2.4A and Table 2.3). The inclination of the facet intersecting the vertical longitudinal section of the core through the center of the borehole (yz plane) was determined by caliper measuring, also with an error of ±1°, which shows inclinations ($\gamma_2$) of several degrees steeper (Figure 2.4A and Table 2.3). There is no visible correlation between inflow rate, finely disseminated impurity content and outlined facet inclination. However, discrete, millimeter-thin layers of impurities influence the triangular shape by undercutting the facet below these layers (e.g., dissolution run RS15, see Figure 2.4B).

#### 2.3.3.2 Microscopic features

Small cup-shaped solution pits cover, in a honeycomb pattern, the horizontal ceiling of all cavities leached. The small pits have an irregular round to oval shape in the dimension of 1 mm (Figure 2.3B). No regularity can be observed in the arrangement of the small solution pits and their genesis appears not to be related to the inhomogeneity of the rock or to the cleavage planes of halite, the latter clearly transecting the small pits. A similar irregular arrangement of solution pits is established on the facet surface with the pits being circular to oval in shape and up to a few mm in size (Figure 2.3A).

### 2.3.4 Flow pattern and cavity enlargement

The uranine-containing freshwater in the inlet Plexiglas tube was observed only within approximately the uppermost millimeter. Gas bubbles developed in this area during a dissolution run. The water below the uranine-containing freshwater and gas bubbles was clear. Therefore, the freshwater had accessed the borehole/solution cavity through a point source and not throughout the entire inlet Plexiglas tube section (see Figure 2.4A).

The recorded flowlines are illustrated in Figure 2.5 and also presented schematically in Figure 2.4A. The results clearly indicate a flow symmetrical to the y-axis. The low-density freshwater accessing the borehole flowed in the center along the y-axis to the horizontal ceiling from where the fluid stream spread sideways, forming a distinct thin horizontal layer. Here the first mineralization and consequently change

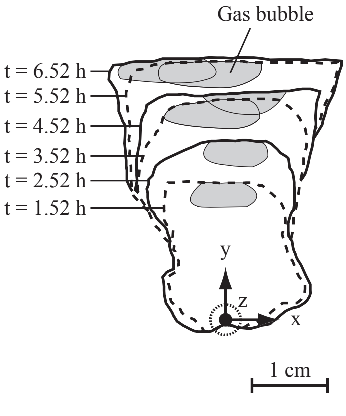

*Figure 2.6* *Enlargement of solution cavity (outline of dye cloud) and position of gas bubble (xy plane) at the entrance of the borehole (dissolution run RS23). The elapsed times after starting the dissolution run: hourly from 1.52 h to 6.52 h. Note that the outlines of the dye cloud are not equal to the intersecting line of the cavity wall and cylinder end at the end of the dissolution run (cf. Figure 2.4B).*

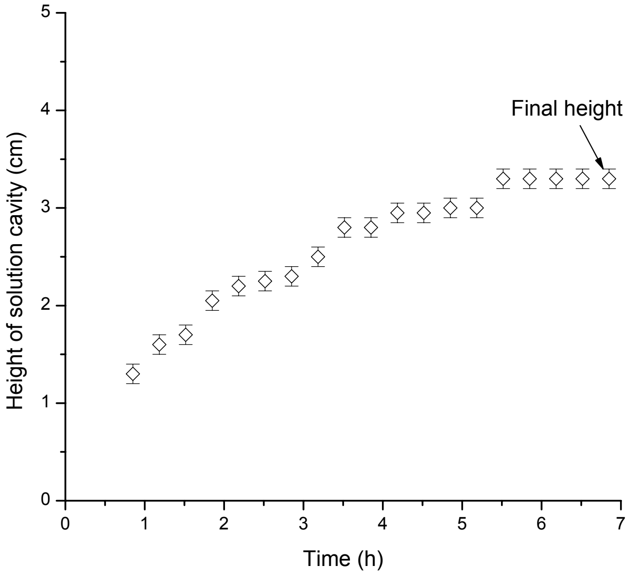

***Figure 2.7*** *Height of solution cavity versus time of dissolution run RS23.*

in water density takes place. At the facet, an approx. 0.5–0.8 mm-thick traced and increasingly mineralized water layer moved downwards as a film or separate fingers to close the convection cycle.

For the dissolution runs RS10 and RS15 the flow velocities at the facet could be visually estimated to be in the order of ~13 m $d^{-1}$ and ~51 m $d^{-1}$, respectively. Thus, the velocity of the downward moving film or fingers was several times faster than the average flow velocity in the z direction of the original borehole. The relief of the facet influenced the path of the downward moving film or fingers, indicating that the downward moving water was in direct contact with the facet and thus flowing along to the salt surface. A gas bubble was always trapped at the horizontal ceiling (Figure 2.5). The gas bubble jerked occasionally sideways due to selective dissolution of halite (Figure 2.6; cf. also Appendix A.1.5). During a dissolution run, in the xy plane the gas bubble at the horizontal ceiling changed in size (Figure 2.6), and fluorescing water was never observed above the gas bubble (Figure 2.5).

Qualitatively, the cavities enlarged through the upward growth of the horizontal ceiling and simultaneously by sideward growth at the upper end of the facet by tilting the latter slightly outward (Figure 2.6; cf. also Appendix A.1.5). In dissolution run RS23, uranine-containing freshwater was continuously injected into the borehole (cf. Table 2.1). In this experiment the height of the evolving solution cavity, i.e. the upper limit of the gas bubble, was measured every 20 minutes using image analysis. As shown in Figure 2.7, these measurements reveal an increasing cavity height, while the upward growth rate declines with time.

## 2.4 Discussion

### 2.4.1 Flow experiments

#### 2.4.1.1 Mass transfer

The overall dissolution reaction of halite

($NaCl(s) \rightleftharpoons Na^+ + Cl^-$)

is a physical, reversible and congruent process. The equilibrium concentration with respect to halite at 20°C amounts to ~317 g $l^{-1}$ (Seidell, 1965). The density differences between undersaturated and saturated waters with respect to halite may reach ~0.2 g $cm^{-3}$ (Seidell, 1965).

Under the experimental conditions, halite dissolution is a transport-controlled process; i.e., diffusion across the boundary (or molecular diffusion) layer is much slower than dissociation of halite ions at the mineral surface (e.g., Lasaga, 1990; Alkattan et al., 1997). Therefore, it can be assumed that the concentration directly adjacent to the halite surface ($c_s$) is approximately that at equilibrium concentration with respect to halite ($c_{eq,c}$). Among others, on that approximation the NaCl detachement rate from the halite surface ($R_c$) can be computed from (Alkattan et al., 1997)

$$\begin{aligned} R_c &= \left(\frac{dm_{Na^+}}{dt}\right)_{s,c} = \left(\frac{dm_{Cl^-}}{dt}\right)_{s,c} \\ &\approx k_c(c_{eq,c} - c_s) \end{aligned} \tag{2.1}$$

where

$$k_c \equiv \frac{R_+ \cdot \gamma_{\pm,NaCl,c_{eq}}}{K^{0.5}} \approx \frac{R_+}{c_{eq,c}}$$

in which $(dm_i/dt)_{s,c}$ signifies the flux of the subscripted aqueous species across the mineral-fluid interface per unit surface area, $R_+$ the halite dissolution rate in an infinitely dilute solution, $\gamma_{\pm,NaCl,c_{eq}}$ the stoichiometric mean activity coefficient for the NaCl electrolyte at the subscripted concentration, and $K$ the equilibrium constant of the overall dissolution reaction. In agreement with Fick's law, the rate of Na-Cl passing through the boundary layer with a certain thickness due to diffusion ($R_t$) follows a linear rate law (Alkattan et al., 1997)

$$R_t = k_t(c_s - c_b) \tag{2.2}$$

where $k_t$ represents the mass transfer coefficient and $c_b$ the Na$^+$ or Cl$^-$ concentration of in the bulk solution. In accordance with Eq. (2.2), with increasing saturation of the bulk solution, a linear decrease in dissolution rates (i.e., mass halite-flux off the rock wall per unit area and time) was demonstrated experimentally (Alkattan et al., 1997). Furthermore, the rate of dissolution depends upon the flow rate of the bulk solution, which reduces the boundary layer thickness resulting in accelerated transport and, therefore, faster dissolution (e.g., Lasaga, 1990). For example, Alkattan et al. (1997) measured the dissolution rate of halite using the rotating disk method. They found a linear increase for the reciprocal of dissolution rates as a function of the inverse square root of the angular velocity of the rotating disk.

Due to the slow water inflow rate and rapid dissolution kinetics of halite (see Eqs. (2.1) and (2.2)), the freshwater was saturated with respect to halite shortly after its initial contact with the rock salt and halite dissolution was restricted to the inflow area of the borehole in the rock salt cylinder. For the range of experimental inflow rates, a regular supply of freshwater induced a constant mass transfer rate from solid to liquid phase during a dissolution run. This is demonstrated by the linear relationships presented in Figure 2.2A, Figure 2.2B, Figure 2.2B* and Figure 2.2C. The initially filled brine was in contact with rock salt for several months, compared to the injected freshwater, whose contact with rock salt amounted to only a few hours at most during its flow through the hole. Consequently, the initially filled halite-saturated brine exhibited a different ionic composition (effect of longer water-rock interaction) and, therefore, a slightly different (lower) electrical conductivity than the injected and later on halite-saturated water after its flow through the hole (see Figure 2.2A). The less soluble mineral anhydrite and poorly soluble minerals (dolomite, quartz and clay) remain largely undissolved during the experimental period.

In a mass balance equation, the mass of removed dissolved halite must be equal to that carried away in the solution. For constant $Q$ and constant $c_{in}$ within any time increment ($dt$) must be

$$P_{rs} \cdot \rho_h \cdot \frac{dV}{dt} = Q(c_{eq} - c_{in}) \tag{2.3}$$

where $P_{rs}$ expresses the volume fraction of halite contained in rock salt (-), $\rho_h$ the halite density (g cm$^{-3}$), $dV/dt$ the solution rate (cm$^3$ h$^{-1}$), $Q$ the inflow rate (cm$^3$ h$^{-1}$), $c_{eq}$ the equilibrium concentration of Na$^+$ and Cl$^-$ with respect to halite (g cm$^{-3}$), and $c_{in}$ the solute concentration of Na$^+$ and Cl$^-$ in the inflow (g cm$^{-3}$).

#### 2.4.1.2 Coupled hydraulic-geochemical consideration

Buoyancy effects on stratified flows are the result of vertical density gradients (in this case due to the dissolved NaCl concentration). Two non-dimensional ratios, the Rayleigh and the densimetric Froude numbers, characterize stability and turbulence of the flows, respectively. Fluid, heavier by density difference $\Delta\rho$ on top of lighter fluid, may reside laminarly despite the static instability, as long as the Rayleigh number $Ra$ (e.g., Turner, 1973)

$$Ra = \frac{g \cdot \Delta\rho \cdot H^3}{\mu \cdot D} <\sim 1700 \tag{2.4}$$

where $g \approx 9.81$ m s$^{-2}$ is the gravitational acceleration, $H$ is the thickness of the unstable layer, and $D$ is the molecular diffusion coefficient of dissolved NaCl in water. In the context of the Boussinesq approximation, the densimetric Froude number $F$ (e.g., Turner, 1973)

$$F = \frac{v}{(g' \cdot H)^{1/2}} \tag{2.5}$$

expresses the buoyancy forces (vertical) acting on the inertial forces (horizontal), where $g' = g\Delta\rho/\rho$ is the reduced gravity. If $F > 1$, the flow is not buoyancy-driven. For a fully saturated saline solution, $D$ is ~1.5 × 10$^{-9}$ m$^2$ s$^{-1}$ at 20°C (Zaytsev and Aseyev, 1992) and with overlying freshwater $g'$ is ~2 m s$^{-2}$.

Initially, the upper third of the hole wall was enlarged upward along the first ~3 cm in the z direction, as the introduced undersaturated, less dense water occupied the uppermost position. At more than ~3 cm down the hole, the brine was always NaCl-saturated; beyond that depth, no halite dissolution occurred (equilibrium control) (cf. Figure 2.4A). Directly at the inlet of the original hole, the accessing freshwater dissolved most halite. Down the hole, solute concentration of less dense water increased continuously until NaCl-saturation was reached (cf. Eqs. (2.1) and (2.2)). In this way, the “tail cavity” developed gradually. Upward enlargement through dissolution led to a horizontal ceiling at the inlet, thus allowing the facet to develop upward (see Figure 2.6). In the further course of a dissolution run, halite dissolved only within the developing half conical frustum cavity.

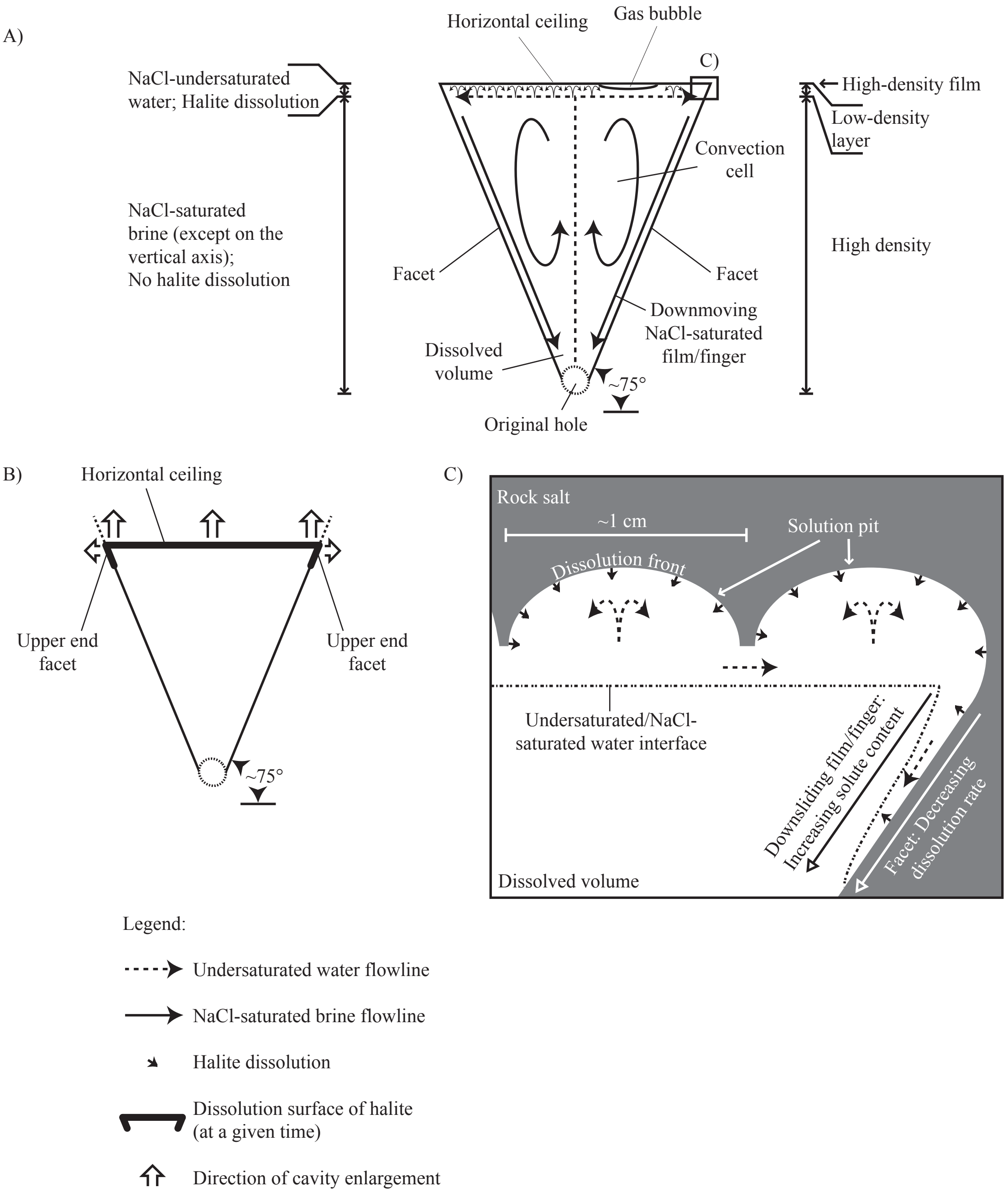

***Figure 2.8*** *A) Schematic flowlines and processes at a given time. B) Model of cavity growth, starting from a circular hole and continuing at the cavity top. C) Schematic close-up of solution pits.*

Figure 2.8A is a schematic illustration of the flowlines and processes taking place in the half conical frustum cavity at a given time. We conclude that a fluid density layering develops with a thick, high-density NaCl-saturated brine and a relatively thin, low-density horizontal layer above, which is in contact with the horizontal ceiling and upper end of the facet. In the horizontal (borehole), the flow is laminar. In the vertical, however, the flow is extremely buoyancy-driven as the densimetric Froude numbers are clearly <1 and the driving density difference $\Delta\rho$ is very large. Furthermore, enormous high Rayleigh numbers (approximately $>1 \times 10^{10}$) indicate that the buoyant flow is fully turbulent. Thus, the inflowing (less dense) freshwater rises straight to the top of the cavity due to buoyancy, caused by the density difference in solute concentration. An inverted density distribution occurs again at the contact of the low-density layer and horizontal ceiling as halite dissolves. Since halite dissolution occurs almost instantaneously (cf. Eqs. (2.1) and (2.2)), the inflowing freshwater is NaCl-saturated after brief contact with the horizontal ceiling and upper end of the facet (Figure 2.8A and Figure 2.8B). The observed heterogeneous distributed solution pits indicate preferential dissolution sites at the mm-scale suggesting small convection cells, on the same scale as the pits, distributed in a honeycomb pattern at the horizontal ceiling (Figure 2.8A and

Figure 2.8C). Given the halite-flux off the rock at the horizontal ceiling, the smallest possible eddies to exist can be determined by using the Kolmogorov length scale $L_K$ (Kolmogorov, 1941)

$$L_K = \left( \frac{\upsilon^3}{\varepsilon} \right)^{1/4} \tag{2.6}$$

where viscous and inertial forces are of the same magnitude. Therefore, the smallest spatial structures in this turbulent flow depend only on the kinematic viscosity $\upsilon$ and the rate of dissipation of turbulent kinetic energy $\varepsilon$. If the Kolmogorov scale is to be compared to absolute length, $L_K$ has to be multiplied by $2\pi$ (e.g., Imboden and Wüest, 1995). In our case, the rate of dissipation of turbulent kinetic energy is equal to the buoyancy flux ($J_b$), which is defined as (e.g., Imboden and Wüest, 1995)

$$J_b = \frac{g \cdot \beta_S}{\rho} F_s \tag{2.7}$$

where $\beta_S$ is the coefficient of haline contraction, and $F_s$ the salt flux from the ceiling. To determine $L_K$ at the end of an experiment, it is assumed that freshwater enters into contact with the horizontal ceiling. Thus $\upsilon$ is ~$1 \times 10^{-6}$ $m^{-2}$ $s^{-1}$ at 20°C (e.g., Weast, 1982) and $\beta_S$ is ~0.8 (e.g., Steinhorn, 1980). Simplifying that halite dissolution occurs only at the horizontal ceiling (neglecting surface irregularities), the average dissolution rate $R_h$ (in such a situation $R_h = F_s$) was estimated to 0.0016 kg $m^{-2}$ $s^{-1}$ (represented by the dissolution run RS23; see Section 2.4.2). Combining Eqs. (2.6) and (2.7) results in an absolute length scale for $L_K$ of ~3 mm. Furthermore, at a critical Rayleigh number (cf. Eq. (2.4)) of 1700 and a $\Delta\rho$ corresponding to the liquid density difference between the concentration directly adjacent to the horizontal ceiling and the low-density layer below (~0.2 g $cm^{-3}$), $H$ results in ~0.2 mm. According to this height, small convection cells that are larger than ~0.5 mm can be considered turbulent. Therefore, we can conclude that the solution pits represent the smallest possible turbulent eddies, which could not be observed during an experiment, as the traced low-density horizontal layer hid this phenomena.

The interface undersaturated/NaCl-saturated water is close to the horizontal ceiling, which itself is a result of the fluid density layering (Figure 2.8C). Since the density interface is horizontal, the formed ceiling must also be horizontal. Solubility of dissolved gas - in the freshwater mainly carbon dioxide ($CO_2$) - decreases with increasing ionic-strength (Harvie et al., 1984; Stumm and Morgan, 1996). Therefore, the accessing freshwater continuously degases during ongoing halite dissolution (salting out effect) leading to the formation of a gas bubble (Figure 2.8A). Due to the density differences, the NaCl-undersaturated water and gas accumulate at the highest part in the cavity – the gas highest, followed by the undersaturated water, and both floating on the NaCl-saturated brine. Since the gas bubble temporarily insulates part of the cavity roof from net dissolution, it interferes with mass transport. As soon as the salt ceiling dissolves around the bubble it will move to reach this newly created higher position. A rapid shifting bubble affects the density driven flow, but only over a short time and quite locally. However, the gas bubble probably has no leveling effect that creates a flat cavity roof. At the horizontal ceiling and upper end of the facet, density of the inlet water therefore rises ~20%. The gas phase must increase as continuously freshwater is recharged. This also explains the layering of the tracered freshwater and the formation of gas bubbles in the inlet Plexiglas tube.

The band width of the upper end of the facet is not known, as it was only possible to determine it qualitatively in the experiments (cf. Figure 2.6); however, its height is assumed to be within a few millimeters. The upper end of the facet tilts slightly outward, resulting in a practically constant facet inclination because the solute content of the downsliding thin film/finger increases continuously downward and because of cavity-scale convection circulation that also carries, however, only a minimal amount of undersaturated water with respect to halite from the buoyant freshwater jet to the upper end of the facet. Dissolution stops when the film/fingers reach saturation with halite (Figure 2.8C). A thin film or fingers of NaCl-saturated brine subsequently flows down the facet, closing the toroidal convection cell around the buoyant freshwater jet (Figure 2.8A). Some of the downward moving brine then flows further down the borehole (z direction) or rejoins the convection cycle. If some saturated solution is entrained in the upward flowing freshwater, mixing occurs. This decreases the concentration difference-driven halite dissolution rate. Within the cavity, the principal process for movement and transport is convection (forced convection, here induced by peristaltic pump, and free convection). Molecular diffusion cannot create a significant mixing due to the very short residence times. As the brine in the cavity is NaCl-saturated, the continuous input of undersaturated freshwater always leads to a gravitationally unstable concentration distribution, thereby maintaining the convection cycle. When combined, convection of the fluid is caused by (1) the hydraulic gradient, (2) a constant supply of buoyant, undersaturated water from point source, (3) an adjustment of a fluid density layering and (4) an increase in solute NaCl-concentration until NaCl-saturation is reached in a thin, undersaturated layer in contact with the horizontal ceiling and upper end of the facet.

The cavity enlarges by upward growth of the horizontal ceiling and, simultaneously, by sideward growth at the upper end of the facet. Hence, the inclined facet is formed with time (Figure 2.8B). The smooth, irregular facet surface with solution pits is formed during cavity growth at the intersection area of the horizontal ceiling and facet. The upward average dissolution rate was faster across the horizontal ceiling than the sideward dissolution at the upper end of the facet, which led to inclinations of >45°.

The fact that the inclination of the facet is always similar can be attributed to an intrinsic property of the highly soluble mineral (in this case halite). In isotropic homogeneous rock samples (e.g., dissolution run RS2, see Figure 2.3A), they attain their most perfect shapes. These shapes may become distorted (e.g., dissolution run RS15, see Figure 2.4B) or even totally inhibited (e.g., dissolution run RS17, see Figure 2.4B) in anisotropic rock samples.

The influence of buoyancy effects would decrease with increasing inflow rates (cf. Eq. (2.5)). At sufficient high inflow rate buoyancy effects would disappear and dissolution rate would decrease uniformly downstream (z direction). Thus, the cavity form would be probably trumpet-shaped with decreasing circular cavity cross section (parallel xy plane) downstream.

## 2.4.2 Model of cavity development

To test our concept and observations of cavity enlargement, the increase in height of the solution cavity, the increase in horizontal ceiling surface area and the decrease in the average dissolution rate of halite versus time were described mathematically. The modeled solution cavity heights versus time were compared to the experimental data obtained, and the modeled average dissolution rates of halite to literature data on halite dissolution kinetics.

Since with onward cavity evolution the surface area of the upper facet end is far smaller than that of the horizontal ceiling, it was neglected. According to this model, it can thus be assumed that dissolution occurs only at the horizontal ceiling. For a half conical frustum (for the sake of simplicity), the incremental volume increase (Figure 2.9A) is given by

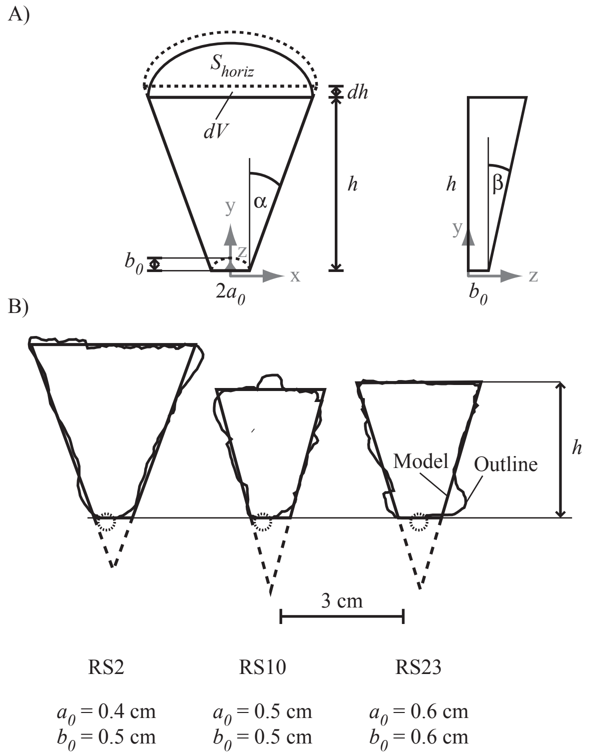

***Figure 2.9*** *A) Conceptual model for cavity enlargement, indicating the formation of a half conical frustum with a horizontal base facing upward. B) Overlay of outline of dissolution runs RS2, RS10 and RS23 and isosceles triangles standing on the apex with a horizontal side facing upward (model). Due to thin layers of impurities and/or slightly offset inlet Plexiglas tube and borehole, the apexes do not have exactly the same horizontal position as the centers of the corresponding original hole.*

$$dV = \frac{1}{2}\pi(\tan\alpha \cdot h + a_0)(\tan\beta \cdot h + b_0)dh \qquad (2.8)$$

where $a_0$ and $b_0$ are the semi-major and semi-minor axis, respectively, of the bottom half ellipse (cm), $\alpha$ is half of the opening angle at outline (°), $\beta$ is half of the opening angle in the yz plane (°), $h$ is the height of the half conical frustum (cm), and $dh$ is the incremental height increase of the half conical frustum.

Combining Eqs. (2.3) and (2.8) results in a cubic equation, solved for *h(t)* yields to the algebraic function

$$\begin{aligned} h(t) = {} & \sqrt[3]{(C_1 - C_2 \cdot t) + \sqrt{(C_1 - C_2 \cdot t)^2 + C_3}} \\ & + \sqrt[3]{(C_1 - C_2 \cdot t) - \sqrt{(C_1 - C_2 \cdot t)^2 + C_3}} - C_4 \end{aligned} \qquad (2.9)$$

where the constants are

$$C_1 = -\frac{\left(b_0 \cdot \tan\alpha + a_0 \cdot \tan\beta\right)^3}{8\left(\tan\alpha \cdot \tan\beta\right)^3} + \frac{3 \cdot a_0 \cdot b_0 \left(b_0 \cdot \tan\alpha + a_0 \cdot \tan\beta\right)}{4\left(\tan\alpha \cdot \tan\beta\right)^2}$$

$$C_2 = -\frac{3 \cdot Q(c_{eq} - c_{in})}{P_{rs} \cdot \rho_h \cdot \pi \cdot \tan\alpha \cdot \tan\beta}$$

$$C_3 = \left(\frac{a_0 \cdot b_0}{\tan\alpha \cdot \tan\beta} - \frac{\left(b_0 \cdot \tan\alpha + a_0 \cdot \tan\beta\right)^2}{4\left(\tan\alpha \cdot \tan\beta\right)^2}\right)^3$$

$$C_4 = \frac{b_0 \cdot \tan\alpha + a_0 \cdot \tan\beta}{2 \cdot \tan\alpha \cdot \tan\beta}$$

and $t$ the running time (h).

To calculate $S_{horiz}$ – the surface area of the horizontal ceiling (cm$^2$) – over time, we obtain for a half conical frustum (cf. Figure 2.9A)

$$S_{horiz}(t) = \frac{\pi(\tan\alpha \cdot h(t) + a_0)(\tan\beta \cdot h(t) + b_0)}{2} \qquad (2.10)$$

$R_h$ (mmol cm$^{-2}$ h$^{-1}$) was computed from

$$R_h(t) = \frac{P_{rs} \cdot Q \cdot c_{eq}}{W_h \cdot S_{horiz}(t)} \cdot 10^3 \qquad (2.11)$$

where $W_h$ expresses the molecular weight of halite (58.44 g mol$^{-1}$) (cf. also Appendix A.4).

The dissolution runs RS2, RS10 and RS23 are interesting to model, as their shapes are close to an exact triangular morphology (Figure 2.9B). $Q$ (RS2: 9.196 ± 0.007 mm$^3$ min$^{-1}$; RS10: 8.628 ± 0.007 mm$^3$ min$^{-1}$; RS23: 77.06 ± 0.06 mm$^3$ min$^{-1}$) and $t$ were measured (see Table 2.1). We assumed in the calculation that $P_{rs} \approx 1$, since the created cavity almost exclusively consisted originally of halite (cf. Table 2.3). $a_0$ was measured by ruler (accuracy of ±0.1 cm), $b_0$ by caliper measuring (accuracy of ±0.1 cm). $\alpha = 90° - \gamma_1$ (cf. Table 2.3), $\beta = 90° - \gamma_2$ (cf. Table 2.3), $c_{in} \approx 0$ g cm$^{-3}$, $c_{eq} \approx 0.317$ g cm$^{-3}$ (Seidell, 1965), $\rho_h = 2.165 \pm 0.005$ g cm$^{-3}$ (Deer et al., 1992).

The computed heights of the cavities are quite consistent with the experimental results obtained in the present study (Figure 2.10A). The computed curve (dissolution run RS23) is slightly too low; however, the shape of the computed curve is very similar to the measured heights and after about halftime of this experiment the measurements are within the margins of error of the simulation. The computed final heights of the dissolution runs RS2 and RS10 are also slightly too low, but within the margins of error of the simulation.

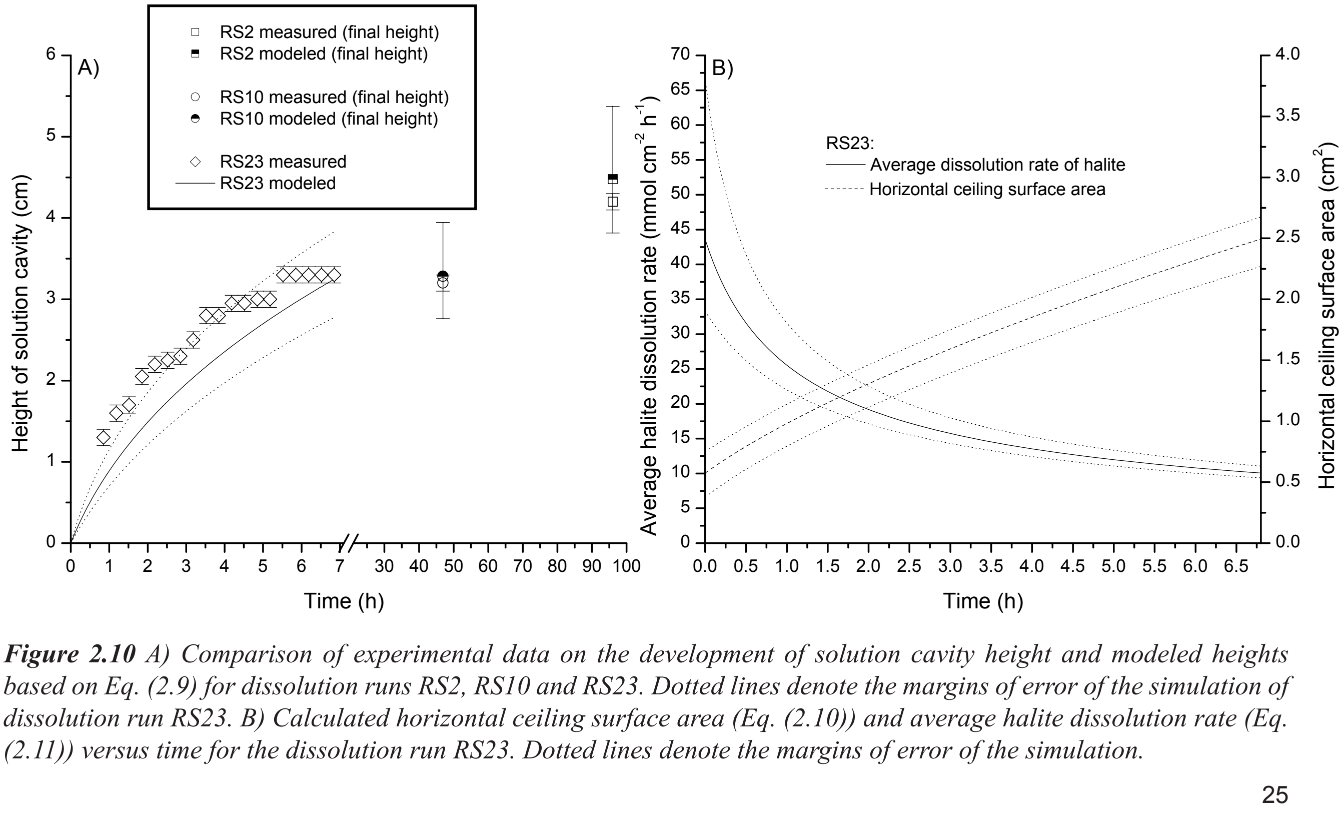

***Figure 2.10*** *A) Comparison of experimental data on the development of solution cavity height and modeled heights based on Eq. (2.9) for dissolution runs RS2, RS10 and RS23. Dotted lines denote the margins of error of the simulation of dissolution run RS23. B) Calculated horizontal ceiling surface area (Eq. (2.10)) and average halite dissolution rate (Eq. (2.11)) versus time for the dissolution run RS23. Dotted lines denote the margins of error of the simulation.*

Figure 2.10B shows in a representative way the calculated surface area of horizontal ceiling and the average halite dissolution rate versus time of dissolution run RS23. The surface area increases in a negative exponential manner, so that the computed average dissolution rate of halite decreases in a positive exponential manner from ~43 to ~10 mmol $cm^{-2}$ $h^{-1}$ during the course of the experiment. The actual average dissolution rate at the horizontal ceiling has to be smaller due to surface irregularities. However, the progression of the curve should be approximately correct, as the calculated dissolution rates correspond to data from the literature. Wagner (1949) measured the average dissolution rate of thin plates of rock salt suspended vertically in unstirred pure water. Since the solution near the surface had a greater concentration and thus a greater density than the bulk of the liquid, a downward flow along the vertical surface occurred. The measured dissolution rates at 16°C ranged between 14.4 and 22.3 mmol $cm^{-2}$ $h^{-1}$. In the experimental studies of Alkattan et al. (1997), at high rotating speed (2000 rpm) and 25°C, the halite dissolution rate amounted to ~14 mmol $cm^{-2}$ $h^{-1}$. The range of the calculated average halite dissolution rates is therefore realistic, which also supports the theory of selective dissolution in the solution cavity described in this paper.

### 2.4.3 Conceptual setting

Inspired by the results obtained and by the well-preserved cave passage morphology with tip-down triangular cross section in gypsum and its geological setting (e.g., Kempe, 1972, 1996), we assume the following two scenarios if NaCl-undersaturated aquifer water gets in contact with a rock salt body from below provided that buoyancy-driven flow adjusts (cf. Eq. (2.5)): Undersaturated water emerging into the NaCl-saturated cavity water rises along a permeable fracture (inflow of freshwater along a line into the cavity) or along a conduit (punctiform source of freshwater) from an underlying NaCl-undersaturated water source (aquifer) to the rock salt stratum (aquitard). Interjacent, low-permeable and poorly soluble stratums (e.g., clay) can be assumed between the aquifer and the rock salt stratum. Further up, the fracture is water-impenetrable. Cavities slowly develop over time starting from the upper end of the fracture/of the conduit as illustrated in Figure 2.11. Along a fracture, the cavity has the shape of a triangular prism with a horizontal base facing upward. A conical cavity with a horizontal base facing upward develops above a conduit. In the field, the motion of the fracture/cavity water could be probably less turbulent than during the conducted laboratory experiments.

In the cavity, the NaCl-undersaturated water rises to the horizontal ceiling along the plane of symmetry of the triangular prism or axis of the cone. At the horizontal ceiling and at the upper end(s) of the facet(s), the water becomes NaCl-saturated. Since the undersaturated water source (aquifer) is under pressure, a flow cycle develops, in which the salt

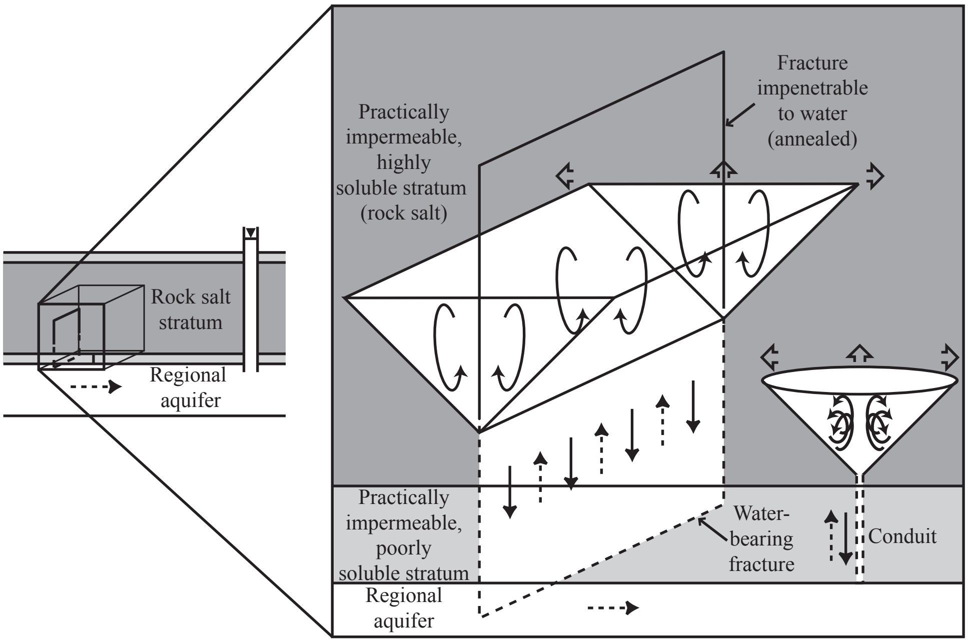

***Figure 2.11*** *Conceptual model for salt cavity developing inside rock salt (soluble stratum) – overlying a confined undersaturated aquifer – along a fracture and above a conduit. Fracture and conduit may not be oriented vertically. See Figure 2.8 for legend.*

dissolution itself supplies the density gradient that becomes the drive mechanism of its own dissolution (free convection). Consequently, two convective cells are formed in a triangular prism cavity. The axes of the cells run parallel to the longitudinal alignment of the cavity (Figure 2.11). In a conical cavity, a toroidal convection cell develops as in the experimental results presented. The brine then moves down the facet(s) and further downward along separate and distinct pathways in the same fracture system or conduit as the buoyant NaCl-undersaturated water, or rejoins the cavity-scale convection circulation. The NaCl-loaded descending saline water is diluted in the aquifer and flows ultimately through the aquifer to a point or area of natural discharge. Since the water is pressurized, the descending dense flow is continuously replaced by fresher water. A good example of such a system is the Delaware Basin in Texas and New Mexico. The dissolution and collapse features in this basin were explained by buoyancy-driven dissolution simulated in the laboratory by simplified channel geometries (Anderson and Kirkland, 1980).

These cavities enlarge under confined conditions by both upward growth of the horizontal ceiling and sideways growth at the upper facet(s) end(s). Mixing occurs in the upward flowing undersaturated water, this decreases the concentration-driven buoyancy effect as well as the halite dissolution rate. The rising horizontal ceiling ends at the latest with the highest groundwater level or at the top of the salt stratum. If a triangular prism-shaped cavity collapses and the overlying rock also collapses or subsides, an elongated collapse or subsidence trough parallel to the strike of the fracture is then formed at the surface. In the case of a conical cavity, a collapse sinkhole or a circular subsidence depression is formed at the surface.

### 2.4.4 Comparison with natural field occurrences

The results of the experiments concur qualitatively with the field observations in, for example, accessible natural salt cave passages (Figure 2.12A) and in solution-mined caverns in rock salt by a top injection brining system (Figure 2.12B). The morphological elements of horizontal ceiling and facet(s) (in the field: several superimposed facets) can be identified clearly. In the case of a solution-mined cavern, the freshwater also accessed through a point source, as in the experimental setup. Unfortunately, companies involved in solution mining of halite generally do not publicize their findings, for reasons of competition. However, such a solution-mined cavern also enlarges upwards (L. Hauber, 2003, personal communication). Leaching led to a mainly vertical axisymmetrical cavern, where the drilling represents roughly the axis of rotation. This cavern reveals a morphology with many notches, corresponding quite well to the zones of interbedded anhydrite (less soluble) and marl (poorly soluble) layers or lentils. During mining, these interbedded lithologies were undercut by undersaturated water until the beds sagged and broke down before a new upper facet was developed (L. Hauber, 2003, personal communication). The natural salt cave passage presented here (see Figure 2.12A) is considered to have developed by upward dissolution (Frumkin, 1994, 1998). The experimental results and theoretic considerations clearly confirm that both cavities evolve in the same way. Thus, the superimposed facets in the natural salt cave passage also may have developed successively; i.e., the deepest first, the highest last.

In relatively stagnant water or where there is extremely slow water circulation, concentration-driven buoyant groundwater flow is expected even at the slightest concentration gradients. Thus, the presented hydrodynamics and enlargement model in a highly soluble rock as presented here could also be applicable to accessible gypsum cave passages (e.g., Kempe, 1996; Klimchouk, 2000) and carbonate rock cave passages (e.g., Skřivánek and Rubin, 1973; Ford and Williams, 2007) showing the same morphological elements, considering that those rocks possess other dissolution kinetics (for gypsum (Jeschke et al., 2001); for limestone (e.g., Dreybrodt and Eisenlohr, 2000)) and far smaller fluid density differences.

## 2.5 Conclusions

This study reveals the advantage of small-scale dissolution experiments when attempting to simulate much larger scale field phenomena. The experimental data and theoretic hydraulic-geochemical considerations allow a coherent explanation of the extremely complex convective and turbulent nature of flow in salt cavities and formation of tip-down triangular cavity cross sections.

Since halite dissolution takes place at the horizontal ceiling and upper end of the facet, the cavities enlarge under confined conditions by upward growth of the horizontal ceiling and also by lateral growth at the upper end of the facet. The resulting morphological elements of the horizontal ceiling and facet reported in the laboratory concur qualitatively with field observations in natural salt caves and solution-mined

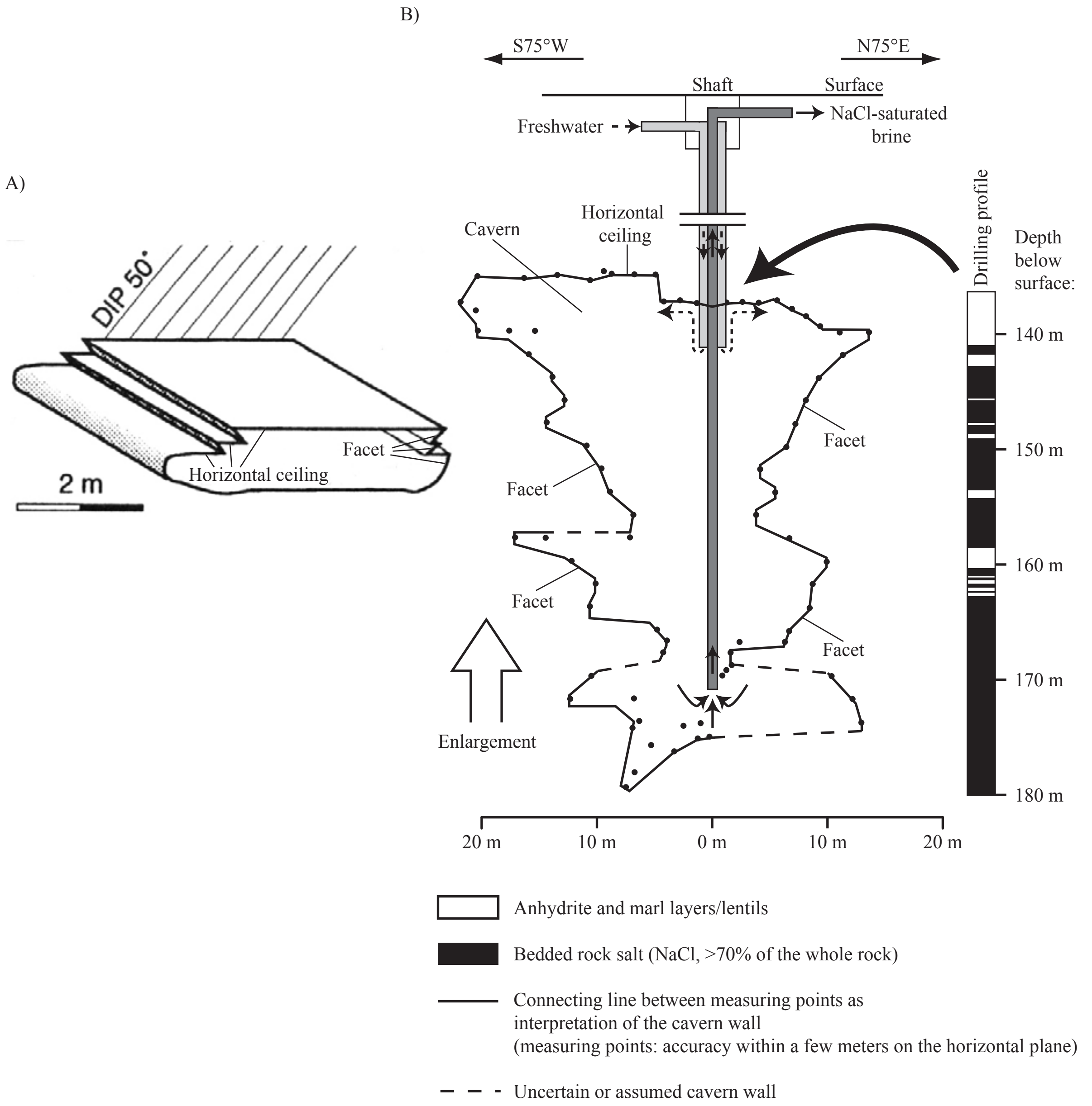

***Figure 2.12*** *A) Isometric view of a vadose passage section in the Mifrazim cave (Mount Sedom salt diapir; Israel) (modified from Frumkin, 1994). At this location, the salt beds dip with 50°. B) Vertical cross section (about parallel to the strike of the strata) of cavern leached in a rock salt layer of the Tabular Jura (Middle Muschelkalk, Triassic) 20 km east of Basel, Switzerland. The shape of the cavern was measured in 1978 by down hole sonar. The measuring points were determined with an accuracy of about ±1 m (L. Hauber, 2006, personal communication). On the right, representation of the corresponding drilling profile. Layers dip gently NNW up to 3° (Hauber, 1980). The extraction of salt by top injection brining is schematically presented. At this time, freshwater was injected near the cavern ceiling, extracting the salt from the cavern wall and hoisting the resultant brine from near cavern bottom to the surface through either an adjacent connecting borehole shaft or an annulus formed by equipping a single hole with concentric casings (Jacoby, 1973). This method worked without a gaseous or liquid roof pad (so-called "blanket"), which was later introduced to prevent the freshwater from dissolving the salt on the cavern ceiling.*

caverns by top injection brining without "blanket" in rock salt. Thus, the mutual data obtained from laboratory experiments and fieldwork experience contributes to enhancing our knowledge of deep-seated salt karst genesis. The morphology of such cavities is an indicator of cavity development; i.e., the hydrodynamics under confined settings and rock-water interactions at the time of cavity evolution (paleohydrogeology). The conceptual model presented could potentially represent a universally applicable theory of the genesis of cave passages with tip-down triangular cross section in evaporite and carbonate rocks under specific flow conditions.

The mechanism of cavity enlargement can, in general, be used as a model for active deep-seated development of natural underground cavities within largely impermeable salt deposits. If a fracture or conduit provides a communication between a confined undersaturated water aquifer and an overlying highly soluble, practically impermeable salt body, cavities of triangular prism or conical shape may develop, even for relatively distant freshwater sources. Cavities developed by concentration-driven buoyant groundwater flow coupled with salt dissolution may cause land subsidence or collapse structures that vertically penetrate or occur within the underground. Moreover, the deep-seated dissolution can have serious consequences for highly sensitive subsurface sites (e.g., mines and waste repositories) situated in highly soluble salt deposits.

## Acknowledgements

We would like to thank the following persons at the Department of Environmental Sciences, University of Basel: H.-R. Rüegg and C. Schneider for technical and laboratory assistance, W. Stern and H. Hürlimann for geochemical analyses and L. Hauber for helpful discussions. Our thanks also go to M. Dürrenberger and D. Mathys, Center of Microscopy, University of Basel, for the experimental setup allowing to visualize and record the uranine dye and for taking SEM pictures, and T. Lehmann from the New Media Center, University of Basel, for digitalization and extraction of video images. At EAWAG we thank A. J. Wüest for assistance in understanding buoyancy effects in fluids. We are also indebted to W. Neubert of the United Swiss Saltworks for providing rock salt cores and data on the shape of a solution-mined cavern. The Swiss National Science Foundation, Grants 21.65092.01 and 200020-105492, provided the financial support for this study. We thank the three anonymous reviewers for their suggestions.

## 2.6 References

Alkattan, M., E. H. Oelkers, J.-L. Dandurand, and J. Schott (1997), Experimental studies of halite dissolution kinetics, 1 The effect of saturation state and the presence of trace metals, *Chem. Geol.*, *137*, 201–219.

Anderson, R. Y., and D. W. Kirkland (1980), Dissolution of salt deposits by brine density flow, *Geology*, *8*, 66–69.

Biese, W. (1931), Über Höhlenbildung; 1. Teil; Entstehung der Gipshöhlen am südlichen Harzrand und am Kyffhäuser, *Abh. Preuss. Geol. Landesanst.*, *137*, 1–70.

Clesceri, L. S., A. E. Greenberg, and A. D. Eaton (1998), *Standard methods for the examination of water and wastewater*, 20th edition, Am. Public Health Assoc., Washington, D. C.

Cooper, A. H. (2002), Halite karst geohazards (natural and man-made) in the United Kingdom, *Environ. Geol.*, *42*, 505–512.

Deer, W. A., R. A. Howie, and J. Zussmann (1992), *An introduction to the rock-forming minerals*, 2nd ed., Longmann Scientific Technical, Harlow.

Dijk, P. E., and B. Berkowitz (2000), Buoyancy-driven dissolution enhancement in rock fractures, *Geology*, *28*(11), 1051–1054.

Dreybrodt, W., and L. Eisenlohr (2000), Limestone dissolution rates in karst environments, in *Speloegenesis – evolution of karst aquifers*, edited by A. B. Klimchouk, D. C. Ford, A. N. Palmer and W. Dreybrodt, pp. 136–148, National Speleological Society, Huntsville.

Ford, D., and P. Williams (2007), *Karst hydrogeology and geomorphology*, John Wiley & Sons, West Sussex, England.

Frumkin, A. (1994), Morphology and development of salt caves, *NSS Bull.*, *56*, 82–95.

Frumkin, A. (1998), Salt cave cross-sections and their paleoenvironmental implications, *Geomorphology*, *23*, 183–191.

Frumkin, A. (2000), Speleogenesis in salt – the Mount Sedom area, Israel, in *Speloegenesis – evolution of karst aquifers*, edited by A. B. Klimchouk, D. C. Ford, A. N. Palmer and W. Dreybrodt, pp. 443–451, National Speleological Society, Huntsville.

Frumkin, A., and E. Raz (2001), Collapse and subsidence associated with salt karstification along the Dead Sea, *Carbonates Evaporites*, *16*(2), 117–130.

Gebhart, B., Y. Jaluria, R. L. Mahajan, and B. Sammakia (1988), *Buoyancy-induced flows and transport*, Hemisphere/Harper and Row, Washington.

Harvie, C. E., N. Møller, and J. H. Weare (1984), The prediction of mineral solubilities in natural waters: The Na-K-Mg-Ca-H-Cl-$SO_4$-OH-$HCO_3$-$CO_3$-$CO_2$-$H_2O$ system to high ionic strengths at 25°C, *Geochim. Cosmochim. Acta*, *48*, 723–751.

Hauber, L. (1980), Geology of the salt field Rheinfelden-Riburg, Switzerland, in *Fifth Symposium on Salt*, vol. 1, edited by A. H. Coogan and L. Hauber, pp. 83–90, N. Ohio Geol. Soc., Cleveland, Ohio.

Imboden, D. M., and A. Wüest (1995), Mixing mechanisms in lakes, in *Physics and chemistry of lakes*, edited by A. Lerman, D. M. Imboden and J. R. Gat, pp. 83–138, Springer-Verlag, Berlin.

Jacoby, C. H. (1973), Solution mining of halite through boreholes, *SME engineering handbook*, vol. 2, edited by A. B. Cummins and I. A. Given, pp. 21.49–21.55, SME-AIME, New York.

James, A. N. (1992), *Soluble materials in civil engineering*. Ellis Horwood, Chichester.

James, A. N. and I. M. Kirkpatrick (1980), Design of foundations for dams containing soluble rocks and soils. *Q. J. Eng. Geol.*, *13*, 189–198.

Jeschke, A. A., K. Vosbeck, and W. Dreybrodt (2001), Surface controlled dissolution rates of gypsum in aqueous solutions exhibit nonlinear dissolution kinetics, *Geochim. Cosmochim. Acta*, *65*(1), 27–34.

Johnson, K. S. (1981), Dissolution of salt on the east flank of the Permian Basin in the southwestern U.S.A., *J. Hydrol.*, *54*, 75–93.

Käss, W. (1998), *Tracing technique in geohydrology*. A. A. Balkema, Rotterdam, Brookfield.

Kegel, K. (1951), Der Salzstock Mirowo bei Provadia in Bulgarien, *Ber. Verh. Saechs. Akad. Wiss. Leipzig*, *Math. Naturwiss. Kl.*, *98*(3), 1–26.

Kempe, S. (1972), Cave genesis in gypsum with particular reference to underwater conditions. *Cave Science*, *Journ. Brit. Spel. Assoc.*, *49*, 1–6.

Kempe, S. (1996), Gypsum karst of Germany, in *Gypsum karst of the world*, *Int. J. Speleol.*, 25, 3-4, edited by A. Klimchouk, D. Lowe, A. Cooper and U. Sauro, pp. 209–224, Società Speleologica Italiana, Italy.

Klimchouk, A. (2000), Speleogenesis of the Great Gypsum Mazes in the Western Ukraine, in *Speloegenesis – evolution of karst aquifers*, edited by A. B. Klimchouk, D. C. Ford, A. N. Palmer and W. Dreybrodt, pp. 261–273, National Speleological Society, Huntsville.

Kolmogorov, A. (1941), The local structure of turbulence in incompressible viscous fluid for very large Reynolds' numbers, *Dokl Akad Nauk USSR*, *30*(4), 301–305.

Kozary, M. T., J. C. Dunlap, and W. E. Humphrey (1968), Incidence of saline deposits in geologic time, *Geol. Soc. Am. Spec. Pap.*, *88*, 43–57.

Lasaga, A. C. (1990), Atomic treatment of mineral-water surface reactions, in *Mineral-water interface geochemistry*, *Rev. Mineral.*, vol. 23, edited by M. F. Hochella Jr. and A. F. White, pp. 17–85, Mineral. Soc. Am., Washington, D. C.

Martinez, J. D., K. S. Johnson, and J. T. Neal (1998), Sinkholes in evaporite rocks, *Am. Sci.*, *86*, 38–51.

McManus, K. M. and J. S. Hanor (1993), Diagenetic evidence for massive evaporite dissolution, fluid flow, and mass transfer in the Louisiana Gulf Coast. *Geology*, *21*, 727–730.

Quinlan, J. F., R. A. Smith, and K. S. Johnson (1986), Gypsum karst and salt karst of the United States of America, *Le Grotte d'Italia*, *4*(XIII), 73–92.

Reuter, F., and D. Stoyan (1993), Sinkholes in carbonate, sulphate, and chloride karst regions: Principles and problems of engineering geological investigations and predictions, with comments for the destruction and mining industries, in *Applied karst geology*, edited by B. F. Beck, pp. 3–25, A. A. Balkema, Rotterdam, Brookfield.

Seidell, A. (1965), *Solubilities inorganic and metal-organic compounds*, vol. II, 4th ed., edited by W. F. Linke, pp. 958–959, Am. Chem. Soc., Washington, D. C.

Skřivánek, F., and J. Rubin (1973), *Caves in Czechoslovakia*, Academia, publishing House of the Czechoslovak Academy of Sciences, Prague.

Steinhorn, I. (1980), The density of Dead Sea water as a function of temperature and salt concentration, *Isr J Earth-Sci*, *29*, 191–196.

Stumm, W., and J. J. Morgan (1996), *Aquatic chemistry*, *Chemical equilibria and rates in natural waters*, 3rd ed., John Wiley & Sons, New York.

Turner, J. S. (1973), *Buoyancy effects in fluids*, Cambridge University Press, London.

Wagner, C. (1949), The dissolution rate of sodium chloride with diffusion and natural convection as rate-determining factors, *J. Phys. Colloid Chem.*, 53, 1030–1033.

Waltham, A. C. (1989), *Ground subsidence*, Blackie & Son, Glasgow and London.

Weast, R. C. (ed.) (1982), *Handbook of Chemistry and Physics*, 63th ed., CRC Press, Boca Raton, Florida.

Zaytsev, I. D., and G. G. Aseyev (Eds.) (1992), *Properties of aqueous solutions of electrolytes*, CRC Press, Boca Raton, Florida.

# 3 How do horizontal fracture-guided gypsum cave passages with a tip-down triangular cross-section develop? A key experimental setup

Daniel Gechter[1], Peter Huggenberger[1], and Alfred Wüest[2]

[1]Department of Environmental Sciences, University of Basel, Basel, Switzerland

[2]Alfred Wüest, Swiss Federal Institute of Aquatic Science and Technology (Eawag), Kastanienbaum, Switzerland

and

Institute of Biogeochemistry and Pollutant Dynamics, ETH Zurich, Switzerland

Submitted to Journal of Hydrology (except references to appendices)

## Abstract

The first part of this paper consists of a literature review of the three main conceptual models applied to describe the genesis of fracture-guided horizontal gypsum cave passages with a tip-down triangular cross-section. All three models are primarily based on the analysis of characteristic morphological elements (horizontal ceiling, facets and solution pits) and their interconnection, as well as different laboratory vessel experiments. One model is additionally based on field experiments. There is, however, no satisfactory explanation of the genesis of such unusual passages given by any model. To shed some light on this issue, a new laboratory experimental setup was developed, where freshwater was pumped slowly through a horizontal borehole (in place of a fracture) into more soluble rock salt cores. The resulting small-scale solution cavities revealed the same morphological elements as observed in natural gypsum caves. Furthermore, visualization of the cavity water streamlines and cavity enlargement, including theoretical hydrogeochemical considerations, led to a comprehensive conceptual model in a regional hydrogeological context. Such a passage starts to develop from the upper end of a permeable fracture, which provides a communication to a confined underlying gypsum-depleted water aquifer with its potentiometric surface above the developing passage. As the aquifer is under pressure, a buoyant turbulent cycle develops in the fracture/cavity void where the gypsum dissolution, at the upper limit of the developing cavity, supplies the density gradient, which becomes the driving mechanism for its own dissolution (free convection). Such a passage is enlarged mainly by upward growth of the horizontal ceiling and simultaneously by lateral growth at the upper end of the facet. Since a stable fluid density interface is horizontal and, in this case, close to the upper limit of the cavity, the formed ceiling must also be horizontal. If such a passage is located in the epiphreatic or vadose zone it can be considered an indicator for paleohydrogeology.

*KEYWORDS*: gypsum cave passage, horizontal ceiling, facets, solution pits, gypsum dissolution, buoyant turbulent flow

## 3.1 Introduction

### 3.1.1 General

Sulfate rocks are widely distributed in continental regions (e.g., Kozary, 1968). The mineral gypsum ($CaSO_4 \cdot 2H_2O$) is moderately soluble, and thus, where gypsum strata occur at depth, circulating groundwater can selectively dissolve and remove the rock leading to gypsum karstification (e.g., Ford and Williams, 2007). Extensive areas of gypsum karst can be found worldwide (e.g., Quinlan et al., 1986; Klimchouk et al., 1996) and may have an effect on formation properties, e.g. land subsidences or catastrophic collapses (e.g., Cooper, 1986, 1998).

A cave is generally a natural underground opening in rock large enough for human passage (e.g., Ford and Williams, 2007) where direct information on a karst system can be obtained. In addition to the analysis of cave patterns, each morphological element is a potential tool facilitating determination of a cave's genesis and main characteristics of past hydrogeological settings (e.g., Lauritzen and Lundberg, 2000).

This paper focuses on the genesis of an unusual horizontal fracture-guided passage encountered mainly in gypsum caves (Ford and Williams, 2007), particularly in Germany (e.g., Kempe, 1996) and in the Ukraine (e.g., Klimchouk, 1997, 2000a, 2000b). Such cave passages are morphologically characterized by a horizontal ceiling and inclined plane sidewalls, the so-called facets (terminology according to Biese, 1931). The ideal passage cross-section is an isosceles triangle standing on the apex (Figure 3.1A). The facets are narrowly inclined between 40 and 50°, and their surfaces are always smooth and covered with solution residues (e.g., Reinboth, 1968, 1971). Only Reinboth segregated a further morphological element, i.e. the lateral overhanging wall sections inclined between >90 and <180° and always clearly bordered against the facets and horizontal ceiling (Figure 3.1B). Furthermore, small unordered, cup-shaped solution pits, the size of finger tips, can be observed on the horizontal ceiling and lateral overhanging wall sections (Figure 3.1B and Figure 3.1C). Their origin is not related to the inhomogeneity of the rock (Kempe, 1969).

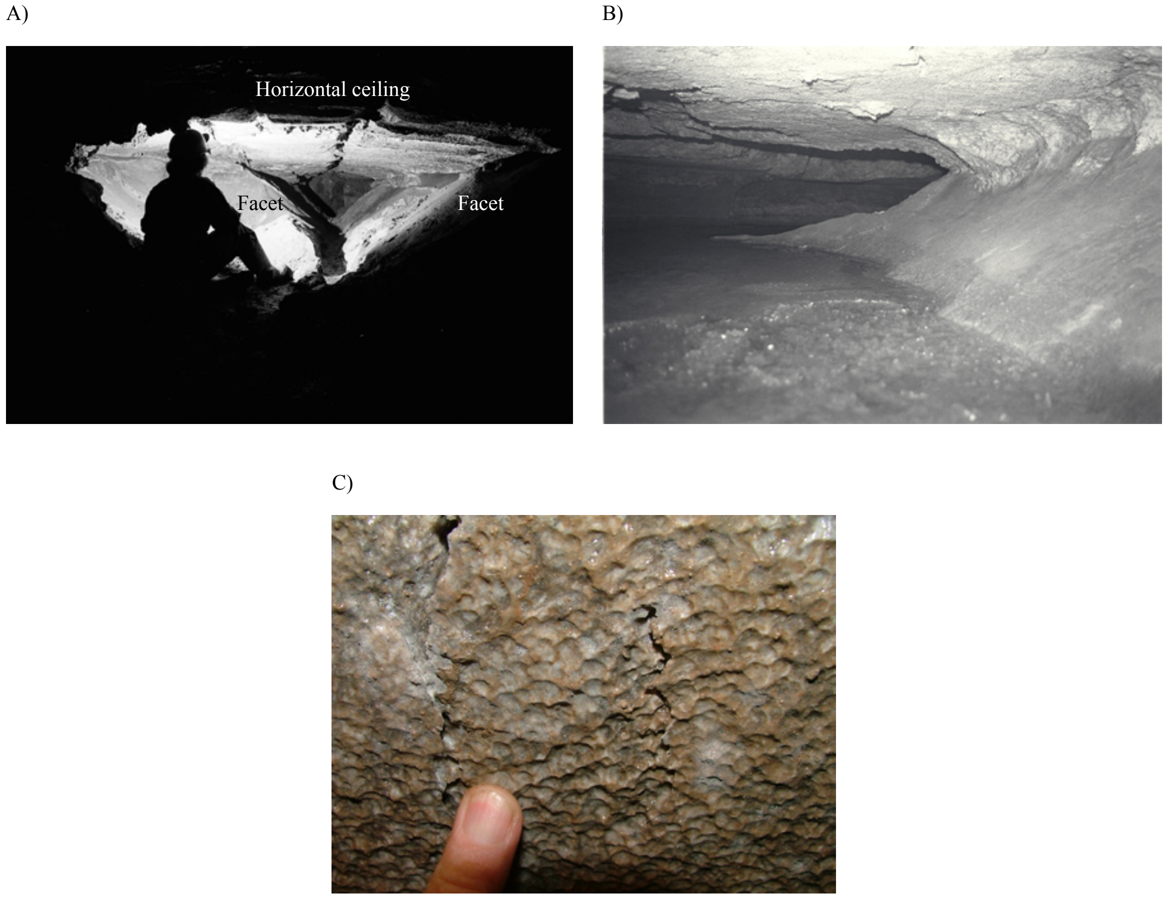

***Figure 3.1*** *A) Typical cave passage profile of the Segeberger gypsum cave, Germany (from Reinboth, 1992). Note the fracture visible along the middle of the ceiling. B) Solution cavity of the Martha gypsum cave, Germany, with horizontal ceiling, lateral overhanging wall section and facet (top down). Cavity height above water table ~0.5 m (photo by F. Reinboth). C) Solution pits of the Heimkehle gypsum cave, Germany (photo by S. Kempe).*

The following section presents the available three main conceptual models on the genesis of such caves. Section 3.1.3 elucidates the statement of the problems and objectives of this paper.

### 3.1.2 Existing conceptual models

An overview of all the hypotheses related to the formation of such caves is described in Reinboth (1992). Most of the studies on these typical morphological elements were conducted last century by Gripp (1913), Reinboth (1968, 1971, 1992), Kempe (1969, 1972, 1996), Kempe et al. (1975, 1976) and Brandt et al. (1976). According to these authors, such a solution cave develops under phreatic conditions, starting from a vertically-oriented, water-filled fracture. The authors also unanimously agree that the cavity water is nearly static and its flow mainly concentration-driven and coupled with gypsum dissolution. Aside from the analysis of morphological elements in the natural caves, all three postulated conceptual models are also based on different vessel experiments compiled and presented in Table 3.1. These were conducted, as observations in caves are normally snap-shots requiring additional laboratory dissolution experiments to understand their development processes (Reinboth, 1992). Furthermore, field measurements are limited by the complexity and cost of the instrumentation. Only one model is additionally based on field experiments in cave pools during periods of low water of still active solution cavities displaying facets on the sides and a horizontal ceiling (Kempe et al., 1975; Brandt et al., 1976).

The vessel experiments were conducted using three different setups with rock salt or gypsum (cf. Table 3.1). Setup 1 was used for the general understanding of the cave development, setup 2 to understand why the facets are always inclined at ~45° or to attempt to produce facets and setup 3 to verify a hypothesis by Kempe et al. (1975) and Brandt et al. (1976) regarding the development of a horizontal ceiling. In the first experimental setup, the lower part of a clearly transparent cubical rock salt block (experiments 1a–b) or a cylindrical molded gypsum block (experiment 1c) with a vertically-oriented borehole in the center was placed in a halite (NaCl) or gypsum-saturated solution, respectively, allowing communication of the liquid in the borehole and the outer completely filled vessel water (constant liquid level). In experiments 1a–b, the borehole was repeatedly filled from above with colored freshwater (to differentiate it from the NaCl-saturated solution) down to a predefined depth: either the supplied water remained only for a short time and was soon replaced by fresh solution in order to always maintain the lower boundary of the undersaturated water at approximately the same depth (experiment 1a), or the supplied water remained each time until it was halite-saturated (experiment 1b). In experiment 1c, the borehole was regularly supplied with freshwater drops from above. In the second experimental setup, only a flat surface (facet) of the soluble rock remained in contact with originally freshwater for a certain time. In experiment 2a, a sealed watertight plaster of Paris plate with a free upper face was placed in freshwater at different inclinations. The behavior of the dissolution rate of gypsum was determined from measurements of dissolved $Ca^{2+}$ concentrations in the water. However, it should be mentioned that this experiment did not provide interpretable data due to a hydrochemical stratification in the vessel that corrupted the measurements. In experiment 2b, a sealed watertight cubical rock salt block with one free face was suspended in water at different facet inclinations. The dissolution rate of halite was determined from the weight loss of the block material. In experiment 2c, the free face was placed perpendicular into water. In the third experimental setup, a rock salt block with a tilted planar underside was suspended in freshwater (experiment 3).

The aforementioned authors developed conceptual models (hereafter referred to as Gripp's model, Reinboth's model and Kempe's model) with different approaches, as schematically presented in Figure 3.2. To reproduce the concepts of these models as accurately as possible, in the following of this section it is assumed that gypsum dissolution finally leads to a gypsum-saturated solution relatively quickly, although this fact could not be confirmed (cf. Section 3.2).

Gripp initially suggested that the solvent supply comes from above through the unsaturated zone (percolation water), and that the horizontal ceiling corresponds to a paleo stable karst groundwater table. As soon as the dammed undersaturated water starts to dissolve the fracture walls (initial facets), a dense solution film with a higher concentration and greater density than the bulk of the cavity fluid forms at the facet. Due to its higher density, this film slides downward, thereby initiating a passage-scale convection flow. With steadily increasing density of the bulk cavity water from the top downwards, the gypsum dissolution rate steadily decreases from top down. The thereby formed facets are the projection of the saturation level of the bulk cavity water. Consequently, the triangular cross-section of the passage is caused by a tilting of the fracture walls from the vertical to the

| Experiment number / Reference | Setup 1 | Setup 2 | Setup 3 | Material | Initial solution in vessel | Objective |
|---|---|---|---|---|---|---|
| 1a / Gripp (1913) | x | | | Transparent rock salt | NaCl-saturated solution | Producing cavity with tip-down triangular cross section |
| 1b / Gripp (1913) | x | | | Transparent rock salt | NaCl-saturated solution | |
| 1c / Kempe (1969, 1972) | x | | | Molded gypsum | $CaSO_4$-saturated solution | |
| 2a / Kempe and Hartmann (1977) | | x | | Plaster of Paris | Freshwater | Study dissolution rate at facets depending on inclination angle |
| 2b / Reinboth (1992) | | x | | Rock salt | Freshwater | |
| 2c / Reinboth (1992) | | x | | Rock salt | Freshwater | Producing facets |
| 3 / Reinboth (1992) | | | x | Rock salt | Freshwater | Producing a horizontal ceiling |

***Table 3.1*** *Conducted vessel experiments. See text for explanation.*

horizontal, provided the boundary between saturated and undersaturated water with respect to gypsum is maintained in the same position. Since the water table is assumed to remain horizontal over small distances, the interface water table/rock must also run horizontally. Gripp (1913) saw his hypothesis confirmed by experiment 1a, where the resulting cavity revealed a tip-down triangular cross-section, whereas experiment 1b led to a cavity with a horizontal ceiling and inclined arced sidewalls.

About half a century later, Reinboth (1968) revised Gripp's (1913) interpretation of the genesis of this unusual solution cavity form (cf. Figure 3.2). He concluded that the facets could not originate by the tilting of the fracture walls, since the inclination of the facets is always ~45°. Furthermore, it is very unlikely that a karst groundwater table remains at a constant level, and that the boundary to the deeper gypsum-saturated water remains at roughly the same depth. Based on these considerations, a downwards increasing concentration of dissolved gypsum in the bulk cavity water cannot be the reason for facets formation, and the horizontal ceiling cannot adhere to the water table. Reinboth suggested that the horizontal ceiling must develop independently and lower than the water level. Gypsum dissolution always occurs at the horizontal ceiling and along lateral overhanging wall sections without any gypsum dissolution at the facets. Solution residues on the facets are only a secondary hindrance of gypsum dissolution at the facets, as in experiment 2c small superimposed facets were produced. In this experiment, he also observed a down sliding film along the salt face, as intuitively introduced by Gripp. He postulated that the cave passage enlarges from a horizontal starting line only through the upward growth of the horizontal ceiling and sideward growth of the lateral overhanging wall sections. In the early stages, the cave ceiling is ellipsoidal. With progressive leaching, the facets extend upwards and their orientations remain constant, while the horizontal ceiling broadens.

The third model (cf. Figure 3.2) considers the cave genesis more in a regional hydrogeological context and proposes two scenarios of regional groundwater flow system (Kempe, 1996). Gypsum-undersaturated water enters the fracture either from the sides or from below. Gypsum-undersatured water entering sideways can, for example, originate from groundwater circulating in an alluvial valley adjacent to the gypsum rock. In the other scenario, gypsum-undersaturated water originates from an underlying confined aquifer. The water in the underlying aquifer is less dense than the gypsum karst water and rises along the fracture into the gypsum rock due to buoyancy. Once saturated with gypsum, it becomes heavier and returns to the underlying aquifer, giving rise to a system of natural convection in the fracture. These cavities are formed closely below the water table (shallow phreatic). Concerning the processes within the developing solution cavity, the basic idea of Gripp (1913) was adapted for this model, i.e. density increases due to gypsum dissolution initiating a descending current on the facet, leading to a stable system of passage-scale convection flow. This idea is supported by conducted field experiments, which reveal a 1 to 3 mm thick film of water descending along the facets at velocities of up to tens of cm $min^{-1}$. If the water had no direct contact with the facets, it stood practically motionless in the water pool. The pool surface water moved towards the edge of the pool at several dm $d^{-1}$ (Kempe et al., 1975; Brandt et al., 1976). Therefore, the flow velocities within the passage-scale convection flow

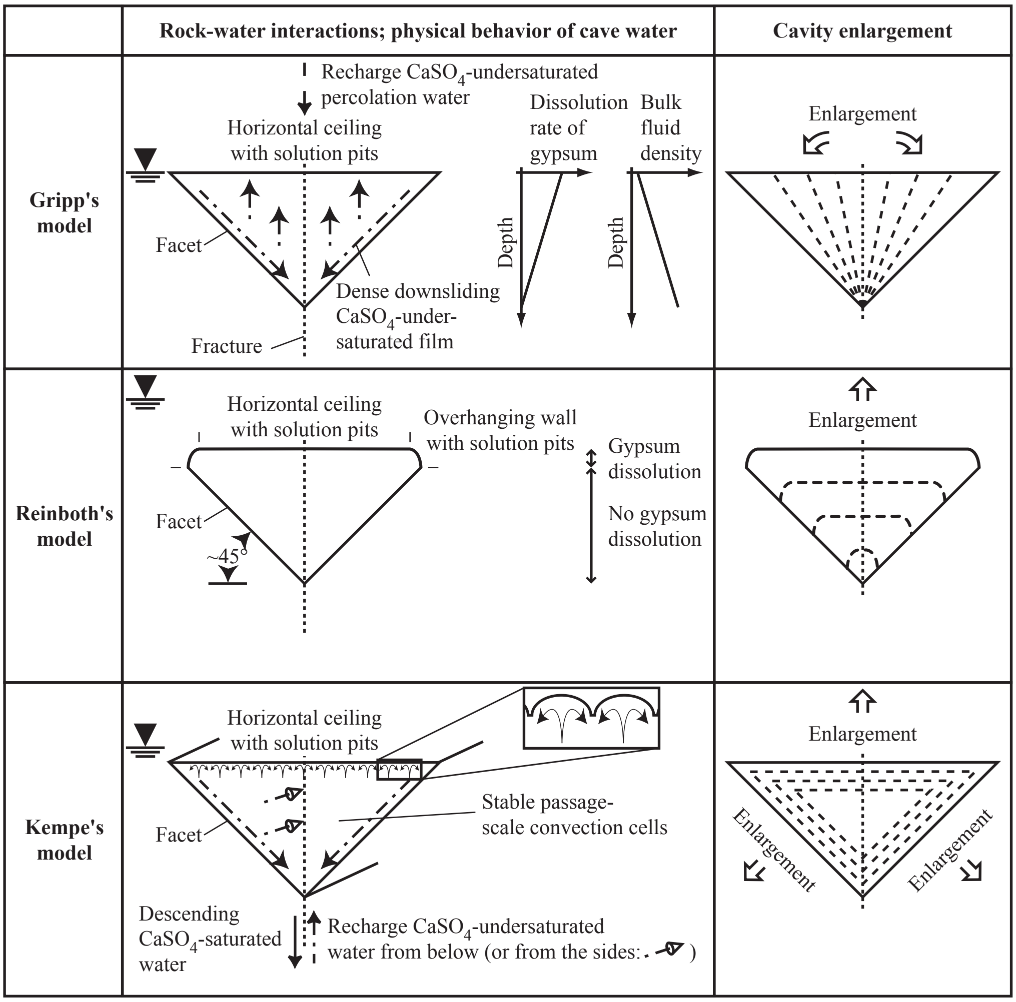

***Figure 3.2*** *Gripp's, Reinboth's and Kempe's model for cave genesis.*

are up to several orders of magnitude lower than those observed at the facets. At the horizontal ceiling, $Ca^{2+}$ and $SO_4^{2-}$ ions diffuse into the gypsum-undersaturated cavity water creating a density instability of the cavity fluid. This leads to the formation of a pattern of small up- and downwelling convection cells (saltwater fingering layer), which form small solution pits on the ceiling. Kempe (1969) showed with experiment 1c that confined, gypsum-undersaturated water below a gypsum rock creates solution pits. Since the surface of the saltwater fingering layer is horizontal, the ceiling should consequently also be horizontal (Kempe et al., 1975; Brandt et al., 1976). The dissolution rate along the facets is uniform (Kempe, 1972, 1996). Thus, when starting from a horizontal line, the horizontal ceiling rises upward at the same time as the facets retreat (Kempe, 1972, 1996; Kempe et al., 1975). As in Reinboth's model, this theory views sediment cover on the facets only as a negligible hindrance of gypsum dissolution (Kempe and Hartmann, 1977).

### 3.1.3 Statement of the problems and objectives of this paper

Despite of the information obtained from field and laboratory studies, major uncertainties remain regarding the formation of such caves. None of the presented models can comprehensively explain the genesis of the morphological elements of the facets, lateral overhanging wall sections, horizontal ceiling, and solution pits. Neither Reinboth's nor Kempe's model can explain why the facets seem to develop best at slopes of ~45°. Also in experiment 2b, no noticeable behavior at ~45° inclination was detected, as dissolution rate of halite increased approximately linear from the 0 inclination (lying free face) to 180° (hanging free face). There is still no explanation for the horizontal orientation of the ceiling. According to Kempe's salt finger theory, the horizontal ceiling represents an upper, naturally-layered horizontal solution. However, a rock surface is not a planar fluid layer and is not influenced by hydrostatic laws. Therefore, as expected by Reinboth (1992), it is not surprising that no horizontal ceiling was formed with time in experiment 3.

Density-driven groundwater flow coupled with gypsum dissolution along a vertically-oriented fracture is extremely complex. Therefore, to understand this solution cavity morphology, the following three ingredients have to be combined: (1) hydrogeological setting (i.e., regional groundwater flow system), (2) fluid mechanics (i.e., forced and free convection) and (3) gypsum dissolution (i.e., equilibrium chemistry and dissolution kinetics), which were only subsidiary considered for interpretation in all of the presented models. Furthermore, to date only vessel experiments have been conducted. In these experiments neither facets nor a horizontal ceiling with solution pits, either individually or concurrently, were able to be produced under confined conditions.

This paper aims at explaining the genesis of natural gypsum caves with a tip-down triangular cross-section by means of a new laboratory experimental setup, taking into consideration the studies conducted by Gripp, Reinboth, Kempe, Kempe et al. and Brandt et al. In these new experiments, freshwater was slowly pumped into rock salt cores through a horizontally-oriented borehole (in place of a vertical fracture). Rock salt (halite) is favored over gypsum rock due to its much faster dissolution kinetics and greater solubility (e.g., Alkattan et al., 1997; Jeschke et al., 2001) allowing rapid adjustment to density stratification, including individual experiments to be completed within a reasonable period of time. To visualize the dynamics of concentration-driven flow coupled with halite dissolution in the forming cavities, the fluorescent property of uranine-containing water was used.

## 3.2 Gypsum/halite dissolution kinetics and buoyancy

Close to chemical equilibrium at ~94% gypsum saturation, gypsum dissolution kinetics switches from linear to nonlinear rate (Jeschke et al., 2001). This implies that dissolution is relatively fast from 0 to ~94% gypsum saturation and that dissolution of gypsum is inhibited close to equilibrium. The solubility of gypsum amounts to ~2 g $CaSO_4$ per kg $H_2O$, the density differences between undersaturated and saturated waters with respect to gypsum may reach ~0.001 g $cm^{-3}$ (Kaltofen et al., 1994). Compared to gypsum, halite has different dissolution kinetics when in contact with halite-undersaturated water. Halite dissolution is a transport-controlled process; i.e. since transport is entirely controlled by molecular diffusion, dissolution rates at the surface are extremely high (e.g., Alkattan et al., 1997). Under experimental conditions, as presented in the next section, solubility amounts to ~358 g per kg $H_2O$ (Kaltofen et al., 1994). Thus far greater fluid density differences to freshwater are encountered, with values up to ~0.2 g $cm^{-3}$. Compared to gypsum, the solubility of halite is roughly 180 times greater than that of gypsum, and the greatest possible density difference between a halite solution and freshwater is roughly 200 times greater than between a gypsum solution and freshwater.

In contact with water saturated with respect to gypsum between 0 and ~94%, typical gypsum dissolution rates decrease towards higher bulk concentration in the order from $1 \times 10^{-3}$ (when in contact with freshwater) down to $3 \times 10^{-5}$ (when in contact with ~94% gypsum saturated water) mol $m^{-2}$ $s^{-1}$ (e.g., Jeschke, 2001). Whereas in the case of halite, the dissolution rates decline from ~2200 (when in contact with freshwater) down to 0 (when in contact with NaCl-saturated water) mol $m^{-2}$ $s^{-1}$ (e.g., Alkattan et al., 1997). As the thickness of the diffusion boundary layer depends strongly on the hydrodynamic conditions, transport by molecular diffusion can change significantly under varying flow conditions (Alkattan et al., 1997; Jeschke et al., 2001).

Buoyancy effects adjust when the solution near the mineral surface has a greater concentration and, thus, a greater density than the bulk of the liquid. Two non-dimensional ratios, the Rayleigh and the densimetric Froude number, characterize stability and turbulence of the flows, respectively. Fluid, heavier by the density difference $\Delta\rho$ on top of lighter fluid, may reside laminar despite the static instability as long as the Rayleigh number $Ra$ (e.g., Turner, 1973) is

$$Ra = \frac{g \cdot \Delta\rho \cdot H^3}{\mu \cdot D} <\sim 1700 \qquad (3.1)$$

where $g \approx 9.81$ m $s^{-2}$ represents the gravitational acceleration, $H$ the thickness of the potentially unstable layer, $\mu$ the dynamic viscosity of the overlying solution and $D$ the molecular diffusion coefficient for the dissolved ions in water. Based on the Boussinesq approximation, Froude's densimetric number $F$ (e.g., Turner, 1973) is expressed by

$$F = \frac{v}{(g' \cdot H)^{1/2}} \qquad (3.2)$$

for the buoyancy forces (vertical) acting on the inertial forces (horizontal), where $v$ stands for the mean horizontal velocity and $g' = g\Delta\rho/\rho_{reference}$ for the

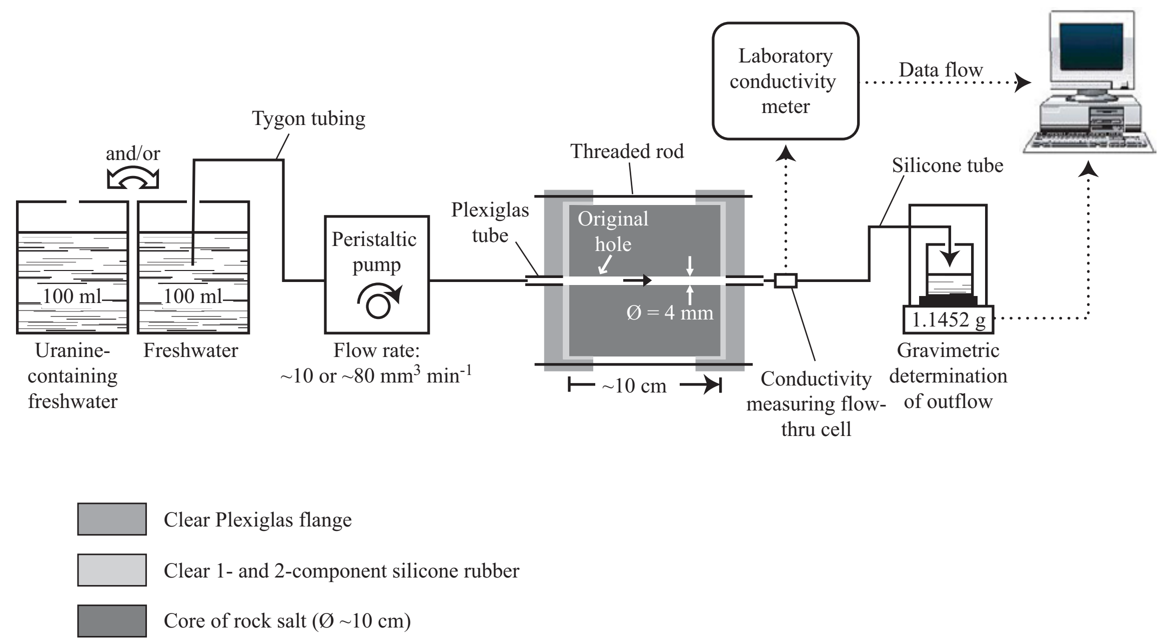

***Figure 3.3*** *Illustration of the key experimental setup.*

reduced gravity ($\rho_{reference}$ is the density of freshwater). The flow is buoyancy-driven if F < 1.

## 3.3 Methodology

Most technical aspects of the methodology are discussed in detail by Gechter et al. (submitted). Sections 3.3.1 and 3.3.2 provide a brief summary of the major issues.

### 3.3.1 Rock samples and experimental technique

Rock salt cylinders of ~10 cm diameter and length were cut from undisturbed drill cores of a Triassic rock salt layer sampled in northern Switzerland. All rock samples used nearly exclusively consist of coarse halite containing minor amounts (impurities) of anhydrite, dolomite, quartz, illite-muscovite and chlorite (cf. also Appendix A.2). The minor minerals may occur as discrete thin layers or are dispersed within the halite.

The experimental setup is schematically presented in Figure 3.3 (cf. also Appendix A.1.1). Dissolution of halite was studied by pumping fresh (tap) water into the rock samples through a horizontally-oriented 4 mm diameter borehole. The polished ends of the core cylinders were molded in clear Plexiglas flanges with clear silicone rubber so that the only flow passage was the borehole. A constant small inflow rate (~10 or ~80 mm$^3$ min$^{-1}$) was ensured by a peristaltic pump over time scales of 4.8 to 96.0 hours. Applied to a 4 mm diameter borehole, this corresponds to a mean horizontal velocity of ~1 or ~10 m d$^{-1}$, respectively. The electrical conductivity of the accessing freshwater (20.8 ± 1.7°C) was ~0.4 mS cm$^{-1}$ and its density to ~0.9973 g cm$^{-3}$. To avoid borehole wall dissolution before the actual start of a dissolution run, the drilled borehole and tubes were filled initially with filtered, halite-saturated brine, with an electrical conductivity range between 242 and 245 mS cm$^{-1}$ and a mean density of ~1.1971 g cm$^{-3}$. Four dissolution runs were

| | Drill core | Peristaltic pump | | Tracer input | | Interval recording | |
|---|---|---|---|---|---|---|---|
| Run number | Borehole length mm | Average inflow rate mm$^3$ min$^{-1}$ | Running time h | After pumping start h | Duration min | Time interval s | Recording time s |
| RS2 | 88 | 9,196 | 96,00 | | | | |
| RS10 | 109 | 8,628 | 46,90 | 38,60 | 45 | 30 | 0,5 |
| RS15 | 102 | 85,15 | 4,80 | 4,50 | 5 | | Continuous |
| RS23 | 99 | 77,06 | 6,80 | 0 | Continuous | 600 | 0,5 |

***Table 3.2*** *Experimental conditions of the four dissolution runs (cf. also Appendix A.3).*

conducted in total. The experimental conditions are given in Table 3.2.

At the outflow side, the electrical conductivity of the mineralized water (brine) was measured in a flow-thru cell connected to a laboratory conductivity meter with an error margin of ±1 mS cm$^{-1}$. Furthermore, the solution emerging from the outflow tube was collected in a flask standing on a scale, and its cumulative weight was measured with an error margin of ±0.1 mg. Simultaneous and continuous reading and registration of the two instruments was performed by a computerized data acquisition system.

All dissolution runs were terminated before a solution cavity could reach the lateral surface area of the core cylinder. After removing the drill core from the holder system, the undisturbed final solution cavities were examined macroscopically and by Scanning Electron Microscope (SEM).

### 3.3.2 Visualization

For visualization of the processes occurring at the visible inlet side of the borehole, freshwater containing 10 mg l$^{-1}$ uranine was pumped into the borehole (Figure 3.3). The fluorescent property of uranine was captured in the darkroom on time-lapse video by a suitable light source, excitation and suppression filters and a digital video camera recorder for subsequent qualitative analysis (cf. also Appendix A.1.1). To visualize streamlines during an experiment (dissolution runs RS10 and RS15), the traced water was injected in a single pulse lasting 45 and 5 minutes, respectively. To study the cavity enlargement (dissolution run RS23), traced water was injected throughout the dissolution run (Table 3.2).

## 3.4 Results

### 3.4.1 Macro and micromorphology

The morphological elements of the horizontal ceiling, facet and cup-shaped solution pits can be clearly identified and are similar to those observed in the presented type of gypsum cave. The dissolution cavities, viewed three-dimensionally at the inlet, are shaped roughly like a symmetrical half cone with a horizontal base facing upward (Figure 3.4A and Figure 3.5; cf. also Appendix A.1.2). In this case, the ends of the cylinders at the inflow (xy plane; cf. Figure 3.5) correspond to a vertical cross-section through the introduced cone. The base itself has a half-ellipsoidal surface shape. The length of the semi-minor axis in the z direction is about half of the semi-major axis situated in the xy plane. The final height of the solution cavities ranged from 2.9 to 4.2 cm. Further down the borehole, an extension ("tail cavity") of ~3 cm was observed (Figure 3.5). The triangular shape can be interfered by mm-thin layers of impurities when undercutting the facet below these layers (e.g., dissolution run RS15; Figure 3.4A). Nevertheless, the outlines of the cavity walls in the xy plane correspond relatively well to an isosceles triangle standing on the apex with a horizontal side facing upward (Figure 3.4A). The inclination of the facet at the inflow surface ($\gamma_1$) exhibited a narrow variation of ~70 to ~78° (Figure 3.5). The inclination of the facet intersecting the yz

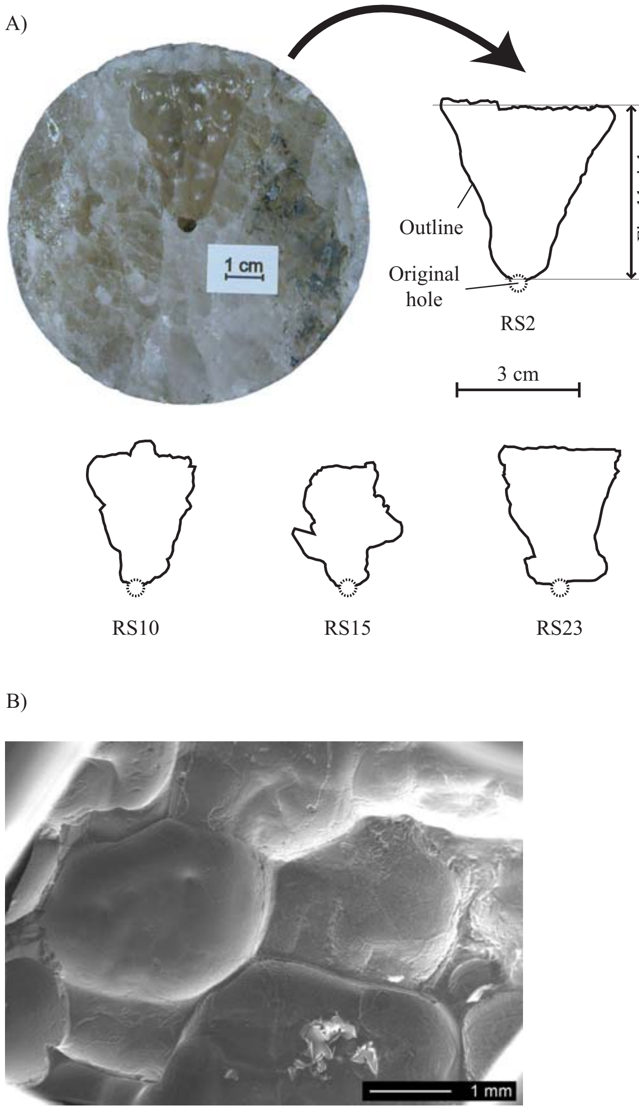

***Figure 3.4*** *A) Photograph of inlet view at the end of dissolution run RS2 and outlines of all dissolution runs. B) SEM photo of solution pits at the horizontal ceiling at the end of the dissolution run RS19 (not listed in Table 2 because it was sectioned; inflow rate of 76.05 mm$^3$ min$^{-1}$).*

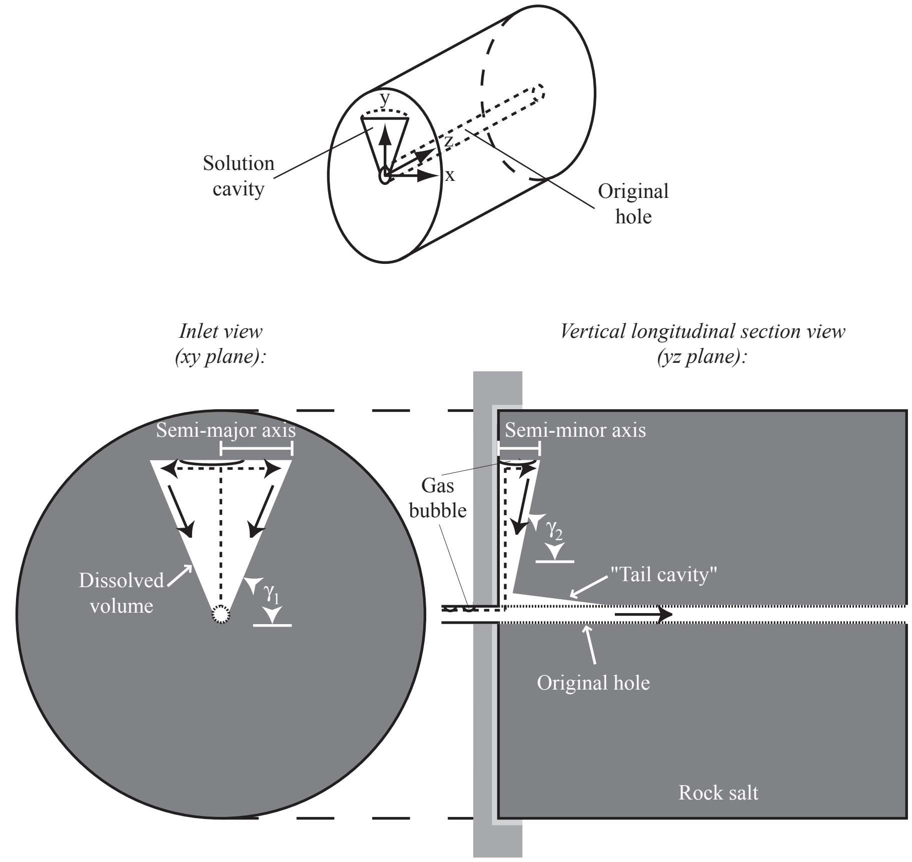

***Figure 3.5** Schematic inlet (xy plane; left) and vertical longitudinal section (yz plane; right) view of a core sample at the end of a dissolution run with indication of streamlines and positions of gas bubbles.*

plane was determined by caliper measurements, also revealing inclinations ($\gamma_2$) within a narrow range, but increasing several degrees in each case.

The macroscopic dissolution features were similar, irrespective of inflow rate and finely disseminated impurity content. Halite dissolution in the original borehole occurred only around the upper third section (over a height of ~1.5 mm; Figure 3.4A) and only within the first ~3 cm along the original borehole (Figure 3.5). This result is also demonstrated in all dissolution runs by (1) a practically invariable electrical conductivity value in the outlet brine (242 to 247 mS cm$^{-1}$); (2) by a linear increase in the cumulative weight of the outlet brine with time and (3) by a simple positive correlation between the final height of the solution cavity divided by running time and average inflow rate.

On a smaller scale, small irregular round to oval-shaped solution pits of ~1 mm diameter (i.e., approximately ten times smaller than in gypsum caves) in a honeycomb pattern cover the horizontal ceiling of all created cavities (Figure 3.4B). Their genesis cannot be related to the inhomogeneity of the rock or to the cleavage planes of halite, which clearly transect the small pits.

### 3.4.2 Temporal evolution

During the dissolution runs RS10 and RS15, the uranine-containing freshwater in the inlet Plexiglas tube was observed only around the uppermost 1 mm. Gas bubbles developed in the same tube and also on the upper limit. The water remained clear below the dyed freshwater and the gas bubbles (Figure 3.5). During a dissolution run, the freshwater had thus accessed the cavity through a point source and not throughout the entire tube section.

Figure 3.6 illustrates the developing convection pattern in such a solution cavity; the flow at the cavity surface is presented schematically in Figure 3.5. The results clearly indicate a flow symmetrical to the y-axis. The low-density freshwater was buoyant in the cavity solution and rised along the y-axis directly to the horizontal ceiling from where the fluid spread sideways, forming a distinct thin horizontal layer. This was where the first mineralization and consequent change in water density occurred. At the facet, an approximately 0.5 to 0.8 mm thick traced water layer moved downwards sometimes like a finger-shaped film to close the convection cell. The downward moving water was in direct contact with the facet as the facet's relief influenced the path of the downward moving

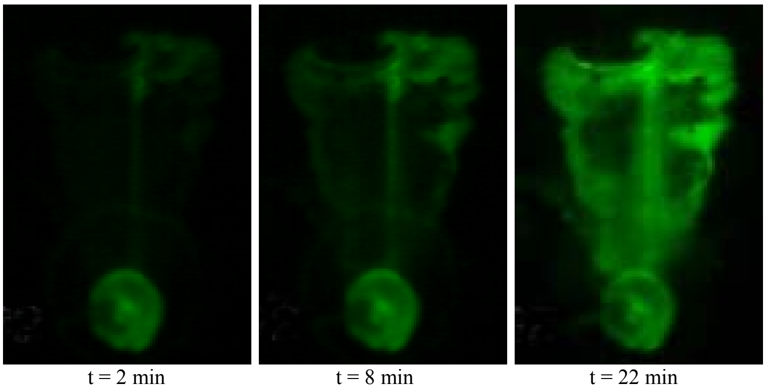
t = 2 min
t = 8 min
t = 22 min

***Figure 3.6*** *Time-lapse, videotape recording of the flow pattern at elapsed times t = 2, 8 and 22 min after injection of uranine-containing water into the cavity (dissolution run RS10). Note the gas bubble at the horizontal ceiling (image, right-hand side). Image width corresponds to 3.3 cm. Remarks: (1) a silicone blob molding the tubing into the inlet Plexiglas tube causes the visible circle below. Therefore, it does not correspond to the original opening. (2) The outline of the dye cloud is not equal to the outline of the dissolution run RS10 (cf. Figure 3.4A).*

film. For the dissolution runs RS10 and RS15, the flow velocities at the facet could be visually estimated at ~13 and ~51 m d$^{-1}$, respectively. The velocity of the downward moving film was therefore several times faster than the average flow velocity in the longitudinal direction through the borehole. Similar to the gas phase observed in the inlet Plexiglas tube, a gas bubble was always trapped at the horizontal ceiling (Figure 3.6). The gas bubble occasionally shifted sideways due to selective dissolution of halite (Figure 3.7). In the xy plane, the gas bubble at the horizontal ceiling changed size during a dissolution run (Figure 3.7), and fluorescent water was never observed above the bubble (Figure 3.6). Qualitatively, the cavities enlarged simultaneously through the upward growth of the horizontal ceiling and sideways at the upper end of the facet by tilting the latter outwards (Figure 3.7; cf. also Appendix A.1.5).

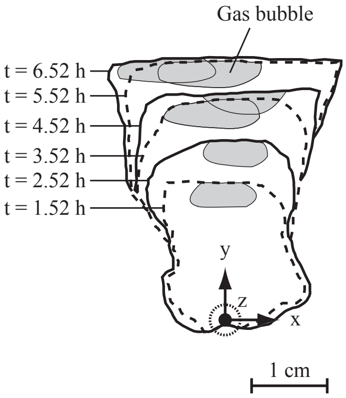

***Figure 3.7*** *Enlargement of solution cavity (outline of dye cloud) and position of gas bubble (xy plane) at the entrance of the borehole (dissolution run RS23). Note that the outlines of the dye cloud are not equal to the intersecting line of the cavity wall and cylinder end at the end of the dissolution run (cf. Figure 3.4A).*

## 3.5 Discussion

### 3.5.1 Scale-up from the laboratory to the field

The shape of the solution cavities formed during the new laboratory experiments is in fact analogous to the shape of the studied gypsum cave type in the meter range, since the artificially created small cavities also reveal this typical symmetry with a horizontal ceiling covered by solution pits and narrow ranged facet inclinations (cf. Figure 3.4A and Figure 3.4B). Moreover, a film sliding downward along the facet was observed in both cases. In other words, under certain conditions, buoyancy effects due to small concentration gradients were or are still present in such gypsum caves. This fact can also be applied to non-accessible gypsum solution cavities of this type. During the experiments, it was a point source of rising freshwater, whereas in a gypsum cavity, the lighter water emerging into the cavity water is expected to rise through the permeable fracture (inflow of lighter water along a horizontal line into the evolving cavity). Therefore, the same kind of flow and dissolution pattern is responsible for this type of gypsum cavity, however, under much more sluggish flow and dissolution conditions.

Section 3.5.2 discusses the genesis of such a natural gypsum solution cavity assuming that the morphological element of the lateral overhanging wall sections corresponds to the experimentally determined role of the upper end of a facet. Section 3.5.3 then presents the same theoretical hydrogeochemical calculations for the obtained small-scale solution cavities, including the phenomena encountered during the conducted flow experiments.

### 3.5.2 Conceptual setting

The authors agree with Gripp's theory concerning the flow field in such a horizontal triangular, prism-shaped cavity, and also with Kempe's speculation that these cavity passages have developed under confined conditions by artesian flow from an underlying aquifer into a gypsum layer. Based on their flow model, looking parallel to the longitudinal alignment of the cavity passage, Klimchouk interpreted intuitively correct the stable system of passage-scale convection circulation with a counter-clockwise flow direction in the left-hand convection cell, and a clockwise flow direction in the right-hand convection cell (Figure 6 in Klimchouk, 1996; Figure 1 in Klimchouk, 1997; and Figure 10 in Klimchouk, 2000a). The saltwater fingering effect at the horizontal ceiling, as proposed by Kempe, has to be responsible for the small solution pits, however, according to Reinboth's correct interpretation, this alone does not explain the horizontalness of the ceiling. Unlike Kempe's model, Reinboth's theory is widely unknown as his studies only were published in German. In principal, Reinboth's interpretation of rock-water interactions in the solution cavity and the cavity enlargement below the lowest groundwater level are confirmed by the new experimental data.

Based on the laboratory experiments presented in this paper and the works of Gripp, Reinboth and Kempe et al., the following overall picture concerning the hydrogeological setting and cavity formation as exemplified by a single developing gypsum cavity passage can be made (Figure 3.8A): a confined non-karstic or karstic aquifer consisting of less soluble materials is assumed to underlie a gypsum layer (confining layer). The potentiometric surface of the aquifer is higher than the developing solution cavity inside the gypsum layer. An interjacent, low-permeable

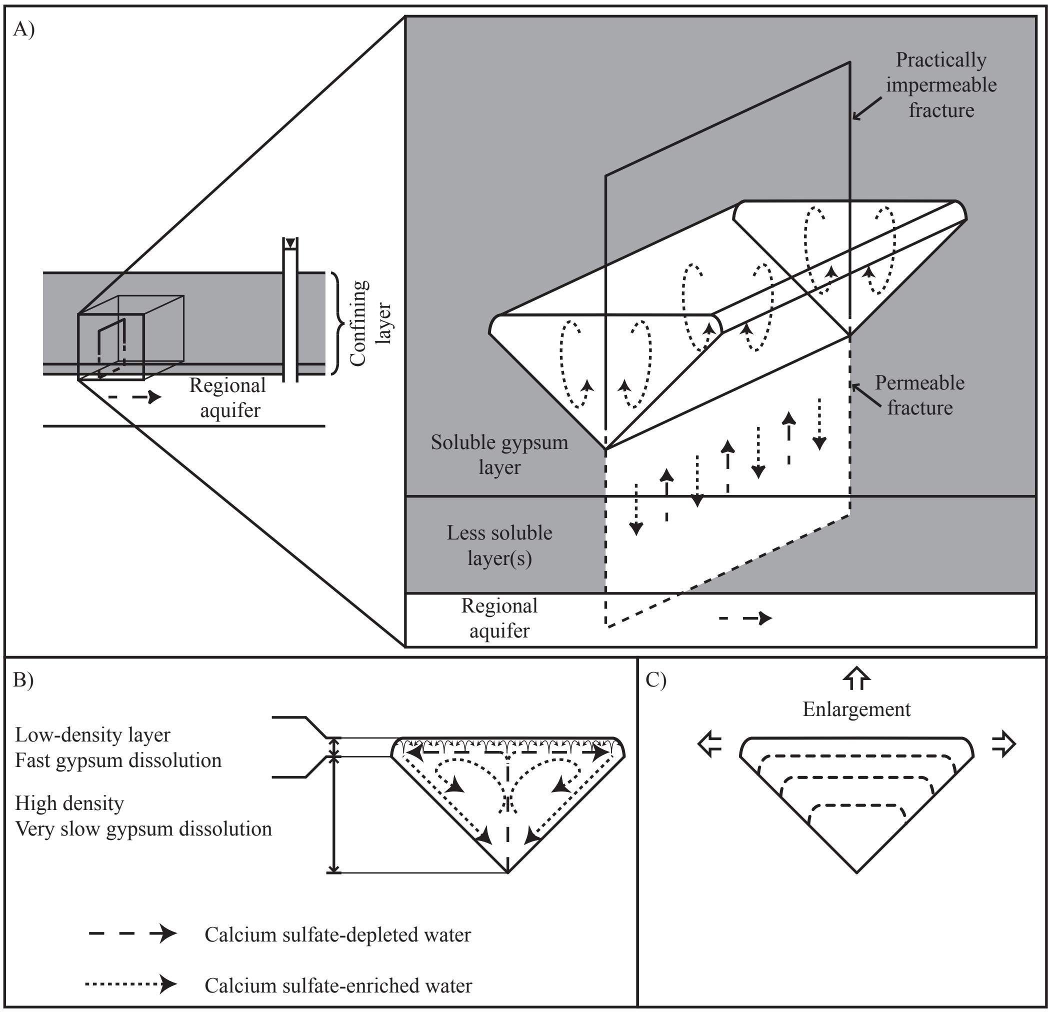

***Figure 3.8*** *A) Conceptual model of (A) triangular, prism-shaped gypsum cavity passage developing inside the gypsum rock, (B) rock-water interactions and physical behavior of cavity water and (C) cavity enlargement taking into account that dissolution at the facets is almost negligible.*

and less soluble layer or layers is or are imaginable. A permeable, vertically-oriented fracture provides communication between the aquifer's gypsum-depleted water and the gypsum body. The continuation upwards of the fracture inside the gypsum layer is supposed to be practically water-impermeable.

Regarding buoyancy, fluids with higher solute concentrations are heavier and sink, while fluids with lower concentrations rise elsewhere (e.g., Turner, 1973). To understand these movements, we assume a 5 m $d^{-1}$ mean horizontal velocity of the aquifer water and a permeable 5 m high fracture from the top of the aquifer. Furthermore, we assume that the fracture water is initially enriched in calcium sulfate (~94% gypsum saturated) resulting in a fluid density difference of ~1 kg $m^{-3}$ between the fracture water and the aquifer freshwater (Kaltofen et al., 1994). In such a model situation $D \approx 1 \times 10^{-9}$ $m^2$ $s^{-1}$ (Barton and White, 1971; Romanov et al., 2003), $g' \approx 0.01$ m $s^{-2}$, and $\mu \approx 1 \times 10^{-3}$ kg $m^{-1}$ $s^{-1}$ (Barton and White, 1971; Romanov et al., 2003). All constants used in the model are listed in Table 3.3. The resulting Rayleigh number (cf. Eq. (3.1)) is extremely high and the resulting densimetric Froude number (cf. Eq. (3.2)) is clearly <1, even if $\Delta\rho$ is far smaller in the presented model. This indicates that the flow in the fracture is initially buoyant and fully turbulent. Therefore, the solution cavity with tip-down triangular cross-section starts to develop at the upper end of the permeable fracture where the ascending lighter water accumulates (hydrochemical stratification). The buoyant turbulent flow remains as the relatively fast gypsum dissolution up to nearly gypsum-saturated water at the upper end of the developing cavity initiates the density gradient that becomes the driving mechanism of its own dissolution (free convection). The dense gypsum solution (~94% gypsum saturated) then moves downwards through the same fracture system as the buoyant turbulent gypsum-depleted aquifer water, but along separate and distinct pathways. The descending denser solution is diluted in the aquifer and finally flows through the aquifer (forced convection) to a point or area of natural discharge. At the upper end of the permeable fracture, a cavity with horizontal ceiling, lateral overhanging wall sections and facets develops upwards.

The flow pattern and gypsum dissolution pattern in the solution cavity are illustrated in Figure 3.8A and Figure 3.8B. A fluid density layering develops with underlying calcium sulfate-enriched water and a relatively thin, low-density horizontal layer above, which is in contact with the horizontal ceiling and overhanging wall sections. The gypsum-depleted (less dense) water emerging into the gypsum-enriched cavity water rises to the horizontal ceiling along the plane of symmetry of the solution cavity. The water becomes enriched in dissolved gypsum along the horizontal ceiling and lateral overhanging wall sections. The residence time of the gypsum-depleted water in the thin overlying layer is sufficient to allow a ~94% gypsum saturation. The dense gypsum solution then moves down the facets and some of it further down the fracture as explained above. Along the facets, receding caused by dissolution is only very small due to very slow gypsum dissolution close to saturation. Two passage-scale convective cells are formed in the gypsum cavity passage. The axes of the cells run parallel to the longitudinal alignment of the cavity (Figure 3.8A). This cavity type expands by upward growth of the horizontal ceiling and sideward growth of the lateral overhanging wall sections (Figure 3.8C). The inclined facets are thus formed over time. Consequently, the height of the passage increases in a negative exponential manner. The fact that the inclination of the facets is always similar is attributed to the special hydrogeological conditions and intrinsic characteristics of gypsum dissolution.

The reason for the horizontalness of the ceiling is related to the fact that the low-density/high-density water interface layer is close to the ceiling. Since this density interface is horizontal due to gravity, the ceiling forms along this "prescribed" guide. The observed heterogeneously distributed solution pits are attributed to an inverted density distribution occurring again at the contact of the low-density layer and the horizontal ceiling/overhanging wall sections during gypsum dissolution. Under such conditions, the smallest possible existing eddies at the ceiling can be determined by using Kolmogorov's length scale $L_K$ (Kolmogorov, 1941; Wüest and Lorke, 2003)

$$L_K = \left( \frac{\upsilon^3}{\varepsilon} \right)^{1/4} \tag{3.3}$$

where viscous and inertial forces are of the same magnitude. In this formula, $\upsilon$ is the kinematic viscosity and $\varepsilon$ the rate of dissipation of turbulent kinetic energy. By multiplying $L_K$ by $2\pi$, this scale can be compared to absolute length. In our case, $\varepsilon$ is equal to the buoyancy flux ($J_b$) defined as (e.g., Imboden and Wüest, 1995; Wüest and Lorke, 2003)

$$J_b = \frac{g \cdot \beta_S}{\rho} F_s \tag{3.4}$$

where $\beta_S$ is the coefficient of haline contraction, $\rho$ the fluid density of the low-density layer, and $F_s$ the salt flux from the ceiling. In order to determine $L_k$, the system is simplified so that freshwater is assumed to only come into contact with a perfect flat horizontal ceiling. In such a situation $F_s = R$, where $R$ is the average dissolution rate. Thus $R \approx 1.4 \times 10^{-4}$ kg $CaSO_4$ $m^{-2}$ $s^{-1}$ (Jeschke et al., 2001), $\beta_S \approx 1$ (Imboden and Wüest, 1995), $\rho \approx 1000$ kg $m^{-3}$, and $\upsilon \approx 1 \times 10^{-6}$ $m^{-2}$ $s^{-1}$ (Weast, 1982). All the constants are also listed in Table 3.4. Combining Eqs. (3.3) and (3.4) leads to an absolute length scale for $2\pi L_k$ of ~6 mm, which is close to the observed solution pit dimension. Furthermore, at a critical Rayleigh number of 1700 (cf. Eq. (3.1)) and a $\Delta\rho \approx 1$ kg $m^{-3}$ corresponding to the liquid density difference between the concentration directly adjacent to the horizontal ceiling/overhanging wall sections and the low-density layer below, $H$ is ~0.6 mm. According to this height, small convection cells larger than ~1 mm can be considered turbulent. These two calculations confirm that the observed solution pits are an imprint of the smallest possible turbulent eddies.

The rising horizontal ceiling ends at the latest with the highest groundwater level or at the top of the gypsum stratum, unless the cavity collapses before. Such solution cavities may exist far below the groundwater table.

### 3.5.3 Laboratory-scale flow experiments

The flow experiments reveal that due to the slow inflow rate and rapid dissolution kinetics of halite, the freshwater was halite-saturated shortly after the initial contact with the rock salt. Therefore, halite dissolution was restricted to the inflow area of the borehole in the rock salt cylinder. Initially, the upper third of the borehole wall was enlarged upward along the first centimeters in the longitudinal direction, as the introduced undersaturated, less dense water occupied the uppermost position. Its solute concentration increased continuously in the longitudinal direction until NaCl-saturation was reached. No halite dissolution occurred beyond that depth, and the “tail cavity” developed gradually. The less soluble mineral anhydrite and the poorly soluble minerals (dolomite, quartz and clay) largely remained undissolved during the experiments. Upward enlargement by dissolution

| Parameter | Symbol | Unit | Value | |
|---|---|---|---|---|
| | | | Conceptual setting | Experiments (small-scale) |
| Soluble mineral | | | Gypsum | Halite |
| Molecular diffusion coefficient (overlying solution) | $D$ | $m^2$ $s^{-1}$ | $1 \times 10^{-9}$ | $1.5 \times 10^{-9}$ |
| Gravitational acceleration | $g$ | m $s^{-2}$ | 9.81 | 9.81 |
| Reduced gravity | $g'$ | m $s^{-2}$ | 0.01 | 2 |
| Thickness of the unstable layer | $H$ | m | 5 | $2.9 \times 10^{-2}$ to $4.2 \times 10^{-2}$ |
| Mean horizontal velocity (underlying solution) | $v$ | m $s^{-1}$ | $1.2 \times 10^{-5}$ | $4.6 \times 10^{-5}$ to $4.5 \times 10^{-4}$ |
| Dynamic viscosity (overlying solution) | $\mu$ | kg $m^{-1}$ $s^{-1}$ | $1 \times 10^{-3}$ | $2 \times 10^{-3}$ |
| Fluid density difference | $\Delta\rho$ | kg $m^{-3}$ | 1 | 200 |

***Table 3.3*** *Model and experimental parameters for Eq. (3.1) and Eq. (3.2).*

| Parameter | Symbol | Unit | Value | |
|---|---|---|---|---|
| | | | Conceptual setting | Experiments (small-scale) |
| Soluble mineral | | | Gypsum | Halite |
| Gravitational acceleration | $g$ | m $s^{-2}$ | 9.81 | 9.81 |
| Average dissolution rate[a] | $R$ | kg $m^{-2}$ $s^{-1}$ | $1.4 \times 10^{-4}$ | $1.6 \times 10^{-3}$ |
| Coefficient of haline contraction | $\beta_S$ | - | 1 | 0,76 |
| Fluid density (low-density layer) | $\rho$ | kg $m^{-3}$ | 1000 | 1000 |
| Kinematic viscosity (low-density layer) | $\upsilon$ | $m^2$ $s^{-1}$ | $1 \times 10^{-6}$ | $1 \times 10^{-6}$ |

[a] For gypsum: kg $CaSO_4$ $m^{-2}$ $s^{-1}$

***Table 3.4*** *Model and experimental parameters for Eq. (3.3) and Eq. (3.4).*

led to a horizontal ceiling at the inlet, thus allowing the facet to develop upward. In the further course of a dissolution run, halite dissolution occurred only within the developing half conical cavity. At the inlet of the borehole, the NaCl-undersaturated water and gas, the latter released by salting out effect (Harvie et al., 1984; Stumm and Morgan, 1996), accumulated in the highest section of the cavity (and of the inlet Plexiglas tube) – the gas was highest followed by the undersaturated water, both floating on the NaCl-saturated brine. Because the gas bubble shielded the rock salt above from further water access, halite dissolution was inhibited above the gas bubble. As soon as the salt ceiling dissolved around the bubble it moved to reach this newly created higher position. When combined, convection of the fluid was caused by (a) hydraulic gradient (here induced by a peristaltic pump), (b) constant supply of buoyant, undersaturated water from a point source, (c) adjustment of a fluid density layering, and (d) increase in solute NaCl concentration to saturation was reached around an overlying thin, undersaturated layer in contact with the horizontal ceiling and the upper end of the facet.

As for the conceptual setting (Section 3.5.2), the model of buoyant turbulent flow coupled with mineral dissolution is also supported here by calculating the dimensionless Rayleigh and densimetric Froude numbers and the Kolmogorov length scale, respectively. Regarding the dissolution runs, the numerical values are presented in Table 3.3 and Table 3.4. The following values are taken from the literature: $D$ (Zaytsev and Aseyev, 1992), $\beta_S$ (Steinhorn, 1980), $\mu$ (Zaytsev and Aseyev, 1992), and $\upsilon$ (Weast, 1982). In order to calculate the smallest possible eddies, an average halite dissolution rate was estimated at the end of dissolution run RS23 by the simplified assumption that halite dissolution occurs only at the horizontal ceiling and by neglecting surface irregularities. Furthermore, $H$ corresponds to the final height of the solution cavity (Table 3.3). The resulting absolute length scale for $2\pi L_k$ amounting to ~3 mm and the correspondingly calculated Rayleigh number of ~0.2 mm (at a critical Rayleigh number of 1700) confirm also here a turbulent flow of smallest possible convection cells directly below the observed solution pits. However, solution pits are about an order smaller on our laboratory setting than in the described gypsum caves in nature as more dissipation of turbulent energy (cf. Eqs. (3.3) and (3.4)) was released.

## 3.6 Conclusions

The field observations of gypsum cave passages with a tip-down triangular cross-section concur qualitatively with the laboratory results. Although the authors never entered such a cave passage, they can provide a coherent hydrogeological explanation for the genesis of such cavities, which is based also on existing models, on the new experimental data reported in this paper and on theoretical considerations. For the first time, the convective flow in an evolving cavity with a tip-down triangular cross-section and its growth were recorded experimentally.

If a permeable fracture provides communication between a confined, practically insoluble gypsum-depleted water aquifer and an overlying soluble gypsum body, caves and cavities with a tip-down triangular cross-section may develop at the upper end of the permeable fracture. Since gypsum dissolution practically occurs only at the horizontal ceiling and upper end of the facet (equivalent to the overhanging wall sections), the cavities enlarge under confined conditions by upward growth of the horizontal ceiling and also by lateral growth at the upper end of the facet. These morphologies are indicators for paleohydrogeology in gypsum deposits if the cavity is in the epiphreatic or vadose zone.

In such an artesian setting, development of a whole gypsum karst system was modeled by a coupled continuum-pipe flow model neglecting density effects (Birk et al., 2003; Birk et al., 2005). However, this paper clearly reveals the need for a more sophisticated, density-dependent fluid dynamics code, since the relatively rapid gypsum dissolution leads to density gradients causing gravitational separation of water and natural convection circulation, at least in the initial stage. The presented conceptual model suggests that similar processes can occur in other evaporites. Cavities developed by buoyant groundwater flow coupled with mineral dissolution may cause near-vertical, natural subsidence or collapse features propagating upward.

### Acknowledgements

We would like to thank S. Kempe and F. Reinboth for their helpful discussions over the telephone and for the gypsum cave photos shown in this paper. The Swiss National Science Foundation (grants 21.65092.01 and 200020-105492) provided the financial support for this study.

## 3.7 References

Alkattan, M., E. H. Oelkers, J.-L. Dandurand, and J. Schott (1997), Experimental studies of halite dissolution kinetics, 1 The effect of saturation state and the presence of trace metals, *Chem. Geol.*, *137*, 201–219.

Barton, A. F. M., and N. M. Wilde (1971), Dissolution rates of polycrystalline samples of gypsum and orthorhombic forms of calcium sulphate by a rotating disc method, *Trans. Faraday Soc.*, *67*, 3590–3597.

Biese, W. (1931), Über Höhlenbildung; 1. Teil; Entstehung der Gipshöhlen am südlichen Harzrand und am Kyffhäuser, *Abh. Preuss. Geol. Landesanst.*, *137*, 1–70.

Birk, S., R. Liedl, M. Sauter, and G. Teutsch (2003), Hydraulic boundary conditions as a controlling factor in karst genesis: A numerical modeling study on artesian conduit development in gypsum, *Water Resour. Res.*, *39*(1), 1004, doi:10.1029/2002WR001308.

Birk, S., R. Liedl, M. Sauter, and G. Teutsch (2005), Simulation of the development of gypsum maze caves, *Environ. Geol.*, *48*, 296–306.

Brandt, A., S. Kempe, M. Seeger, and F. Vladi (1976), *Geochemie, Hydrographie und Morphogenese des Gipskarstgebietes von Düna/Südharz*, Geologisches Jahrbuch, Reihe C, Heft 15, Bundesanstalt für Geowissenschaften und Rohstoffe und den Geologischen Landesämtern der Bundesrepublik Deutschland, Stuttgart.

Cooper, A. H. (1986), Subsidence and foundering of strata caused by the dissolution of Permian gypsum in the Ripon and Bedale areas, North Yorkshire, in *The English Zechstein and related topics*, No. 22, edited by G. M. Harwood and D. B. Smith, pp. 127–139, Geological Society Special Publication, Oxford.

Cooper, A. H. (1998), Subsidence hazards caused by the dissolution of Permian gypsum in England: geology, investigation and remediation, in *Geohazards in engineering geology*, 15, edited by J. G. Maund and M. Eddleston, pp. 265–275, Geological Society, Engineering Geology Special Publications, London.

Ford, D., and P. Williams (2007), *Karst hydrogeology and geomorphology*, John Wiley & Sons, West Sussex, England.

Gechter, D., P. Huggenberger, P. Ackerer, and H. N. Waber (2008), Genesis and shape of natural solution cavities within salt deposits, revised manuscript submitted to *Water Resour. Res.*, minor revisions requested.

Gripp, K. (1913), Über den Gipsberg in Segeberg und die in ihm vorhandene Höhle, *Jb. Hamburg wiss. Anst. 30*, *6*, 35–51.

Harvie, C. E., N. Møller, and J. H. Weare (1984), The prediction of mineral solubilities in natural waters: The Na-K-Mg-Ca-H-Cl-$SO_4$-OH-$HCO_3$-$CO_3$-$CO_2$-$H_2O$ system to high ionic strengths at 25°C, *Geochim. Cosmochim. Acta*, *48*, 723–751.

Imboden, D. M., and A. Wüest (1995), Mixing mechanisms in lakes, in *Physics and chemistry of lakes*, edited by A. Lerman, D. M. Imboden and J. R. Gat, pp. 83–138, Springer-Verlag, Berlin.

Jeschke, A. A., K. Vosbeck, and W. Dreybrodt (2001), Surface controlled dissolution rates of gypsum in aqueous solutions exhibit nonlinear dissolution kinetics, *Geochim. Cosmochim. Acta*, *65*(1), 27–34.

Kaltofen, R., R. Opitz, K. Schumann, and J. Ziemann (1994), *Tabellenbuch Chemie*, Harri Deutsch, Thun und Frankfurt am Main.

Kempe, S. (1969), Laugnäpfe und ihre Entstehung, *Die Höhle*, *20*, *4*, 111–113.

Kempe, S. (1972), Cave genesis in gypsum with particular reference to underwater conditions. *Cave Science*, *Journ. Brit. Spel. Assoc.*, *49*, 1–6.

Kempe, S. (1996), Gypsum karst of Germany, in *Gypsum karst of the world*, *Int. J. Speleol.*, 25, 3-4, edited by A. Klimchouk, D. Lowe, A. Cooper and U. Sauro, pp. 209–224, Società Speleologica Italiana, Italy.

Kempe, S., A. Brandt, M. Seeger, and F. Vladi (1975), "Facetten" and "Laugdecken", the typical morphological elements of caves developing in standing water, *Ann. Spéléol.*, *30*, *4*, 705–708.

Kempe, S., A. Brandt, M. Seeger, and F. Vladi (1976), Fünf Aspekte der Entwicklung der Gipshöhlen im Hainholz/Südharz, *Mittl. Verb. dt. Höhlen- u. Karstforsch.*, *22*, *1*, 7–10.

Kempe, S., and R. Hartmann (1977), Solution velocities on facets: vessel experiments, in *Proceedings 7th Int. Speleol. Congress*, pp. 256–258, Sheffield.

Klimchouk, A. (1996), Speleogenesis in gypsum, in *Gypsum karst of the world*, *Int. J. Speleol.*, 25, 3-4, edited by A. Klimchouk, D. Lowe, A. Cooper and U. Sauro, pp. 61–82, Società Speleologica Italiana, Italy.

Klimchouk, A. (1997), Speleogenetic effects of water density differences, in *Proceedings of the 12th International Congress of Speleology*, vol. 1, pp. 161–164, International Union of Speleology / Swiss Speleology Society, La Chaux-de-Fonds, Switzerland.

Klimchouk, A. (2000a), Speleogenesis of the Great Gypsum Mazes in the Western Ukraine, in *Speloegenesis – evolution of karst aquifers*, edited by A. B. Klimchouk, D. C. Ford, A. N. Palmer and W. Dreybrodt, pp. 261–273, National Speleological Society, Huntsville.

Klimchouk, A. (2000b), Speleogenesis in Gypsum, in *Speloegenesis – evolution of karst aquifers*, edited by A. B. Klimchouk, D. C. Ford, A. N. Palmer and W. Dreybrodt, pp. 431–442, National Speleological Society, Huntsville.

Klimchouk, A., D. Lowe, A. Cooper, and U. Sauro (Eds.) (1996), Gypsum karst of the world. *International Journal of Speleology*, *25*, *3-4*.

Kolmogorov, A. (1941), The local structure of turbulence in incompressible viscous fluid for very large Reynolds' numbers, *Dokl Akad Nauk USSR*, *30*(4), 301–305.

Kozary, M. T., J. C. Dunlap, and W. E. Humphrey (1968), Incidence of saline deposits in geologic time, *Geol. Soc. Am. Spec. Pap.*, *88*, 43–57.

Lauritzen, S.-T., and R. Ewers (2000), Solutional and erosional morphology, in *Speloegenesis – evolution of karst aquifers*, edited by A. B. Klimchouk, D. C. Ford, A. N. Palmer and W. Dreybrodt, pp. 408–426, National Speleological Society, Huntsville.

Quinlan, J. F., R. A. Smith, and K. S. Johnson (1986), Gypsum karst and salt karst of the United States of America, *Le Grotte d'Italia*, *4*(XIII), 73–92.

Reinboth, F. (1968), Beiträge zur Theorie der Gipshöhlenbildung, *Die Höhle*, *19*, *3*, 75–83.

Reinboth, F. (1971), Zum Problem der Facetten- und Laugdeckenbildung in Gipshöhlen, *Die Höhle*, *22*, *3*, 88–92.

Reinboth, F. (1992), Laborversuche zur Entstehung von Stillwasserfacetten und Laugdecken – mit einem kritischen Überblick zum Stand der Diskussion, *Die Höhle*, *43*, *1*, 1–18.

Romanov, D., F. Gabrovšek, and W. Dreybrodt (2003), Dam sites in soluble rocks: a model of increasing leakage by dissolutional widening of fractures beneath a dam, *Engineering Geology*, *70*, 17–35.

Steinhorn, I. (1980), The density of Dead Sea water as a function of temperature and salt concentration, *Isr J Earth-Sci*, *29*, 191–196.

Stumm, W., and J. J. Morgan (1996), *Aquatic chemistry, Chemical equilibria and rates in natural waters*, 3rd ed., John Wiley & Sons, New York.

Turner, J. S. (1973), *Buoyancy effects in fluids*, Cambridge University Press, London.

Weast, R. C. (ed.) (1982), *Handbook of Chemistry and Physics*, 63th ed., CRC Press, Boca Raton, Florida.

Wüest, A., and A. Lorke (2003), Small-scale hydrodynamics in lakes, *Annu. Rev. Fluid Mech.*, *35*, 373–412.

Zaytsev, I. D., and G. G. Aseyev (Eds.) (1992), *Properties of aqueous solutions of electrolytes*, CRC Press, Boca Raton, Florida.

# 4 Understanding the processes of natural interstratal karstification at the top of a salt layer in a horst and graben structure

## 4.1 Introduction

Salt dissolution or "subrosion" (term used in German literature since 1926; cf. Murawski, 1992) in the subsurface is a well-known and long-recognized phenomenon. Groundwater can interact with a practically impervious, but highly soluble salt body from all three directions, i.e. from above, from the side (e.g., McManus and Hanor, 1993) or from below (cf. Chapter 2). Slightly modified, the four requirements for subsurface salt dissolution are according to Johnson (1981, 1992): (a) a deposit of salt; (b) a supply of undersaturated water with respect to the highly soluble salt minerals such as through permeable faults; (c) an outlet for removal of salt-enriched water; and (d) energy to move the water flow through the system. If undersaturated groundwater interacts with the salt body from above, this process causes the development of solution cavities at the top of the subsurface (e.g., Quinlan et al., 1986; Waltham, 1989) or submarine salt (e.g., Lohmann, 1972; Belderson et al., 1978) into which overlying strata can settle or collapse chaotically. This process is apparently self-perpetuating, as the resulting fracturing of overlying units provides improved access to the salt for salt-depleted water (Johnson, 1981, 1992). In such areas, broad areal subsidence is prevalent (e.g., Belderson et al., 1978; Reuter and Tolmačëv, 1990; Reuter et al., 1992; Reuter and Stoyan, 1993).

In more detail, the term interstratal salt karst is applied to salt dissolution taking place beneath a covering layer of relatively insoluble rock (e.g., Quinlan et al., 1986). In such a karst system, drillings revealed that brine-filled solution cavities (corresponding to zones of loss of circulation) are common at the top of the salt layer and enlarge only to a height of approximately one meter (Spackeler, 1957; Johnson, 1981, 1992; Reuter and Tolmačëv, 1990; Reuter et al., 1992; Reuter and Stoyan, 1993). These solution cavities are, therefore, flat expanded (quasi-2D solution cavities). A mainly areal dissolution on the top of the salt layer is considered (Quinlan et al., 1986; Reuter and Tolmačëv, 1990; Reuter et al., 1992; Reuter and Stoyan, 1993). Solution cavities within the salt unit are generally absent (Johnson, 1981). The same phenomena of tabular cavities at the top of a salt layer and overlying areal subsidence are monitored in a region southeast of the city of Basel in the Tabular Jura as presented in Chapter 1. Furthermore, as described from this region, elongate subsidence zones parallel to faults are also known from other regions underlain by salt (e.g., Belderson et al., 1978; Gustavson et al., 1982; Baer et al., 2002). Nevertheless, a greater understanding of the genesis of a tabular solution cavity at the top of a salt layer and reason for the overlying subsidence pattern remain unexplained.

To overcome the complexity of field measurements (cf. Chapter 1), the study of fluid density effects at the top of a salt layer was scaled down to laboratory dissolution experiments, where freshwater was slowly pumped from above into rock salt cores through an axial borehole. Since faults displace salt horizons in horst and graben structures, and since faults may constitute very important types of discontinuities in rocks from a hydrogeological point of view, in another type of experiment the influence under more realistic geological conditions was studied. Two cases (there are endless variations) were studied in this type of experiment: a normal fault juxtaposing a developing interstratal salt karst against a salt layer, and a normal fault juxtaposing a developing interstratal salt karst against a largely impermeable, poorly soluble layer. To visualize the flow field and cavity genesis, the fluorescence property of uranine-containing water was used.

This approach, simulating salt dissolution at the top of a non-displaced or displaced non-folded salt layer allowed to study the genesis of flat expanded solution cavities, well-known in many areas. An understanding of the hydrodynamics coupled with salt dissolution in a developing interstratal salt karst is crucial for effective planning control and engineering practice,

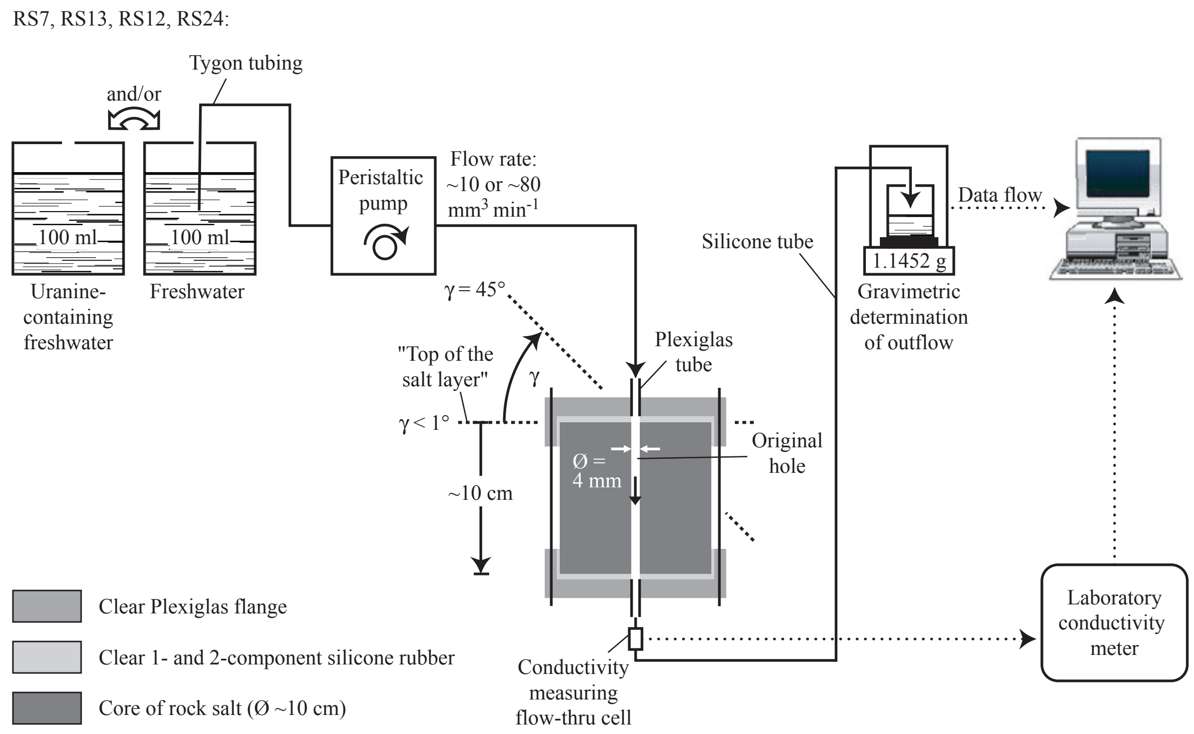

***Figure 4.1*** *Schematic diagram of the experimental setup for the laboratory dissolution runs.*

as well as for management and protection of water resources.

This Chapter often refers to details already presented or discussed in Chapter 2.

## 4.2 Methodology

Two types of dissolution experiments were carried out. Both series simulated the development of solution cavities when freshwater comes into contact with the top of a salt layer from above. One type simulated a 2D and the other a 3D (step like) top of a salt layer.

The same experimental setup and procedure was used as described in detail in Chapter 2.2, where dissolution of rock salt (halite) was examined by pumping freshwater through an axial borehole in ~10 cm long undisturbed cores of rock salt consisting mainly of halite (NaCl). However, this chapter describes the effect induced by freshwater contacting from above the upper end of the core cylinder (top of the salt layer) showing a $\gamma$ inclination (accuracy about ±1°). The Plexiglas/silicone top cover functions as a practically impermeable and poorly soluble stratum (covering layer). A schematic diagram of the experimental setup is illustrated in Figure 4.1 and photographs of the setup are presented in Appendix A.1.1. Mineralogical and chemical analyses from some drilling powders are described in Appendix A.2.1. Compared to a field situation (cf. Chapter 1), the main laboratory constraints were (1) the supply of NaCl-undersaturated water through a pipe (quasi-1D input) and not through a more realistic linear input (permeable fault); and (2) the dissolved salt water was transported through the salt core (salt layer) instead of being transported upwards/laterally away from the top of the salt layer, such as in an overlying freshwater aquifer.

In the first type of experiments, a total of four dissolution runs were conducted (RS7, RS13, RS12, and RS24) as presented in Figure 4.1. The average inflow rate amounted to ~10 or ~80 $mm^3 min^{-1}$ over time scales of 3.4–31.2 hours, and the inclination of the top of the salt layer varied between <1° and 45°. In the second type of experiments, two dissolution runs (RS27 and RS28) were conducted, where the aforementioned Plexiglas/silicone top was extended by a silicon-filled groove placed parallel to the strike of the inclined top of the salt layer in order to simulate a horst and graben structure (displaced layers; fault). In dissolution run RS27, the silicon-filled groove was 2.3 cm wide and 1.0 cm deep, including the entrance of the borehole (Figure 4.2). In dissolution run RS28, the silicon-filled groove was 0.3 cm wide and 1.7 cm deep and was placed up dip from the borehole entrance (Figure 4.2). In both dissolution experiments, the upper top of the salt layer was relatively steep parallel to the layers (30 or 45°, respectively) and the average inflow rate was ~70 $mm^3 min^{-1}$ over 11.6 or 5.2 hours, respectively. The experimental conditions for all

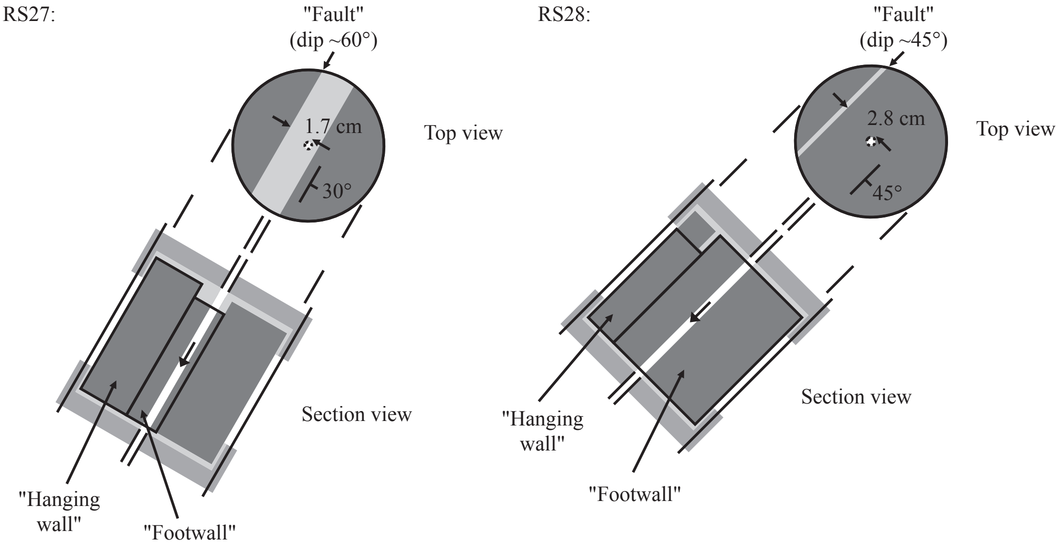

***Figure 4.2*** *Cut rock samples used in the dissolution runs RS28 and RS27.*

| | Drill core of rock salt | | Peristaltic pump | | Tracer input | | Interval recording | |
|---|---|---|---|---|---|---|---|---|
| Run number | Borehole length cm | Inclination top rock salt ° | Average inflow rate $mm^3\ min^{-1}$ | Running time h | After pumping start h | Duration min | Time interval s | Recording time s |
| First type of dissolution experiments: | | | | | | | | |
| RS7 | 9.6 | <1 | 10.626 | 31.15 | | | | |
| RS13 | 10.7 | <1 | 76.84 | 3.40 | 2.73 | 15 | 30 | 0.5 |
| RS12 | 11.0 | 10 | 9.210 | 10.17 | | | | |
| RS24 | 10.4 | 45 | 83.81 | 2.28 | 0 | Continuous | 30 | 0.5 |
| Second type of dissolution experiments: | | | | | | | | |
| RS27 | 11.0 | 30 | 74.35 | 11.56 | 0 | Continuous | | |
| RS28 | 9.5 | 45 | 66.30 | 5.13 | 0 | Continuous | 30 | 0.5 |

***Table 4.1*** *Experimental conditions for the six dissolution runs (cf. also Appendix A.3).*

dissolution runs are given in Table 4.1.

Dissolution runs RS13, RS24, RS27, and RS28 were captured in the darkroom on time-lapse video for subsequent qualitative analysis (Table 4.1). To visualize and record the flow pattern, the traced water was injected for 15 minutes towards the end of dissolution run RS13. To study the cavity enlargement (dissolution runs RS24, RS27 and RS28), traced water was injected throughout the experiment. Additionally, continuous tracer input helped terminate a dissolution run before a solution cavity reached the lateral surface area of the rock salt core. The electrical conductivity of the initial freshwater and outflow brine was measured

| | Initially filled NaCl-saturated brine | | Freshwater | | Outlet brine |
|---|---|---|---|---|---|
| Run number | Fluid density $g\ cm^{-3}$ | Electrical conductivity $mS\ cm^{-1}$ | Fluid density $g\ cm^{-3}$ | Electrical conductivity $mS\ cm^{-1}$ | Electrical conductivity $mS\ cm^{-1}$ |
| First type of dissolution experiments: | | | | | |
| RS7 | 1.1941 | 244 | 0.9964 | 0.392 | 244-247 |
| RS13 | 1.1997 | 245 | 0.9974 | 0.403 | 245-247 |
| RS12 | 1.1971 | 244 | 0.9978 | 0.393 | 244 |
| RS24 | 1.1944 | - | 0.9968 | - | - |
| Second type of dissolution experiments: | | | | | |
| RS27 | 1.1950 | - | 0.9976 | - | - |
| RS28 | 1.1986 | - | 0.9978 | - | - |

- Not measured

***Table 4.2*** *Fluid density and electrical conductivity data of initially filled NaCl-saturated brine, injected freshwater and outlet brine of all dissolution runs (cf. also Appendix A.3).*

only in dissolution runs RS7, RS13 and RS12. Due to the constant values of the measurements, these were omitted in the final three dissolution runs (RS24, RS27 and RS28).

After unmounting the drill core from the holder system, the undisturbed final solution cavities were examined macroscopically. Refer to Chapter 2 for details of the experimental setup and procedure.

## 4.3 Results

The measurements and calculated volumes of solution residues and dissolved halite of all dissolution runs are presented prior to the dissolution phenomena of the 2D and 3D top of rock salt experiments as outlined above.

### 4.3.1 Instrumentation results

The same type of data was obtained during the experiments as presented in Chapters 2.3.1 and 2.3.2. Table 4.2, Table 4.3 and Figure 4.3 contain the measured data and calculated volumes of the dissolution runs. Similar to the dissolution runs with a horizontally oriented borehole, the electrical conductivity of the outlet brine revealed a negligibly small increase in electrical conductivity until attaining stable values (Figure 4.3A). Only dissolution run RS12 showed a constant value throughout the experiment. However, this can be related to the low inflow rate and short running time resulting in a low discharge volume. The cumulative weight of the outlet brine

| Run number | Solution cavity<br>Solution residue weight[a] mg | Solution residue volume $cm^3$ | Dissolved halite volume $cm^3$ |
|---|---|---|---|
| First type of dissolution experiments: | | | |
| RS7 | 26,9 | 0,010 | 2,9 |
| RS13 | 16,3 | 0,006 | 2,5 |
| RS12 | 8,3 | 0,003 | 0,7 |
| RS24 | 2,7 | 0,001 | 1,7 |
| Second type of dissolution experiments: | | | |
| RS27 | 15,7 | 0,006 | 8,3 |
| RS28 | 2,4 | 0,001 | 3,0 |

[a] Solution residue weight = Weight of filter with dried residue minus weight of filter

***Table 4.3*** *Measured weight of solution residue, calculated volume of solution residue and dissolved halite of all dissolution runs (cf. also Appendix A.3).*

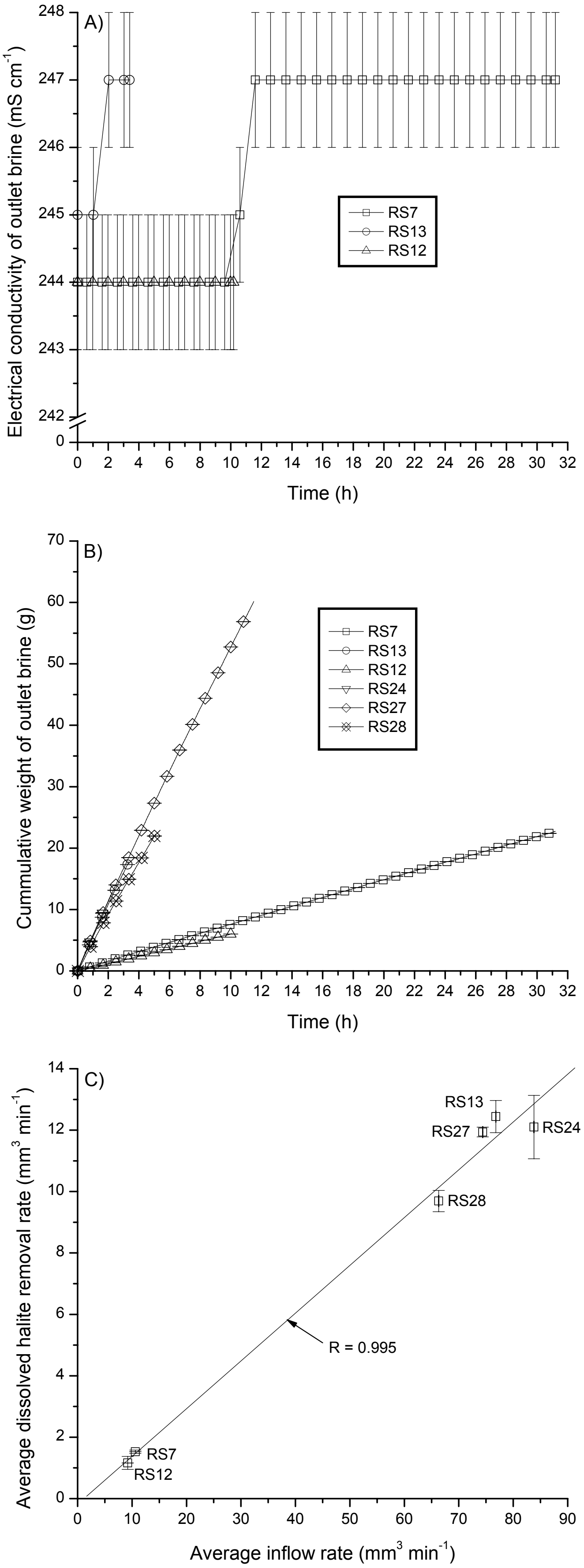

***Figure 4.3*** *A) Electrical conductivity of outlet brine as a function of time. B) Cumulative weight of discharging solution as a function of time. Every 10th data point is displayed as a symbol. C) Average dissolved halite removal rate versus average inflow rate (cf. Appendix A.3). The solid line represents a linear fit. R = correlation coefficient.*

also increased linearly with time (Figure 4.3B), and a linear relationship between the average dissolved halite removal rate and average inflow rate was observed (Figure 4.3C).

### 4.3.2 Experiments with a flat top of the salt layer

In these dissolution runs, a flat solution cavity developed at the top of the salt layer (Figure 4.4A). These voids enlarged to a constant height of ~1–~2 mm in z direction. A small trumpet-shaped inlet formed, but only a few mm down in z direction. No salt dissolution occurred further down in the cylindrical hole. As in the dissolution runs with a horizontally oriented borehole (cf. Chapter 2), the macroscopic dissolution features were similar irrespective of inflow rate and disseminated impurity content. However, discrete, millimeter-thin layers of impurities influence the regular shapes.

At γ = 30 and 45° (dissolution runs RS12 and RS24), respectively, the outlines of the cavity walls at the inflow surface of the salt cores (xy plane) are between triangular and rectangular, respectively. In these two dissolution runs, practically the entire solution cavity is situated up dip of the borehole inlet (Figure 4.4B; Appendix A.1.3). Based on these two dissolution runs and visualization of buoyancy-driven flow (Figure 4.5), the direction of dip of the almost horizontal top of the salt layer of the dissolution runs RS7 and RS13 was determined as presented in Figure 4.4B (cf. also Appendix A.1.3). In these two cases, the outlines are ellipsoidal. The original boreholes are situated in the

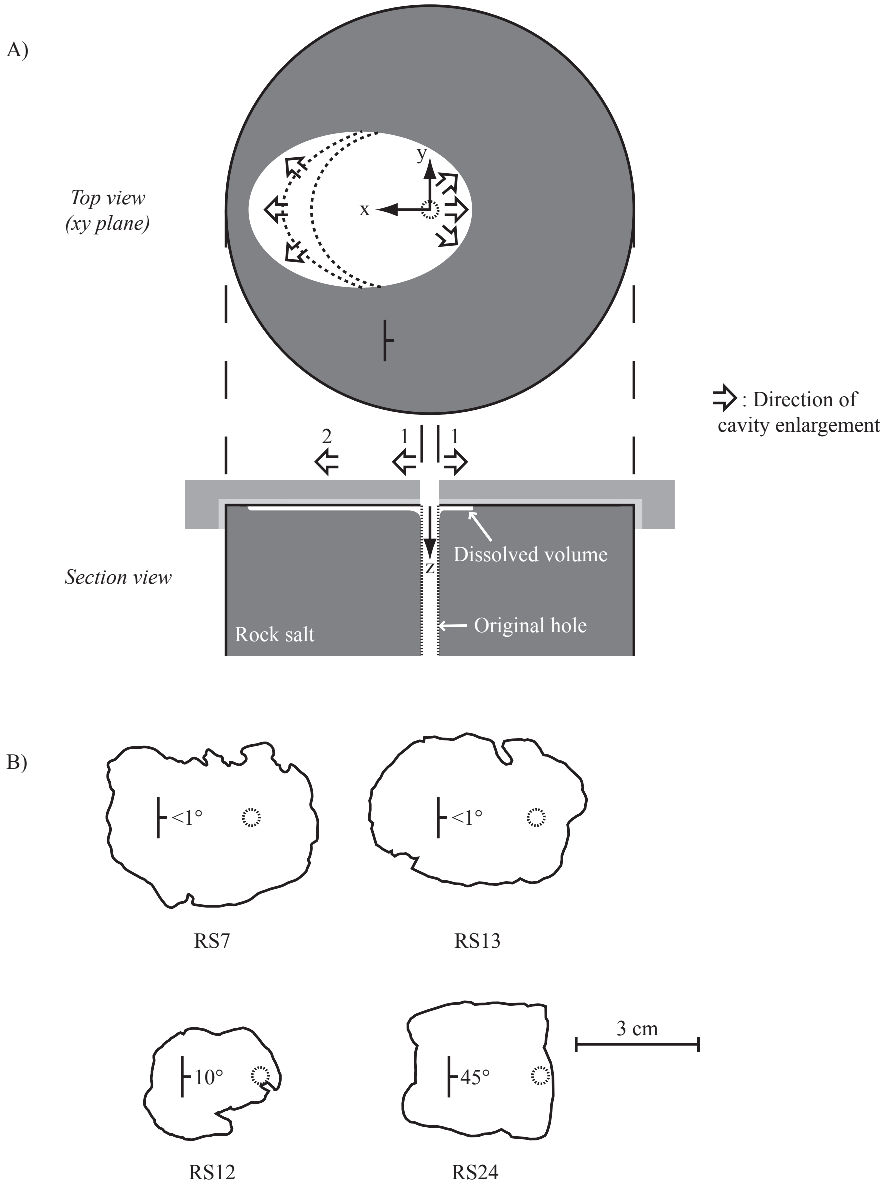

***Figure 4.4*** *Dissolution runs RS7, RS13, RS12, and RS24: A) Schematic diagram of a drill core with final solution cavity. B) Outlines at the inlet at the end of the four dissolution runs.*

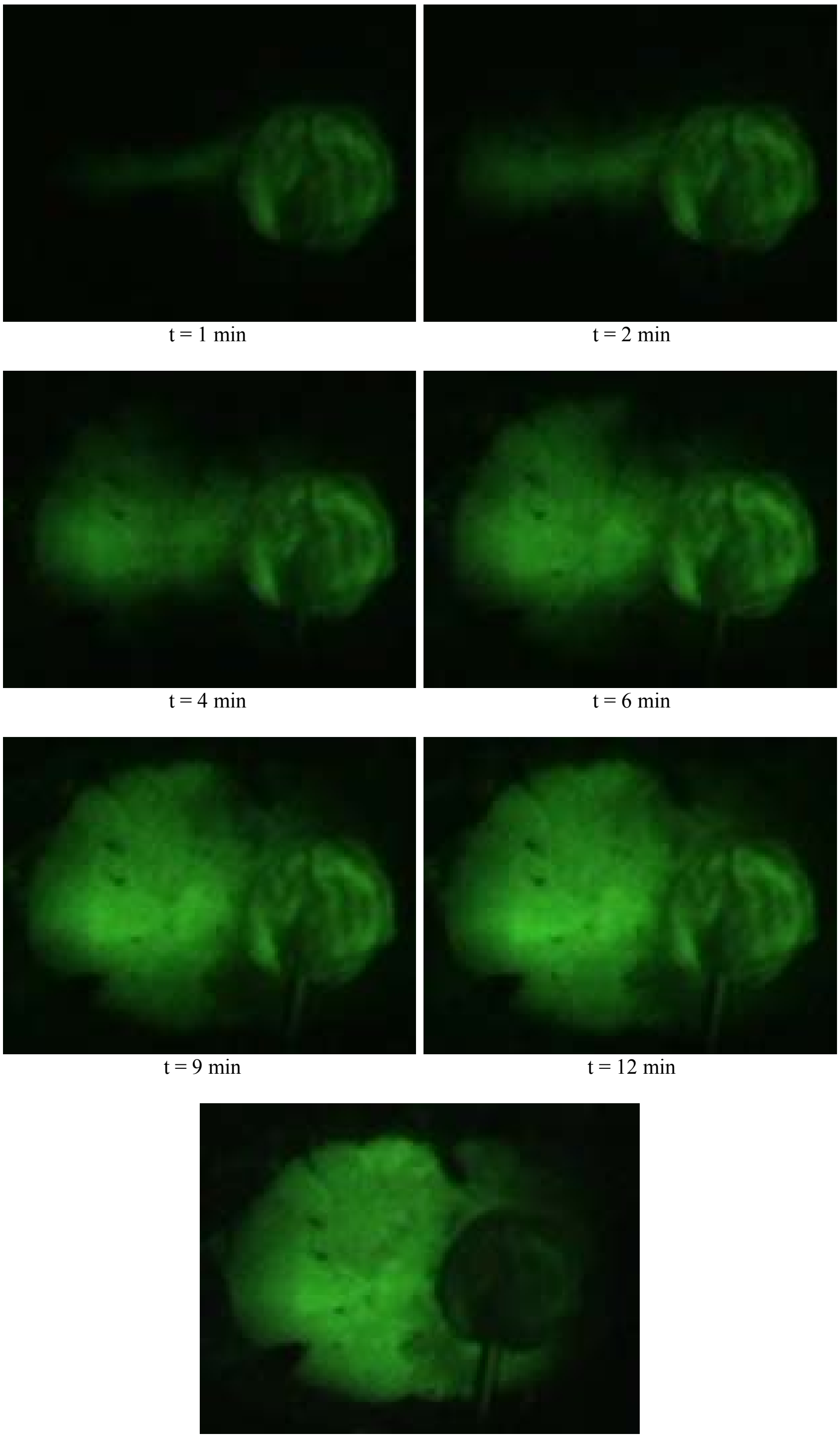

t = 1 min t = 2 min

t = 4 min t = 6 min

t = 9 min t = 12 min

t = 22 min

Full-scale

***Figure 4.5** Time-lapse, videotape recording of the flow pattern at elapsed times t = 1, 2, 4, 6, 9, 12, and 22 minutes after injection of uranine-containing water into the cavity (dissolution run RS13). The visible circle on the right is caused by a silicone blob molding the Tygon tubing into the Plexiglas tube.*

down dip half of the solution cavities and the cavities are elongated parallel to the direction of dip of the top of the salt layer.

The recorded development of the flow pattern is illustrated in Figure 4.5. The results clearly indicate a symmetrical flow. The borehole accessing freshwater ascend straight up dip along the x-axis to the highest section of the solution cavity. The fluid stream then spread fan-wise over the entire solution cavity. Figure 4.4A illustrates schematically how the cavities enlarged in general. At first, these cavities enlarged radially outward (parallel to the xy plane) from the borehole at the inlet side (1), afterwards they enlarged mainly in x direction (2). With a clear inclination of

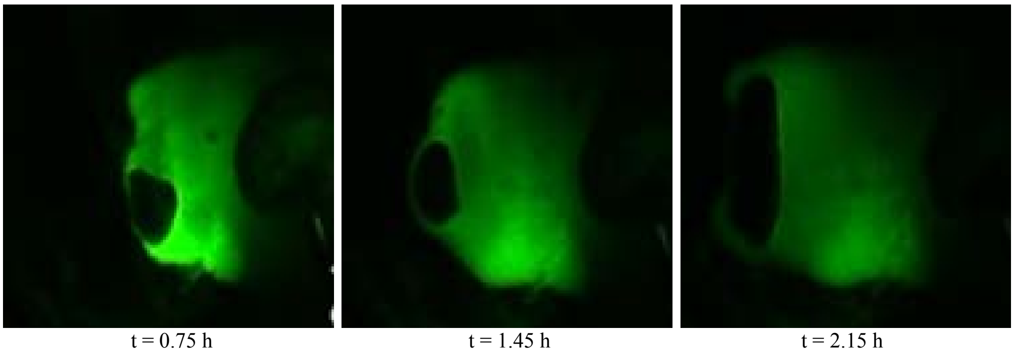

***Figure 4.6*** *Time-lapse, videotape recording of the enlargement of solution cavity and position of gas bubble at the entrance of the borehole at elapsed times t = 0.75, 1.45 and 2.15 hours after injection of uranine-containing water into the cavity (dissolution run RS24).*

the top of the salt layer, the cavities enlarged mainly in the up dip direction (2) right from the start. The latter is illustrated in Figure 4.6, where a gas bubble can also be clearly seen trapped always at the up dip limit of the solution cavity.

### 4.3.3 Experiments with a step like top of the salt layer

More complex solution cavities formed in the second type of dissolution experiments. The genesis and shape of the solution cavity of the dissolution run RS27 is presented schematically in Figure 4.7, that of the dissolution run RS28 in Figure 4.8. As in the other type of dissolution experiments, a gas bubble was always trapped at the up dip limit of the solution cavity. The solution cavity reached a maximum vertical height of ~17 mm along the fault (dissolution run RS27) or ~8 mm (dissolution run RS28), respectively. The scanned inflow ends of the drill cores are presented in Appendix A.1.4.

At the beginning of dissolution run 27, and similar to the first type of dissolution experiments, a flat solution cavity enlarged mainly in x direction along the top of the salt layer (2). The cavity reached the fault after only ~1/14 of the total running time. At this stage salt (hanging wall) was overlying the up dip limit of the cavity at the top of the footwall (cf. Figure 4.2), thereby resulting in a cavity enlargement upwards and simultaneously sidewards along the fault plane (3a), such as the one presented in Chapter 2 for development of a conical solution cavity with a horizontal base facing upwards. The morphological elements of the horizontal ceiling and facet also developed in this dissolution run. During (3a), a gas bubble, jerking occasionally sideways due to selective dissolution of halite, was always clearly seen at the horizontal ceiling. As soon as the cavity reached the covering layer of the hanging wall, another two flat solution cavities developed (4), enlarging again mainly in x direction. Between the two solution cavities (4), salt dissolution was inhibited by the gas bubble at the horizontal ceiling, thus preventing the formation of one continuous void (4).

Comparable to the first type of experiments and phase (2) of dissolution run RS27, the solution cavity of dissolution run RS28 enlarged relatively fast along the top of the salt (2) and reached the fault after ~1/2.5 of the total running time (cf. Figure 4.2). When in contact with the fault, the solution cavity enlarged along the fault plane sideways and downwards (3b), resulting in a more or less flat horizontal cavity floor in contact with the fault.

## 4.4 Discussion

### 4.4.1 Flow experiments

Similar to the dissolution runs with a horizontally oriented borehole (cf. Chapter 2), the flow in these two types of experiments is also extremely buoyancy-driven and coupled with salt dissolution. When combined, convection of the fluid is therefore caused by (a) hydraulic gradient (induced by peristaltic pump), (b) constant supply of buoyant, undersaturated water from a point source, (c) adjustment of a stable fluid density layering, and (d) increase in solute NaCl-concentration until saturation around an overlying thin, undersaturated layer in contact with the highest section of the cavity wall. At the inlet side of the borehole, the NaCl-undersaturated water and gas, the latter released by salting out effect, accumulate

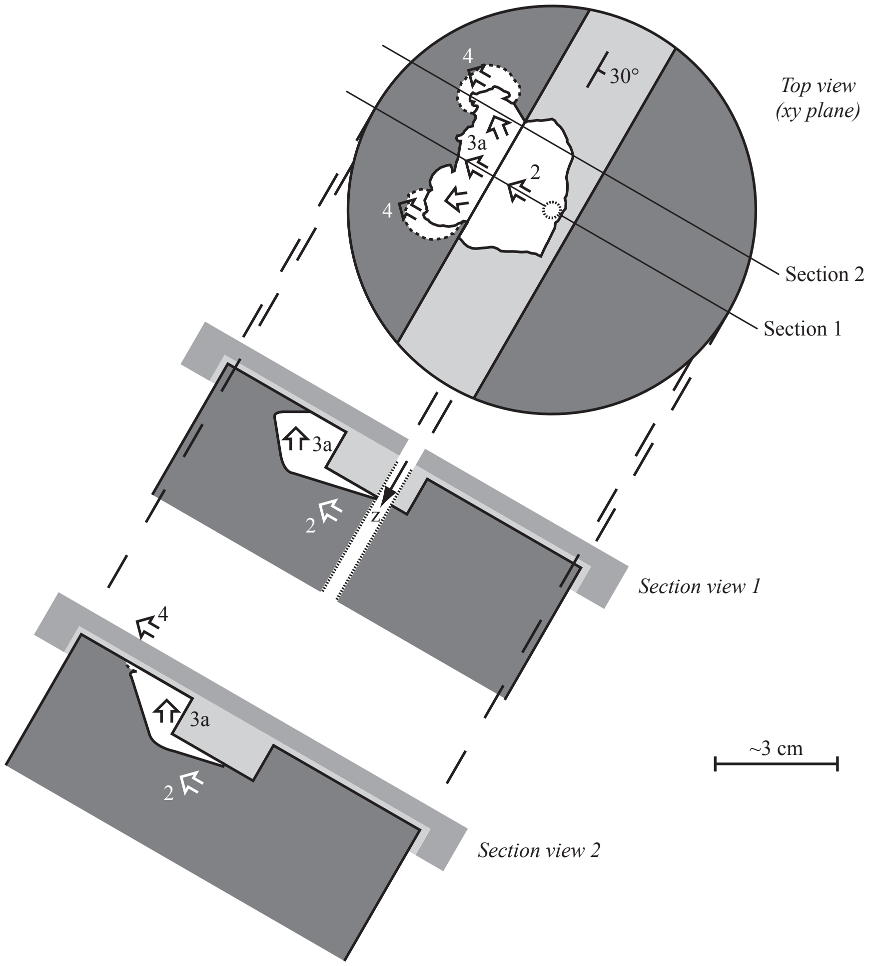

***Figure 4.7** Solution cavity outline of dissolution run RS27 presented in a schematic diagram.*

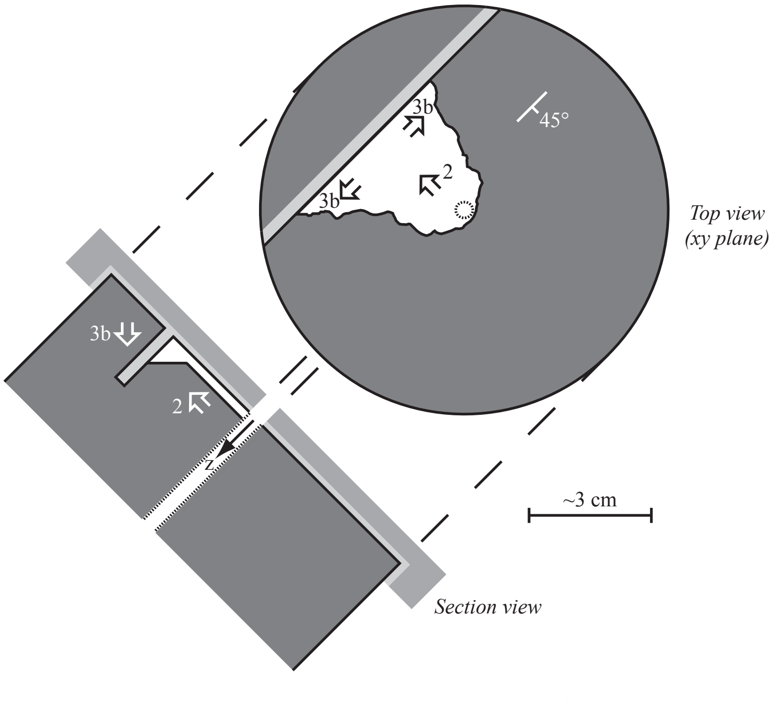

***Figure 4.8** Solution cavity outline of dissolution run RS28 presented in a schematic diagram.*

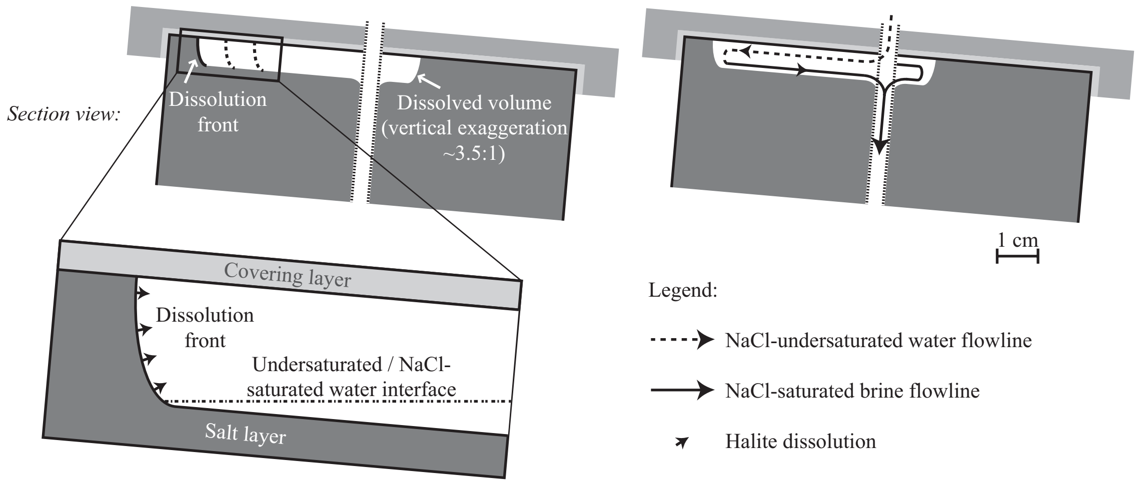

***Figure 4.9*** *Model of solution cavity genesis.*

in the highest section of the cavity – the gas highest followed by the undersaturated water, both floating on the NaCl-saturated brine.

Due to a layering effect, the top-surface-parallel component of cavity growth and displacement of the dissolution front (xy directions), respectively, is much stronger than the vertical one. With increasing γ, the cavity grows predominantly in x direction. A quasi-2D geometry of convection cell forms. However, an explanation for the tracer movement presented in Figure 4.5 is difficult, as the position of the traced, undersaturated water in contact with the upper and lower boundary of the solution cavity is not clear. Schematically presented, the inflowing, less dense freshwater jet flows upslope along the upper solution cavity boundary (on the x-axis) forming a thin, low-density horizontal layer where halite dissolution occurs instantaneously (Figure 4.9). A thin film of NaCl-saturated brine subsequently moves down along the bottom boundary of the solution cavity. The NaCl-saturated solution, above the bottom boundary of the solution cavity, protects the halite from further dissolution (Figure 4.9). The solution cavity would show a quasi-2D tabular and circular cavity only with a perfectly horizontal salt top. If γ is relatively small, a horseshoe-shaped dissolution front develops and leads to an elliptically formed solution cavity as presented by the dissolution runs RS7 and RS13. With rising γ, the dissolution front turns horizontal. The solution cavities of the dissolution runs RS12 and RS24 represent a transition towards a quasi-3D conical solution cavity as presented in Chapter 2. Since stable fluid density interfaces are horizontal, the formed ceiling or "salt table", respectively, must also be horizontal during phase (3a) of dissolution run RS27 (cf. also Chapter 2) and during phase (3b) of dissolution run RS28 (cf. e.g., Farkas et al., 1951).

### 4.4.2 Interstratal salt karstification and overlying surface subsidence pattern

The findings of the flow experiments can be upscaled and integrated into a conceptual model for interstratal salt karst development by density-dependent groundwater flow and corresponding overlying land subsidence pattern in the context of horst and graben structures as for example observed in the Muttenz-Pratteln region (cf. Chapter 1).

Since there are endless variations in natural geological subsurface settings and regional groundwater circulation systems, only a limited number of four hypothetical situations are illustrated and discussed: a fault bringing a salt layer against a largely impervious, poorly soluble block under two different regional groundwater circulation systems (Figure 4.10A and Figure 4.10B), a fault bringing a salt layer opposite a salt layer under two different fault trends (Figure 4.10C and Figure 4.10D).

The interstratal salt karst develops along the top of the salt layer analog as presented by the flow experiments. The permeable normal faults and inclination of the top of the salt layer clearly influence the development and spread of this karst system. Normal faults act as preferred channels of groundwater flow resulting in a recharge with salt-depleted water from above to the salt and discharge with salt-enriched water away from the salt. The movement of these two solutions occurs along separate and distinct paths in the same fault(s) and/or along respective fault(s). At the beginning, unless salt dissolution starts at the up dip limit of the salt layer (Figure 4.10B), the main dissolution front displaces along the top of the salt layer, mainly against the direction of the dip (2) (Figure 4.10A, Figure 4.10C and Figure 4.10D). A fault-associated, large solution cavity section filled with salt-enriched

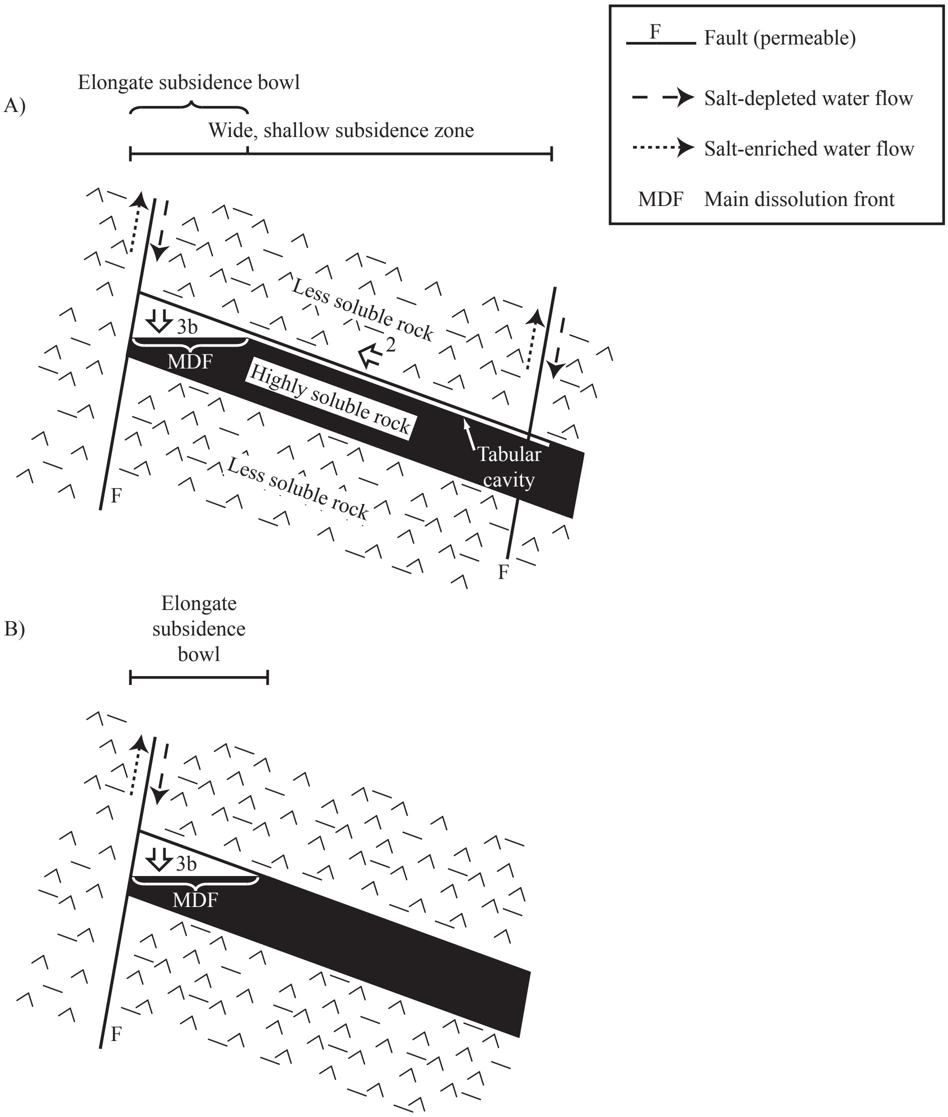

*Figure 4.10 Possible developments (A–D) of an interstratal salt karst at the top of a salt layer in the context of extensional tectonics and inclined beds.*

water (3b) develops if the developing interstratal salt karst reaches a largely impermeable, poorly soluble block (Figure 4.10A) as the one presented in Figure 4.10B. Such fault-associated cavity geometries are comparable to fault-associated oil traps found in the petroleum geology (e.g., North, 1985). Such a developing section may also lead to a continuation (4) of this karst system along the top of the displaced salt layer (Figure 4.10C). Another continuation (3a) is presented in Figure 4.10D, however, a fault-associated NaCl-saturated filled solution cavity developed here, whose horizontal cross-section increases upwards. Salt dissolution occurs mainly at the sideways displacing main dissolution front (2, 4) or horizontal main dissolution front at the up dip limit of the displaced salt layer (3b) or simultaneously at the horizontal ceiling and at the upper end of a facet (3a). Aside from the main dissolution front of 3b, along the lower boundary of the tabular cavities only very small dissolutional receding is observed due to limited advective and diffusive mixing. The salting out effect mainly leads to carbon dioxide gas (e.g., Harvie et al., 1984; Stumm and Morgan, 1996) in association with this high-density karst water. At field scale for example, such degassing was reported from drilled through brine-filled solution cavities at the top of a salt unit (Belchic, 1960).

Such a subsurface conceptual model may explain the subsidence pattern detected in a region as Muttenz Pratteln. The wide, shallow subsidence zones may owe their location to the underlying thin and flat-expanded section of the interstratal salt karst. Elongate subsidence bowls parallel to the fault system within these zones, revealing stronger subsidence velocities, may be related to underlying, fault-bound (higher) solution cavities (Figure 4.10). A fault may also act as a subsidence barrier as shown in Figure 4.10A and Figure 4.10B.

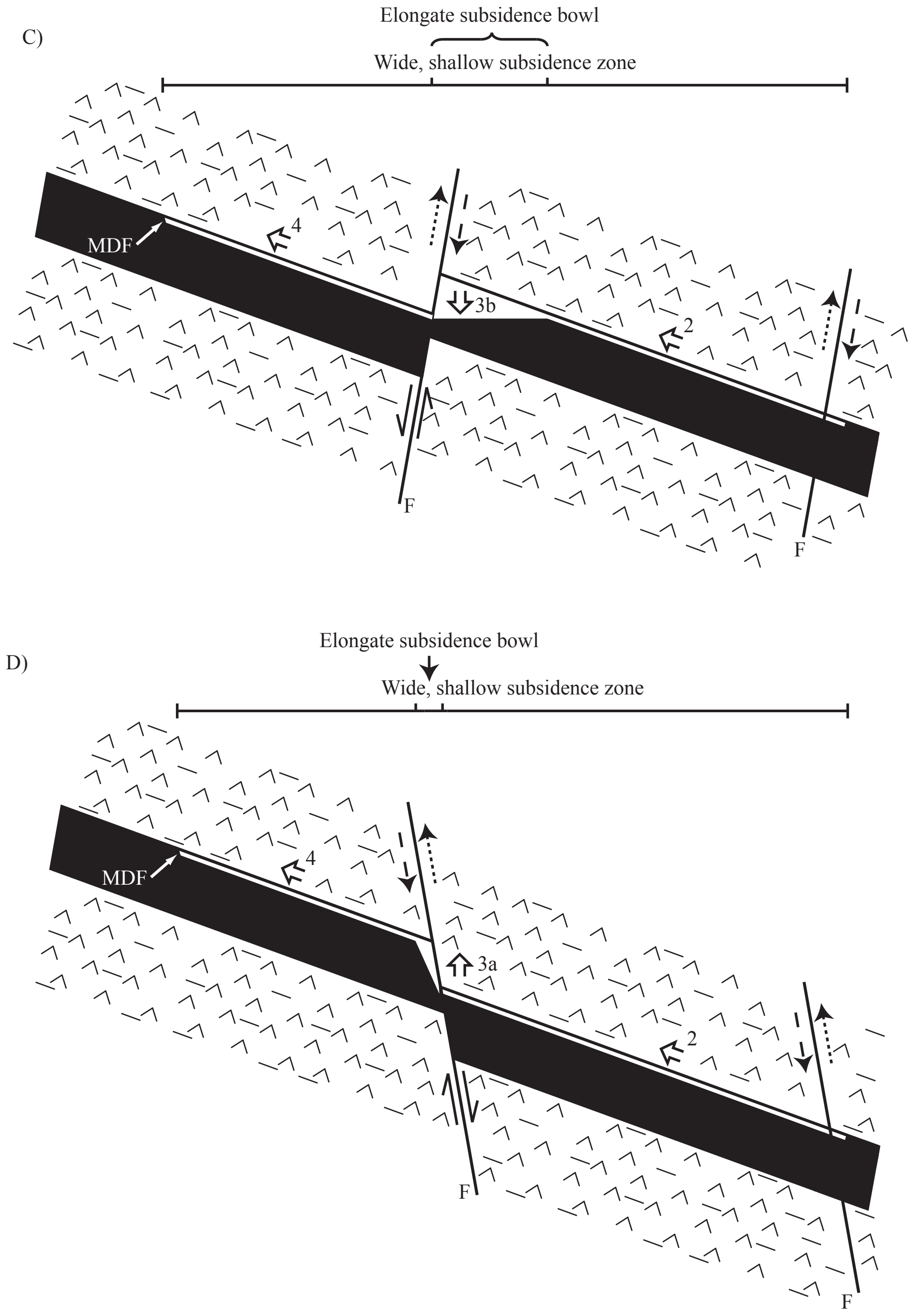

***Figure 4.10*** *(continued)*

## 4.5 Summary and conclusions

The investigations reveal the advantage of small-scale dissolution experiments when trying to understand the complex processes underlying natural (and possibly anthropogenically induced) interstratal salt karstification. The experimental data allows to explain the genesis of flat expanded solution cavities at the top of a salt layer inside horst and graben structures and may be also the overlying subsidence pattern. The close correlation of the experimental solution cavities and cavity geometries in the field indicates a development of the interstratal salt karst along the top of the rock salt layer at the beginning mainly in the up dip direction by a sideward displacement of the main dissolution front. When in contact with a fault, an areal horizontal salt dissolution front mainly broadens the solution cavity downwards or upwards, leading to a fault-associated solution cavity (section) possibly responsible for the overlying fault-parallel subsidence bowl.

A morphological land surface analysis of an affected area (time series of subsidence, spatial distribution) allows to obtain an overview of the distribution of the underlying interstratal salt karst system. Widespread leveling measurements of land subsidence are required if morphologies are difficult to detect visually, such as in the Muttenz-Pratteln region.

In the future theoretical aspects of density-dependent groundwater circulation in contact with an interstratal salt karst and rock mechanics (subsidence of the overlying geological materials) have to be implemented in this work to verify the presented hypotheses.

## 4.6 References

Baer, G., U. Schattner, D. Wachs, D. Sandwell, S. Wdowinski, and S. Frydman (2002), The lowest place on Earth is subsiding – An InSAR (interferometric synthetic aperture radar) perspective, *Geol. Soc. Am. Bull.*, *114*(1), 12–23.

Belchic, H. C. (1960), The Winnfield salt dome, Winn Parish, Louisiana, Guidebook 1960 Spring Field Trip, *Shreveport Geol. Soc.*, 29–48.

Belderson, R. H., N. H. Kenyon, and A. H. Stride (1978), Local submarine salt-karst formation on the Hellenic Outer Ridge, eastern Mediterranean, *Geology*, *6*, 716–720.

Farkas, L., H. L. Litman, and M. R. Bloch (1951), The formation of “salt tables” in natural and artifical solar pans, *Bull Research Council of Israel*, *1*(1–2), 36–39.

Gustavson, T. C., W. W. Simpkins, A. Alhades, and A. Hoadley (1982), Evaporite dissolution and development of karst features on the rolling plains of the Texas panhandle, *Earth Surface Processes and Landforms*, *7*, 545–563.

Harvie, C. E., N. Møller, and J. H. Weare (1984), The prediction of mineral solubilities in natural waters: The Na-K-Mg-Ca-H-Cl-$SO_4$-OH-$HCO_3$-$CO_3$-$CO_2$-$H_2O$ system to high ionic strengths at 25°C, *Geochim. Cosmochim. Acta*, *48*, 723–751.

Johnson, K. S. (1981), Dissolution of salt on the east flank of the Permian Basin in the southwestern U.S.A., *J. Hydrol.*, *54*, 75–93.

Johnson, K. S. (1992), Evaporite karst in the Permian Blaine Formation and associated strata in Western Oklahoma, USA, *Int. Contributions to Hydrogeology*, *13*, 405–420.

Lohmann, H. H. (1972), Salt dissolution in subsurface of British North Sea as interpreted from seismograms, *American Association of Petroleum Geologists Bulletin*, *56*(3), 472–479.

Murawski, H. (1992), *Geologisches Wörterbuch*, dtv, Ferdinand Enke Verlag, Stuttgart.

McManus, K. M. and J. S. Hanor (1993), Diagenetic evidence for massive evaporite dissolution, fluid flow, and mass transfer in the Louisiana Gulf Coast. *Geology*, *21*, 727–730.

North, F. K. (1985), *Petroleum geology*, Allen & Unwin, Boston.

Quinlan, J. F., R. A. Smith, and K. S. Johnson (1986), Gypsum karst and salt karst of the United States of America, *Le Grotte d’Italia*, *4*(XIII), 73–92.

Reuter, F., K. J. Klengel, and J. Pašek (1992), *Ingenieurgeologie*, Deutscher Verlag für Grundstoffindustrie GmbH, Leipzig, Stuttgart.

Reuter, F., and D. Stoyan (1993), Sinkholes in carbonate, sulphate, and chloride karst regions: Principles and problems of engineering geological investigations and predictions, with comments for the destruction and mining industries, in *Applied karst geology*, *Proceedings of the fourth multidisciplinary conference on sinkholes and the engineering and environmental impacts of karst*, edited by B. F. Beck, pp. 3–25, A.A.Balkema, Rotterdam.

Reuter, F., and V. V. Tolmačëv (1990), *Bauen und Bergbau in Senkungs- und Erdfallgebieten. Eine Ingenieurgeologie des Karstes*, Schriftreihe für Geologische Wissenschaften, 28, Akademie-Verlag Berlin.

Spackeler G. (1957), *Berg- und Aufbereitsungstechnik - Lehrbuch des Kali- und Steinsalzbergbaus*, W. Knapp Verlag, Halle.

Stumm, W., and J. J. Morgan (1996), *Aquatic chemistry*, *Chemical equilibria and rates in natural waters*, 3rd ed., John Wiley & Sons, New York.

Waltham, A. C. (1989), *Ground subsidence*, Blackie & Son, Glasgow and London.

# 5 Development of a resistance measuring cell for in situ determination of solute concentration in a flow tank

## 5.1 Introduction

Saltwater upconing in a freshwater aquifer was studied and numerically modeled in a 2D flow tank (Chapter 6). An adequate non-commercial measuring technique had to be developed first to measure salt concentrations at different sites in the upconing salt mass.

Various methods are available for quantitative analysis of spatial and temporal measurement of solute concentrations in a flow tank containing a water-saturated porous medium. According to Silliman et al. (1998), three approaches can be used to characterize solute concentrations in a flow tank. The first approach is based on visualization and relates dye concentration to visual intensity on a recording device; the second withdraws microsamples for analysis by standard analytical techniques; the third applies in-situ measurement. The third approach was chosen in this study conducted in collaboration with Edi Meier + Partner AG (Technopark Winterthur, Switzerland). A set of electrodes (resistance measuring cell) was developed to allow indirect measurement of solute concentrations of Na-Cl over a wide range (from 0 to ~300 g $l^{-1}$) in a flow tank. Indirect measurement over such a wide range has, as yet, rarely been conducted in-situ in flow tank experiments before (e.g., Hassanizadeh and Leijnse, 1995).

This new technique (the prototype is presented in Section 5.2) was tested in a flow tank and calibrated to analyze the suitability of the measured data (Section 5.3.1). To determine the equivalent NaCl background concentration, a standard conductivity flow-thru cell was also calibrated with the same calibration solutions. In a second pilot batch (Section 5.3.2), different electrode arrangements were tested while pumping a Na-Cl brine bottom-up into a small container to determine the most appropriate electrode arrangement for the experiments presented in Chapter 6. The latter tests also provide information on the approximate measuring volume of a resistance measuring cell. An ongoing discussion about the measurements and theory related to the measurement technology (e.g., Telford et al., 1990) is beyond the scope of this work.

## 5.2 Prototype of resistance measuring cell (RMC)

The original RMC design (array 1) is illustrated in Figure 5.1. It consists of five gilded stainless steel electrodes (Ø 0.4 cm, length 13 cm) mounted on a Plexiglas flange. The electrodes are fixed in parallel on a plane and equally spaced (1 cm). They can be fitted through the Plexiglas front plate extending 6.4 cm into the porous medium of the flow tank. Furthermore, due to small borehole deviations when drilling through Plexiglas, the electrodes are not exactly parallel to each other. The output voltage between the electrodes $P_1$ and $P_2$ was measured while electrical current flowed through the porous media between the outer pair of electrodes $C_1$ and $C_2$. The grounding electrode is located in the center. The measuring principle is based on a 4-electrode resistance measurement technique, where the current is supplied via an accurately regulated sinusoidal oscillator signal. The measured AC output voltage is rectified through a demulator circuit in phase to the oscillator. The resulting DC output voltage was recorded using a micro-logger and a relay-based multiplexer to measure all the RMCs sequentially (cf. Chapter 6). An alternating current was applied in all measurements to minimize polarization in the cell and to prevent ion movement of the ions caused by the presence of a voltage potential (E. Meier, 2007, personal communication).

Since this measuring method is sensitive to temperature variations, sensors were also inserted in the porous medium to monitor pore water temperature. Each temperature sensor (YSI 4006; accuracy ±0.01°C)

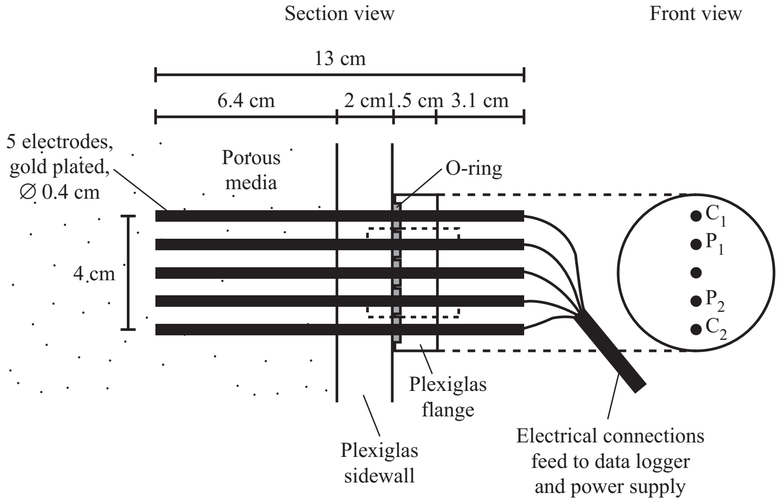

***Figure 5.1*** *Schematic of prototype of a resistance measuring cell showing basic dimensions. $C_1$ and $C_2$ represent the current electrodes, $P_1$ and $P_2$ the potential electrodes.*

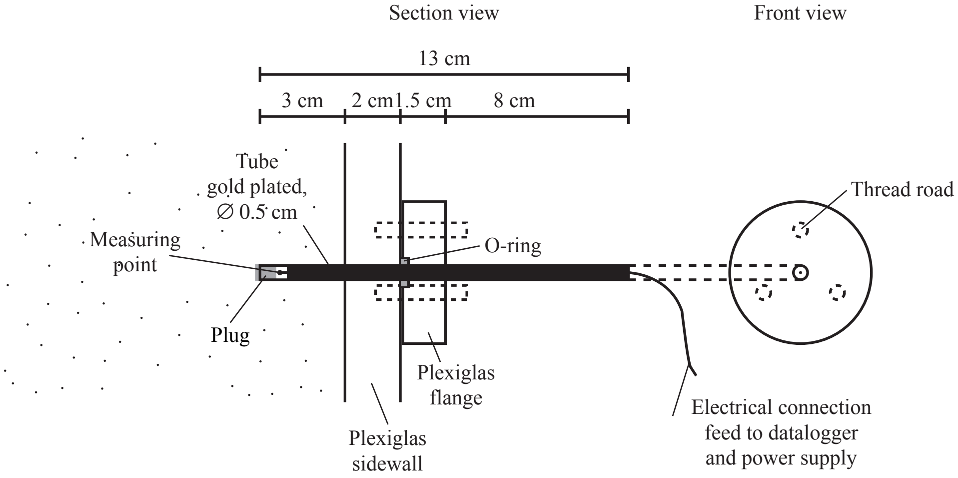

***Figure 5.2*** *Schematic of a temperature sensor showing basic dimensions.*

| Data logger recording software | Input voltage range of the data acquisition (mV) | Used for |
|---|---|---|
| ELCOL-1 | 0-2500 | Testing cell (this Chapter) |
| ELCOL-2 | 0-2500 | |
| ELCOH-1 | 0-250 | |
| ELCOH-2 | 0-250 | |
| ELCONDU-1 | 0-2500 | First experiments (Chapter 6) |
| ELCONDU-2 | 0-250 | |

***Table 5.1*** *Technical data of the three different data logger recording software used.*

was fitted into a gilded stainless steel tube (∅ 5 mm) and inserted in the porous medium at a 3-cm depth (Figure 5.2).

Different data logger recording software was used for the tests. Since a wide range of voltage values had to be measured, two different measuring ranges (e.g., ELCOL-1/-2) were used for each time step (each measurement). *-1* is suitable for low salt concentrations (less current is supplied than in *-2*) and *-2* is suitable for high salt concentrations. Table 5.1 presents an overview of the different software programs used (including the one for the experiments presented in Chapter 6).

## 5.3 Testing: Calibration approach and electrode arrangement

### 5.3.1 Calibration of the measuring cells

The testing objective of the RMC technique was to find a mathematical function relating output voltage to solute concentration. The calibration was carried out in a 2D flow tank as desribed in detail in Chapter 6. The 1.68 m long, 1.31 m high and 0.20 m wide tank was set up in the same way as described under step 1 in Chapter 6 and with the same sand as described in Chapter 6. Thirty-two RMCs with vertically aligned electrodes (cf. Figure 5.1) were placed in the lowest two RMC rows in the front of the flow tank, including one temperature sensor (T3) (Figure 5.3 and Figure 5.4A).

Beside the initially filled tank freshwater (tap water), thirteen calibration solutions (each 120 l) of specific amounts of sodium chloride (table salt from Salins, Montpellier, France) dissolved in freshwater were prepared using an electric mixer with regard to the fact that the initial water volume increases considerably when a lot of salt is added to the water (e.g., Wolf et al., 1982). The following Na-Cl calibration solutions were prepared: 1, 2, 5, 10, 20, 30, 40, 50, 100, 150, 200, 250, and 300 g $l^{-1}$. A standard conductivity flow-thru cell (WTW model TetraCon DU/T) connected to a laboratory conductivity meter (WTW model inolab Cond Level 2) was also calibrated with the same solutions.

The calibration procedure is presented in Figure 5.3 and Table 5.2. The initially filled tank freshwater was the first calibration solution. The salt (Na-Cl) concentration of the freshwater is assumed to be 0 g $l^{-1}$. The output voltage was measured in stagnant pore water over several hours (Table 5.2). The recharge reservoir was subsequently connected via a plastic tube to the filling valve. Each of the prepared calibration solutions (in sequential order from low-density to high-density solutions) was injected with a peristaltic pump through four equidistant holes (Ø 1 cm) in the bottom plate of the flow tank. The outflow was led through two overflows (Figure 5.3). Therefore, flow was always directed upward with the heavier solution displacing the lighter resident one. Thus, all the calibration solutions injected may be regarded as stable displacements. About double (100 l) the estimated pore volume (50 l) was injected each time. The inflow rate was always ~10 l $h^{-1}$ and each pumping sequence ~10 h. Each calibration solution was injected until the measured output voltage of each individual RMC, located in the porous medium, had reached a constant value over some hours. From the moment the breakthrough curves leveled out to a constant value, the average output voltage value with its standard deviation was calculated for each RMC.

The data logger recording software ELCOL-1/-2 was used for the calibration solutions containing 0–40 g $l^{-1}$. For the 50–300 g $l^{-1}$ calibration solutions, the data logger recording software ELCOH-1/-2 was applied (cf. Table 5.1). The cells/sensor were automatically and sequentially scanned every 6 min (Table 5.2). One measurement was also conducted with the complementary data logger recording software at the end of each calibration pass.

### 5.3.2 Different electrode arrays

In another experimental setup, different electrode

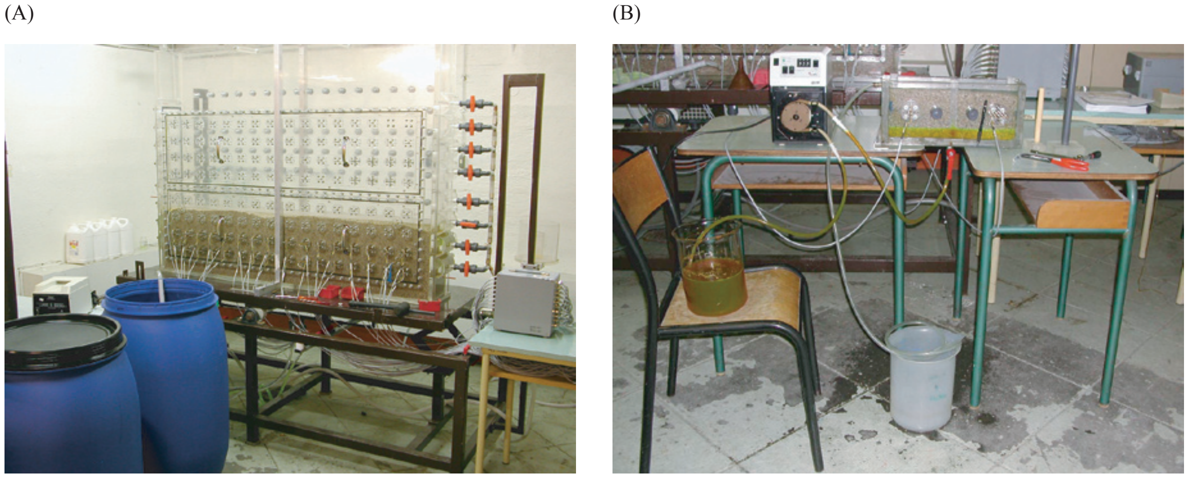

*Figure 5.4* *Experimental setup for tests in the (A) 2D flow tank and in the (B) small container, respectively. The horizontal saltwater layer can be clearly observed in (B) (reddish color of the brine, yellowish color of the transition zone).*

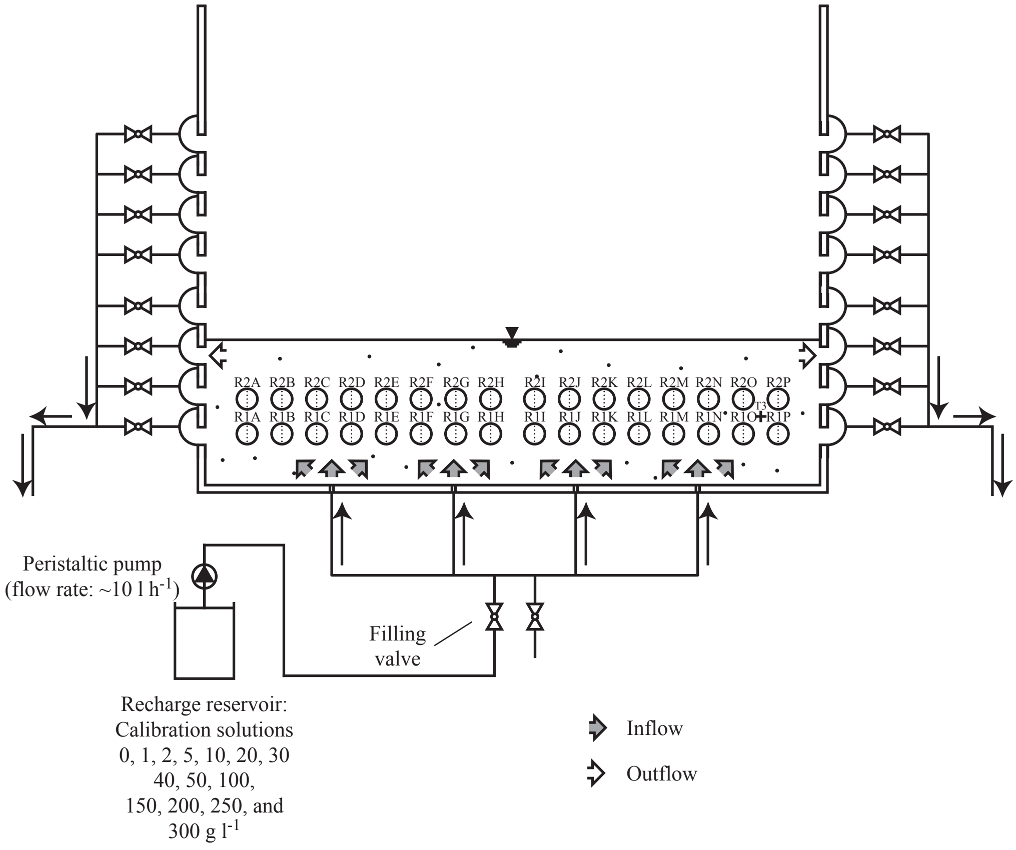

*Figure 5.3 Location of the resistance measuring cells in the flow tank and calibration procedure. The grey arrows indicate the spread of the injected calibration solutions.*

| Displaced calibration solution | Injected calibration solution | | Pump on | Mean inflow rate | Scan rate |
|---|---|---|---|---|---|
| g $l^{-1}$ | l | g $l^{-1}$ | h | l $h^{-1}$ | min |
| 0[a] | - | - | - | - | 6[b] |
| 0 | 90.4 | 1 | 10.08 | 8.97 | 6 |
| 1 | 92.2 | 2 | 10.28 | 8.97 | 6 |
| 2 | 105.5 | 5 | 10.42 | 10.12 | 6 |
| 5 | 102.4 | 10 | 10.12 | 10.12 | 6 |
| 10 | 102.4 | 20 | 10.12 | 10.12 | 6 |
| 20 | 103.7 | 30 | 10.25 | 10.12 | 6 |
| 30 | 103.4 | 40 | 10.22 | 10.12 | 6 |
| 40 | 102.8 | 50 | 10.16 | 10.12 | 6 |
| 50 | 102.5 | 100 | 10.13 | 10.12 | 6 |
| 100 | 108.0 | 150 | 10.67 | 10.12 | 6 |
| 150 | 107.6 | 200 | 10.63 | 10.12 | 6 |
| 200 | 108.0 | 250 | 10.67 | 10.12 | 6 |
| 250 | 105.8 | 300 | 10.45 | 10.12 | 6 |

[a] Pore water not displaced

[b] Measured during 4.97 h

***Table 5.2** Specifications of the calibration procedure.*

arrays were tested to determine the most appropriate electrode arrangement showing a small dependence from the position of the saltwater front being at the same distance from the grounding electrode.

The tests were conducted in a small container of 35.8 cm length, 15.9 cm height, 9.2 cm depth and open top. The prepared container was always positioned horizontally on two tables. Two RMC attachments at the tank's head and one in the rear were available to test up to three RMCs simultaneously (Figure 5.4B and Figure 5.5). The tank preparation and sand material were set up as illustrated in Section 5.3.1. A new sand pack was used for each test.

To test different electrode arrays, a Na-Cl brine (300 g $l^{-1}$) containing a small amount of a reddish fluorescent dye (uranine, 1.0 g $l^{-1}$) was injected slowly into the

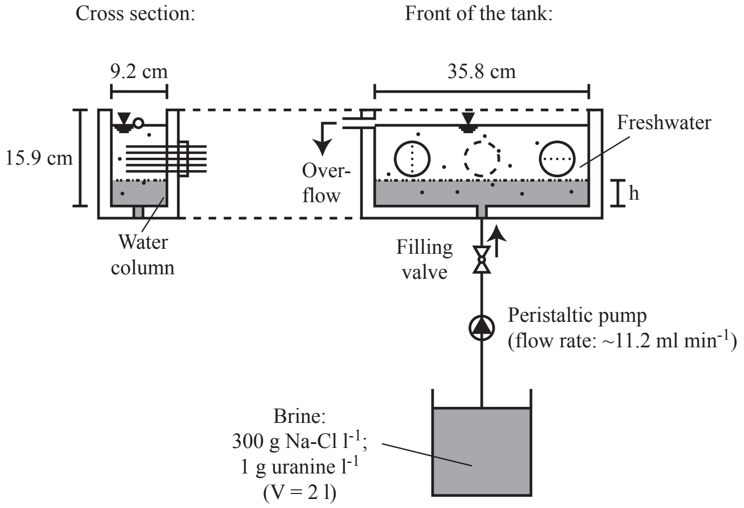

***Figure 5.5*** *Schematic view of the small container for testing different electrode arrays. h represents the height of the freshwater-saltwater interface above the inner side of the bottom plate.*

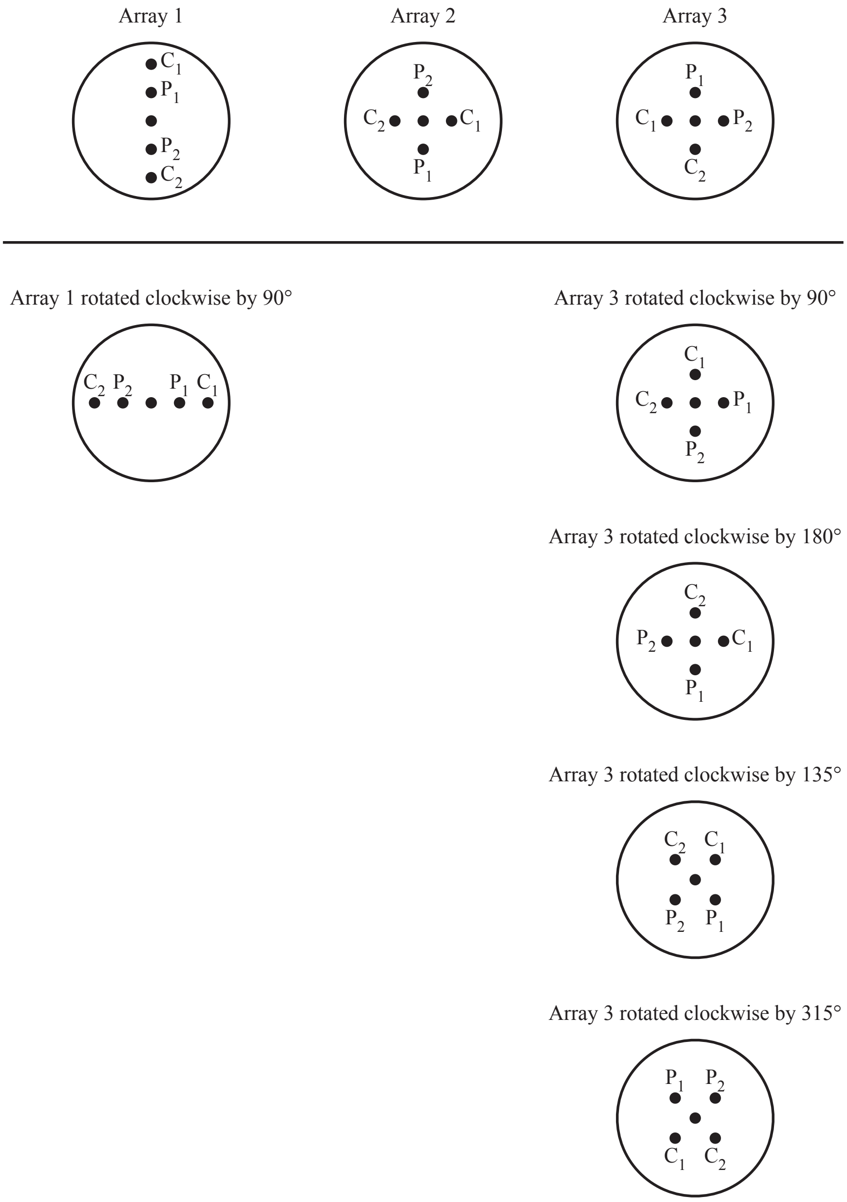
Array 1

Array 2

Array 3

Array 1 rotated clockwise by 90°

Array 3 rotated clockwise by 90°

Array 3 rotated clockwise by 180°

Array 3 rotated clockwise by 135°

Array 3 rotated clockwise by 315°

***Figure 5.6*** *Tested basic electrode arrays 1, 2, and 3. $C_1$ und $C_2$ represent the current electrodes, $P_1$ und $P_2$ the potential electrodes. The grounding electrode was placed in the center.*

porous medium through the hole (Ø 1 cm) in the center of the bottom plate. The outflow was led through an overflow (Figure 5.5). The inflow rate was set at ~11.2 ml min$^{-1}$. The difference in density between freshwater and brine amounts to ~0.2 g cm$^{-3}$. Therefore, buoyancy effects at the beginning of the tests caused the brine body to move laterally forming a horizontal planar freshwater-saltwater interface, which rose steadily upward during injection. The brine was dyed with uranine as the reddish color of the fluorescein at this concentration rendered it clearly visible in the pore water (Figure 5.4B). It was therefore possible to trace quantitatively the freshwater-saltwater interface during injection. As all RMC attachments are at the same height above the bottom plate, a comparison of the measurements of different electrode arrays was possible when the horizontal saltwater front was rising.

Three basic electrode arrays were tested as presented in Figure 5.6. In array 1 (cf. Figure 5.1), the five parallel electrodes were spaced uniformly in a plane. In another mounting, the two current and potential electrodes were arranged in a square with the grounding electrode in the center. In this mounting, the surrounding electrodes were spaced at 1 cm from the center electrode. Either the current electrodes ($C_1$, $C_2$) and the potential electrodes ($P_1$, $P_2$) were crossed to each other (array 2; Figure 5.6) or they were placed in parallel (array 3; Figure 5.6). For the basic array 1, the distance between the grounding electrode/lowermost electrode from the inner side of the bottom Plexiglas plate amounted to 7.8 cm and 5.8 cm, respectively. For the arrays 2 and 3, the distance between the grounding electrode/lowermost electrode from the inner side of the bottom plate amounted to 7.8 cm and 6.8 cm, respectively. Arrays 1 and 3 were also rotated around their own axis to study the measuring behavior when the saltwater front is approaching the measuring volume of an RMC from different sides. Here, array 1 was rotated 90° clockwise and array 3 was rotated 90, 135, 180, and 315° clockwise (Figure 5.6).

Four tests (A–D) were carried out with the following electrode arrays in the small container:

A) Array 1; array 1 rotated 90° clockwise

B) Array 2; array 3 rotated 90° clockwise

C) Array 3; array 3 rotated 180° clockwise

D) Array 3; array 3 rotated 135° clockwise; array 3 rotated 315° clockwise

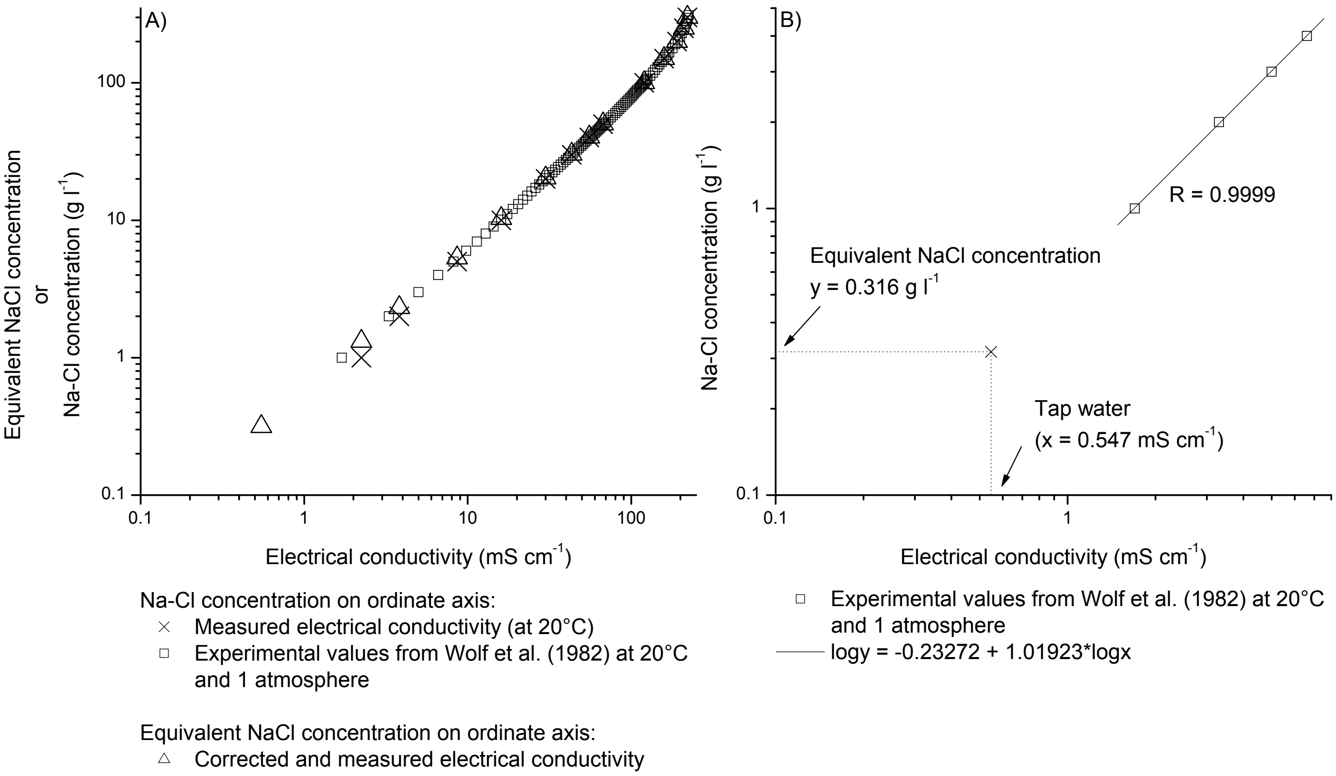

***Figure 5.7*** *A) Log-log plot of equivalent NaCl concentration or Na-Cl concentration versus electrical conductivity of standard measuring flow-thru cell: measured electrical conductivity (crosses), experimental data from Wolf et al. (1982) (open squares) and corrected and measured electrical conductivity (open triangles). Note that the measured electrical conductivity of 0 g l$^{-1}$ Na-Cl concentration is not represented as log0 = –∞. B) Linear regression line on linearized scale based on data by Wolf et al. (1982). R = correlation coefficient.*

Recording was performed by the data logger recording software ELCOL-1/-2 (cf. Table 5.1). Output voltage was conducted every minute; the height of the visible freshwater-saltwater interface (h) was determined regularly by naked eye in 3 of 4 tests (A–C).

## 5.4 Results

### 5.4.1 Calibration

The complexity of mathematical functions can be avoided by linearizing the relations (e.g., Yevdjevich, 1964). All measurements are thus presented on double logarithmic plots, which allow achieving a linear relationship up to high salt concentrations.

The measured electrical conductivity (symbol crosses) of the standard measuring flow-thru cell is presented in Figure 5.7A. The symbol of freshwater (electrical conductivity of 0.547 mS cm$^{-1}$ or Na-Cl concentration of 0 g l$^{-1}$, respectively) is not given in Figure 5.7A as the logarithm of 0 equals minus infinite.

To determine the equivalent NaCl concentration of the freshwater, experimental data (at 20°C, and 1 atmosphere) of electrical conductivity is also plotted as a function of Na-Cl concentration in Figure 5.7A (open squares). The missing equivalent NaCl background concentration of the measured electrical conductivity

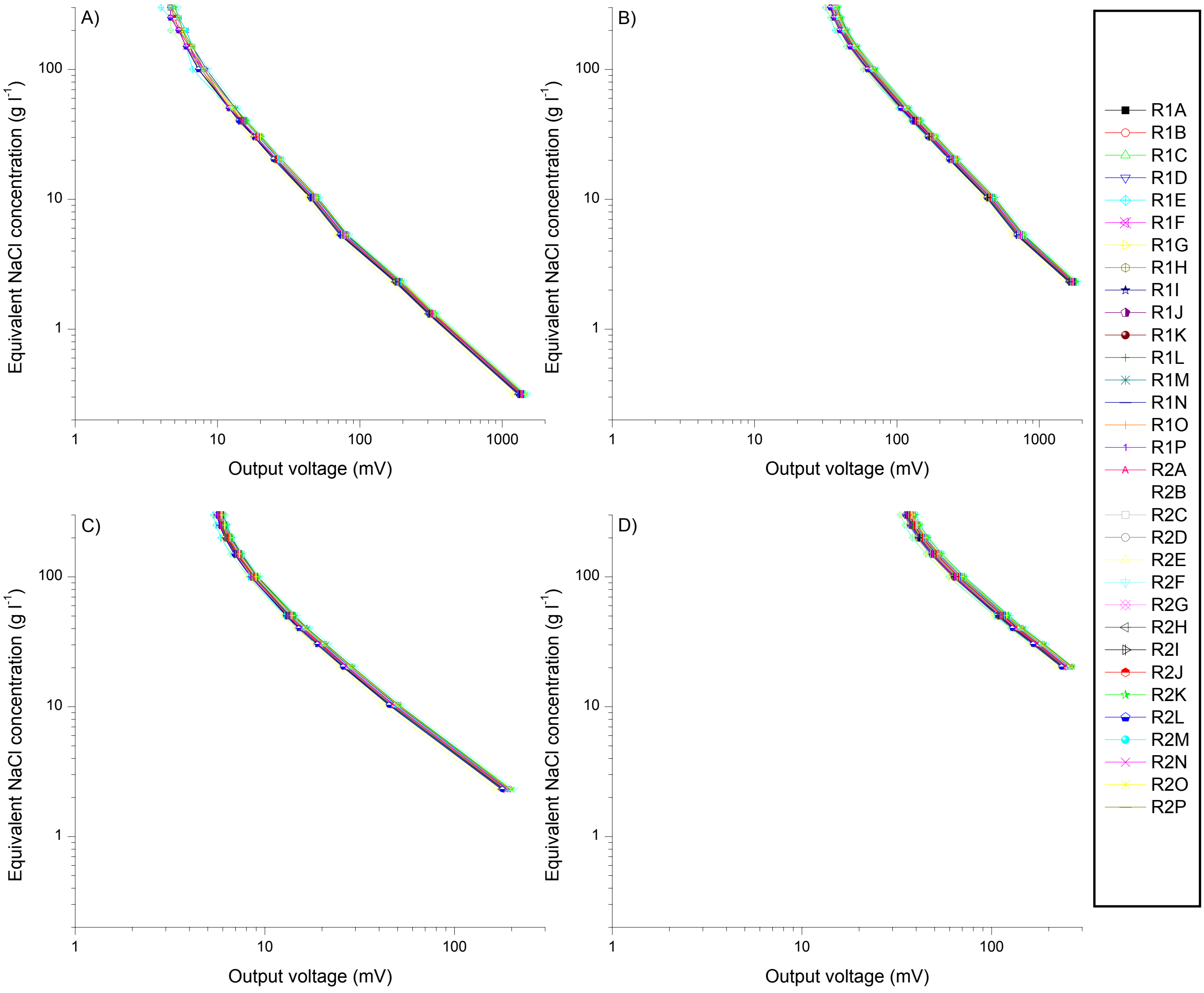

***Figure 5.8*** *Relation between output voltage and equivalent NaCl concentration for all resistance measuring cells, A) ELCOL-1, B) ELCOL-2, C) ELCOH-1, and D) ELCOH-2. Error bars showing standard deviation are included, however, they are smaller than the data points. It is important to note that this is a line + symbol plot (regression lines are not represented).*

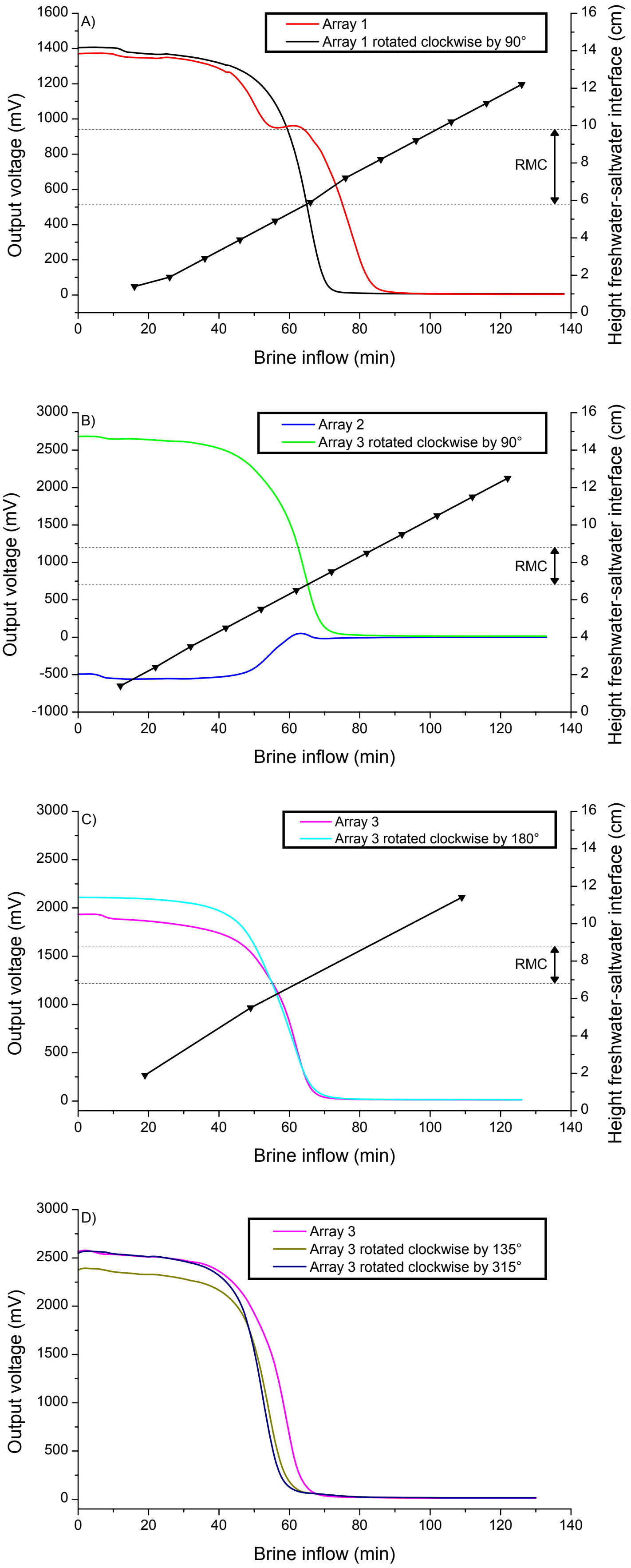

***Figure 5.9** Breakthrough curves of output voltage (A–D) and heights of freshwater-saltwater interface (closed triangles; A–C) observed in the small container tests.*

can be seen at lower Na-Cl concentrations, where the measured electrical conductivities are clearly lower than those of the experimental values from Wolf et al. (1982). To find the equivalent NaCl background concentration, the experimental values from Wolf et al. (1982) at solute concentrations 1.0, 2.0, 3.0, and 4.0 g l$^{-1}$, covering also the range of salt concentration at outflow measured in the experiments (Chapter 6), were fitted by a straight line (Figure 5.7B). The linear form of the equation is expressed as

$$\log y = A + B \cdot \log x \qquad (5.1)$$

where $y$ is the solute concentration of NaCl (g l$^{-1}$), $x$ the electrical conductivity (mS cm$^{-1}$) and $A$ and $B$ are cell constants. Eq. (5.1) can be transformed into a power-law form,

$$y = 10^{A + B \cdot \log x} \qquad (5.2)$$

Eq. (5.2) transformed again gives

$$y = 10^{A} \cdot 10^{B \cdot \log x} \qquad (5.3)$$

Substituting $a = 10^{A}$ and $x = 10^{\log x}$ in Eq. (5.3)

yields the power law

$$y = a \cdot x^{B}$$

where $a$ is a constant and $B$ a power exponent.

In the presented fit (Figure 5.7B), $a = 10^{-0.23} = 0.59$ and $B = 1.02$. If $x = 0.547$ mS cm$^{-1}$, $y = 0.316$ g l$^{-1}$. Therefore, the electrical conductivity of freshwater (equaling the initial electrical conductivity) is equivalent to a 0.316 g l$^{-1}$ Na-Cl solution. Adding 0.316 g l$^{-1}$ to the measured data with the standard conductivity measuring flow-thru cell, we obtain the corrected and measured electrical conductivity (open triangles) correlating well with the experimental data from Wolf et al. (1982) (Figure 5.7A). This linear relationship exists up to nearly a Na-Cl concentration of ~100 g l$^{-1}$. A curvilinear relationship above ~100 g l$^{-1}$ is obtained. Therefore, to calculate the Na-Cl concentration in the flow-thru cell (see Chapter 6), the following equation can be used:

$$y = 0.59 \cdot x_{m}^{1.02} - 0.316 \qquad (5.4)$$

where $x_m$ is the measured electrical conductivity.

Similar to Eq. (5.4), to calculate the solute concentration of NaCl of each RMC in the flow tank, the following equation is used:

$$y = a \cdot x_{ov}^{B} - 0.316$$

where $x_{ov}$ is the measured output voltage and $a$ and $B$

the cell/location constants. For each cell, a very strong negative correlation is found between log(equivalent NaCl concentration) and log(output voltage). As for the standard conductivity flow-thru cell there is a linear relationship up to ~100 g $l^{-1}$ and a curvilinear relationship above this amount (Figure 5.8).

For completeness sake, the measured breakthrough curves of output voltage are presented in the Appendices B.1.1–B.1.4 and the corresponding pore water temperature is given in Appendix B.1.5.

### 5.4.2 Electrode arrangement

In this pilot batch, the freshwater-saltwater interface developed very well into a horizontal plane with a transition zone that is ~1 cm thick (see Figure 5.4B).

The breakthrough curves of the output voltage and the measured heights are illustrated in Figure 5.9. The breakthrough curves of array 1 and array 1 rotated 90° clockwise clearly show the dependence of these alignments on the position of the saltwater front situated at the same distance from the grounding electrode (Figure 5.9A). There is a temporal shift between both curves, and array 1 even shows a temporarily constant value amidst a general decrease in output voltage. However, the rotated or not rotated array 3 reveals breakthrough curves far less dependent on the position of the saltwater front (Figure 5.9B, Figure 5.9C and Figure 5.9D). Furthermore, the measured output voltage in array 3 decreased continuously as soon as the current flowlines of the RMC, initially surrounded by freshwater (high resistivity), get in contact with the rising saltwater (low resistivity). A comparison of the output voltage measurements of arrays 1 and 3 with the corresponding measured heights of the freshwater-saltwater interface (Figure 5.9B and Figure 5.9C) reveals that the RMC measurements were influenced by the rising saltwater front at approximately h > 3 cm. Array 2 delivers no breakthrough curve (Figure 5.9B).

## 5.5 Discussion and conclusions

The calibration results of array 1 clearly reveal that calibration lines relating output voltage to equivalent NaCl concentration on double logarithmic plot can be used to convert output voltage measurements to local salt concentrations. Each RMC has to be calibrated in situ before starting an experiment. The tests also showed that array 3 is the most suitable and also less dependent on the position of the saltwater front (being at the same distance from the grounding electrode) than array 1. Array 2 is not suitable, as this configuration can only display unsymmetry effects of the liquid and the electrodes (E. Meier, 2007, personal communication).

Based on these facts, the electrodes were arranged as in array 3 (Figure 5.10) and the data logger recording software ELCONDU-1/-2 (see Table 5.1) was chosen for the first experiments in the flow tank (Chapter 6). Depending on the measured range of salt concentrations in an experiment 1–2 calibration lines have to be fitted for each RMC. The measuring volume of this RMC is estimated to be a volume of a circular right cylinder of ~3 cm radius with the axis corresponding to the grounding electrode.

A more detailed discussion of this measuring technique (array 3) is given in Chapter 6 documenting the results of three experiments conducted.

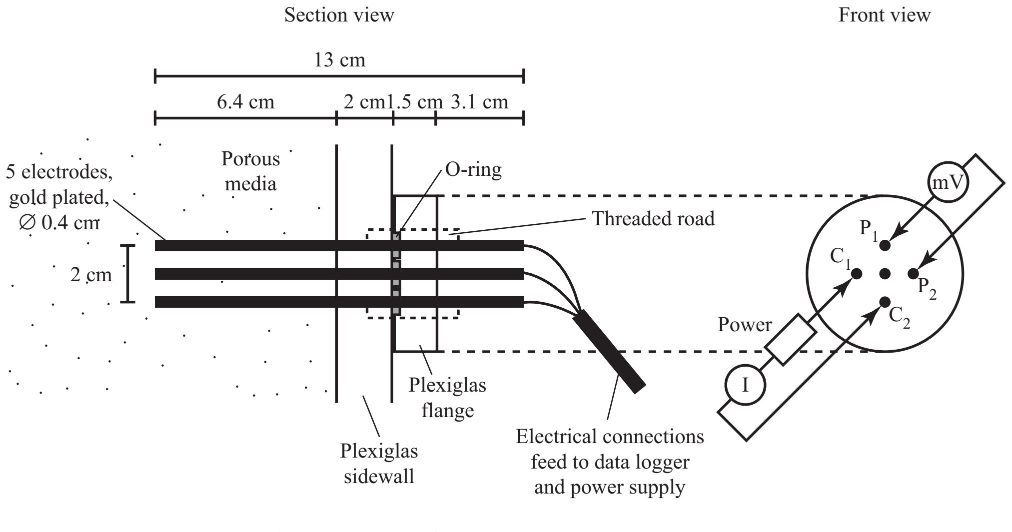

***Figure 5.10** Resistance measuring cell used in the first experiments (see Chapter 6). $C_1$ and $C_2$ represent the current electrodes, $P_1$ and $P_2$ the potential electrodes.*

## 5.6 References

Hassanizadeh, S. M., and A. Leijnse (1995), A non-linear theory of high-concentration-gradient dispersion in porous media, *Advances in Water Resources*, *18*, 203–215.

Silliman, S. E., L. Zheng, and P. Conwell (1998), The use of laboratory experiments for the study of conservative solute transport in heterogeneous porous media, *Hydrogeology Journal*, *6*, 166–177.

Telford, W. M., Geldart, L. P., and R. E. Sheriff (1990), *Applied geophysics*, Cambridge University Press, Cambridge.

Wolf, A. V., M. G. Brown, and P. G. Prentiss (1982), Concentrative properties of aqueous solutions: Conversion tables, in *Handbook of Chemistry and Physics*, 63th ed., edited by R. C. Weast, pp. D261–D262, CRC Press, Boca Raton, Florida.

Yevdjevich, V. M. (1964), Statistical and probability analysis of hydrologic data – Part II. Regression and correlation analysis, in *Handbook of applied hydrology*, edited by V. T. Chow, pp. 8.43–8.67, McCraw-Hill, New York.

# 6 Development of an intermediate scale 2D physical flow tank model to test a variable density flow model

## 6.1 Introduction

Strongly density-driven groundwater flow in aquifers may occur naturally or anthropogenically if for example the aquifer is hydraulically connected to fossil brine aquifers (e.g., Ma et al., 1997) or to geological salt deposits occurring as saltdomes (e.g., Klinge et al., 2002) or salt beds (e.g., Anderson and Kirkland, 1980).

In the Muttenz-Pratteln region, the evolution of the salt (Na-Cl) concentration in the Upper Muschelkalk aquifer could play a key role in the formation of interstratal evaporite karst caused by hydraulic connections between this karstic system and the large-scale groundwater pumping including the topography-driven regional groundwater circulation system (see Chapter 1). An understanding of the individual processes at relevant time scales is necessary to study this complex groundwater flow regime, including mixing and transport of dissolved NaCl in the main aquifer. A regional numerical model could be developed to predict the possible effect of the regional groundwater flow system on saltwater upconing. However, numerical simulation of strongly density-driven flow in pore aquifers is already a complex mathematical problem (e.g., Diersch and Kolditz, 2002), let alone in double-continuum media (conduit network and matrix) of karstic aquifers. Controlled laboratory experiments in porous media, designed as a test problem (benchmarking) for density-dependent flow computer codes, is an approach to solve this problem. Spatial flow and concentration data are much more accessible in the laboratory than in the field. Furthermore, laboratory studies are more suited for investigating basic concepts.

Oswald (1998) proposed a 3D physical benchmark (so-called saltpool experiment) for variable density flow in porous media. It consists of a 3D, time-dependent saltwater upconing process in a cubic box. The experimental setup comprises a cubic Plexiglas container of 20 cm side length filled with a homogeneous and saturated porous medium. At the beginning of the main experiments (see Oswald (1998) and Oswald and Kinzelbach (2004)), a stable layering of the saltwater (up to 107 g $l^{-1}$ of Na-Cl) was achieved below deionized and degassed freshwater, forming a narrow horizontal transition zone. At this initial stage, density contrasts amounted up to ~0.08 g $cm^{-3}$. Inflow and outflow occurred only via small holes in the opposite top corners of the test cube. The 3D salt concentration distribution, including its evolution in time, was determined by the Nuclear Magnetic Resonance Imaging (NMRI) technique. At the outflow opening, salinity breakthrough curves were measured on the basis of electrical conductivity. See Oswald (1998) and Oswald and Kinzelbach (2004) for a complete description of the conducted saltpool experiments. These provide reliable quantitative results for a 3D saltwater mixing process under density effects not available before Oswald's work (Diersch and Kolditz, 2002). This saltpool problem is currently well known and has been modeled by various authors but with varying success (Oswald, 1998; Ackerer et al., 2000; Diersch and Kolditz, 2002; Johannsen et al., 2002; Younes, 2003; Oswald and Kinzelbach, 2004). 2D and 3D presentations of distributed salt concentrations can be obtained with the NMRI technique, however, salt concentration breakthrough curves from within the salt upconing salt mass cannot be received.

We therefore developed a 2D flow tank allowing also to study and numerically model the saltwater upconing process. As in the saltpool experiment, a stable layering of saltwater below the freshwater was the initial condition achieved. Taking into account the rock salt (halite) dissolution process, a higher saltwater concentration (300 g $l^{-1}$) was chosen. Indirect solute concentration measurements were conducted with newly developed resistance measuring cells (see Chapter 5). With this technique, salt concentration breakthrough curves can be measured in the saline plume.

## 6.2 Overview of the 2D flow tank model

The schematic view of the experimental setup is illustrated in Figure 6.1 and Figure 6.2. The quasi-2D flow tank model containing a water-saturated porous medium is made of 2 cm thick Plexiglas plates and has an open top. The inner dimensions of the tank are 1.68 m long, 1.31 m high and 0.20 m wide. A vertical standing steel support girder was built around the center of the flow tank to avoid deflection of the front and back sidewall (Figure 6.2 and Figure 6.3C). The flow tank was built in such a way as to represent a vertical 2D cross-section of a porous aquifer in the flow direction with a thin third dimension.

Eight water-filled chambers on the left (inflow) and right (outflow) end of the tank placed at eight different levels provide flow control (Figure 6.3C and Figure 6.3E). The chambers were connected by rectangular openings (inlets $I_1$–$I_8$ and outlets $O_1$–$O_8$; numbered top down) to the porous medium. The inlets/outlets are 14.7 cm long and 4 cm high (Figure 6.1). The lower border of $I_1$ and $O_1$ is situated 11 cm above the inner side of the bottom Plexiglas plate. The vertical distances between adjacent lower borders of the inlets and between adjacent lower borders of the outlets are 11 cm, except between $I_4$ and $I_5$ and between $O_4$ and $O_5$, respectively, where the distance amounts to 14 cm. The inflow/outflow chambers were separated from the porous medium by fine-mesh nylon screens to prevent grains from washing out. At both ends of the tank, tubes connect the chambers with the freshwater inflow and saltwater outflow container (Figure 6.1 and Figure 6.3C). The water level in these two containers is maintained at a prescribed level defining the hydraulic boundary conditions. The water surface is free in the flow tank. During the experiments, a flow field was produced by applying a constant head gradient between the open inlets and open outlets. If several adjacent valves are open, they can buffer the effect of the inflow and/or outflow by redistributing the flow across the porous medium.

Since the indirect salt (Na-Cl) concentration measuring method (Section 6.2.1.1) is sensitive to temperature variations, tap water (hereafter referred to as “freshwater”) at controlled ambient temperature had to be supplied continuously to the freshwater inflow container. A water-heating system was therefore placed alternately in one of the two ~1600 l freshwater reservoirs (Figure 6.1 and Figure 6.3A). One of the two freshwater reservoirs was connected via a three-way valve to the intermediate ~200 l freshwater reservoir by a peristaltic pump (Figure 6.1 and Figure 6.3B). The intermediate freshwater reservoir was also connected to the freshwater inflow container. The setting up of an intermediate freshwater reservoir allowed the supply of a continuous, pulse free freshwater flow by gravity in the inflow freshwater container. Meanwhile, the twin freshwater reservoir was filled with freshwater from the water distribution network (12–13°C) and heated to ambient temperature (~21°C) by a heating rod coupled to a thermostat. During heating, the water was stirred by a motor-driven propeller-mixing device. The electrical conductivity (at 20°C) of the freshwater varied from about between 0.500 to 0.600 mS cm$^{-1}$.

The recharge reservoir, connected via a peristaltic pump and filling valve to the four equidistant holes (Ø 1 cm) at the bottom of the tank, was only used for tank preparation: either to fill the tank with freshwater or to calibrate the resistance measuring cells or to inject a brine into the tank.

### 6.2.1 Instrumentation

The instrumentation comprised resistance measuring cells combined with temperature sensors for determining indirectly solute concentrations of pore water, pressure transmitters to determine the hydrostatic pressure of pore water and/or indirectly the hydraulic head, and a standard conductivity flow-thru cell to measure indirectly solute concentration at the tank’s outflow. The effluent flow rate was measured by sampling water at free drain. Data was collected automatically at regular intervals using a data acquisition system.

#### 6.2.1.1 Solute concentration and temperature measurements of pore water

Laboratory-scale resistance measuring cells (RMCs) were used where electrodes were installed through the front Plexiglas plate in the porous medium. These cells were subject to relatively extensive development and testing to ensure their reliability with the salt concentration range measured during the experiments (for details, see Chapter 5). An RMC consists of five gilded stainless steel electrodes fitted through the front Plexiglas plate extending 6.4 cm into the porous medium perpendicular to the flow direction. The measuring volume of an RMC was estimated to amount to the volume of a circular right cylinder of ~3 cm radius. Calibration lines relating output voltage to equivalent NaCl concentration on double logarithmic plots were applied to convert output voltage measurements to local salt concentration measurements. Accuracy of this measuring technique is provided and discussed in the Chapter below.

Possible locations for RMCs were placed at 9.5 to 15.5-cm interval in horizontal (x direction) and vertical (z direction) direction, respectively. If Cartesian coordinates (x, z) are measured from the inner lower left corner of the tank, as shown in Figure

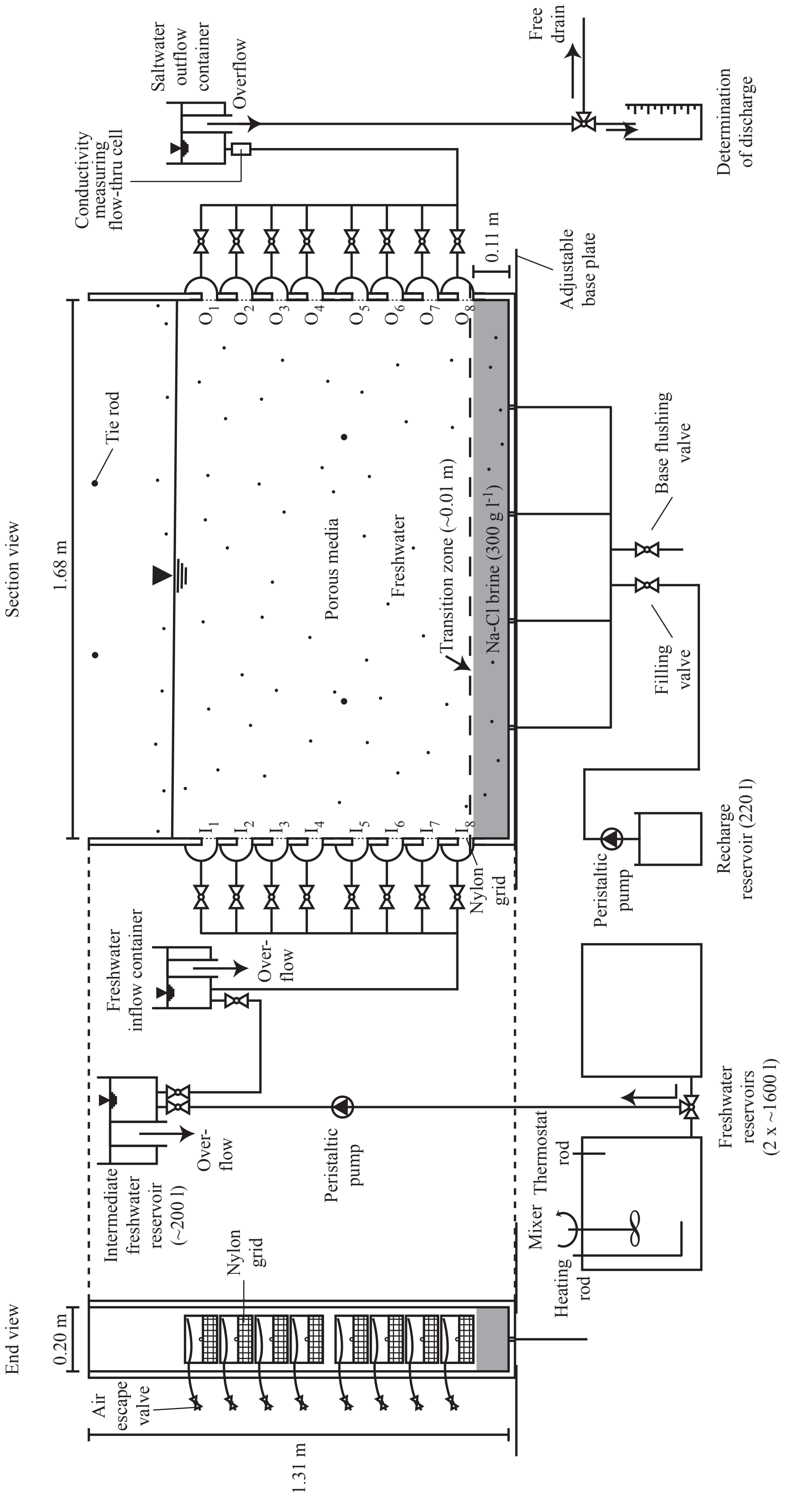

*Figure 6.1* *Diagrammatic plan of the 2D flow tank at the beginning of an experiment.*

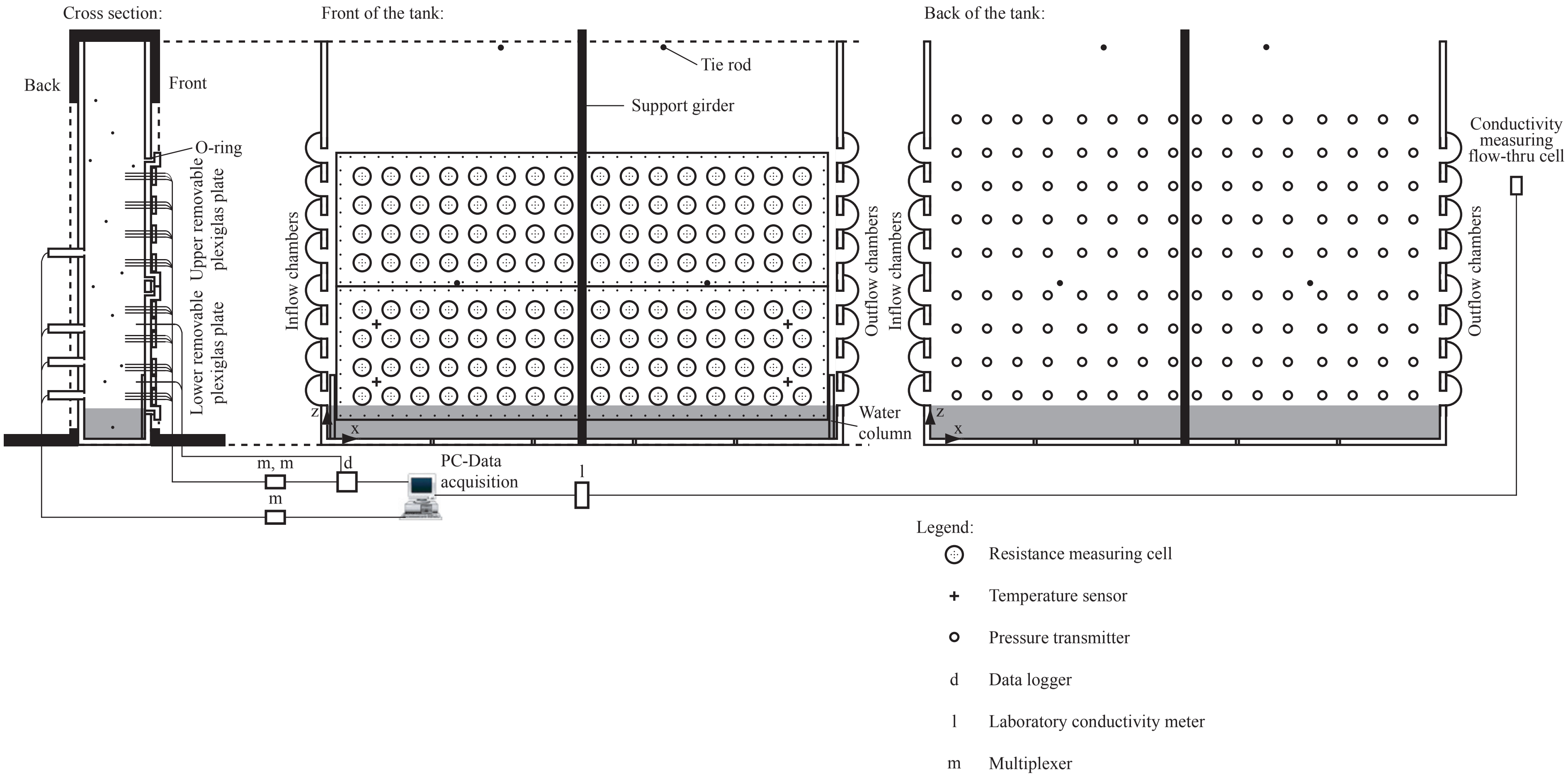

***Figure 6.2*** *Possible attachments for internal instrumentation in the flow tank: Resistance measuring cells and temperature sensors (front of the tank) and pressure transmitters (rear of the tank). The data acquisition system is presented schematically.*

***Figure 6.3*** *Photographs of the (A) two freshwater reservoirs with heating rod, thermostat rod and mixer, the (B) intermediate freshwater reservoir, the (C) front view of the 2D flow tank during an experiment, the (D) back view of the 2D flow tank with pressure transmitters, and (E) view of the outflow end.*

6.2, the vertical columns of possible measuring points were located at x = 11.5, 21.0, 30.5, 40.0, 49.5, 59.0, 68.5, 78.0, 90.0, 99.5, 109.0, 118.5, 128.0, 137.5, 147.0, and 156.5 cm. The horizontal rows of possible measuring points were located at z = 14.0, 23.5, 33.0, 42.5, 58.0, 67.5, 77.0, and 86.5 cm. Therefore, the tank theoretically allowed installation of 128 RMCs (16 columns × 8 rows) in the front plate.

As this measuring method is sensitive to temperature variations, YSI 4006 sensors were also fitted in the porous medium (for details, see Chapter 5) to control fluid temperature during experimental runs. The pore water temperature was measured with an error deviation of ±0.01°C. The four possible measuring points of the pore water temperature (see Figure 6.2): left down (x = 16.3 cm / z = 18.8 cm), middle left (16.3/37.8), right down (151.8/18.8), and middle right (151.8/37.8). The attachments not used were sealed by inserting stainless steel sticks.

#### 6.2.1.2 Pressure measurements of pore water

Highly accurate pressure transmitters (Keller AG model PR-35H/80797-0.1) to measure the pore water pressure in the tank were installed in the rear of the tank's Plexiglas sidewall (Figure 6.2 and Figure 6.3D).

Possible locations were placed lattice-like at 7.8 to 14.0-cm intervals in the horizontal and vertical direction, respectively. The columns of potential measuring points were located at x = 10.0, 20.0, 30.0, 40.0, 50.0, 60.0, 70.0, 80.0, 87.8, 97.8, 107.8, 117.8, 127.8, 137.8, 147.8, and 157.8 cm. The rows of possible measuring points were located at z = 13.0, 24.0, 35.0, 46.0, 60.0, 71.0, 82.0, 93.0, 104.0, and 115.0 cm. Thus, 160 (16 columns × 10 rows) pressure transmitters can be theoretically installed in the tank's rear side. Attachments not used for pressure transmitters were sealed by screw-in stoppers (see Figure 6.3D).

#### 6.2.1.3 Solute concentration and flow rate measurements at outflow

The breakthrough curve of the solute concentration was monitored at the tank's outflow by passing the total discharge through a calibrated (for details, see Chapter 5), standard conductivity flow-thru cell (WTW model TetraCon DU/T) connected to a laboratory conductivity meter (WTW model inolab Cond Level 2) (Figure 6.1, Figure 6.2, and Figure 6.3C). Electrical conductivity (at 20°C) was measured at ±0.5% error deviation.

The overflow from the saltwater outflow container is regarded as the total volumetric discharge rate through the tank. During an experiment, the volumetric discharge rate was determined by sampling one liter of water in a narrow-necked volumetric flask at free drain (Figure 6.1). Measurement accuracy amounted to about $\pm 0.012 \ \mathrm{l\ h^{-1}}$.

Integration of the breakthrough curves multiplied by the discharge resulted in about the total amount of dissolved salt mass discharged from the porous medium. The total flux of solute can be determined as follows:

$$M = \int Q(t) \cdot c_{out}(t) dt$$

where $Q$ is the average volumetric flux and $c_{out}$ the solute concentration of $Na^+$ and $Cl^-$ in the outflow.

#### 6.2.1.4 Data acquisition system

Simultaneous and continuous reading and registration of all the instruments was made possible by a computerized data acquisition system (Figure 6.2).

Two multiplexers with 16 channels each (Campbell Scientific Inc model AM16/32), a data logger (Campbell Scientific Inc model SC32A) and a multiplexer (manufactured by the Institut de Mécanique des Fluides et des Solides, Université Louis Pasteur) were used for data acquisition. The two AM16/32 and the data logger were controlled by Campbell Scientific Inc PC208W 2.3 software. The third multiplexer and the laboratory conductivity meter were controlled by the Agilent VEE Pro 6.01 software.

## 6.3 First solute transport experiments

Three experiments (named 2D_8/8h, 2D_8/2h and 2D_8/2s) on the variable-density flow and transport behavior were conducted for a stable layering situation prepared prior to starting the experiment by saltwater recharge containing $300 \ \mathrm{g\ l^{-1}}$ Na-Cl (thereafter referred to as "brine") from below forming a narrow transition zone (Figure 6.1 and Table 6.1). The names of the experiments indicate the following: 2D_8/8h refers to 2D experiment, all 8 valves of the inlets $I_1$–$I_8$ were open, all 8 valves of the outlets $O_1$–$O_8$ were open, *h* refers to high total hydraulic head difference, *s* to small total hydraulic head difference.

It was assumed that the lower boundary of the experimental scale corresponds to the top of a natural rock salt layer. Due to the fast halite dissolution kinetics (e.g., Alkattan et al., 1997), it can also be assumed

| | Experiment | | | |
|---|---|---|---|---|
| | 2D_8/8h | 2D_8/2h | 2D_8/2s | Error |
| Inlets | $I_1$ - $I_8$ | $I_1$ - $I_8$ | $I_1$ - $I_8$ | - |
| Outlets | $O_1$ - $O_8$ | $O_1$ - $O_2$ | $O_1$ - $O_2$ | - |
| Duration (d) | 2.00 | 18.98 | 25.85 | - |
| Initial inflow/discharge (l $h^{-1}$) | 27.9 | 27.3 | 14.2 | ±0.012 |

***Table 6.1*** *Specifications of the experiments.*

that water in contact with rock salt is always saturated with respect to halite (NaCl). However, to avoid halite precipitation in the tank, a brine concentration of 300 g $l^{-1}$ was chosen as it is close to the equilibrium concentration of $Na^+$ and $Cl^-$ with respect to halite (~0.95 saturation index) (e.g., Seidell, 1965) thereby resulting in a maximum density contrast of ~0.2 g $cm^{-3}$ during experiments.

Experiments 2D_8/2h and 2D_8/2s were conducted to simulate the vertical movement (upconing) of saltwater in a discharging well. Here the valves at the inlets $I_1$–$I_8$ (groundwater flow practically throughout the aquifer's thickness) and at the outlets $O_1$–$O_2$ (discharging well) were opened. In experiment 2D_8/8h, a complete well was simulated. Furthermore, these experiments served as a benchmark for numerical simulation of saltwater upconing in a porous medium. The experiments were simulated with a 2D variable density flow computer code, named TVDV-2D for Transport with Variable Density and Viscosity. The numerical model is based on mixed hybrid finite elements for flow and a combination of discontinuous finite elements for the convection part and mixed hybrid finite elements for the dispersion part of the transport equation. The density was set to vary linearly between freshwater and maximum saltwater concentration. For details see Younes (1998), Ackerer et al. (1999), and Younes et al. (1999).

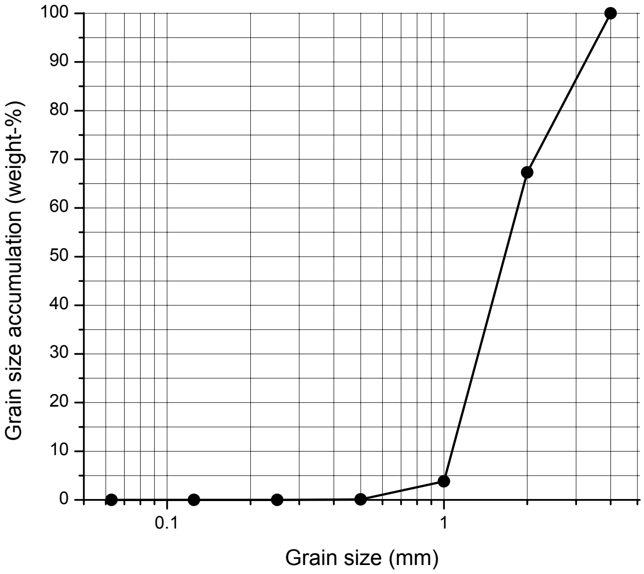

***Figure 6.4*** *Grain-size distribution of sand with fine gravel.*

The tank was packed with commercial quartz sand from the Rhine valley (Quartz d'Alsace, type K10, Kaltenhouse, France). To characterize the packed material and hydraulic properties of the porous medium, a grain size analysis was carried out in accordance with European Standard SN EN 933-1 (Figure 6.4). The material consists of ~67% coarse sand (0.6–2 mm diameter) with ~33% fine gravel (2–4 mm diameter). The uniformity index ($U = d_{60}/d_{10}$) is ~1.6 and the median grain size (mean particle diameter) is ~1.7 mm. However, this material also contains a small fraction of silt and clay. The total volume of recharged brine amounted to ~15 l (Table 6.3). The initial quantity of dissolved halite in the tank totaled ~4.5 kg.

Thirty-two RMCs, three temperature sensors, twelve pressure transmitters, and one standard conductivity measuring flow-thru cell were used for the experiments. The arrangement and labeling of the positioned RMCs and temperature sensors (T1, T2 and T3) are illustrated in Figure 6.5. The RMCs were distributed in or close to the area of the expected saltwater upconing during the experiments. Nine RMCs were placed on each of the lowest two RMC rows, six in the third row, three in the fourth row, two in the fifth row, and in each case one in the sixth to eighth row. The RMC columns were located at x = 21.0, 49.5, 78.0, 109.0, 118.5, 128.0, 137.5, 147.0, and 156.5 cm. The RMC rows were positioned at z = 14.0, 23.5, 33.0, 42.5, 58.0, 67.5, 77.0, and 86.5 cm. To label the location of the RMCs, we named them for example R1E. The letter at the beginning stands for the technique (R for resistance), the number refers to the RMC row counting bottom-up, and the end letter for the RMC column from left to right. By using this pattern, the variation in spatial distribution of solute concentration in the upconing saltwater mass can be followed temporally during an experiment. Comparable to the arrangement of the RMCs, the pressure transmitters were placed in the first row, two in the second row and in each case one in the third and fifth row. Indirect solute concentration of outflowing

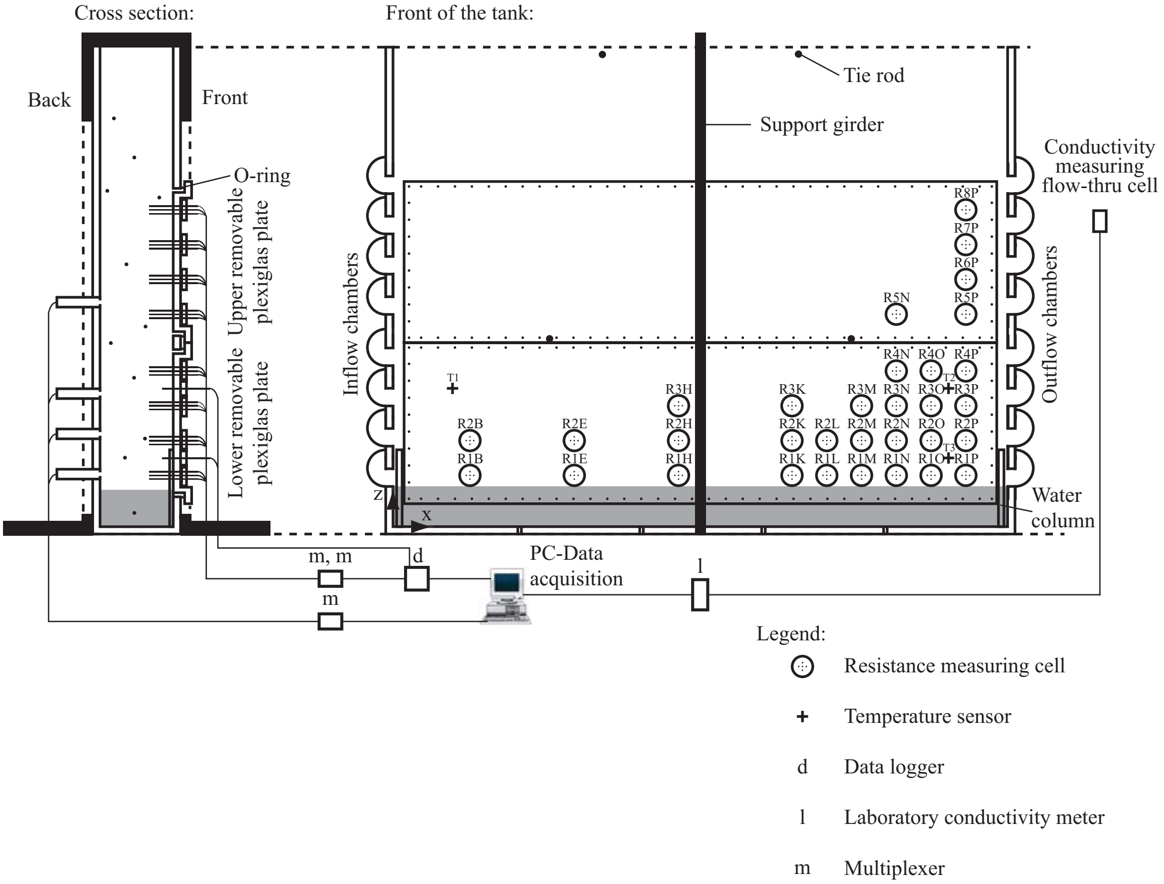

***Figure 6.5*** *Resistance measuring cells and temperature sensors positioned in the tank and data acquisition system.*

water was measured by a standard conductivity flow thru-cell and the discharged salt was determined together with the volumetric rate of discharge. The volumetric rate was determined several times daily.

An eight-step procedure was used for preparation and realization of an experiment.

1. *Positioning the cells/sensors and filling the tank with freshwater/sand* (the valves at the inlets $I_1$–$I_8$ and outlets $O_1$–$O_8$ and the filling valve were opened): the pressure transmitters were placed in position. The electrodes and the temperature sensors were inserted until the inner wall of the tank and fixed. Thus, the side plates were sealed and the electrodes/sensors were not entering the volume designated for the porous medium. Freshwater from the recharge reservoir was pumped into the empty tank through the four holes at the bottom of the tank. The wetted sand was sprinkled manually through standing water to avoid trapped air and thus ensure saturation of the porous medium. The sand compacted in ~10 cm thick layers formed a ~110 cm high homogenous and isotropic porous medium. The filling valve was subsequently closed and air escape valves were opened until the attached sideways chambers were completely filled with water. The electrodes and temperature sensors were finally inserted into the porous medium.
2. *Rinse out of fine-grained particles* (the valves at the inlets $I_1$–$I_8$ and outlets $O_1$–$O_8$ were opened; the outflow at the base flushing valve at the bottom of the tank was throttled): the tank was completely flushed with freshwater for several days to discharge fine-grained particles (silt, clay).
3. *In situ calibration of resistance measuring cells* (the filling valve and the valve at outlet $O_1$ were opened): the prepared calibration solutions (in sequential order from low-density to high-density) were injected into the porous medium by a peristaltic pump one by one through four equidistant holes (Ø 1 cm) in the bottom plate of the tank thus preventing instabilities and allowing a uniform filling of the pore space. The calibration procedure is presented in Figure 6.6 and Table 6.2 (during injection the pump was stopped once either overnight or on a weekend).
4. *Rinse out of salt*: the pore volume of the tank was thoroughly flushed with freshwater for several days until all RMCs and the standard measuring flow-thru cell indicated steadily freshwater.

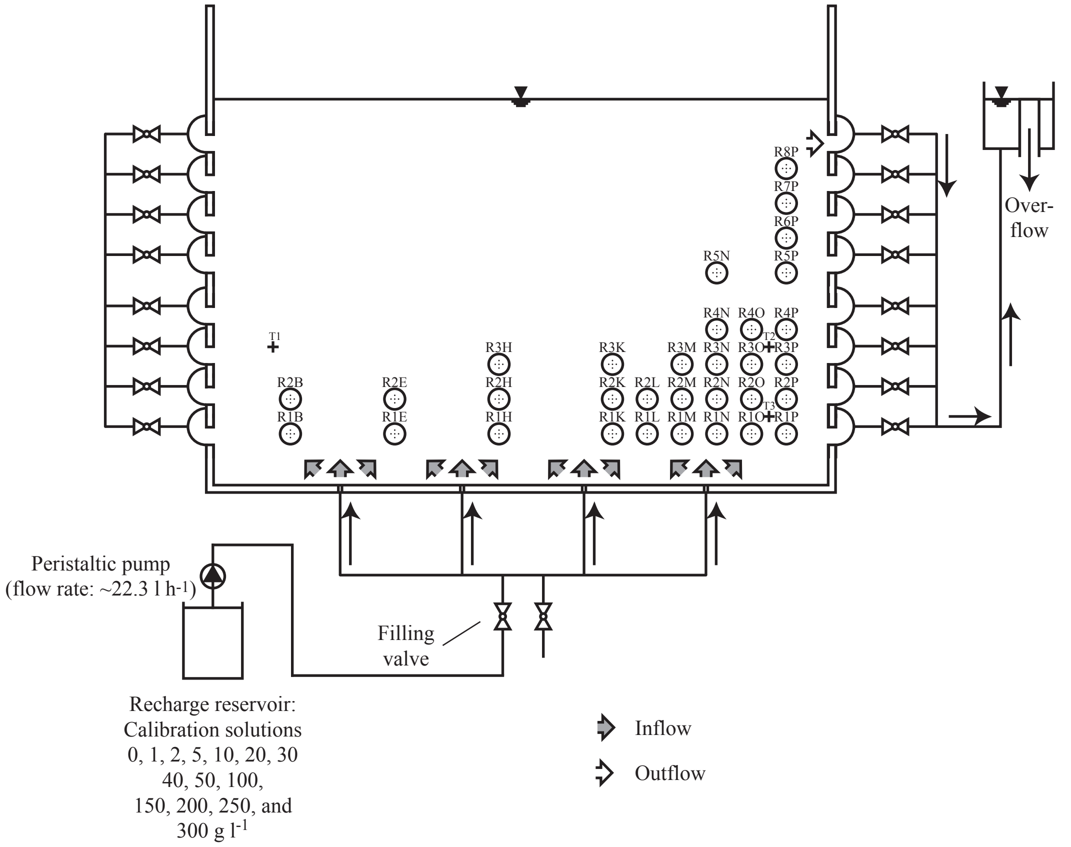

***Figure 6.6** Scheme of calibration of resistance measuring cells. Grey arrows indicate the spread of the injected calibration solutions.*

| Displaced calibration solution | Injected calibration solution | | Step 1 | | Step 2 | | Step 3 | | |
|---|---|---|---|---|---|---|---|---|---|
| | | | Pump on | Scan rate | Pump shutdown | Scan rate | Pump on | Scan rate | Mean inflow rate |
| $g\ l^{-1}$ | l | $g\ l^{-1}$ | h | min | h | min | h | min | $l\ h^{-1}$ |
| 0[a] | - | - | - | 6[b] | - | - | - | - | - |
| 0 | 216.8 | 1 | 4.90 | 6 | 13.33 | 133 | 4.69 | 6 | 22.61 |
| 1 | 216.3 | 2 | 5.02 | 6 | 14.15 | 133 | 4.73 | 6 | 22.18 |
| 2 | 216.6 | 5 | 5.00 | 6 | 14.05 | 133 | 4.89 | 6 | 21.90 |
| 5 | 219.0 | 10 | 5.02 | 6 | 61.95 | 133 | 4.53 | 6 | 22.93 |
| 10 | 216.2 | 20 | 5.00 | 6 | 14.75 | 133 | 4.35 | 6 | 23.12 |
| 20 | 216.6 | 30 | 5.00 | 6 | 13.22 | 133 | 4.55 | 6 | 22.68 |
| 30 | 216.0 | 40 | 5.00 | 6 | 14.25 | 133 | 4.63 | 6 | 22.43 |
| 40 | 216.6 | 50 | 5.00 | 6 | 62.42 | 133 | 4.54 | 6 | 22.70 |
| 50 | 136.7 | 100 | 6.22 | 6 | 12.75 | 133 | - | - | 21.98 |
| 100 | 136.4 | 150 | 6.25 | 6 | - | - | - | - | 21.82 |
| 150 | 136.6 | 200 | 6.23 | 6 | 11.12 | 133 | - | - | 21.93 |
| 200 | 136.7 | 250 | 6.04 | 6 | - | - | - | - | 22.63 |
| 250 | 136.0 | 300 | 6.13 | 6 | 11.17 | 133 | - | - | 22.19 |

[a] Pore water not displaced

[b] Measured during 6.70 h

***Table 6.2** Specifications of the RMCs calibration procedure.*

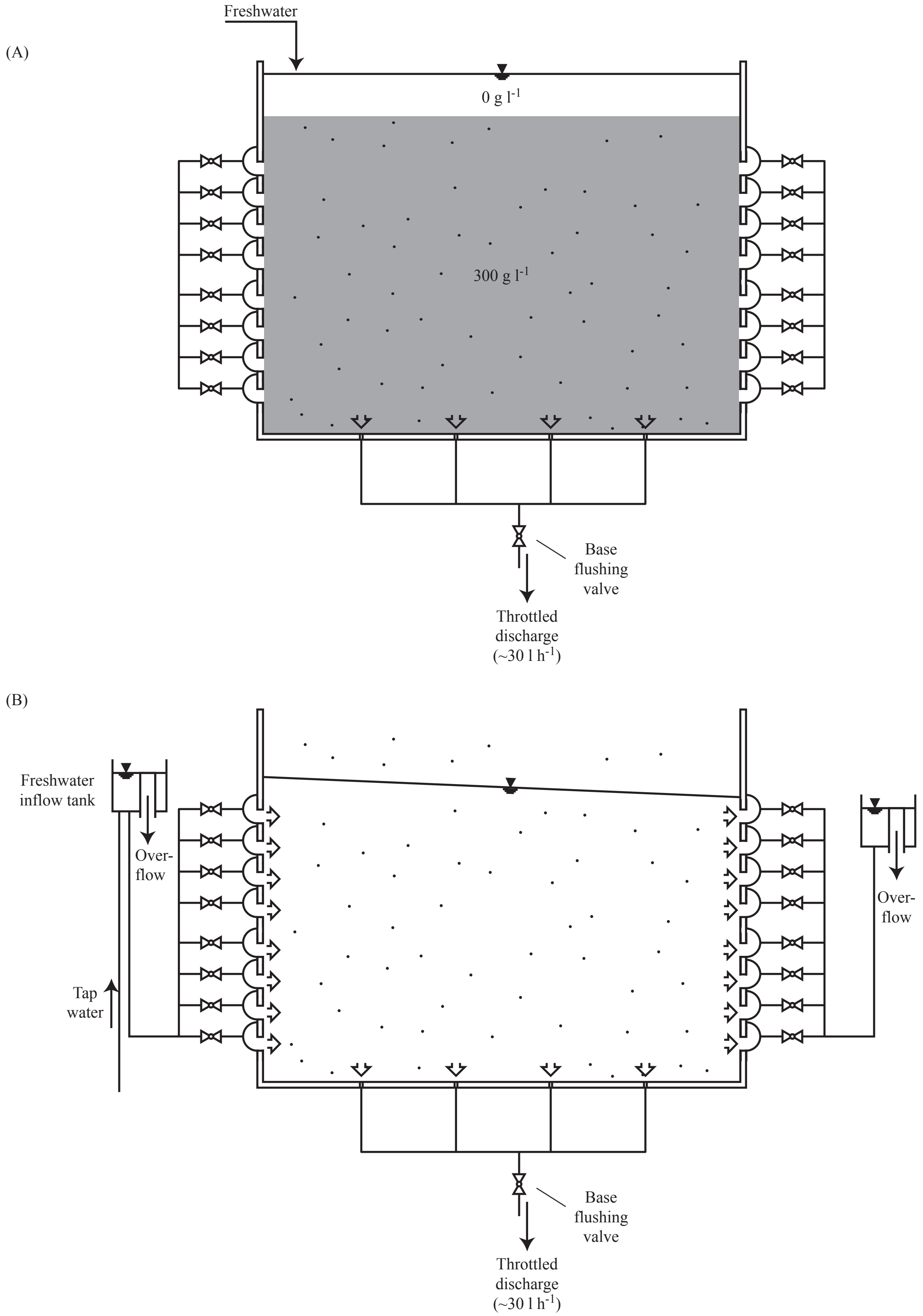

***Figure 6.7** Rinse out of salt: initially as presented in (A), subsequently as presented in (B).*

Here, first freshwater was filled uninterruptedly into the tank through the open top and saltwater flushed out continuously through the open base flushing valve (at ~30 l h$^{-1}$ throttled discharge) (Figure 6.7A). This activity was conducted for several hours until most of the dissolved salt was removed by top down flow (stable displacement). All the available valves at both ends of the tank

| | Experiment | | | |
|---|---|---|---|---|
| | 2D_8/8h | 2D_8/2h | 2D_8/2s | Error |
| **Brine injection** | | | | |
| Duration of inflow (h) | 6.35 | 6.39 | 6.39 | - |
| Average inflow rate (l $h^{-1}$) | 2.30 | 2.36 | 2.33 | ±0.03 |
| Volume of brine recharged (l) | 14.6 | 15.1 | 14.9 | ±0.2 |
| | | | | |
| **Stabilization of the brine layer** | | | | |
| Initial thickness of the brine layer (m) | 0.11 | 0.11 | 0.11 | ±0.005 |
| Duration (h) | 157.71 | 35.88 | 35.57 | - |

***Table 6.3*** *Specifications of the injections and local stabilization of the brine layer. All the cells were automatically and sequentially scanned every 6 min during pumping and every 133 min during the stabilization phase.*

($I_1$–$I_8$ and $O_1$–$O_8$) were subsequently opened and the outflow at the base flushing valve was further on throttled at ~30 l $h^{-1}$ (Figure 6.7B). This flushing lasted for several days. The two-step flushing procedure was conducted to reduce water degassing during flushing, as solubility of dissolved gas decreases with increasing salt concentration (salting out effect) (e.g., Harvie et al., 1984; Stumm and Morgan, 1996). Enhanced degassing can lead to the formation of gas bubbles and thus distort later experimental results.

5. *Total discharge adjustment* (the valves at the inlets $I_1$–$I_8$ and outlets $O_1$–$O_8$ were opened): the required discharge was adjusted by shifting the freshwater container vertically.
6. *Injection of the brine and ultimate stabilization of the brine layer*: the brine (300 g $l^{-1}$ dissolved NaCl) containing a small amount of uranine tracer (0.1 g $l^{-1}$) was injected slowly (~2.3 l $h^{-1}$) into the porous medium through the four holes at the bottom of the tank. The outflow was led through the outlet $O_1$. The upward movement of the upper horizontal limit of the brine body was traced visually along the transparent walls of the tank, as the yellowish color of the fluorescein-containing brine solution was slightly visible to the naked eye in the pore water. However, it was clearly visible in the two water columns at the inner side of the tank's front near each end of the tank (see Figure 6.2). (The water columns consisting of U-shaped Plexiglas profiles, 21 cm high, 1.5 cm wide and 1 cm deep, separated by fine-mesh nylon screens from the sand inflow). Injection was stopped at a final height of the brine body at ~0.11 ± 0.005 m. The filling valve was subsequently closed and, since no external flow was applied, the flow in the porous medium was driven entirely by free convection (stabilization phase of the brine layer). The specifications of this step are presented in Table 6.3.
7. *In situ calibration of pressure transmitters* (the valve at inlet $I_1$ was opened): the water level in the tank was set at the same level as in the freshwater inflow container. Each pressure transmitter was set to zero by a digital pressure indicator (Keller AG model EV-120).
8. *Experiment*: first inlet valves were opened and later the outlet valves. No further salt could enter the tank but only leave it via the open outlets (cf. Figure 6.1).

All three experiments were conducted with the same sand pack. Steps 4–8 were repeated for each new experiment. The experiments were conducted until a quasi-steady state of salt concentration was reached at the RMC-locations and at the outlet.

*These experiments required a great deal of preliminary work. Since experience with this new experimental setup was limited, potentially negative effects had to be determined first.*

*M. Konz (PhD thesis in preparation, 2008) conducted an additional experiment with open valves at the inlets $I_1$–$I_8$ and outlets $O_1$–$O_8$ and pores filled initially with undyed freshwater. In this experiment, uranine-dyed freshwater was recharged through the inlets $I_1$–$I_8$. In place of the expected more or less vertical tracer front above the level $I_8$ /$O_8$, an inclined tracer front was observed, thus, indicating a different hydraulic head at inlets $I_1$–$I_8$. This was attributed to the selected tube arrangement connecting the chambers with the inflow and outflow container (cf. Figure 6.1). M. Konz solved the problem by connecting in each case a tube directly from the freshwater inflow container to an inlet and repeated the procedure with the outflow end. Furthermore, he discovered that the porous medium was not homogeneous isotropic due to the calcareous deposits forming during periods when the tank contained a water-saturated porous medium.*

*Since the left boundary condition for flow and the porosity pattern in the tank are unknown, the results obtained cannot be used for benchmarking. Therefore, the three experimental (step 8) and the simulation*

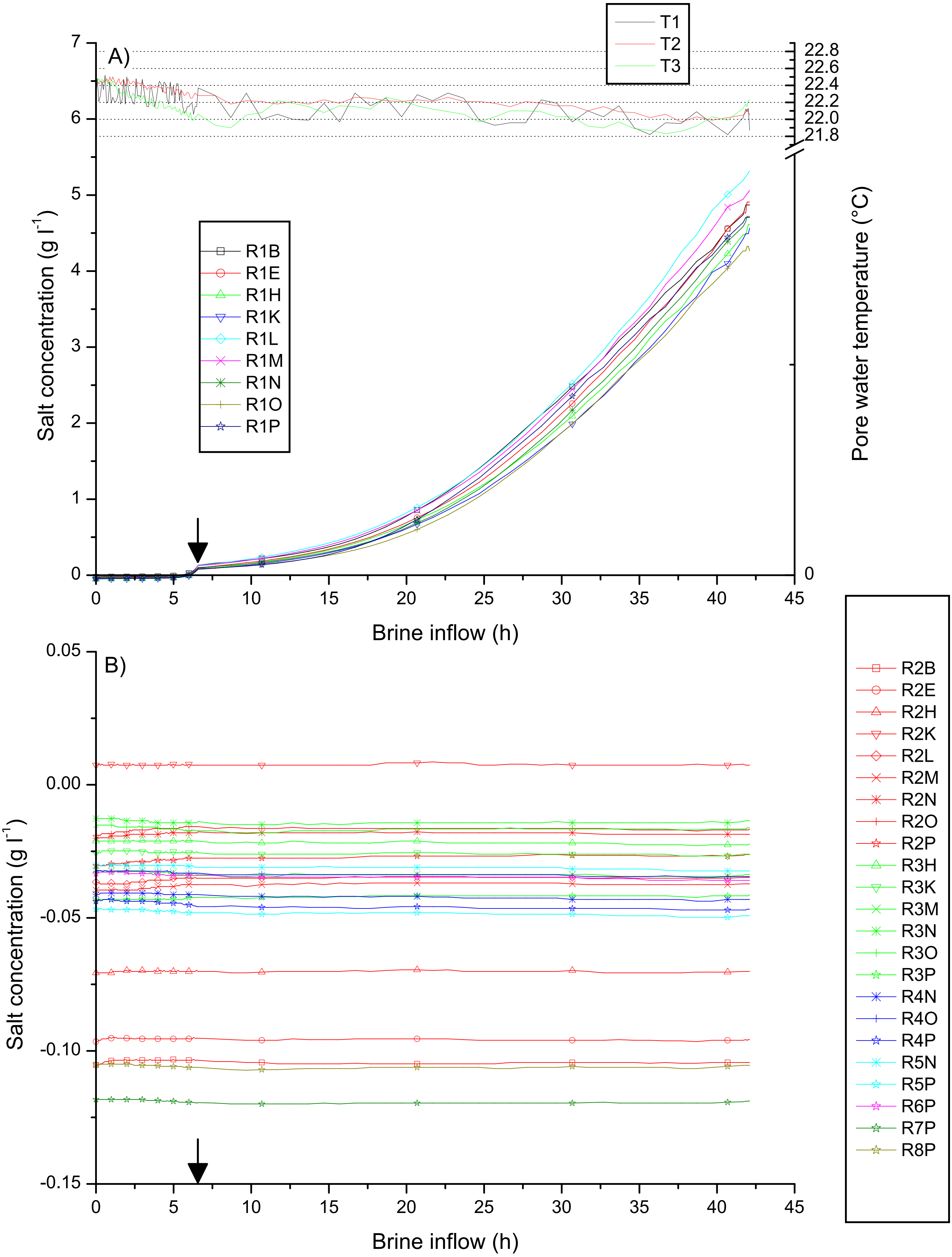

***Figure 6.8*** *Brine injection and stabilization (experiment 2D_8/2s): A) salt concentration versus time for first row. B) salt concentration versus time for 2nd–8th row. Every 10th salt concentration data point is displayed as a symbol. Arrows indicate time of pump shutdown.*

*results have not been included in this work. However, the observations during salt rinse out (step 4) and some results related to injection of the brine and ultimate stabilization of the brine layer (step 6) are presented and discussed. Furthermore, experiences with the resistance measuring technique, calibration (step 3) and long-term behavior if several experiments are conducted successively (steps 4–8) are also presented and discussed. The discussion also contains some remarks for future experiments and simulations.*

## 6.4 Observations and results

### 6.4.1 Rinse out of salt (step 4)

During salt rinse out, as illustrated in Figure 6.7A, fine-grained particles in the water-filled chambers at the inflow and outflow end were observed: first in the water-filled chamber at $I_1$ and $O_1$, then at $I_2$ and $O_2$ etc. up to $I_8$ and $O_8$. During subsequent flushing, as illustrated in Figure 6.7B, the fine-grained particles were gradually removed from the water-filled chambers.

### 6.4.2 Injection of the brine and stabilization of the brine layer (step 6)

The high-density contrast revealed that the brine (yellowish color) entering the porous medium had spread instantly in horizontal direction. The upper limit developed very well to a horizontal plane and over it a transition zone (only faintly yellowish in color) of ~1 cm thickness was observed (cf. Figure 6.1). Furthermore, the horizontal freshwater-saltwater interface plane was also confirmed by RMC measurements during the injection and stabilization phase, as the indirectly measured salt concentrations in the lowest RMC row were always within a narrow range. Figure 6.8 (experiment 2D_8/2s) is representative of the RMC measurements during the brine inflow and stabilization phase. In this experiment, first row concentrations of 4.8 ± 0.5 g $l^{-1}$ were measured at the end of the stabilization phase (Figure 6.8A). Form the second to the eighth row, no increasing salt concentrations were detected (Figure 6.8B).

### 6.4.3 Resistance measuring cells: calibration (step 3) and long-term behavior (steps 4−8)

The breakthrough curves of output voltage during calibration of the RMCs are presented in the Appendices B.2.1−B.2.2, and the corresponding pore water temperature is given in Appendix B.2.3. The resulting constant average output voltage values are plotted on log-log plots in Figure 6.9A and Figure 6.9B versus equivalent NaCl concentration. As derived in detail in Chapter 5 for the prototype of RMC, a very strong correlation was found for each RMC between log(equivalent NaCl concentration) and log(output voltage). To determine indirectly solute concentrations, 2 × 32 least-mean-square fits were fitted: for salt concentrations 0–5 g $l^{-1}$, measurements with ELCONDU-1 were used, higher salt concentration measurements with ELCONDU-2, which were fitted up to 60 g $l^{-1}$ (60 g $l^{-1}$ corresponds to the maximum indirectly measured concentration during experimental runs). The equation and correlation coefficients ($R \approx 0.999$) of the least-mean-square fits are listed in Table 6.4, which again clearly shows a high degree of linear correlation for each RMC. The pore water temperature variation during calibration amounted to 21.9 ± 0.6°C (Figure 6.9C). As regards the ionic conductivity, the sensitivity of the measuring method on pore water temperature variations is evident. A temperature increase leads to lower measured output voltages and higher calculated salt concentrations. A comparison of temperature curve progressions (Appendix B.2.3) and corresponding output voltage (Appendices B.2.1−B.2.2) reveals that the calculated salt concentrations increase per degree Celsius by ~0.15 to ~0.20 g $l^{-1}$.

The three aforementioned experiments were conducted in the following order: 2D_8/8h, 2D_8/2h and 2D_8/2s. To determine the quality of the RMCs over several successively conducted experiments, the measured average output voltage and related calculated salt concentration of each RMC in contact with freshwater are compared at initial calibration (step 3), before and after an experiment. In this case, “before an experiment” corresponds to the time before brine injection (step 6), and “after an experiment” corresponds to the time after the experiment (step 8) and ensuing rinse out of salt (step 4). Figure 6.10 represents this comparison:

- Experiment 2D_8/8h (Figure 6.10A and Figure 6.10D): the phenomenon of rinse out of fine-grained particles during step 4 (see Section 6.4.1) had no obvious impact on the output

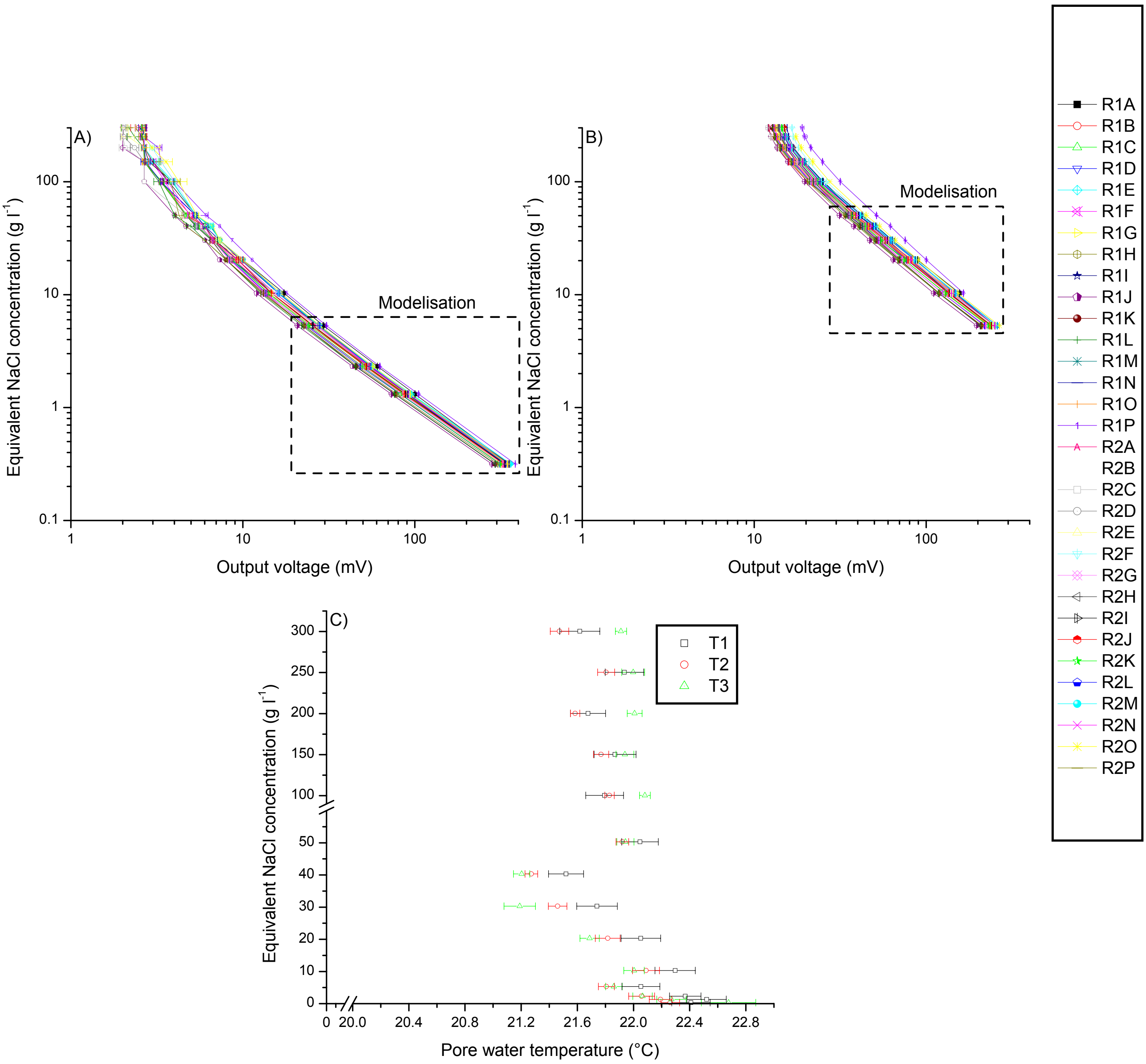

***Figure 6.9*** *Relation between output voltage and equivalent NaCl concentration for all resistance measuring cells: (A) data logger recording software ELCONDU-1 (cf. Table 1 in Chapter 5) and (B) data logger recording software ELCONDU-2. C) Temperature pattern during calibration. It is important to note that a line + symbol plot (no regression lines) are presented in (A) and (B). Error bars for standard deviation are included, however, in (A) and (B) they are smaller than the data points.*

voltage measurement. The maximum measured average output voltage difference for each RMC ranged between 13 and 27 mV, the related salt concentration difference between ~–0.008 and ~–0.07 g $l^{-1}$.

- Experiment 2D_8/2h (Figure 6.10B and Figure 6.10E): for each RMC, variation of the measured average output voltages was greater, mainly as regards RMCs R7P and R8P, revealing clearly different values after the experiment. The maximum measured output voltage difference for each RMC ranged between 2 and 149 mV, and the calculated salt concentration difference ranged between ~0.006 and ~–0.12 g $l^{-1}$.
- Experiment 2D_8/2s (Figure 6.10C and Figure 6.10F): after this experiment, the output voltage measurements and the calculated salt concentrations remained in the same range as after the experiment 2D_8/2h.

All the data in Figure 6.10D, Figure 6.10E, and

| Data logger recording software | ELCONDU-1 | | | ELCONDU-2 | | |
|---|---|---|---|---|---|---|
| Resistance measuring cell identification | Equation coefficients | | Correlation coefficient | Equation coefficients | | Correlation coefficient |
| | a | B | | a | B | |
| R1B | 284.70166 | -1.16979 | -0.99975 | 4729.33415 | -1.21326 | -0.99997 |
| R1E | 279.35085 | -1.19374 | -0.99984 | 3607.11510 | -1.17752 | -0.99980 |
| R1H | 230.31912 | -1.16157 | -0.99973 | 4852.88500 | -1.24995 | -0.99988 |
| R1K | 202.66558 | -1.14790 | -0.99957 | 4154.12920 | -1.23970 | -0.99989 |
| R1L | 249.00037 | -1.15362 | -0.99965 | 4766.50442 | -1.22548 | -0.99995 |
| R1M | 189.61819 | -1.12408 | -0.99969 | 4000.82910 | -1.23048 | -0.99982 |
| R1N | 221.33495 | -1.14310 | -0.99975 | 4251.57652 | -1.21846 | -0.99996 |
| R1O | 201.95286 | -1.12785 | -0.99973 | 3990.15715 | -1.21947 | -0.99974 |
| R1P | 205.77850 | -1.12191 | -0.99969 | 4039.52221 | -1.21376 | -0.99975 |
| R2B | 171.69593 | -1.13892 | -0.99973 | 3522.24856 | -1.23455 | -0.99977 |
| R2E | 212.97077 | -1.17691 | -0.99962 | 4161.98011 | -1.25025 | -0.99983 |
| R2H | 187.70680 | -1.14803 | -0.99979 | 4149.63597 | -1.25318 | -0.99979 |
| R2K | 237.59648 | -1.14932 | -0.99992 | 2943.54039 | -1.14338 | -0.99984 |
| R2L | 275.63223 | -1.18980 | -0.99976 | 5823.57939 | -1.26774 | -0.99995 |
| R2M | 233.92681 | -1.16668 | -0.99980 | 4194.59466 | -1.22371 | -0.99997 |
| R2N | 294.32015 | -1.16617 | -0.99965 | 11488.41195 | -1.37429 | -0.99979 |
| R2O | 209.00660 | -1.12381 | -0.99985 | 4213.47091 | -1.22196 | -0.99972 |
| R2P | 246.68344 | -1.17189 | -0.99980 | 5436.88316 | -1.26599 | -0.99967 |
| R3H | 240.85186 | -1.15407 | -0.99992 | 3453.34526 | -1.17222 | -0.99998 |
| R3K | 232.01710 | -1.14135 | -0.99990 | 4091.94700 | -1.20439 | -0.99994 |
| R3M | 252.76678 | -1.17855 | -0.99968 | 5054.17180 | -1.24686 | -0.99996 |
| R3N | 283.52411 | -1.18909 | -0.99979 | 5774.30873 | -1.26022 | -0.99992 |
| R3O | 184.20016 | -1.11430 | -0.99991 | 4289.53287 | -1.24324 | -0.99961 |
| R3P | 203.03457 | -1.16548 | -0.99973 | 4820.25485 | -1.28189 | -0.99980 |
| R4N | 222.71014 | -1.14808 | -0.99986 | 5502.11926 | -1.27065 | -0.99972 |
| R4O | 226.24553 | -1.15489 | -0.99982 | 4694.18282 | -1.24259 | -0.99980 |
| R4P | 216.58082 | -1.15936 | -0.99977 | 4364.85680 | -1.23974 | -0.99974 |
| R5N | 280.07220 | -1.18876 | -0.99984 | 4620.61730 | -1.21897 | -0.99997 |
| R5P | 257.01591 | -1.16230 | -0.99984 | 5110.46008 | -1.23913 | -0.99988 |
| R6P | 235.74908 | -1.15069 | -0.99982 | 4489.00408 | -1.22427 | -0.99981 |
| R7P | 284.87215 | -1.18653 | -0.99969 | 6155.45272 | -1.26669 | -0.99982 |
| R8P | 188.81218 | -1.14061 | -0.99987 | 3575.60882 | -1.21984 | -0.99977 |

***Table 6.4*** *Equation and correlation coefficients of the curve fittings.*

Figure 6.10F should reach an 0 g l$^{-1}$ value. Therefore, the average systematic error of all the calculated salt concentrations amounts to 0.04 g l$^{-1}$ with a maximum standard deviation of 0.02 g l$^{-1}$. With each additional experiment, accuracy of measurement decreased slightly. The standard deviation increased from 0.012 g l$^{-1}$ (experiment 2D_8/8h) to 0.025 g l$^{-1}$ (experiment 2D_8/2s).

## 6.5 Discussion and conclusions

### 6.5.1 Resistance measuring cell technique

The measured output voltage is a function of the porous medium type, porosity, pore water composition, temperature, and geometrical arrangement of the electrodes (see also Chapter 5). If all the factors, except the salt content of the pore water, are maintained constant and considering that the salt concentration is uniform throughout the entire RMC measuring volume, the measured output voltage can be related directly to the salt concentration of the solution. In this case, the total measurement error of an RMC is attributed to (1) instrument error, (2) calibration error (making calibration solutions, variation of pore water temperature during calibration, curve fitting), (3) variation of pore water temperature, and (4) variation in freshwater source composition. The most significant error is likely to be attributed to pore water temperature variation. During the experiments, higher flow velocities and/or flocculated/deflocculated particles (see Section 6.5.2) and/or gas bubbles could also be responsible for a slight decrease in time of RMC measurement accuracy. However, if all the calculated salt concentrations are corrected by the systematic error, accuracy of the concentration data is quite high. Since measurement accuracy can decrease during an experiment, all RMCs should be checked

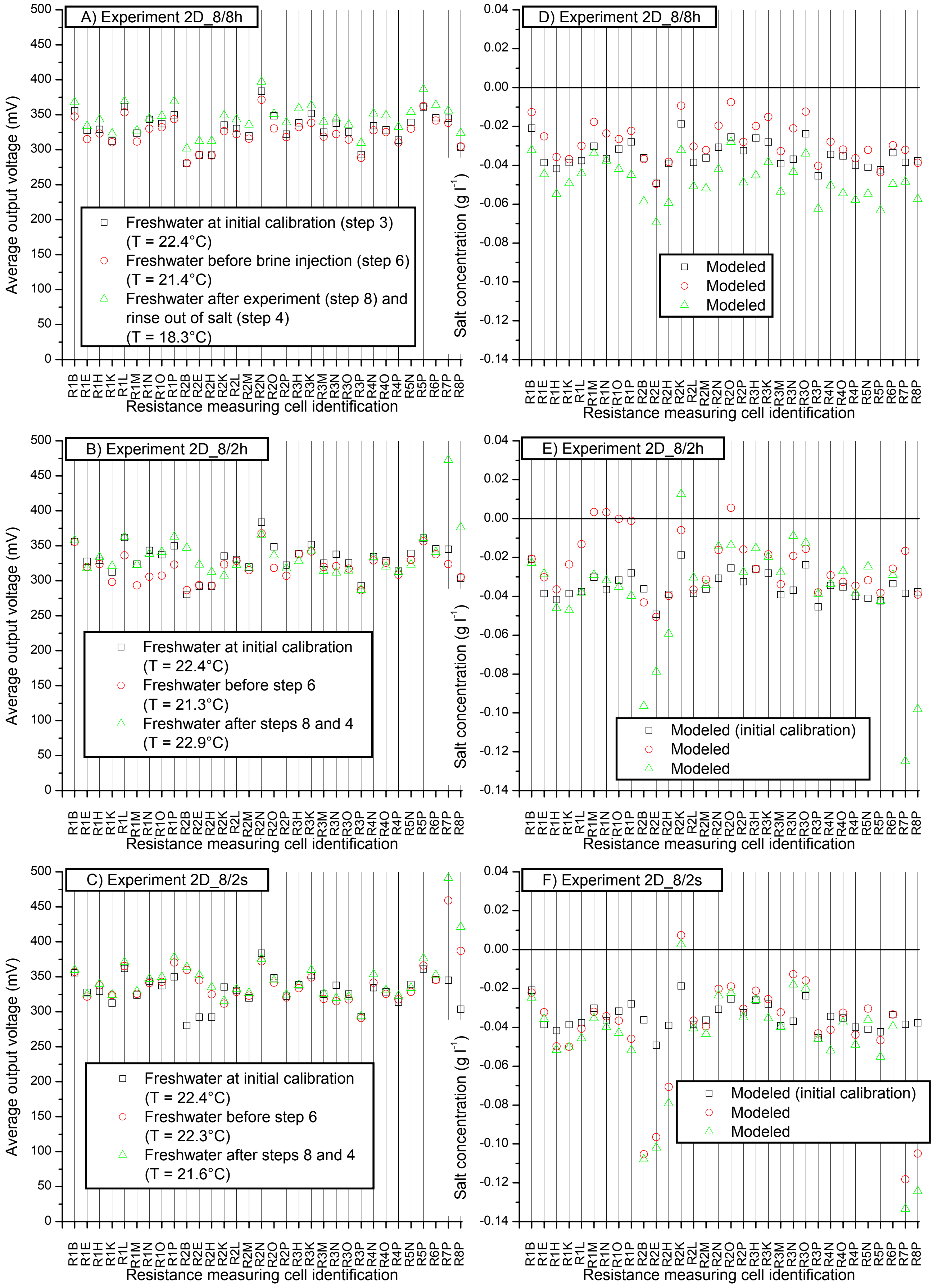

***Figure 6.10*** *Experiments 2D_8/8h, 2D_8/2h, and 2D_8/2s: average RMC values (A–C) and corresponding modeled salt concentrations (D–F) of the tank's freshwater during initial calibration (open squares), before brine injection (open circles) and after the experiment/rinse out of salt (open triangles).*

after each experiment as presented in Figure 6.10.

The developed method has the following advantages:

- It allows online, indirect and simultaneous measurements of salt concentrations up to saturation with halite at different points in the tank (in situ measurement) without significantly affecting the flow field during an experiment.
- If the salt concentration is uniform throughout the measuring volume, measurement accuracy is quite high.

Apart from a time-consuming calibration of each individual RMC, the main drawback of this measuring technique is the fact that the measurement error is not known if a salt concentration gradient occurs within the measuring volume or if a freshwater-saltwater interface intersects the RMC measuring volume. Therefore, additional (cf. Chapter 5) and extensive testing of the RMC should be conducted.

### 6.5.2 Experiences to be considered in follow-up experiments

This work includes many important findings dealt with in M. Konz's work (PhD thesis in preparation, 2008), which also contains further experimental modification attempts. If M. Konz's findings on the experimental setup are taken into consideration and if the measurement error of the RMC technique in solutions showing concentration gradients can be assessed, this newly developed experimental setup forms a good basis to finally obtain an excellent benchmark for testing density-dependent flow computer codes. In addition to data obtained from the saltpool experiments, a comparison can be drawn between the received breakthrough curves of salt concentrations at all RMC sites and the simulated data.

Based on our findings with the experimental setup and the first results, the following points have to be considered in future experiments:

- Porous medium: the rinse out of fine-grained particles from the tank during step 4 can lead to changes in the fluid phase composition. When saltwater flows through a porous medium, clay is found in a flocculated form and is fixed as a loosely built and permeable framework between the larger mineral grains. However, when freshwater flows through a porous medium, clay is deflocculated. Therefore, as the saltwater was gradually washed out by freshwater (cf. Figure 6.7A), clay started to deflocculate and the individual deflocculated particles were entrained by the fluid. This deflocculating effect is one of the basic phenomena of colloid chemistry (e.g., van Olphen, 1991). Consequently, individual deflocculated particles can also deposit as microscopic filter cakes on narrow-pore openings such as for example on the fine-mesh nylon screens at the outlets and may thus reduce the discharge considerably and distort the experimental results. For this kind of experiment and in agreement with M. Konz's findings, it is recommended to pack the tank for example with industrial glass beads instead of natural sand, and to use deionized (and degassed) water instead of tap water.
- Calibration solutions: depending on the range of expected solute concentrations during the experiments, only a few injected calibration solutions during step 3 would be sufficient, as the correlation between equivalent NaCl concentration and output voltage is very strong. This significantly advances RMCs calibration during tank preparation.
- Stabilization phase of the brine layer: with a high brine concentration, a stabilization phase of the brine after brine injection and start of the experiment is superfluous, as no additional time is necessary to allow stabilization of the brine layer. Furthermore, density effects limit mixing across the interface between freshwater and saltwater. This fact is also shown by the formula $2\sigma = 2\sqrt{2 \cdot D \cdot t}$, which allows to assess the mean diffusion length (e.g., Appelo and Postma, 1996). In this formula, $\sigma^2$ represents the variance of the distribution, $D$ the pore water diffusion coefficient and $t$ the time. With $D = 1.4 \times 10^{-10}$ m s$^{-1}$ (see below) and $t = 36$ h (cf. Table 6.3) the transition zone enlarged to ~3 cm, which correlates approximately with the measurements presented in Figure 6.8.
- Arrangement of pressure transmitters: the pressure transmitters can be used to measure the pore pressures in the tank; however, the hydraulic head can also be determined indirectly under certain conditions. To obtain the hydraulic head $h$, the measured pore water pressure has to be converted in pressure head. The hydraulic head $h$ (m) is represented by the sum of the elevation head $z$ (m) and the pressure head $P/\rho_w \cdot g$ (e.g., Dominco and Schwartz, 1998), i.e.

$$h = z + \frac{P}{\rho_w \cdot g} \tag{6.1}$$

where $P$ is the pressure (kg m$^{-1}$ s$^{-2}$), $\rho_w$ the fluid density (kg m$^{-3}$) and $g$ (m s$^{-2}$) the gravitational acceleration. However, if the pressure transmitters are in contact with saltwater (as in this work), hydraulic heads cannot be calculated as $\rho_w$ is unknown. For this kind of experiment, the pressure transmitters should, therefore, best be installed near the free water surface where they are in contact with freshwater and where the water flows in sub-horizontal direction. Therefore, considering $\rho_w$ = 996 kg m$^{-3}$ (e.g., Weast, 1982) and $g$ = 9.81 m s$^{-2}$ with Eq. (6.1) we obtain

$$h = z + \frac{P}{996 \cdot 9.81}$$

Elevation of the free surface can be determined and, based on Dupuit-Forchheimer's groundwater free surface approximation, also the total hydraulic head difference (hydraulic boundary conditions of the experiment). Based on the pressure transmitters measurements in this work and on experience with former laboratory experiments (F. Lehmann, 2004, personal communication), the error of $P/\rho_w \cdot g$ is about ±1 mm.

For numerical simulations, the model geometry would be that of a rectangle representing a longitudinal section of the tank. Except at the positions of flow through inlets/outlets, the lower and lateral borders of the tank would be maintained as no-flow boundaries.

The effects caused by dissolved salt entering into the chambers at the closed outlets (dead ends) can be neglected. If the measuring volume of an RMC is considered (see Chapter 5), all the calculated salt concentrations at each node point within each measuring volume can be averaged.

For this kind of experiment, the determination method for boundary and initial conditions as well as the parameters are given in Table 6.5. Focus is placed on the following points:

- *Boundary and initial conditions*: the hydraulic gradient can be determined as proposed above. At open inlets and initially above the brine layer, the salt concentration of freshwater amounts to 0 g l$^{-1}$. The thickness of the brine layer can be determined visually and its salt concentration is known at preparation.
- *Permeability*: permeability can be assessed by supplying flowing freshwater through the tank with open valves at the inlets $I_1$–$I_8$ and outlets $O_1$–$O_8$. By measuring the total discharge, cross-sectional area of flow and hydraulic gradient, and by taking freshwater density ($\rho$) and viscosity ($\mu$) from the literature (e.g., Weast, 1982), the intrinsic permeability ($k$) can be calculated by Darcy's law $K = QL/[A(h_1 - h_2)]$. In this formula the hydraulic conductivity of the medium ($K$) is proportional to the flow rate ($Q$) and length of the tank ($L$), and inversely proportional to the cross section

| | Unit | Means of determination |
|---|---|---|
| **Boundary conditions for flow** | | |
| Hydrostatic pressure at open inlets | m | Experimental |
| Hydrostatic pressure at open outlets | m | Experimental |
| **Boundary condition for transport** | | |
| Salt concentration of freshwater at open inlets | kg m$^{-3}$ | Defined |
| **Initial conditions for transport** | | |
| Salt concentration of freshwater | kg m$^{-3}$ | Defined |
| Salt concentration of brine | kg m$^{-3}$ | By making solution |
| Thickness of the brine layer | m | Visual measurement |
| **Parameter** | | |
| Permeability $k$ ($k_x/k_z = 1$) | m$^2$ | Estimation by calculation, literature |
| Porosity $w$ | - | By step 6 |
| Longitudinal dispersivity $\alpha_L$ | m | Literature |
| Dispersivity ratio $\alpha_T/\alpha_L$ | m | Literature |
| Pore water diffusion coefficient $D$ | m$^2$ s$^{-1}$ | Literature |
| Specifc storage | - | Negligence |

***Table 6.5*** *Boundary conditions, initial conditions and parameters for this kind of experiment.*

area ($A$) with different inlet and outlet hydraulic heads ($h_1$–$h_2$) and $K = k\rho g/\mu$. This derived value can also be compared with empirical equations used to assess permeability. The horizontal and vertical permeability ratio is estimated at $k_x/k_z = 1$.

- *Porosity*: the effective porosity of the grains can be assessed by $LWh/V$, where $W$ is the width of the tank, $h$ the height of the freshwater-saltwater interface above the inner side of the bottom plate plus half of the transition zone height, and $V$ the volume of brine recharged during step 6.
- *Dispersivities*: typical values for dispersivities at the pore-grain scale are $\alpha_L \approx d_{50}$ and $\alpha_L \approx 1/10\ \alpha_T$ (e.g., Spitz and Moreno, 1996).
- *Pore water diffusion coefficient*: the molecular diffusion coefficient of dissolved NaCl for the relevant molarities in water is quoted in the literature to range between $1.4 \times 10^{-9}$ and $1.5 \times 10^{-9}$ m$^2$ s$^{-1}$ at 20°C (Zaytsev and Aseyev, 1992). The diffusion coefficient at such a pore-grain scale is about 10 times smaller or ~$1.4 \times 10^{-10}$ m$^2$ s$^{-1}$ (P. Ackerer, 2004, personal communication) due to collision with the solids of the medium.

## 6.6 References

Ackerer, Ph., A. Younes, and R. Mose (1999), Modeling variable density flow and solute transport in porous medium: 1. Numerical model and verification, *Transport in Porous Media*, *35*, 345–373.

Ackerer, P., A. Younes, S. E. Oswald, and W. Kinzelbach (2000), On modeling of density driven flow, in *Calibration and reliability in groundwater modeling*, *Proceedings of the ModelCARE99 Conference*, 265, edited by F. Stauffer et al., pp. 377–384, IAHS Publ., Zurich.

Alkattan, M., E. H. Oelkers, J.-L. Dandurand, and J. Schott (1997), Experimental studies of halite dissolution kinetics, 1 The effect of saturation state and the presence of trace metals, *Chem. Geol.*, *137*, 201–219.

Anderson, R. Y., and D. W. Kirkland (1980), Dissolution of salt deposits by brine density flow, *Geology*, *8*, 66–69.

Appelo, C. A. J., and D. Postma (1996), *Geochemistry, groundwater and pollution*, A. A. Balkema, Rotterdam.

Diersch, H.-J. G., and O. Kolditz (2002), Variable-density flow and transport in porous media: approaches and challenges, *Advances in Water Resources*, *25*, 899–944.

Dominco, P. A., and F. W. Schwartz (1998), *Physical and chemical hydrogeology*, John Wiley & Sons, New York.

Harvie, C. E., N. Møller, and J. H. Weare (1984), The prediction of mineral solubilities in natural waters: The Na-K-Mg-Ca-H-Cl-$SO_4$-OH-$HCO_3$-$CO_3$-$CO_2$-$H_2O$ system to high ionic strengths at 25°C, *Geochim. Cosmochim. Acta*, *48*, 723–751.

Johannsen, K., W. Kinzelbach, S. Oswald, and G. Wittum (2002), The saltpool benchmark problem – numerical simulation of saltwater upconing in a porous medium, *Advances in Water Resources*, *25*, 335–348.

Klinge, H., K. Schelkes, A. Rübel, A. Suckow, F. Schildknecht, and R. Ludwig (2002), The saltwater/freshwater regime in the sedimentary cover of the Gorleben Salt Dome, *Transport in Porous Media*, *47*, 125–148.

Ma, T. S., M. Sophocleous, Y.-S. Yu, and R. W. Buddemeier (1997), Modeling saltwater upconing in a freshwater aquifer in south-central Kansas, *J. Hydrol.*, *201*, 120–137.

Oswald, S. E. (1998), Dichteströmungen in porösen Medien: Dreidimensionale Experimente und Modellierung, PhD thesis, ETH Zürich.

Oswald, S. E., and W. Kinzelbach (2004), Three-dimensional physical benchmark experiments to test variable-density flow models, *J. Hydrol.*, *290*, 22–42.

Seidell, A. (1965), *Solubilities inorganic and metal-organic compounds*, vol. II, 4th ed., edited by W. F. Linke, pp. 958–959, Am. Chem. Soc., Washington, D. C.

Spitz, K., and J. Moreno (1996), *A practical guide to groundwater and solute transport modeling*, John Wiley & Sons, New York.

Stumm, W., and J. J. Morgan (1996), *Aquatic chemistry*, *Chemical equilibria and rates in natural waters*, 3rd ed., John Wiley & Sons, New York.

van Olphen, H. (1991), *An introduction to clay colloid chemistry*, John Wiley & Sons, New York.

Younes, A. (1998), Modélisation de l'écoulement et du transport de masse en milieu poreux avec les éléments finis mixtes et discontinus - prise en compte du contraste de masse volumique et de viscosité, Thèse de Doctorat de l'Université Louis Pasteur, Institut de Mécanique des Fluides et des Solides, Strasbourg, France.

Younes, A. (2003), On modelling the multidimensional coupled fluid flow and heat or mass transport in porous media, *International Journal of Heat and Mass Transfer*, *46*, 367–379.

Younes, A., Ph. Ackerer, and R. Mose (1999), Modeling variable density flow and solute transport in porous medium: 2. Re-evaluation of the salt dome flow problem, *Transport in Porous Media*, *35*, 375–394.

Weast, R. C. (ed.) (1982), *Handbook of Chemistry and Physics*, 63th ed., CRC Press, Boca Raton, Florida.

Zaytsev, I. D., and G. G. Aseyev (Eds.) (1992), *Properties of aqueous solutions of electrolytes*, CRC Press, Boca Raton, Florida.

# 7 Conclusions and perspectives

## 7.1 Summary

The main objectives of this thesis were to investigate (1) the genesis and shape of natural, deep-seated, non-accessible cavities within salt deposits, (2) the genesis of an unusual horizontal fracture-guided passage with tip-down cavity cross-section encountered mainly in gypsum caves, (3) the genesis of an interstratal salt karst at the top of a salt layer, and (4) to test a density-dependent flow computer code. An experimental approach was selected to meet all these objectives.

The genesis and shape of natural solution cavities within a salt body was studied by an experimental lab setup, where freshwater was slowly pumped into rock salt cores through a horizontally oriented borehole (Chapter 2). Eight dissolution runs at two different average inflow rates were conducted. The dynamics of concentration-driven turbulent buoyant flow coupled with salt dissolution was thereby visualized by the fluorescent property of uranine. The results revealed that due to slow inflow rate, as well as fast halite dissolution kinetics and its extremely high solubility, halite dissolution took place only in the inflow of the rock salt cylinders. The shape of the small-scale solution cavities created is roughly a symmetrical half of a cone with a horizontal base facing upward. It can be concluded that halite dissolution took place at the horizontal ceiling and upper end of the facet. The cavities therefore enlarged simultaneously at the horizontal ceiling by upward and lateral growth at the upper end of the facet. A theoretical analysis was subsequently conducted to describe the cavity enlargement mathematically. The computed variables are quite consistent with the experimental results. Moreover, the experimental results concur qualitatively with natural and man-made salt cavities on a field scale. Solution cavities of triangular prism or conical shape may develop if a fracture or conduit, respectively, provides a communication between a confined undersaturated water aquifer and an overlying salt body. Such a cavity enlargement may cause land subsidence or collapse structures.

Due to similarities between small-scale salt and natural gypsum solution cavities, the formation of fracture-guided gypsum cave passages with tip-down triangular cross-section is derived from knowledge from rock salt dissolution experiments, because none of the existing conceptual models provide a satisfactory explanation of the genesis of such natural caves (Chapter 3). According to the new data, the newly developed experimental setup is of key importance, as the resulting, small-scale solution cavities revealed qualitatively the same morphological symmetry with a horizontal ceiling covered by solution pits and narrow-ranged facet inclinations as that observed in natural gypsum caves. A comprehensive conceptual model in a regional hydrogeological context is provided based on the existing models, on the new experimental data and on theoretical, hydrogeochemical analysis. Generally, as described in the previous chapter, the same genesis model can be applied to such gypsum caves. Therefore, such a passage starts to develop from the upper end of a permeable fracture, providing a communication to a confined underlying, gypsum-depleted water aquifer with its potentiometric surface above the developing passage. Since the aquifer is under pressure, a buoyant turbulent cycle develops in the fracture/cavity void, where the gypsum dissolution at the upper limit of the developing cavity supplies the density gradient that becomes the driving mechanism for its own dissolution. Since a stable fluid density interface is horizontal and, in this case, close to the upper limit of the developing cavity, the formed ceiling must also be horizontal. If the cavity is situated in the epiphreatic or vadose zone, this triangular morphology is an indicator for paleohydrogeology.

Two types of rock salt dissolution experiments were conducted to investigate the subrosion process at the top of a salt layer in a horst and graben structure, such as for example in the Muttenz-Pratteln region (Chapter 4). Freshwater was slowly pumped from above into the rock salt cores through an axial, nearly vertical or inclined-oriented borehole. In these experiments, the upper end of the core cylinder represented the top of a salt layer situated below a covering layer. Furthermore, the supply of NaCl-undersaturated water flowed through a pipe and not through a more realistic linear input (permeable fault). Under different inclinations of the top of the salt layer, one type of experiment simulated groundwater flow and salt dissolution at a 2D, the other at a more realistic step like 3D top of a salt layer. Six dissolution runs were conducted totally. In some, the flow field and cavity genesis was visualized by fluorescent uranine. The close correlation of the experimental solution cavities and cavity geometries in the field indicates at first the development of an interstratal salt karst along the top of the rock salt layer mainly in the up-dip direction. When in contact with a poorly soluble layer or displaced salt layer (i.e., at a fault), the solution cavity mainly broadens downward or upward, respectively, leading to a fault-associated solution cavity section possibly exhibiting a larger cavity height. Elongated subsidence bowls parallel to the fault system may be related to underlying, fault-bound solution cavities.

For the solute transport experiments in a laboratory flow tank containing a water-saturated porous medium, an adequate non-commercial measuring technique (resistance measuring cell) was developed in collaboration with Edi Meier + Partner AG to measure in situ and indirectly solute concentrations of Na-Cl over a wide range (Chapter 5). Three basic electrode arrays were tested by pumping calibration solutions or a high-density brine bottom-up into one of two different flow tanks. One suitable array comprises five electrodes fixed in parallel on a plane. The grounding electrode is thereby located in the center, flanked by two potential electrodes and an outer pair of current electrodes. Another suitable array consists of electrodes arranged in a square (current electrodes and potential electrodes placed in parallel) with the grounding electrode in the center. The analysis revealed that calibration lines can be used in both cases to convert output voltage measurements to local salt concentrations. The second array mentioned is even more suitable as it is less dependent on the position of a saltwater front influencing the cell measurements. Thus, the latter array was chosen to conduct the experiments in the flow tank described in Chapter 6.

In Chapter 6, the developed measuring technique was used in the newly developed 2D flow tank designed as a benchmark for variable-density computer codes. The developed flow tank model is ~1.7 m long, ~1.3 m high and 0.2 m wide. Water-filled chambers at both ends of the tank placed at different levels regulate flow control. Three transport experiments simulating a pumping well (saltwater upconing) were carried out with thirty-two resistance measuring cells and three temperature sensors (at the front of the tank), twelve pressure transmitters (at the rear of the tank) and one standard conductivity measuring cell (at the outflow end of the tank). A computerized data acquisition system was setup to allow simultaneous and continuous reading and registration of all the instruments. Although the first results were very promising, they clearly showed the limitations of the initial setup. Nevertheless, this chapter comprises much preliminary work (flow tank setup, instrumentation and realization of an experiment) included in M. Konz's thesis (PhD thesis in preparation, 2008). Regarding the new measuring technique, the first three experiments revealed that if the salt concentration is uniform throughout the measuring volume, measurement accuracy remains quite high even if several experiments are conducted with the same sand pack. The measurement error is not known if a salt concentration gradient occurs within the measuring volume or if a freshwater-saltwater interface intersects the cell measuring volume (which is often the case in salt upconing experiments). Yet, this newly developed experimental setup forms a good basis in obtaining an excellent benchmark.

## 7.2 Limitations and perspectives

In the framework of this thesis it could be shown that beside the hydraulic gradients, tectonic structures play a major role in the development of the geometry of the solution cavities. The motion of dissolved salt and its mixing in the aquifers based on natural and forced hydraulic conditions is subject of an ongoing thesis (M. Konz).

The results of this research will be used as a basis for further experimental and conceptual model developments on salt dissolution and solute transport by density-driven groundwater flow. These may ultimately help provide predictions on land subsidence and other risks.

Experience with both developed general experimental setups is limited, as these were newly developed for this thesis. This is one of the reasons why M. Konz (PhD thesis in preparation, 2008) has further improved the 2D flow tank experimental setup. The new resistance measuring technique could be also further developed to be applied in natural underground (e.g., for borehole measurements). Regarding the other general experimental setup, potential improvements can certainly be achieved, mainly for the tracer visualization technique and its evaluation methodology (image processing and analysis). Furthermore, there is quite a bit of room for improvement of the presented models and validation of up scaling.

Further investigations will require an even more interdisciplinary approach, involving close collaboration between physicists/engineers (fluid mechanics; image processing and analysis; rock mechanics), geochemists (rock-water interaction), and hydrogeologists. The results of Chapter 4 could form the basis of a regional scale model combining interstratal salt karst development and transport processes. It could represent a combined hydraulic-hydrochemical approach explaining the consequences for the rock mechanical behaviour of the different overlying units.

# Appendices

## A Rock salt dissolution experiments

### A.1 Photographs of experimental setup and solution cavities

### A.2 Mineralogical and chemical analyses

### A.3 Combining experimental errors

### A.4 Mathematical model half conical frustum

## B Solute transport experiments

### B.1 Breakthrough curves during calibration of RMCs in tests

### B.2 Breakthrough curves during calibration of RMCs for experiments

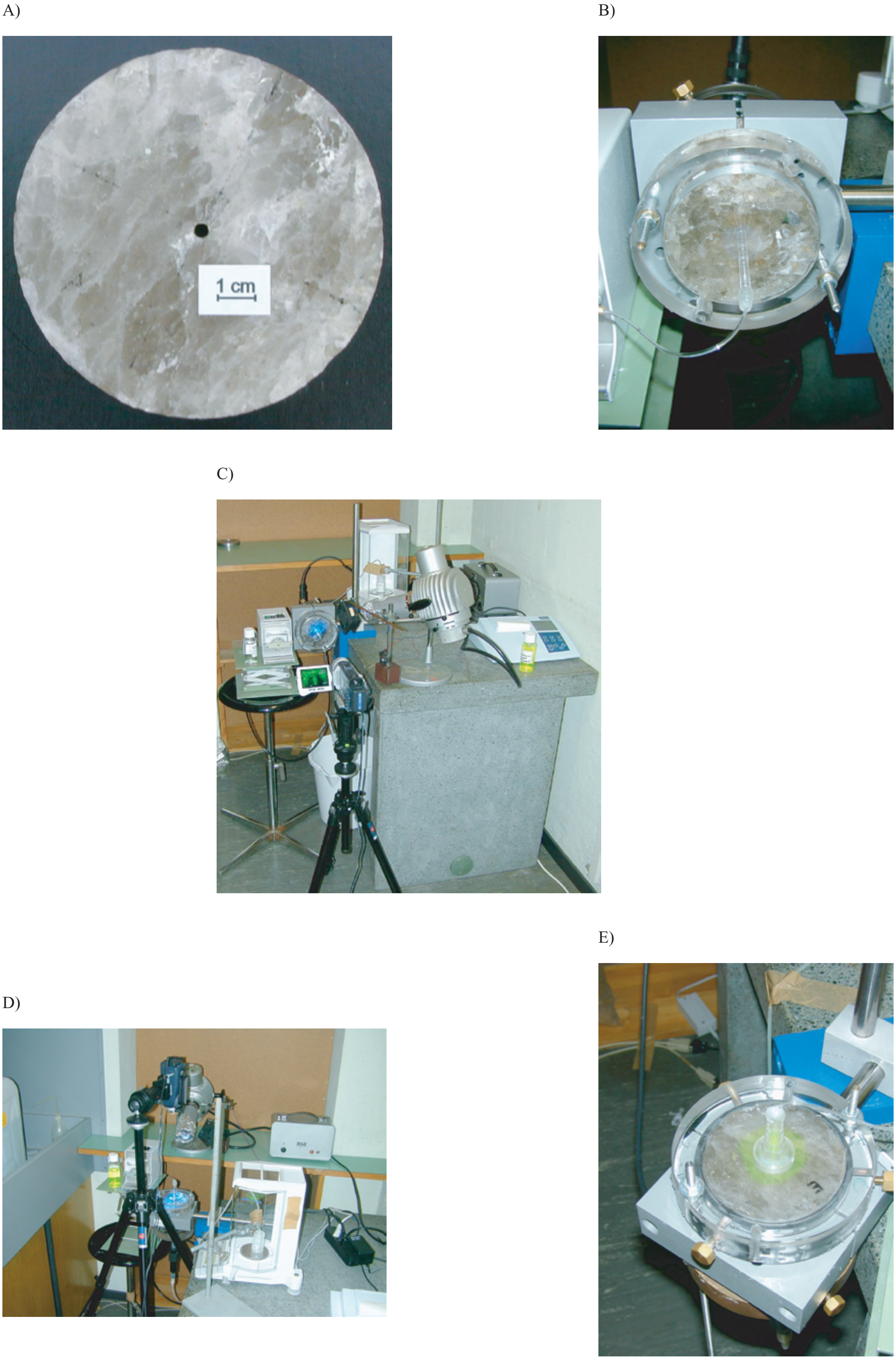

***A.1.1*** *Photographs of the (A) core of rock salt with drilled hole (Ø = 4 mm), the (B) prepared core ready for experimental run, the (C) experimental setup (horizontally oriented borehole), the (D) experimental setup (vertically oriented borehole), and the (E) injection of uranine.*

RS2: RS10:

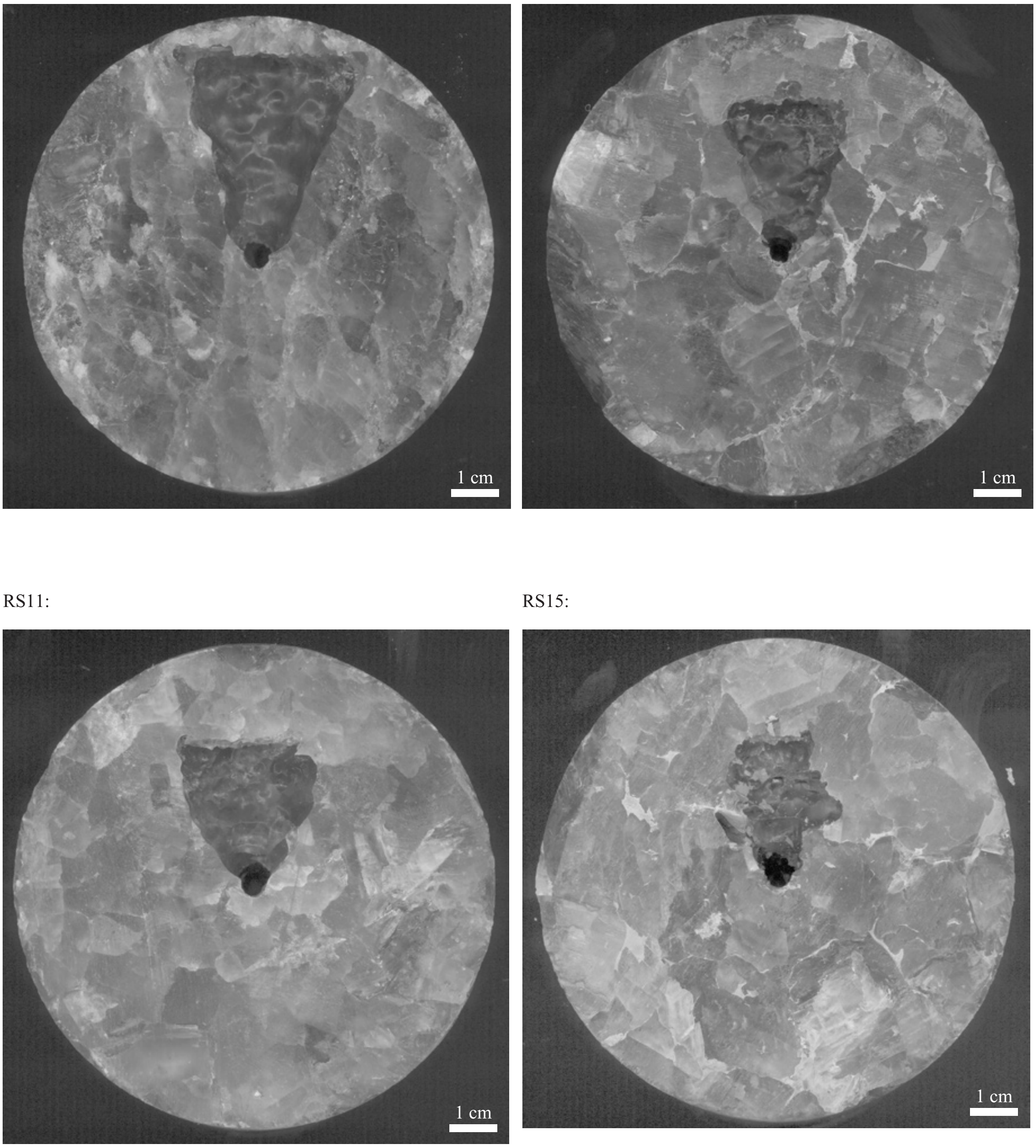

RS11: RS15:

***A.1.2*** *Scanned inflow ends of the drill cores after dissolution runs with a horizontally oriented borehole (dissolution runs RS2, RS10, RS11, RS15, RS17, RS21, and RS23).*

RS17:

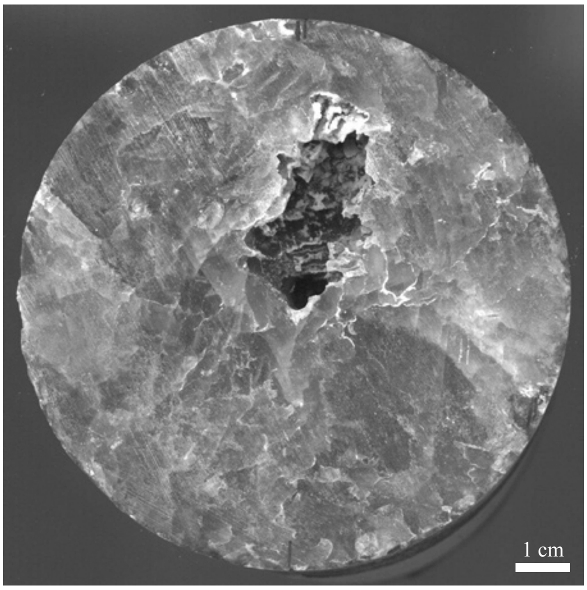

RS21:

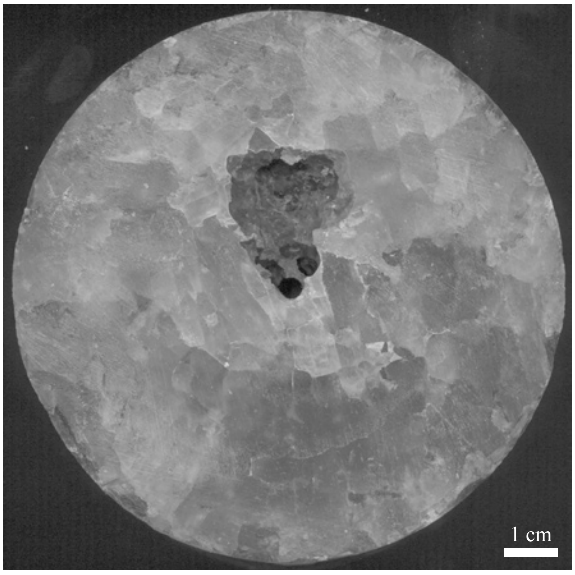

RS23:

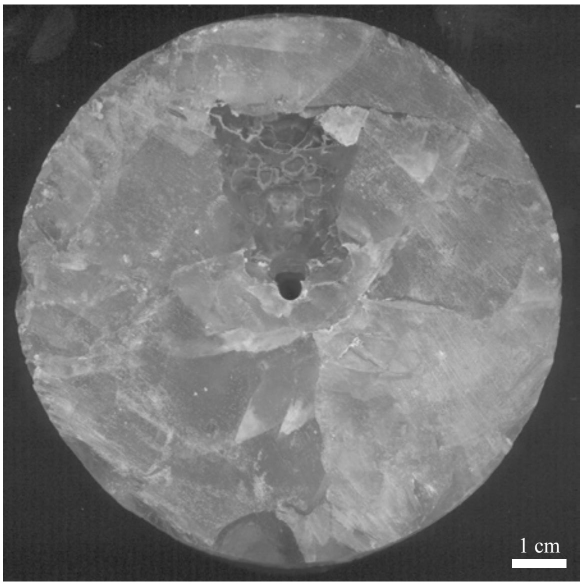

***A.1.2** (continued)*

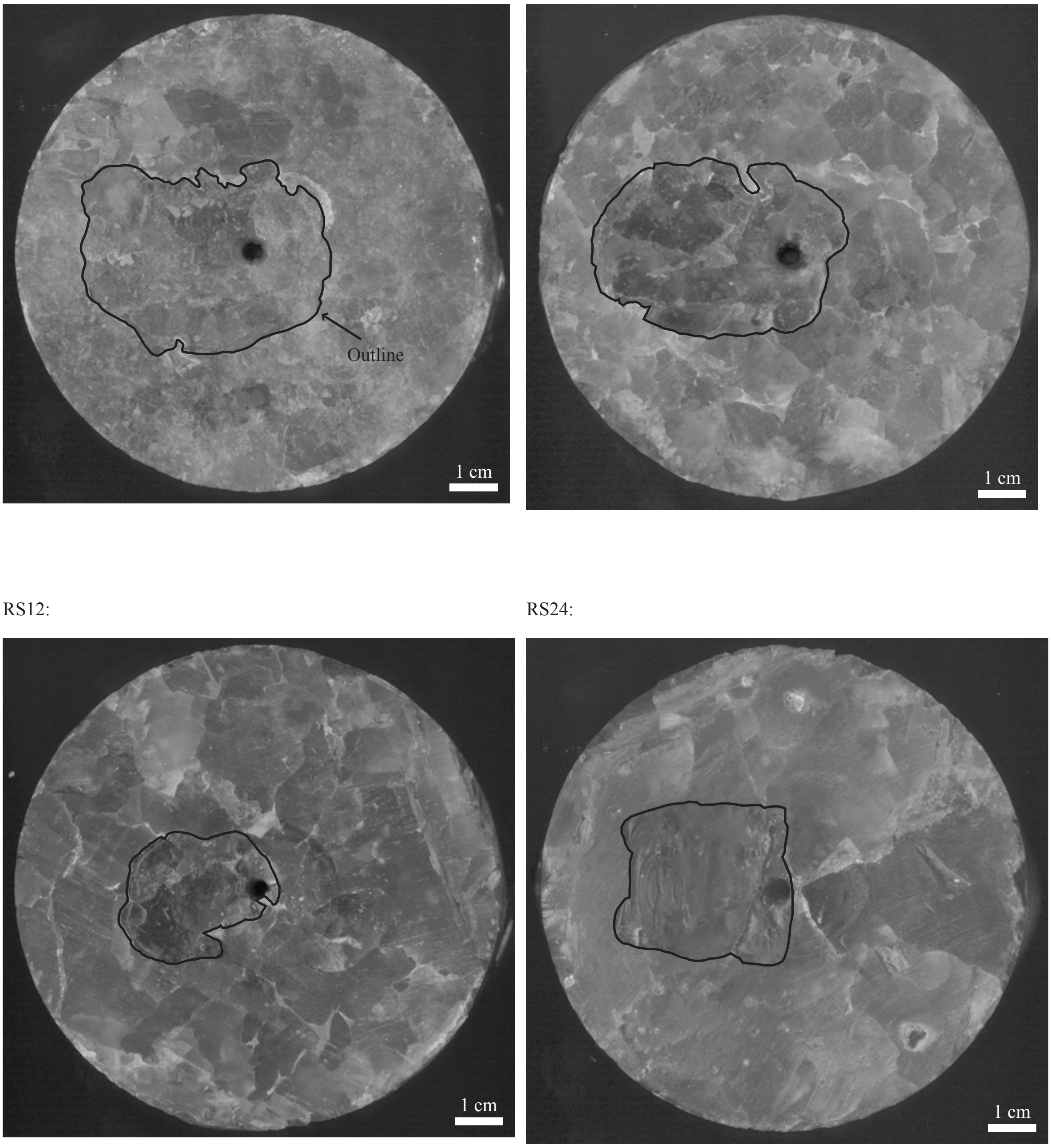

RS7: RS13:

RS12: RS24:

***A.1.3*** *Scanned inflow ends of the drill cores after dissolution runs with a 2D upper end of the core cylinder (dissolution runs RS7, RS13, RS12, RS24).*

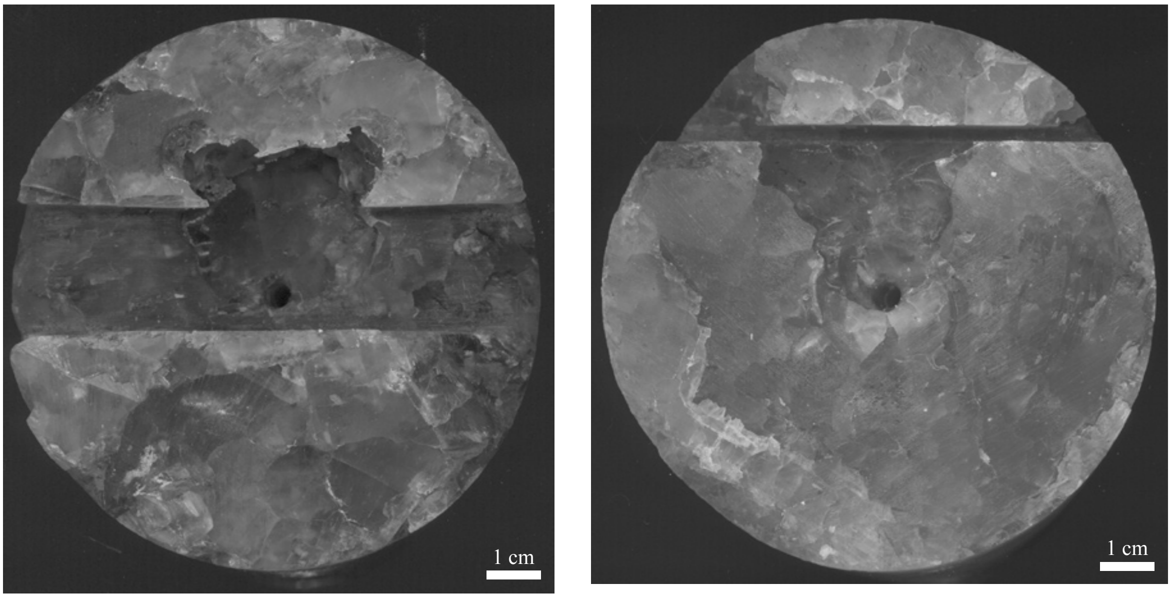
RS27:

RS28:

***A.1.4*** *Scanned inflow ends of the drill cores after dissolution runs with a 3D upper end of the core cylinder (dissolution runs RS27 and RS28).*

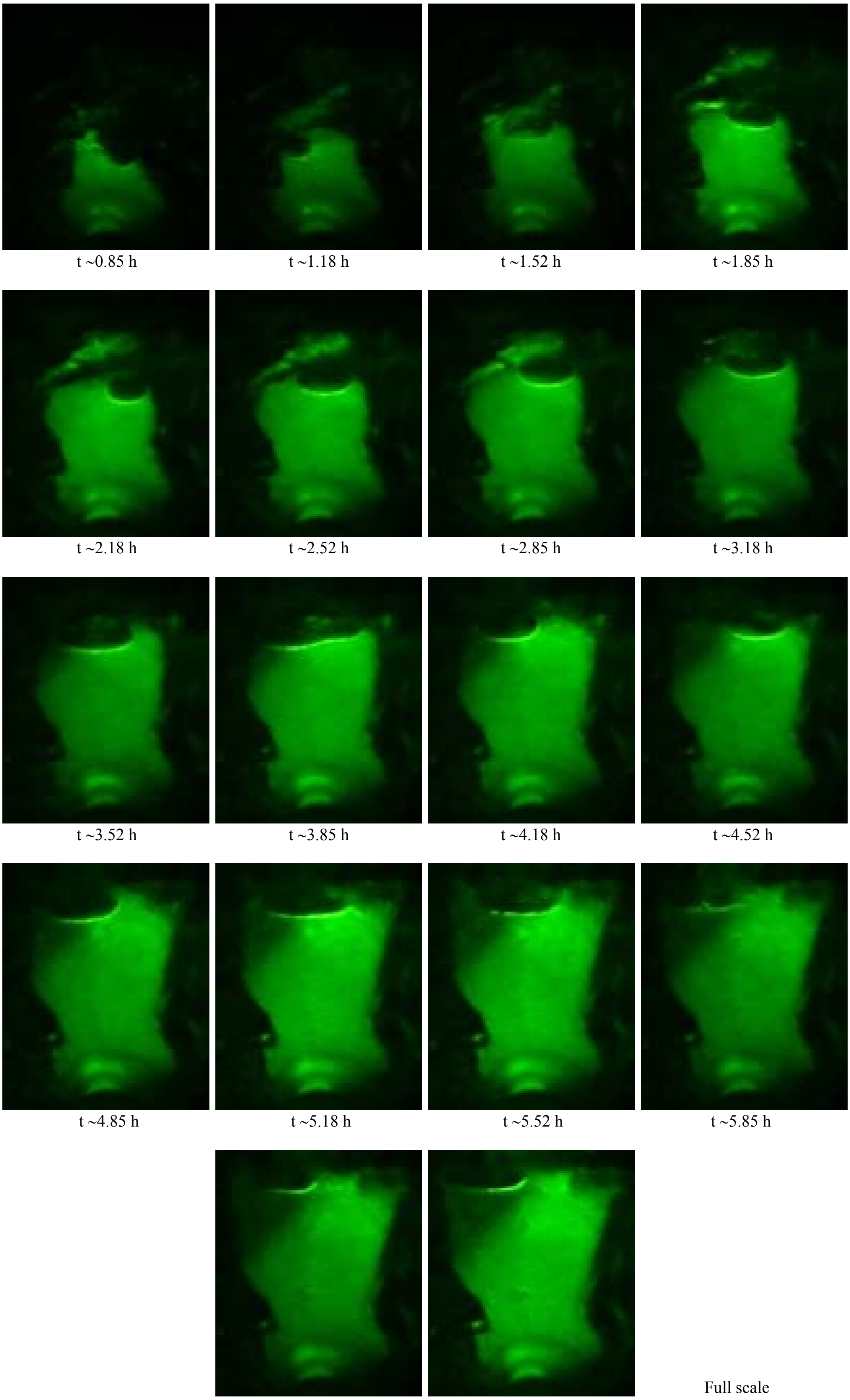

t ~0.85 h

t ~1.18 h

t ~1.52 h

t ~1.85 h

t ~2.18 h

t ~2.52 h

t ~2.85 h

t ~3.18 h

t ~3.52 h

t ~3.85 h

t ~4.18 h

t ~4.52 h

t ~4.85 h

t ~5.18 h

t ~5.52 h

t ~5.85 h

t ~6.18 h

t ~6.52 h

Full scale

***A.1.5*** *Times-lapse, videotape recording of the enlargement of solution cavity (dissolution run RS23) at the entrance of the borehole. The elapsed times after starting the dissolution run: every twenty minutes from 0.85 h to 6.52 h.*

A)

| | Major constituent | Minor constituents | | | | |
|---|---|---|---|---|---|---|
| Analytical method | XRD[d], WD-XFA[e] | XRD | XRD | XRD | XRD | XRD |
| | Halite | Quartz | Chlorite | Illite-muscovite | Dolomite | Anhydrite |
| ICDD-No.[a] | 88-2300 | 33-1161 | 29-701 | 6-263 | 36-426 | 72-503 |
| Density (g $cm^{-3}$)[b] | 2.16-2.17 | 2.65 | 2.6-3.3 | 2.6-2.9 | 2.86-2.93 | 2.9-3.0 |
| Drilling powder number[c] | Weight-% | | | | | |
| ***Horizontally oriented borehole:*** | | | | | | |
| RS2 | 97 | x | x | x | x | x |
| RS10 | 99 | x | xx | xx | - | x |
| RS11 | 98 | x | x | x | x | x |
| RS15 | 98 | x | x | x | x | - |
| RS17 | 92 | - | - | - | - | xx |
| RS19 | 95 | x | x | x | x | x |
| RS21 | 85 | x | x | x | - | x |
| RS23 | 94 | - | - | x | - | x |
| ***Vertically or inclined oriented borehole:*** | | | | | | |
| RS7 | 97 | x | x | x | x | - |
| RS13 | 97 | x | x | x | - | x |
| RS12 | 97 | x | x | x | x | x |

[a] International Centre for Diffraction Data

[b] From Deer et al. (1992)

[c] Corresponds run number

[d] X-ray diffraction

[e] Wavelength-dispersive X-ray fluorescence analysis

x Minor component

xx Major component

\- Not detected

B)

| | |
|---|---|
| $SiO_2$ (Wt%) | 2.32 |
| $Al_2O_3$ | 0.958 |
| $Fe_2O_3$ | 0.468 |
| MnO | 0.113 |
| MgO | 0.0 |
| CaO | 0.583 |
| NaCl | 93.5 |
| $K_2O$ | 0.259 |
| $TiO_2$ | 0.080 |
| $P_2O_5$ | 0.382 |
| $SO_3$ | 0.780 |
| Br | 0.032 |
| Total | 99.475 |

***A.2.1*** *A) Mineralogical and chemical analyses from drilling powders of all dissolution runs. B) Detailed chemical analyses from drilling powder represented by the dissolution run RS23.*

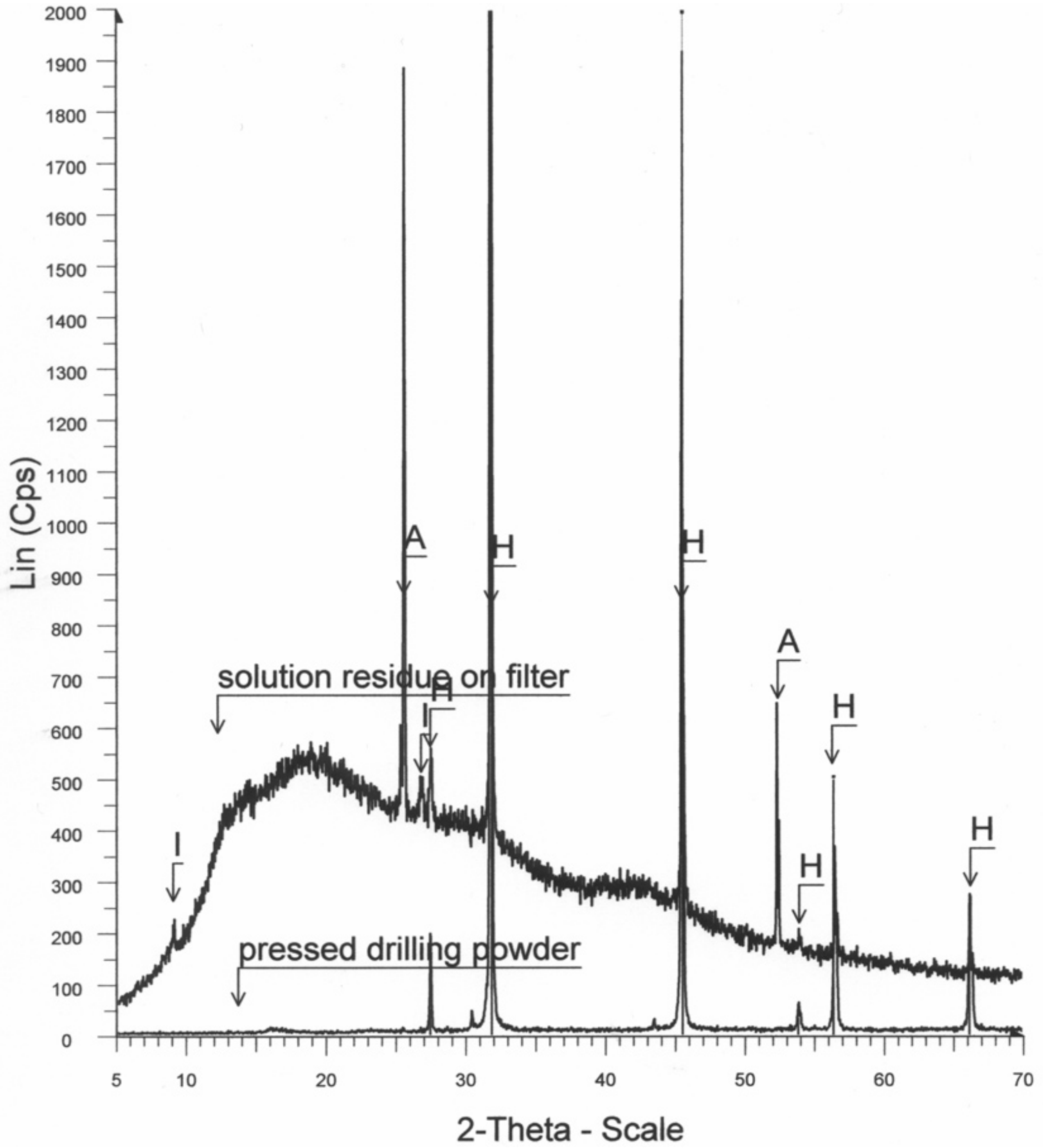

*__A.2.2__ Mineralogical analyses from drilling powder and solution residue represented by the dissolution run RS23 (A = anhydrite peaks, H = halite peaks; I = Illite-muscovite peaks).*

## A.3 Combining experimental errors

Regarding the measurements conducted during the laboratory dissolution experiments, the formulas of propagating uncorrelated errors are expressed as (Lyons, 1991[1])

$$\Delta(a+b)=\sqrt{(\Delta a)^2+(\Delta b)^2}$$

$$\Delta(a-b)=\sqrt{(\Delta a)^2+(\Delta b)^2}$$

$$\Delta(a\cdot b)=a\cdot b\sqrt{\left(\frac{\Delta a}{a}\right)^2+\left(\frac{\Delta b}{b}\right)^2}$$

$$\Delta\left(\frac{a}{b}\right)=\frac{a}{b}\sqrt{\left(\frac{\Delta a}{a}\right)^2+\left(\frac{\Delta b}{b}\right)^2}$$

The following conducted calculations are presented at the example of dissolution run RS11.

### A.3.1 Density freshwater (g cm$^{-3}$)

$$\text{density freshwater}=\frac{a-b}{c}$$

where:
a = weight of flask filled with 100 ml freshwater, g
b = weight of empty flask, g
c = freshwater volume (100 ml), cm$^3$

($\Delta a = 0.0001$ g; $\Delta b = 0.0001$ g; $\Delta c = 0.08$ cm$^3$)

For RS11:

$$\text{density freshwater}=\frac{120.5123\pm0.0001\text{ g}-20.7856\pm0.0001\text{ g}}{100\pm0.08\text{ cm}^3}$$

Calculation of combined error:

$$d=a-b=99.7267$$

$$\Delta d=\sqrt{(\Delta a)^2+(\Delta b)^2}=\sqrt{0.0001^2+0.0001^2}=0.000141421$$

$$e=\frac{d}{c}=\frac{99.7267}{100}=0.997267$$

$$\Delta e=\frac{d}{c}\sqrt{\left(\frac{\Delta d}{d}\right)^2+\left(\frac{\Delta c}{c}\right)^2}=0.997267\sqrt{\left(\frac{0.000141421}{99.7267}\right)^2+\left(\frac{0.08}{100}\right)^2}=0.000797814\approx0.0008$$

---

[1] Lyons, L. (1991), *A practical guide to data analysis for physical science students*, Cambridge University Press, Cambridge.

$$\Rightarrow \text{density freshwater} = 0.9973 \pm 0.0008 \text{ g cm}^{-3}$$

## A.3.2 Density NaCl-saturated brine (g cm$^{-3}$)

$$\text{density NaCl-saturated brine} = \frac{a - b}{c}$$

where:
a = weight of flask filled with 25 ml NaCl-saturated brine, g
b = weight of empty flask, g
c = NaCl-saturated brine volume (25 ml), cm$^3$

($\Delta a = 0.0001$ g; $\Delta b = 0.0001$ g; $\Delta c = 0.03$ cm$^3$)

For RS11:

$$\text{density NaCl-saturated brine} = \frac{39.9516 \pm 0.0001 \text{ g} - 11.0495 \pm 0.0001 \text{ g}}{25 \pm 0.03 \text{ cm}^3}$$

Calculation of combined error:

$$d = a - b = 28.9021$$

$$\Delta d = \sqrt{(\Delta a)^2 + (\Delta b)^2} = \sqrt{0.0001^2 + 0.0001^2} = 0.000141421$$

$$e = \frac{d}{c} = \frac{28.9021}{25} = 1.156084$$

$$\Delta e = \frac{d}{c}\sqrt{\left(\frac{\Delta d}{d}\right)^2 + \left(\frac{\Delta c}{c}\right)^2} = 1.156084\sqrt{\left(\frac{0.000141421}{28.9021}\right)^2 + \left(\frac{0.03}{25}\right)^2} = 0.001387312 \approx 0.001$$

$$\Rightarrow \text{density NaCl-saturated brine} = 1.156 \pm 0.001 \text{ g cm}^3$$

## A.3.3 Average inflow rate (mm$^3$ min$^{-1}$)

$$\text{average inflow rate} = \frac{a - b}{\frac{a - c}{d} e} = \frac{(a - b)d}{(a - c)e}$$

where:
a = weight of flask filled with 100 ml freshwater at the beginning of an experiment, g
b = weight of flask with freshwater at the end of an experiment, g
c = weight of empty flask, g
d = freshwater volume (100 ml), cm$^3$
e = running time, min

($\Delta a = 0.0001$ g; $\Delta b = 0.0001$ g; $\Delta c = 0.0001$ g; $\Delta d = 0.08$ cm$^3$; $\Delta e = 0$ min)

For RS11:

$$\text{average inflow rate} = \frac{(120.5123 \pm 0.0001 \text{ g} - 87.4205 \pm 0.0001 \text{ g})100 \pm 0.08 \text{ cm}^3}{(120.5123 \pm 0.0001 \text{ g} - 20.7856 \pm 0.0001 \text{ g})3405 \pm 0 \text{ min}}$$

Calculation of combined error in three steps:

1) $f = a - b = 33.0918$

$$\Delta f = \sqrt{(\Delta a)^2 + (\Delta b)^2} = \sqrt{0.0001^2 + 0.0001^2} = 0.000141421$$

$$g = f \cdot d = 3309.18$$

$$\Delta g = f \cdot d \sqrt{\left(\frac{\Delta f}{f}\right)^2 + \left(\frac{\Delta d}{d}\right)^2} = 3309.18 \sqrt{\left(\frac{0.000141421}{33.0918}\right)^2 + \left(\frac{0.08}{100}\right)^2} = 2.647381773$$

2) $h = a - c = 99.7267$

$$\Delta h = \sqrt{(\Delta a)^2 + (\Delta c)^2} = \sqrt{0.0001^2 + 0.0001^2} = 0.000141421$$

$$i = h \cdot e = 339569.4135$$

$$\Delta i = h \cdot e \sqrt{\left(\frac{\Delta h}{h}\right)^2 + \left(\frac{\Delta e}{e}\right)^2} = 339569.4135 \sqrt{\left(\frac{0.000141421}{99.7267}\right)^2 + \left(\frac{0}{3405}\right)^2} = 0.481538485$$

3) $j = \frac{g}{i} = \frac{3309.18}{339569.4135} = 0.009745224$

$$\Delta j = \frac{g}{i} \sqrt{\left(\frac{\Delta g}{g}\right)^2 + \left(\frac{\Delta i}{i}\right)^2} = 0.009745224 \sqrt{\left(\frac{2.647381773}{3309.18}\right)^2 + \left(\frac{0.481538485}{339569.4135}\right)^2} = 0.000007796 \approx 0.000008$$

$$\Rightarrow \text{average inflow rate} = 0.009745 \pm 0.000008 \text{ cm}^3 \text{ min}^{-1} = 9.745 \pm 0.008 \text{ mm}^3 \text{ min}^{-1}$$

### A.3.4 Dissolved halite volume (cm$^3$) and average dissolved halite removal rate (mm$^3$ min$^{-1}$)

$$\text{average dissolved halite removal rate} = \frac{\left(\frac{\frac{a-b}{a-c}}{g} - \frac{\frac{d-e}{d-f}}{g}\right) \pm \Delta i}{h} = \frac{\left(\frac{(a-b)g}{a-c} - \frac{(d-e)g}{d-f}\right) \pm \Delta i}{h}$$

where after the experiment:

a = weight of flask filled with 25 ml NaCl-saturated brine before filling in tubes/borehole, g
b = weight of flask with NaCl-saturated brine after filling in tubes/borehole, g
c = weight of empty flask, g

where before the experiment:

d = weight of flask filled with 25 ml NaCl-saturated brine before filling in tubes/borehole, g
e = weight of flask with NaCl-saturated brine after filling in tubes/borehole, g
f = weight of empty flask, g

where:

g = NaCl-saturated brine volume (25 ml) before filling in tubes/borehole, cm$^3$
h = running time, min

$\Delta i = \pm 0.005\ \text{cm}^3$ (estimation of the analytical error when filling the borehole/tubes until the outlet level of the Plexiglas tube on the outflow side of the borehole)

($\Delta a = 0.0001$ g; $\Delta b = 0.0001$ g; $\Delta c = 0.0001$ g; $\Delta d = 0.0001$ g; $\Delta e = 0.0001$ g; $\Delta f = 0.0001$ g $\Delta g = 0.03$ cm$^3$; $\Delta h = 0$ min)

For RS11:

$$\text{average dissolved halite removal rate} = \frac{\left(\frac{(40.6149 \pm 0.0001\ \text{g} - 30.3873 \pm 0.0001\ \text{g})25 \pm 0.03\ \text{cm}^3}{(40.6149 \pm 0.0001\ \text{g} - 10.9857 \pm 0.0001\ \text{g})} - \frac{(39.9516 \pm 0.0001\ \text{g} - 36.5809 \pm 0.0001\ \text{g})25 \pm 0.03\ \text{cm}^3}{(39.9516 \pm 0.0001\ \text{g} - 11.0495 \pm 0.0001\ \text{g})}\right) \pm 0.005\ \text{cr}}{3405 \pm 0\ \ \text{min}}$$

Calculation of combined error in four steps:

1) $j = a - b = 10.2276$

$$\Delta j = \sqrt{(\Delta a)^2 + (\Delta b)^2} = \sqrt{0.0001^2 + 0.0001^2} = 0.000141421$$

$$k = j \cdot g = 255.69$$

$$\Delta k = j \cdot g \sqrt{\left(\frac{\Delta j}{j}\right)^2 + \left(\frac{\Delta g}{g}\right)^2} = 255.69 \sqrt{\left(\frac{0.000141421}{10.2276}\right)^2 + \left(\frac{0.03}{25}\right)^2} = 0.306848369$$

$$l = a - c = 29.6292$$

$$\Delta l = \sqrt{(\Delta a)^2 + (\Delta c)^2} = \sqrt{0.0001^2 + 0.0001^2} = 0.000141421$$

$$m = \frac{k}{l} = \frac{255.69}{29.6292} = 8.62966263$$

$$\Delta m = \frac{k}{l} \sqrt{\left(\frac{\Delta k}{k}\right)^2 + \left(\frac{\Delta l}{l}\right)^2} = 8.62966263 \sqrt{\left(\frac{0.306848369}{255.69}\right)^2 + \left(\frac{0.000141421}{29.6292}\right)^2} = 0.010356364$$

2) $n = d - e = 3.3707$

$$\Delta n = \sqrt{(\Delta d)^2 + (\Delta e)^2} = \sqrt{0.0001^2 + 0.0001^2} = 0.000141421$$

$$o = n \cdot g = 84.2675$$

$$\Delta o = n \cdot g \sqrt{\left(\frac{\Delta n}{n}\right)^2 + \left(\frac{\Delta g}{g}\right)^2} = 84.2675 \sqrt{\left(\frac{0.000141421}{3.3707}\right)^2 + \left(\frac{0.03}{25}\right)^2} = 0.101182788$$

$$p = d - f = 28.9021$$

$$\Delta p = \sqrt{(\Delta d)^2 + (\Delta f)^2} = \sqrt{0.0001^2 + 0.0001^2} = 0.000141421$$

$$q = \frac{o}{p} = \frac{84.2675}{28.9021} = 2.915618588$$

$$\Delta q = \frac{o}{p}\sqrt{\left(\frac{\Delta o}{o}\right)^2 + \left(\frac{\Delta p}{p}\right)^2} = 2.915618588\sqrt{\left(\frac{0.101182788}{84.2675}\right)^2 + \left(\frac{0.000141421}{28.9021}\right)^2} = 0.003500909$$

3) $r = m - q = 8.62966263 - 2.915618588 = 5.714044042$

Considering Δi, then

$$\Delta r = \sqrt{(\Delta o)^2 + (\Delta q)^2} + \Delta i = \sqrt{0.101182788^2 + 0.003500909^2} + 0.005 = 0.106243335$$

$$\Rightarrow \text{dissolved halite volume} = 5.7 \pm 0.1 \text{ cm}^3$$

4) $s = \frac{r}{h} = \frac{5.714044042}{3405} = 0.001678133$

$$\Delta s = \frac{r}{h}\sqrt{\left(\frac{\Delta r}{r}\right)^2 + \left(\frac{\Delta h}{h}\right)^2} = 0.001678133\sqrt{\left(\frac{0.106243335}{5.714044042}\right)^2 + \left(\frac{0}{3405}\right)^2} = 0.000031202 \approx 0.00003$$

$$\Rightarrow \text{average dissolved halite removal rate} = 0.00175 \pm 0.00003 \text{ cm}^3 \text{ min}^{-1} = 1.75 \pm 0.03 \text{ mm}^3 \text{ min}^{-1}$$

### A.3.5 Final height of solution cavity/running time (mm h$^{-1}$)

$$\frac{\text{final height of solution cavity}}{\text{running time}} = \frac{a}{b}$$

where:

a = final height of solution cavity, mm

b = running time, h

(Δa = 1 mm; Δb = 0 h)

For RS11:

$$\frac{\text{final height of solution cavity}}{\text{running time}} = \frac{30 \pm 1 \text{ mm}}{57 \pm 0 \text{ h}}$$

Calculation of combined error:

$$\Delta\left[\frac{a}{b}\right] = \frac{a}{b}\sqrt{\left(\frac{\Delta a}{a}\right)^2 + \left(\frac{\Delta b}{b}\right)^2} = \frac{30}{57}\sqrt{\left(\frac{1}{30}\right)^2 + \left(\frac{0}{57}\right)^2} = 0.0175... \approx 0.02$$

$$\Rightarrow \frac{\text{final height of solution cavity}}{\text{running time}} = 0.53 \pm 0.02 \text{ mm h}^{-1}$$

## A.4 Mathematical model half conical frustum

### A.4.1 Mass balance equation

The mass balance equation is expressed as

$$P_{rs} \cdot \rho_h \frac{dV}{dt} = Q(c_{eq} - c_{in}) \tag{A.1}$$

Eq. (A.1) transformed gives

$$\frac{dV}{dt} = \frac{Q(c_{eq} - c_{in})}{P_{rs} \cdot \rho_h} \tag{A.2}$$

### A.4.2 Geometry half conical frustum

From Figure 2.9A[1], we obtain

$$\tan\alpha = \frac{a - a_0}{h} \tag{A.3}$$

Eq. (A.3) transformed gives

$$a = \tan\alpha \cdot h + a_0 \tag{A.4}$$

Also from Figure 2.9A[2], we obtain

$$\tan\beta = \frac{b - b_0}{h} \tag{A.5}$$

Eq. (A.5) transformed gives

$$b = \tan\beta \cdot h + b_0 \tag{A.6}$$

Ditto from Figure 2.9A, we obtain

$$dV = \frac{1}{2}\pi \cdot a \cdot b \cdot dh \tag{A.7}$$

Substituting Eqs. (A.4) and (A.6) in Eq. (A.7) yields

$$dV = \frac{1}{2}\pi(\tan\alpha \cdot h + a_0)(\tan\beta \cdot h + b_0)dh \tag{A.8}$$

Eq. (A.8) transformed gives

$$dV = \frac{1}{2}\pi(\tan\alpha \cdot \tan\beta \cdot h^2 + b_0 \cdot \tan\alpha \cdot h + a_0 \cdot \tan\beta \cdot h + a_0 \cdot b_0)dh \tag{A.9}$$

Subsequently, dividing both sides of Eq. (A.9) by *dt* equals

---

[1] a is the semi-major axis of the top half ellipse

[2] b is the semi-minor axis of the top half ellipse

$$\frac{dV}{dt} = \frac{1}{2}\pi(\tan\alpha \cdot \tan\beta \cdot h^2 + b_0 \cdot \tan\alpha \cdot h + a_0 \cdot \tan\beta \cdot h + a_0 \cdot b_0)\frac{dh}{dt} \tag{A.10}$$

### A.4.3 Derivation of *h(t)*

Combining Eqs. (A.2) and (A.10) yields

$$\frac{1}{2}\pi(\tan\alpha \cdot \tan\beta \cdot h^2 + b_0 \cdot \tan\alpha \cdot h + a_0 \cdot \tan\beta \cdot h + a_0 \cdot b_0)\frac{dh}{dt} = \frac{Q(c_{eq} - c_{in})}{P_{rs} \cdot \rho_h}$$

$$\int(\tan\alpha \cdot \tan\beta \cdot h^2 + b_0 \cdot \tan\alpha \cdot h + a_0 \cdot \tan\beta \cdot h + a_0 \cdot b_0)dh = \frac{2 \cdot Q(c_{eq} - c_{in})}{P_{rs} \cdot \rho_h \cdot \pi}\int dt$$

$$\frac{1}{3}\tan\alpha \cdot \tan\beta \cdot h^3 + \frac{1}{2}b_0 \cdot \tan\alpha \cdot h^2 + \frac{1}{2}a_0 \cdot \tan\beta \cdot h^2 + a_0 \cdot b_0 \cdot h + C_0 = \frac{2 \cdot Q(c_{eq} - c_{in})}{P_{rs} \cdot \rho_h \cdot \pi}t \tag{A.11}$$

If $t = 0$ and $h = 0$ then $C_0 = 0$, and therefore Eq. (A.11) becomes

$$\frac{1}{3}\tan\alpha \cdot \tan\beta \cdot h^3 + \left(\frac{1}{2}b_0 \cdot \tan\alpha + \frac{1}{2}a_0 \cdot \tan\beta\right)h^2 + a_0 \cdot b_0 \cdot h - \frac{2 \cdot Q(c_{eq} - c_{in})}{P_{rs} \cdot \rho_h \cdot \pi}t = 0 \tag{A.12}$$

Eq. (A.12) is a cubic equation also expressed as

$$C_1 \cdot h^3 + C_2 \cdot h^2 + C_3 \cdot h + C_4 = 0 \tag{A.13}$$

where

$$C_1 = \frac{1}{3}\tan\alpha \cdot \tan\beta$$

$$C_2 = \frac{1}{2}b_0 \cdot \tan\alpha + \frac{1}{2}a_0 \cdot \tan\beta$$

$$C_3 = a_0 \cdot b_0$$

$$C_4 = -\frac{2 \cdot Q(c_{eq} - c_{in})}{P_{rs} \cdot \rho_h \cdot \pi}t$$

As

$$\left(\frac{C_3}{3 \cdot C_1} - \frac{C_2^{\,2}}{9 \cdot C_1^{\,2}}\right)^3 + \left(\frac{C_2^{\,3}}{27 \cdot C_1^{\,3}} - \frac{C_2 \cdot C_3}{6 \cdot C_1^{\,2}} + \frac{C_4}{2 \cdot C_1}\right)^2 > 0$$

the solution of Eq. (A.13) equals

$$\begin{aligned} h = &\sqrt[3]{\left(-\frac{C_2^{\,3}}{27 \cdot C_1^{\,3}} + \frac{C_2 \cdot C_3}{6 \cdot C_1^{\,2}} - \frac{C_4}{2 \cdot C_1}\right) + \sqrt{\left(-\frac{C_2^{\,3}}{27 \cdot C_1^{\,3}} + \frac{C_2 \cdot C_3}{6 \cdot C_1^{\,2}} - \frac{C_4}{2 \cdot C_1}\right)^2 + \left(\frac{C_3}{3 \cdot C_1} - \frac{C_2^{\,2}}{9 \cdot C_1^{\,2}}\right)^3}} \\ &+ \sqrt[3]{\left(-\frac{C_2^{\,3}}{27 \cdot C_1^{\,3}} + \frac{C_2 \cdot C_3}{6 \cdot C_1^{\,2}} - \frac{C_4}{2 \cdot C_1}\right) - \sqrt{\left(-\frac{C_2^{\,3}}{27 \cdot C_1^{\,3}} + \frac{C_2 \cdot C_3}{6 \cdot C_1^{\,2}} - \frac{C_4}{2 \cdot C_1}\right)^2 + \left(\frac{C_3}{3 \cdot C_1} - \frac{C_2^{\,2}}{9 \cdot C_1^{\,2}}\right)^3}} - \frac{C_2}{3 \cdot C_1} \end{aligned} \tag{A.14}$$

(e.g., Bronstein and Semendjajew, 1991[3]; Bewersdorff, 2002[4]). The Eq. (A.14) as *h(t)* equals

$$\begin{aligned} h(t) = {} & \sqrt[3]{\left(-\frac{C_2^{\,3}}{27\cdot C_1^3}+\frac{C_2\cdot C_3}{6\cdot C_1^2}-\frac{C_5\cdot t}{2\cdot C_1}\right)+\sqrt{\left(-\frac{C_2^{\,3}}{27\cdot C_1^3}+\frac{C_2\cdot C_3}{6\cdot C_1^2}-\frac{C_5\cdot t}{2\cdot C_1}\right)^2+\left(\frac{C_3}{3\cdot C_1}-\frac{C_2^{\,2}}{9\cdot C_1^2}\right)^3}} \\ & +\sqrt[3]{\left(-\frac{C_2^{\,3}}{27\cdot C_1^3}+\frac{C_2\cdot C_3}{6\cdot C_1^2}-\frac{C_5\cdot t}{2\cdot C_1}\right)-\sqrt{\left(-\frac{C_2^{\,3}}{27\cdot C_1^3}+\frac{C_2\cdot C_3}{6\cdot C_1^2}-\frac{C_5\cdot t}{2\cdot C_1}\right)^2+\left(\frac{C_3}{3\cdot C_1}-\frac{C_2^{\,2}}{9\cdot C_1^2}\right)^3}}-\frac{C_2}{3\cdot C_1} \end{aligned} \tag{A.15}$$

where

$$C_5 = -\frac{2\cdot Q(c_{eq}-c_{in})}{P_{rs}\cdot\rho_h\cdot\pi}$$

Eqs. (A.14) and (A.15) also expressed as

$$h(t)=\sqrt[3]{\left(C_6-C_7\cdot t\right)+\sqrt{\left(C_6-C_7\cdot t\right)^2+C_8}}+\sqrt[3]{\left(C_6-C_7\cdot t\right)-\sqrt{\left(C_6-C_7\cdot t\right)^2+C_8}}-C_9 \tag{A.16}$$

where

$$\begin{aligned} C_6 &= -\frac{C_2^{\,3}}{27\cdot C_1^3}+\frac{C_2\cdot C_3}{6\cdot C_1^2} \\ &= -\frac{\left(\frac{1}{2}b_0\cdot\tan\alpha+\frac{1}{2}a_0\cdot\tan\beta\right)^3}{27\left(\frac{1}{3}\tan\alpha\cdot\tan\beta\right)^3}+\frac{\left(\frac{1}{2}b_0\cdot\tan\alpha+\frac{1}{2}a_0\cdot\tan\beta\right)a_0\cdot b_0}{6\left(\frac{1}{3}\tan\alpha\cdot\tan\beta\right)^2} \\ &= -\frac{\left(b_0\cdot\tan\alpha+a_0\cdot\tan\beta\right)^3}{8\left(\tan\alpha\cdot\tan\beta\right)^3}+\frac{3\cdot a_0\cdot b_0\left(b_0\cdot\tan\alpha+a_0\cdot\tan\beta\right)}{4\left(\tan\alpha\cdot\tan\beta\right)^2} \end{aligned}$$

$$\begin{aligned} C_7 &= \frac{C_5}{2\cdot C_1} \\ &= -\frac{2\cdot Q(c_{eq}-c_{in})}{P_{rs}\cdot\rho_h\cdot\pi\cdot 2\cdot\frac{1}{3}\tan\alpha\cdot\tan\beta} \\ &= -\frac{3\cdot Q(c_{eq}-c_{in})}{P_{rs}\cdot\rho_h\cdot\pi\cdot\tan\alpha\cdot\tan\beta} \end{aligned}$$

---

[3] Bronstein, I. N. & Semendjajew, K. A. (1991): Taschenbuch der Mathematik. Nauka, Moskau; Teubner Verlagsgesellschaft, Stuttgart; Harri Deutsch, Thun.

[4] Bewersdorff, J. (2002): Algebra für Einsteiger. Vieweg, Braunschweig/Wiesbaden.

$$C_8 = \left( \frac{C_3}{3 \cdot C_1} - \frac{C_2{}^2}{9 \cdot C_1{}^2} \right)^3$$

$$= \left( \frac{a_0 \cdot b_0}{3 \cdot \frac{1}{3} \tan\alpha \cdot \tan\beta} - \frac{\left( \frac{1}{2} b_0 \cdot \tan\alpha + \frac{1}{2} a_0 \cdot \tan\beta \right)^2}{9 \cdot \left( \frac{1}{3} \tan\alpha \cdot \tan\beta \right)^2} \right)^3$$

$$= \left( \frac{a_0 \cdot b_0}{\tan\alpha \cdot \tan\beta} - \frac{\left( b_0 \cdot \tan\alpha + a_0 \cdot \tan\beta \right)^2}{4\left( \tan\alpha \cdot \tan\beta \right)^2} \right)^3$$

$$C_9 = \frac{C_2}{3 \cdot C_1}$$

$$= \frac{\frac{1}{2} b_0 \cdot \tan\alpha + \frac{1}{2} a_0 \cdot \tan\beta}{3 \cdot \frac{1}{3} \tan\alpha \cdot \tan\beta}$$

$$= \frac{b_0 \cdot \tan\alpha + a_0 \cdot \tan\beta}{2 \cdot \tan\alpha \cdot \tan\beta}$$

### A.4.4 Derivation of $S_{horiz}(t)$

From Figure 2.9A, we obtain

$$S_{horiz} = \frac{\pi \cdot a \cdot b}{2} \tag{A.17}$$

Substituting Eqs. (A.4), (A.6) and (A.16) in Eq. (A.17) yields

$$S_{horiz}(t) = \frac{\pi(\tan\alpha \cdot h(t) + a_0)(\tan\beta \cdot h(t) + b_0)}{2}$$

### A.4.5 Derivation of $R_h(t)$ of a half conical frustum

The average dissolution rate $R_h$ was computed from

$$R_h(t) = \frac{P_{rs} \cdot Q \cdot c_{eq}}{W_h \cdot S_{horiz}(t)} \cdot 10^3$$

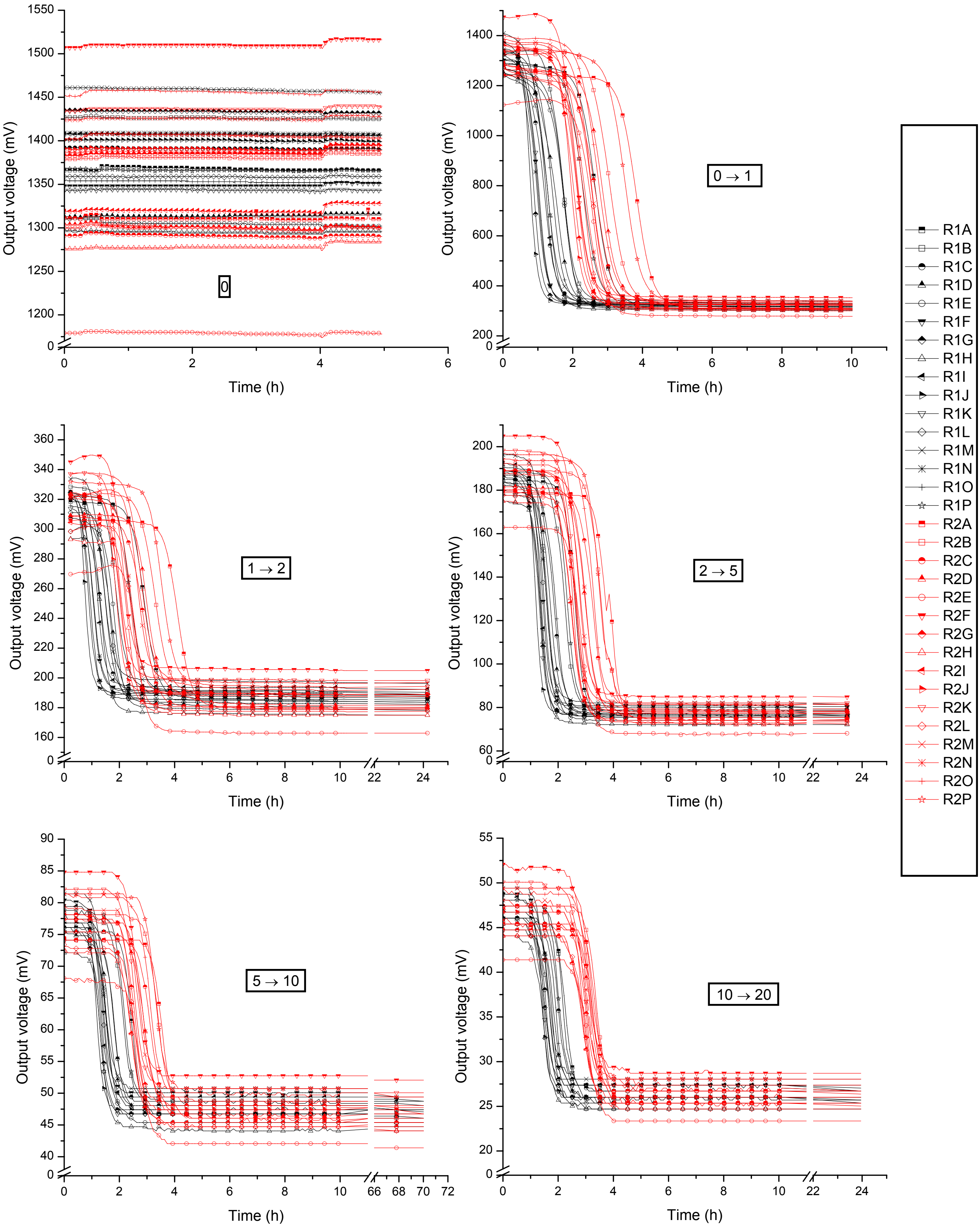

***B.1.1*** *Breakthrough curves during calibration (ELCOL-1) of vertically aligned electrodes. Salt concentrations 0–40 g* $l^{-1}$*. [Concentration displaced calibration solution → concentration injected calibration solution]. Every 5th data point is displayed as a symbol.*

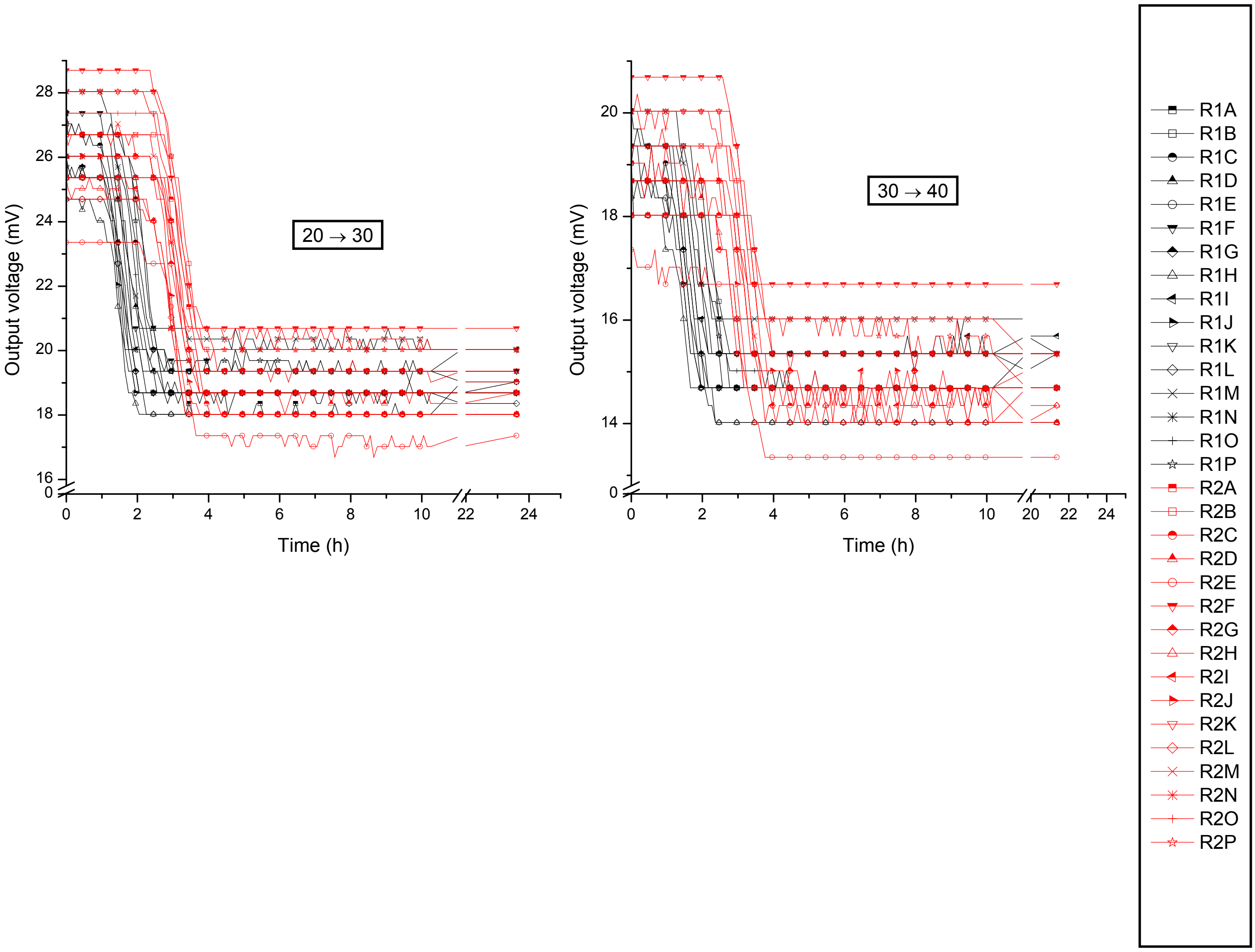

***B.1.1*** *(continued)*

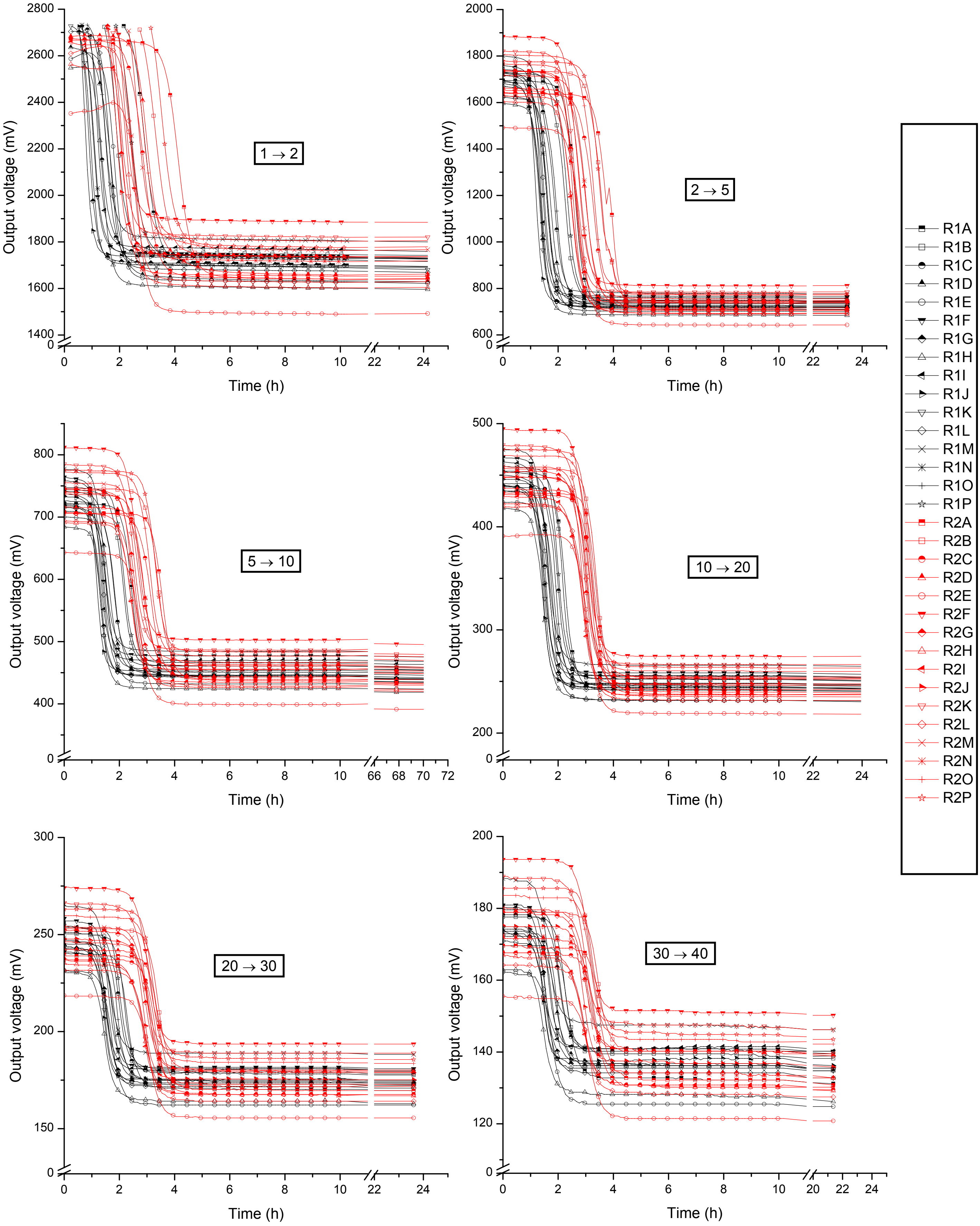

***B.1.2*** *Breakthrough curves during calibration (ELCOL-2) of vertically aligned electrodes. Salt concentrations 1–40 g l*$^{-1}$*. [Concentration displaced calibration solution → concentration injected calibration solution]. Every 5th data point is displayed as a symbol.*

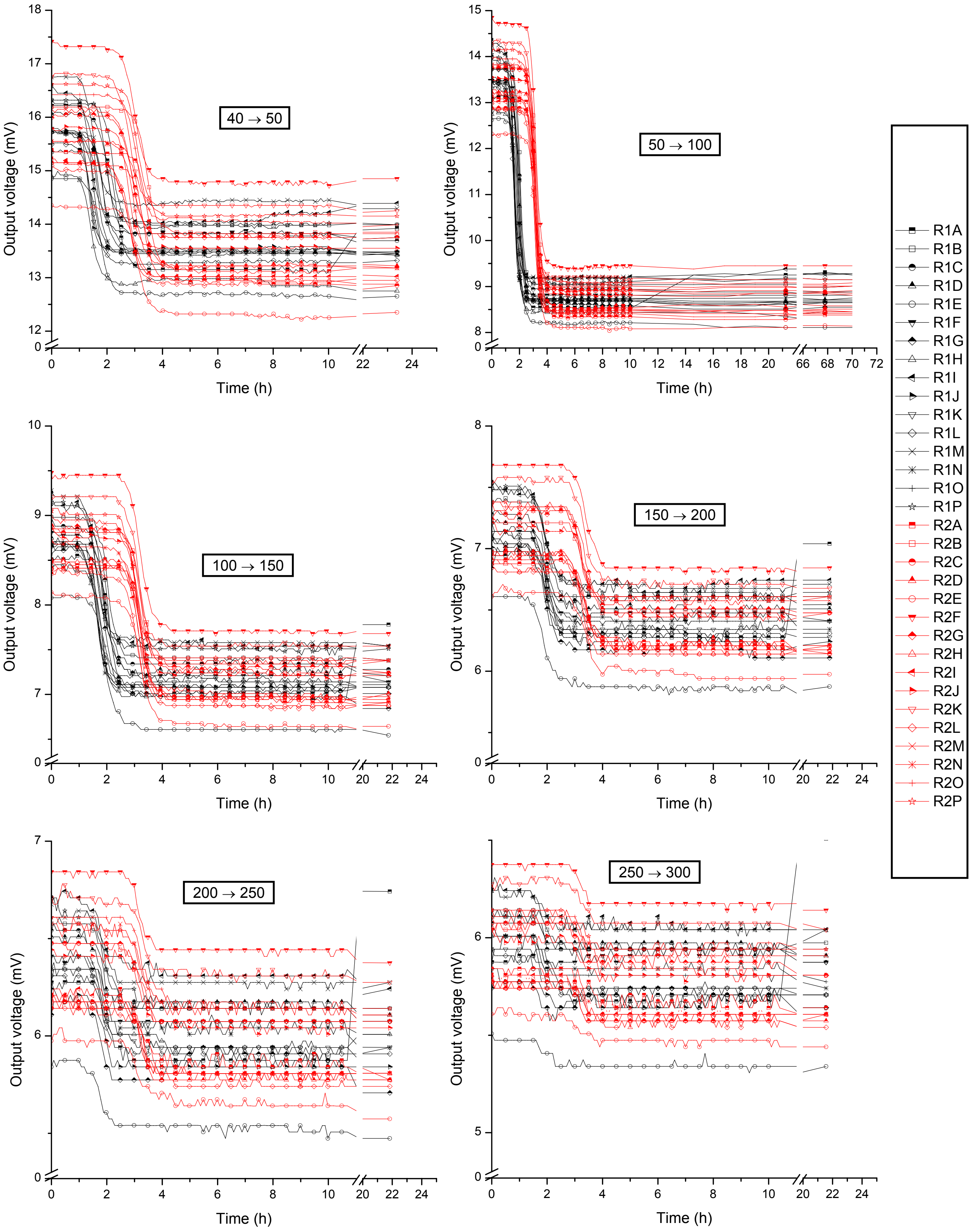

**B.1.3** *Breakthrough curves during calibration (ELCOH-1) of vertically aligned electrodes. Salt concentrations 40–300 g l$^{-1}$. [Concentration displaced calibration solution → concentration injected calibration solution]. Every 5th data point is displayed as a symbol.*

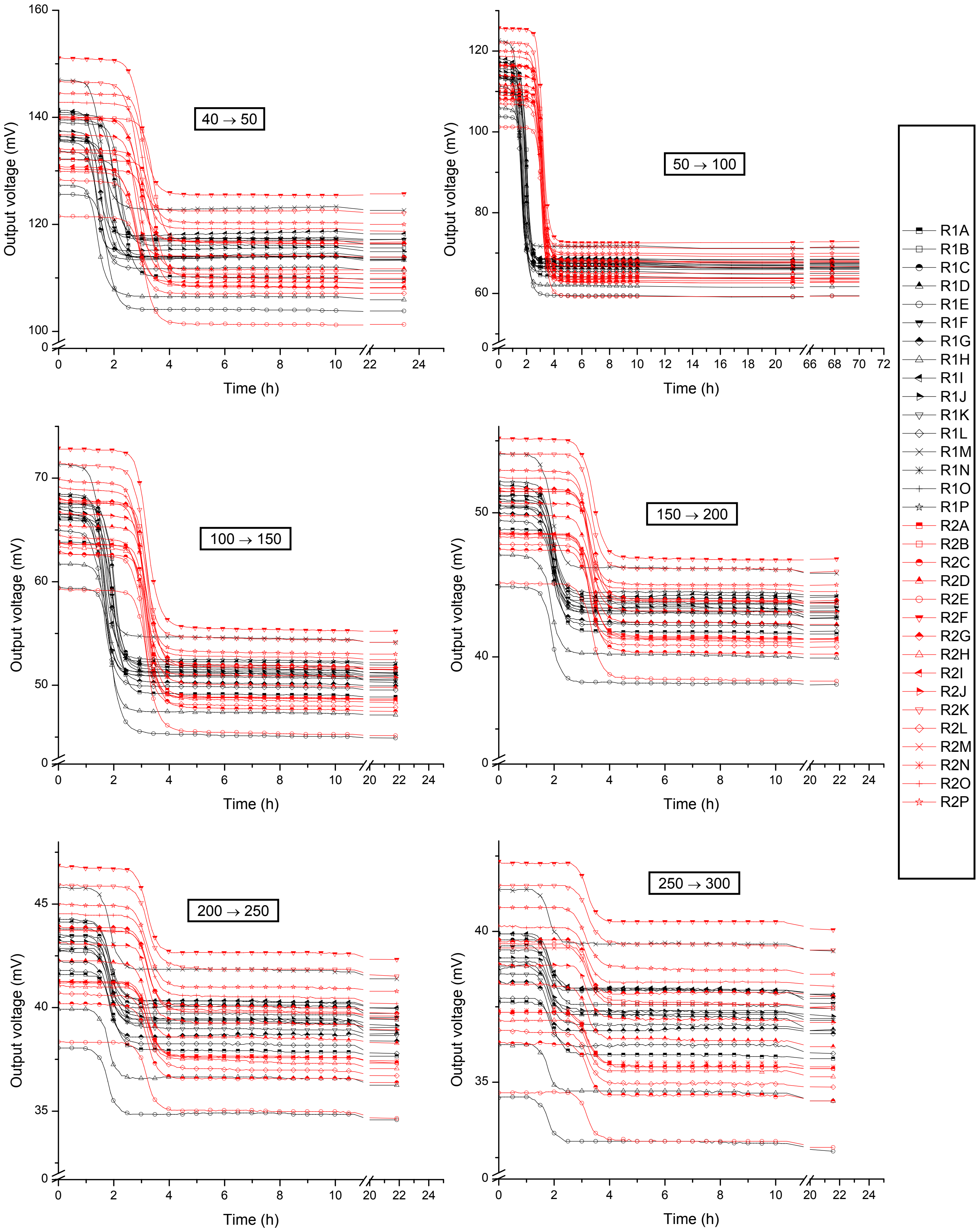

***B.1.4*** *Breakthrough curves during calibration (ELCOH-2) of vertically aligned electrodes. Salt concentrations 40–300 g $l^{-1}$. [Concentration displaced calibration solution → concentration injected calibration solution]. Every 5th data point is displayed as a symbol.*

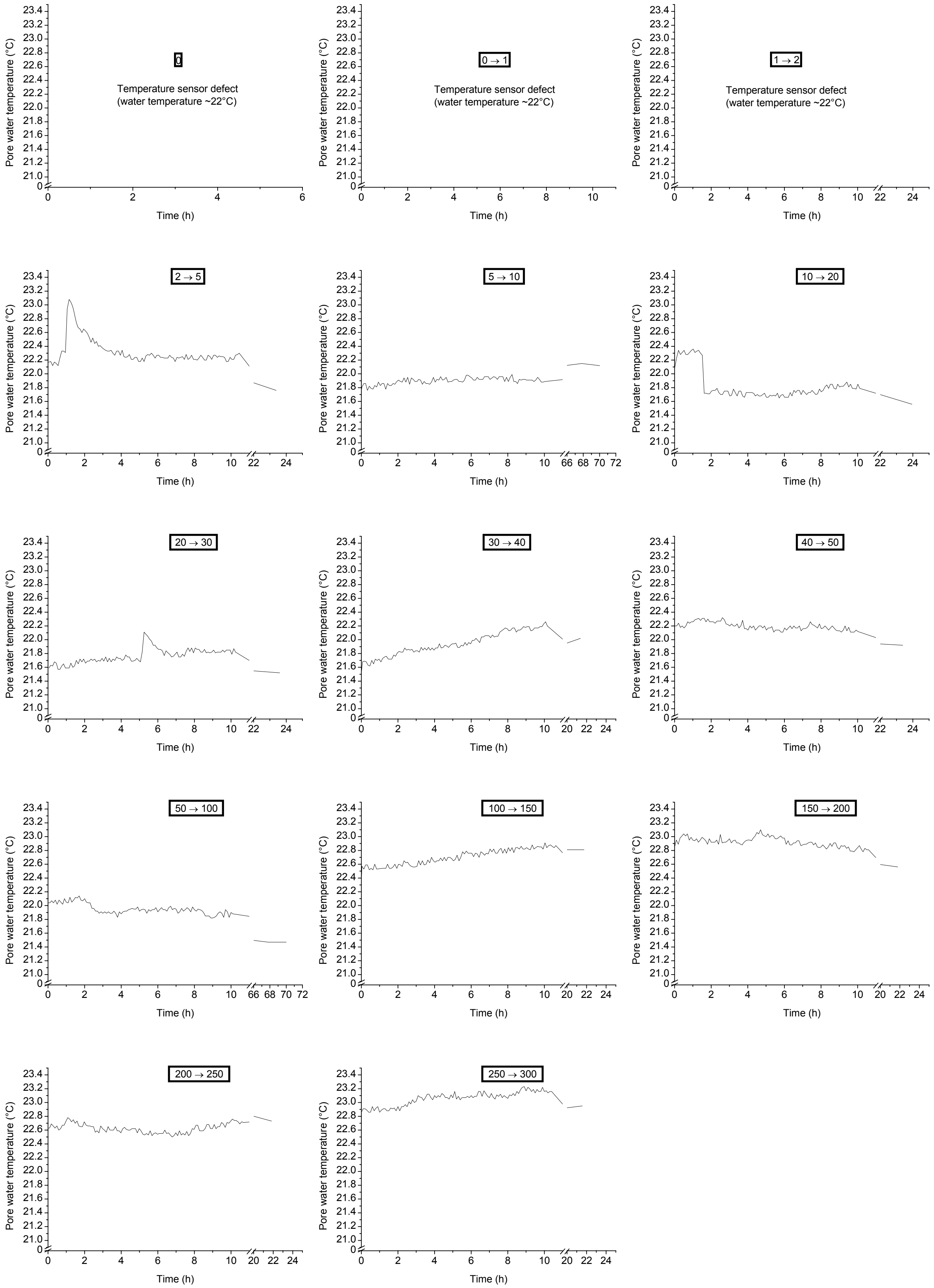

***B.1.5** Pore water temperature pattern during calibration. Salt concentrations 0–300 g $l^{-1}$. [Concentration displaced calibration solution → concentration injected calibration solution].*

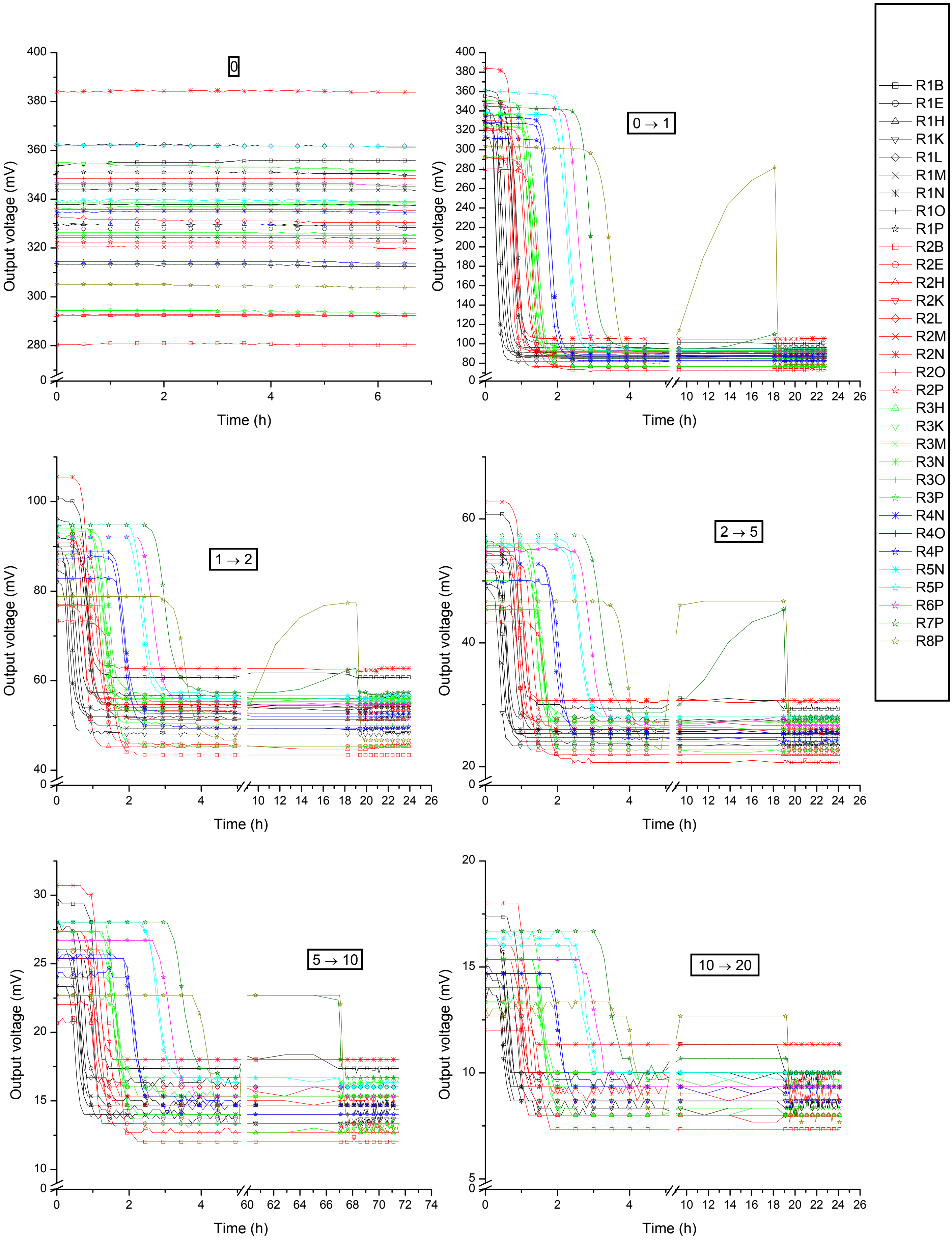

***B.2.1*** *Breakthrough curves during calibration (ELCONDU-1) of RMCs. Salt concentrations 0–300 g l$^{-1}$. [Concentration displaced calibration solution → concentration injected calibration solution]. Every 5th data point is displayed as a symbol.*

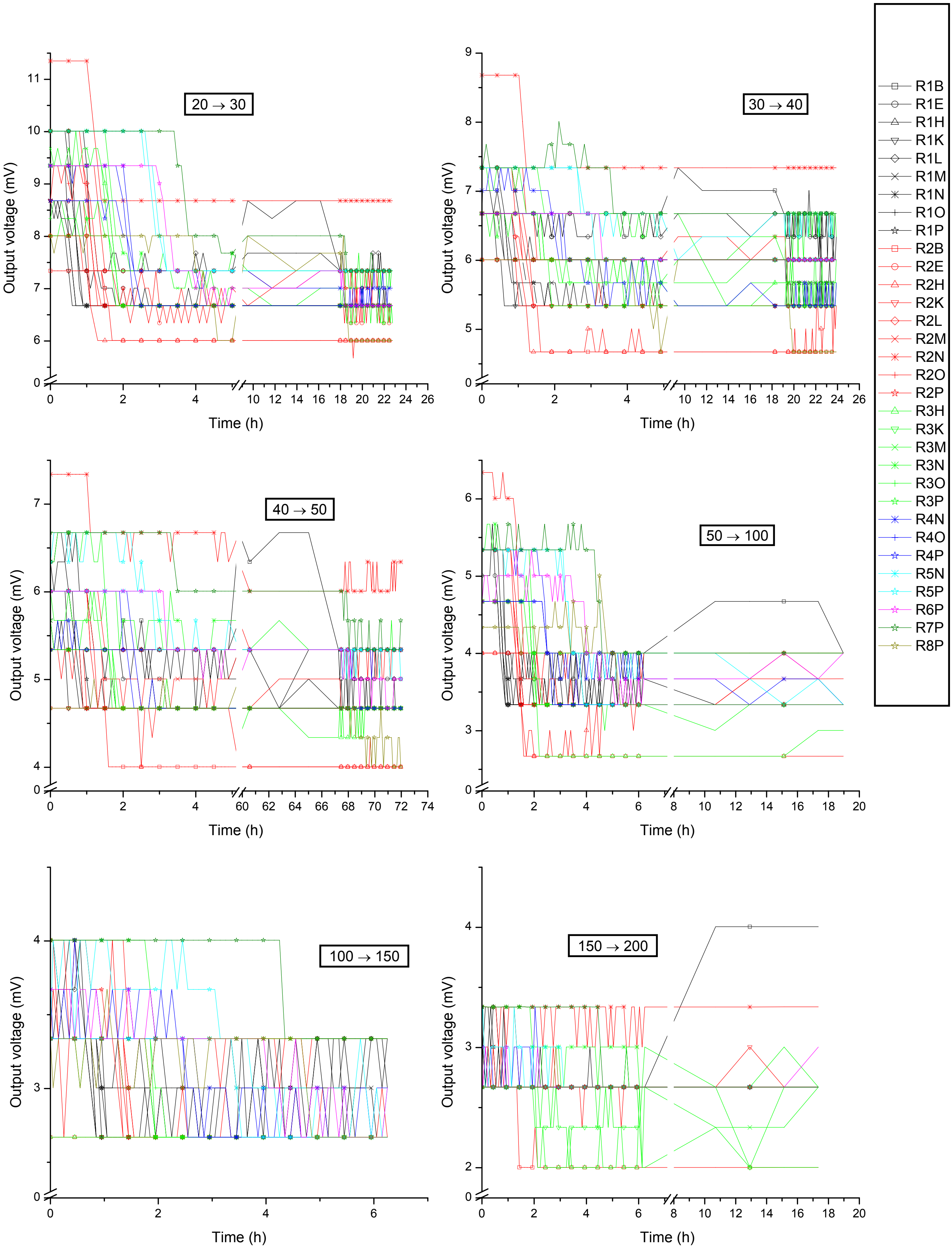

***B.2.1*** *(continued)*

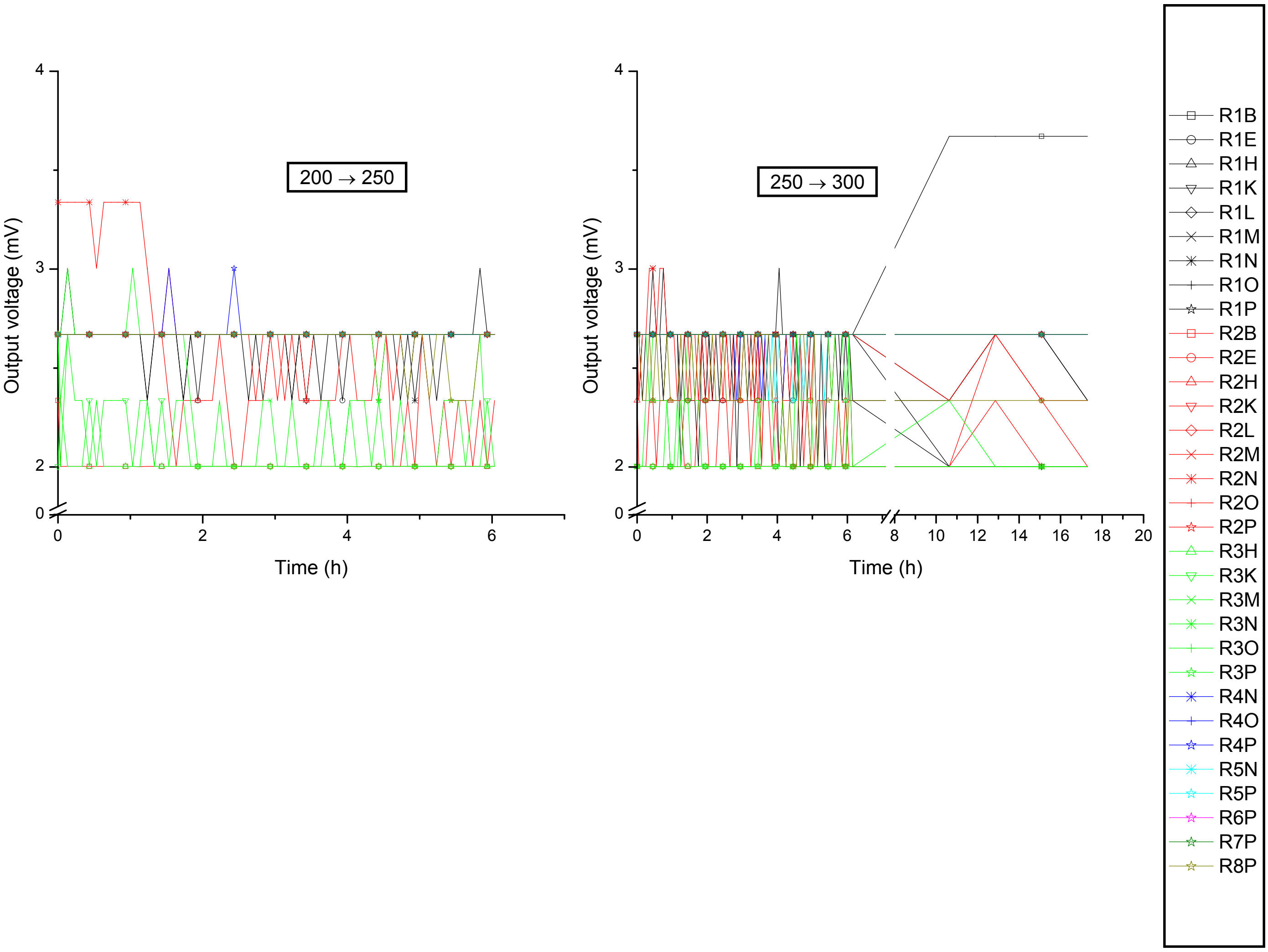

***B.2.1*** *(continued)*

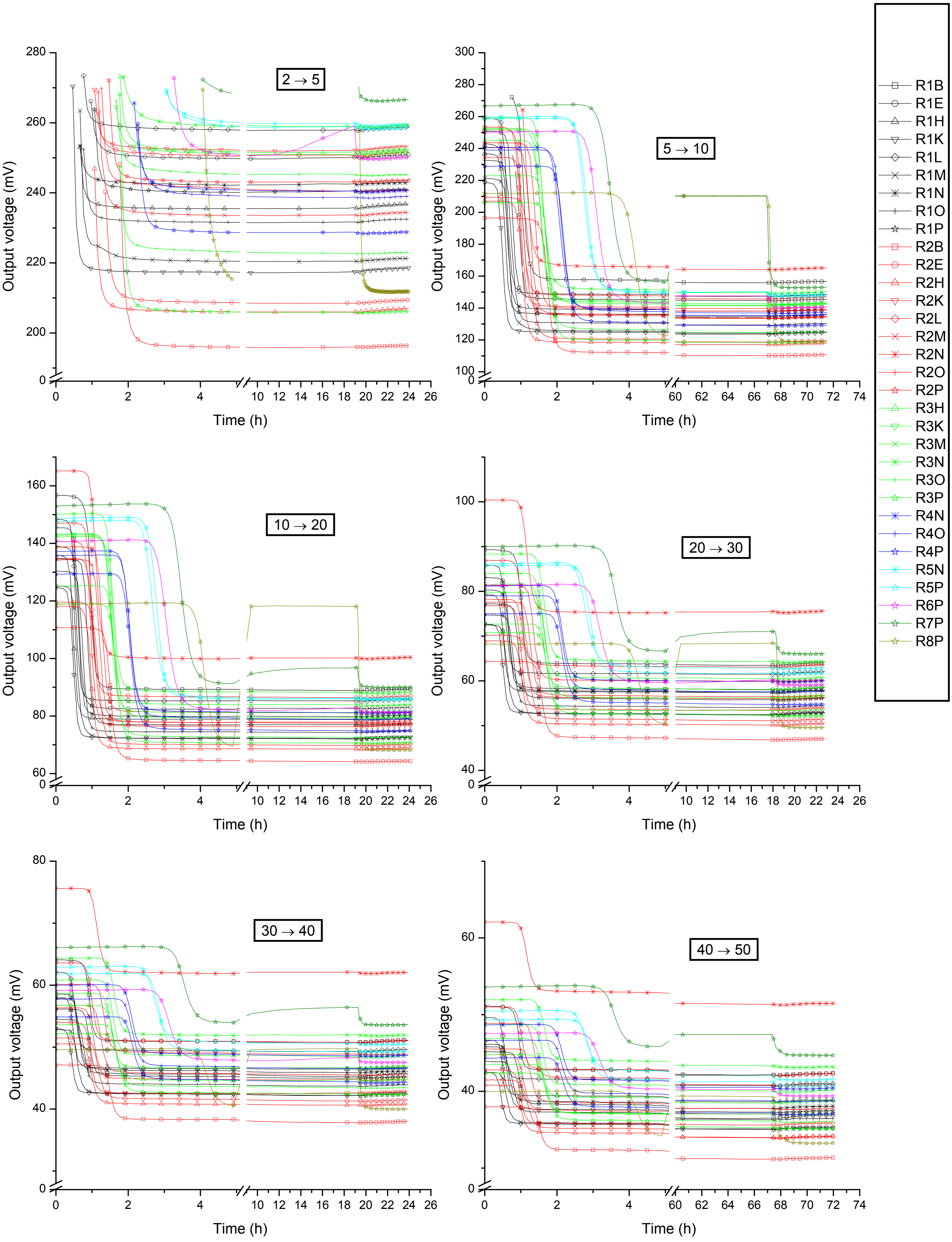

***B.2.2*** *Breakthrough curves during calibration (ELCONDU-2) of RMCs. Salt concentrations 2–300 g l$^{-1}$. [Concentration displaced calibration solution → concentration injected calibration solution]. Every 5th data point is displayed as a symbol.*

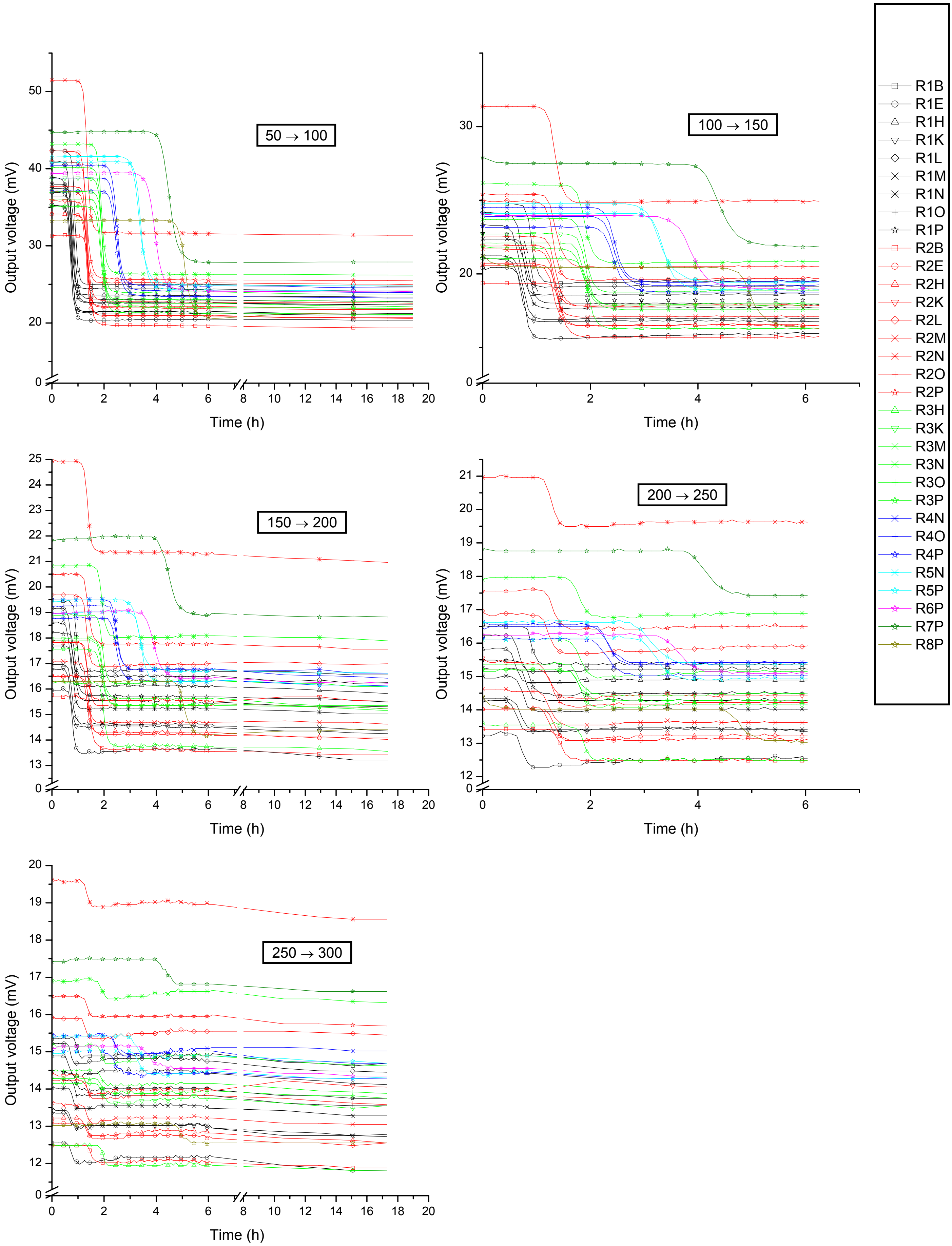

***B.2.2** (continued)*

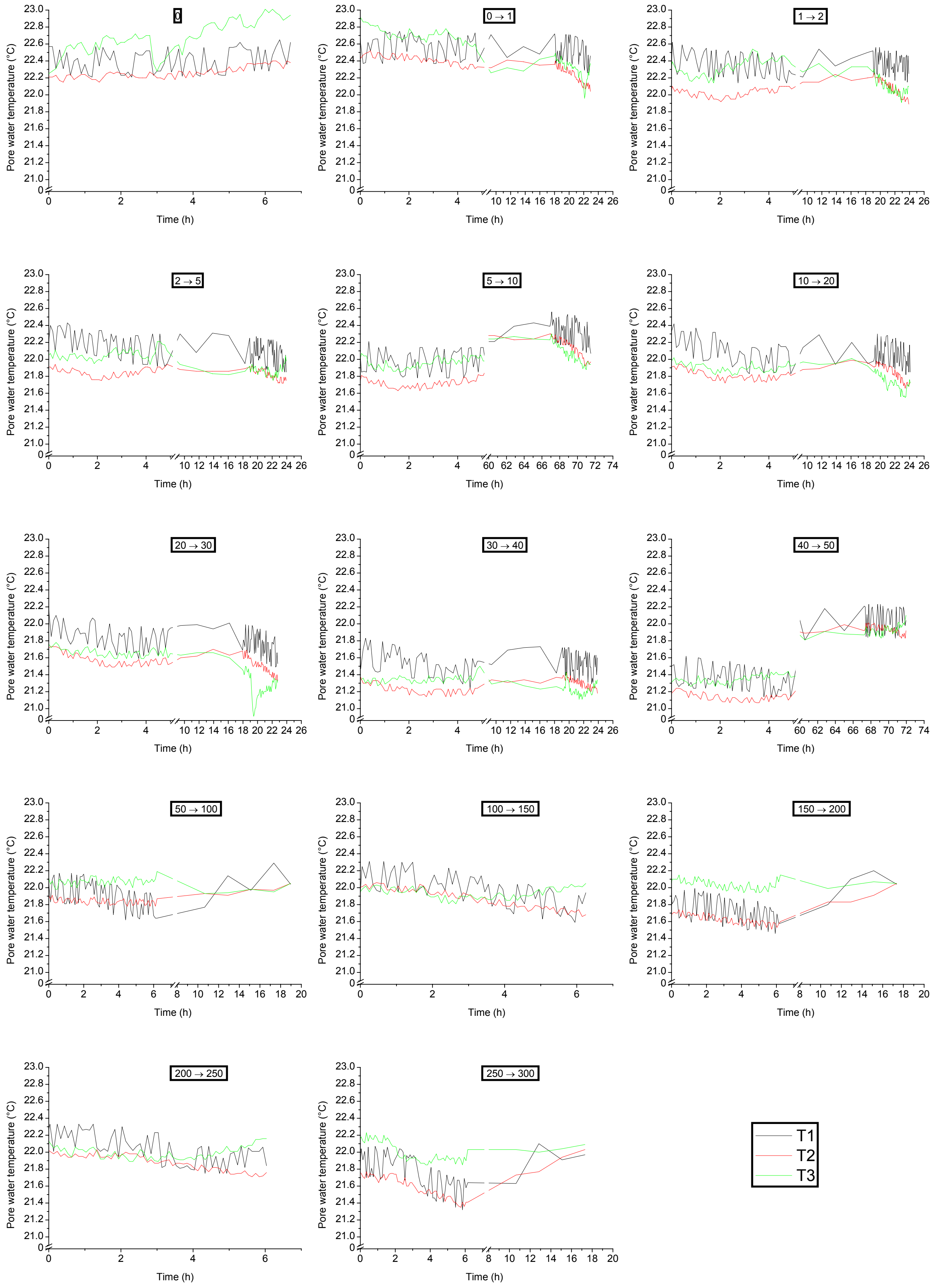

***B.2.3*** *Pore water temperature pattern during calibration. Salt concentrations 0–300 g l*$^{-1}$*. [Concentration displaced calibration solution → concentration injected calibration solution].*